Aerodynamics of Fibrous Particles

PhD Thesis

By

Guo Qiang QI

School of Mechanical Engineering

Faculty of Engineering, Computer and Mathematical Sciences

The University of Adelaide

October 2016

An Errata Sheet of This Thesis

The following figures in this thesis did not obtain written permissions from the copyright owners. The library staff can remove them from the digital version of the thesis.

Page 11, Figure 1.3: Pulverized coal particles

Page 14, Figure 1.5: Saw dust particles

Page 15, Figure 1.5: Bagasse

Page 28, Figure 2.1: The calculated and measured C_D of various regular shapes at right angles of incidence to the flow as a function of a particle Re_p

Table of Contents

List of Figures and Tables

Abstract

This thesis presents the first measurements of the velocities and orientation of nylon fibrous particles with length to diameter ratios of between 35 and 60 where the density ratio between the two phases is of order 1,000. One set of data was obtained with the fibres settling in air at a fibre Reynolds number in the range of 10 – 100 based on the fibres' lengths under conditions that avoided any influence of secondary flows and at a mean volume fraction of 10^{-5}. The other data were obtained with the fibres transported in a turbulent co-flowing jet at the jet Reynolds number of 70,000 in the super-dilute regime. These data are of relevance to the combustion of biomass particles in furnaces and boilers. As such, the data will contribute to the replacement of fossil fuels with biomass, which is an attractive fossil-fuel alternative because it is renewable and the net greenhouse gas emissions are lower than for fossil fuels.

The measurements described above were undertaken with a novel implementation of Particle Tracking Velocimetry (PTV) in which a fibre's orientation, the vertical and horizontal components of velocity, were measured simultaneously based on each fibre's two end-points. The laser used in the experiments was a Quantel Brilliant Twins double-cavity pulsed Nd: YAG 10 Hz laser. The thickness of the light sheet was about 5 mm, which is a value found experimentally to provide a good compromise between a sufficiently high fraction of fibres fully within the light sheet and a reasonable spatial resolution. The one key feature of this method is that the "part-in" fibres within the laser sheet were detected and rejected through an assessment of the signal intensity and signal

intensity gradients. The other key feature is that the volume fraction of the fibres was measured by counting the number of particles in the viewing volume.

Firstly, the drag coefficient of long aspect ratio fibrous particles has been investigated experimentally. A “sphericity” parameter has been widely introduced in previous work to define the drag coefficient of fibrous particles. However it is not suitable for long aspect ratio fibres. In the present work, the relationship between the drag coefficient and a fibre’s Reynolds number based on the diameter for a long fibre was derived and investigated. An equation was proposed to describe the relationship between the volume fraction and settling velocity. It was also found that the scatter of horizontal velocity increases significantly with the volume fraction. The equivalent diameter of a settling fibre in air is reported. Two previous models of the drag coefficients of fibrous particles were also assessed.

Secondly, the influence of volume fractions of the fibrous particles on their settling velocities and orientations was investigated. It was found that the mean settling velocities of the fibrous particles increased significantly with the number density of the fibres for the low volume fractions. This is attributed to the fibres’ orientation transition from the horizontal to the vertical state because of increasing interactions between the fibres, together with the influence of the cloud-like motion on the fibres. The volume fraction also has a strong influence on the mean orientations of the fibrous particles such that the fibres’ orientation tends to be more vertical with an increase in the number density of the fibres.

Thirdly, for a bulk settling motion of the fibrous particles, it has been found that the distributions of the fibres' vertical and horizontal components of settling velocity are nearly Gaussian. The bulk mean settling velocity of the fibres is much higher than that of a single fibre. This is attributed to the bulk motion effect and orientation transition mentioned above. The orientations of the majority of the fibrous particles are nearly horizontal. A key new finding is that the horizontal velocity of the fibres, whilst settling in air, is preferentially aligned with the major axis of the fibres, because a horizontal fibre moving horizontally in this direction has the minimum drag force. Furthermore it has been found that the majority of fibres exhibit rotation and tumbling while settling in air, which contrasts with the previous measurements in water. This is attributed to the fibre's pressure centre being behind the mass centre whilst settling. It has also been found that the fibres' tumbling is inhibited by a decrease in the aspect ratio. Angular velocities of the fibrous particles and their distributions for four types of the fibres are reported.

Fourthly, the influence of the aspect ratio of the fibrous particles on their settling velocities and orientations was investigated for aspect ratios of 35, 48 and 60. For fibres with a constant diameter but different length, it was found that the settling velocity normalized by that of an equivalent sphere ($V_{cx}/V_{eq\text{-}sph}$) decreases with an increase in fibre length. For fibres with the same length but different diameter, both the mean settling velocity and the normalized settling velocity (V_{cx} /$V_{eq\text{-}sph}$) decrease with an increase in diameter. For fibres with the same aspect ratio but different length and diameter, the normalized settling velocity (V_{cx} /$V_{eq\text{-}sph}$) decreases with an increase in particle size.

Lastly, the measurements in a turbulent jet found both that the fibres' most probable orientation tends to be approximately 50° to the axial direction and that there are few fibres that are aligned with the direction of the flow at the centre-line of the jet, which is consistent with the simulation of inertial fibres in a turbulent channel flow. However it contrasts with the previous work of small fibres in a turbulent pipe flow, where the fibres were reported as being predominately aligned with the direction of the flows at the centre-line of a pipe. This difference is attributed to the fibres' inertia. The fibres' inertia is significant for the present jet flow because the density ratio between the particle and fluid phases for the present case is three orders of magnitude larger than that of the turbulent pipe flow. At the centre of the co-flowing jet, the fibres' axial velocity and orientation were found to change little with an increase in volume fractions in the super-dilute regime, which contrasts with the findings of the free-falling cases in which the settling velocity and orientation change significantly with the volume fraction. These differences are attributable to a reduction in the relative significance in the interactions between the wakes of the proximate particles. The fibres' vertical angular velocity is the lowest at the centre-line of the jet and increases significantly in the radial direction, which is consistent with the previous simulations. At the centre-line of the jet, the fibres' normalized radial velocity is much higher than that of the spheres with a similar Stokes number based on diameter. This is attributed to the dual effects of significant orientation of the fibres to the flow and to their tumbling, both of which induce a radial velocity that does not occur with spheres.

Preface

This thesis by publication is submitted in partial fulfillment of the requirements for a Doctor of Philosophy Degree (PhD) at The University of Adelaide. The work outlined in this thesis was performed in The Two-Phase Laboratory of the School of Mechanical Engineering at North Terrace Campus under the supervision of Professor G. J. "Gus" Nathan and A/Professor R.M. Kelso. This thesis consists of ten chapters and an appendix, covering four peer-reviewed journal papers and two conference papers that were first-authored by the author of the present thesis.

The first chapter introduces the significance and the objectives of this research, together with some background information about this work. Chapter 2 presents the literature review for this thesis, covering the known information about the drag coefficient of a fibrous particle, the motion equations of a fibre and the bulk motion of aerosols and fibrous particles in turbulent flows.

Chapters 3 to 6 cover the four papers published in an international journal, *Powder Technology*, which are: Paper 1) PTV measurements of drag coefficient of fibrous particles with large aspect ratio; Paper 2) Aerodynamics of long fibres settling in air at $10 < Re < 100$; Paper 3) The influence of aspect ratio on distribution of settling velocities and orientation of long fibres and Paper 4) Velocity and orientation distribution of fibrous particles in the near-field of a turbulent jet.

Chapters 7 and 8 cover the two conference papers, which are: Paper 1) The influence of number density of fibrous particles on the distribution of settling velocities and fibre orientation and Paper 2) Aerodynamics of long aspect ratio fibrous particles under settling.

Chapters 3 to 8 present the key findings of the aerodynamics of the fibrous particles both whilst settling in air and whilst being transported by a turbulent co-flowing jet. Chapter 9 summarises the conclusions reached and recommends future directions for research work in this field. Following this, Chapter 10 presents the bibliographies, while the principle computer codes written for the work are contained in the Appendix.

Declarations

I certify that this work contains no material which has been accepted for the award of any other degree or diploma in my name, in any university or other tertiary institution and, to the best of my knowledge and belief, contains no material previously published or written by another person, except where due reference has been made in the text. In addition, I certify that no part of this work will, in the future, be used in a submission in my name, for any other degree or diploma in any university or other tertiary institution without the prior approval of the University of Adelaide.

I give consent to this copy of my thesis when deposited in the University Library, being made available for loan and photocopying, subject to the provisions of the Copyright Act 1968. I acknowledge that copyright of published works contained within this thesis (as listed in List of Publications, pages XII–XIII) resides with the copyright holder(s) of those works.

I also give permission for the digital version of my thesis to be made available on the web, via the University's digital research repository, the Library Search and also through web search engines, unless permission has been granted by the University to restrict access for a period of time.

Guo Qiang Qi

List of Publications

Journal paper I:

G.Q. Qi, G.J. Nathan and R.M. Kelso, PTV measurement of drag coefficient of fibrous particles with large aspect ratio, Powder Technology, 229 (2012), 261–269.

Journal paper II:

G.Q. Qi, G.J. Nathan and R.M. Kelso, Aerodynamics of long fibres settling in air at $10 < Re < 100$, Powder Technology, 235 (2013), 550–555.

Journal paper III:

G.Q. Qi, G.J. Nathan and R.M. Kelso, The influence of aspect ratio on distributions of settling velocities and orientations of long fibres, Powder Technology, 257 (2014), 192–197.

Journal paper IV:

G.Q. Qi, G.J. Nathan and T.C.W. Lau, Velocity and orientation distributions of fibrous particles in the near-field of a turbulent jet, Powder Technology, 276 (2015), 10–17.

Conference paper I:

G.Q. Qi, G.J. Nathan and R.M. Kelso, The influence of number density of fibrous particles on the distribution of settling velocities and fibre orientations, 3th

International Solar Cities Congress 2008, ISBN978-0-9803168-7-2, pp201–210, Adelaide, Australia, 2008.

Conference paper II:

G.Q. Qi, G.J. Nathan and R.M. Kelso, Aerodynamics of long aspect ratio fibrous particles under settling, Proceedings of the ASME/JSME 2011 8th Thermal Engineering Joint Congress AJTEC 2011, Honolulu, Hawaii, USA.

Acknowledgements

The completion of this thesis could not have been achieved without the contributions and support from those people listed below.

My thanks go to Professor G. J. “Gus” Nathan, for his guidance, support and meticulous supervision of this work. I would like to express my gratitude to Gus for providing me this opportunity to do research in such interesting areas of aerodynamics of fibrous particles. I really appreciate his unwavering supervision throughout my PhD candidature. Thank you Gus. Dedicated support from my first co-supervisor, Associate Professor Richard Kelso, in providing me with the insight into aerodynamics of fibres, and also his additional supervision is gratefully acknowledged. In the early part of my candidature, my second co-supervisor, Dr Chong Wong also helped me and I thank him for this help.

This study has been supported financially by the Faculty of Engineering, Computer & Mathematical Sciences of The University of Adelaide and by an ARC Discovery Grant (Grant Number: DP120102961), both of which are gratefully acknowledged.

The support of many people within the School of Mechanical Engineering, such as the workshop staff, postgraduates, research fellows and teachers, is also appreciated. Special thanks go to Dr Paul Medwell, Mr Difan Tang, and Dr Adam Langman who assisted with the data processing. Also thanks go to Dr Peter Kalt who assisted with the

experimental setup. I am grateful for the efforts in the lab of my co-researchers, Richard Forman and Christine Mayer. The support from Mr Steven Kloeden in the workshop and Dr Erwin Gamboa for photomicrography is acknowledged here too. I also thank Miss Alison-Jane Hunter for her help in proof-reading my thesis. Also I would like to thank, Dr Collin Hansen, Tien-Fu Lu, Benjamin Cazzolato, late Russell Luxton, Bassam Dally, Anthony Zander, Cristian Birzer, Collin Kestell, Carl Howard, Gerald Schneider, Michael Riese, Lei Chen, Peter Lanspeary, Steven Grainger, Timothy Lau, Grant England, Karen Adams, Maziar Arjomandi, Woei Lean Saw, Phuc Nguyen, John Codrington, Stuart Wildy, George Szego, Ms Dorothy Missingham, Sarah Crook, Fei Gao, Elizabeth Smith, Wendy Brown, Kathy Cooper, Yvette Knapp, Jingjing Ye, Bailey Spaven, Tracy Miller, Mr Shi Zhao, Billy Constantine, Stephen Slape, Dejun Gao, Jiyun Qin, Michael Evans, Kuan Tan and Eyad Hassan, for their helps to my work. I also thank the following people for their helps to my work: Zebb Prime, Valerie Linton, Justin Hardi, Ming Gao, Sean Dillon, Max Bull, Manfred Zokel, Lindsay Doherty, Ian Brown, Laura Brooks, Marcus Boyd, Bob Dyer, Bill Finch, Zahra Bagheri, Awadalla Mohamed, Amir Anvar, Erica Smith, ZhenZhang Liu, Lydia Zhang, Lancy Xie, Junwei Wu, Will Roberson, Victoria Samra, Rae Tyler, Shahrooz Afsharvahid, Adrian Selby, Philip Schmidt, Margaret Schiller, Carlo Sansour, Sam Lu, Ashley Rowland, Robertson Graeme, Rebecca Jones, Bryce Pearce, Richard Pateman, Jordan Parham, David Osborne, Grant Nelson, Narges Miri, Maung Myo, Rick Morgans, Danielle Moreau, Mo Jangoh, Alan Mittler, Akhilesh Mimani, Mat Ali Mohamed Sukri, Mohammadamin Miremadi, Patrick Marshallsay, Mahmoud Saleh, Toby Lightheart, Tan Liddy, Xun Li, Letton Scott, S-K Lee, Damien Leclercq, Mike Kidner, Joel Walker, Javad Farrokhi Derakhshandeh, Ron Jager, Jafarian Seyed Mehdi, Hao Huang, Eric Hu, David Harvey, Steven Harding and Nader Qamar.

I also want to express my gratitude to my Chinese friends, Miss Yi Yuan, Mr Zhenjun Wang, Dr Yincheng Guo and Jianzhong Lin, Mr Yuan Wu, Pingfei Xia and Changdi Mu, Ms Ran Mu, for their helps to my work.

The editors and the anonymous journal reviewers are gratefully acknowledged for their insight comments on each of the papers listed in this thesis.

I have been fortunate to have been blessed with the support, love and understandings of my son, Jialun Qi, my late mother, Guizhen Liu, throughout the course of this research. I have also been blessed with my late father Lianzhou Qi. This thesis is dedicated to the three of them.

Lastly, but most importantly of all, I would like to thank my God who loves me and who gave me the ability to do this work. May All Glory be to God on High/the Lord, our God.

Summary of Each Paper

Paper I: PTV measurement of drag coefficient of fibrous particles with large aspect ratio

This paper reports the simultaneous laser-based measurements of the orientation and velocities of the fibrous particles, whilst settling in air, under super dilute conditions without any influence of secondary flows (which contrasts with the previous investigations), and at the fibre Reynolds numbers of 0.5 – 2 based on the fibre diameter. This technique employs a two-dimensional Particle Tracking Velocimetry (PTV) to calculate the fibres' orientation by the use of fibres of near-constant length and velocities based on the two end-points. The method found a way to detect whether a fibre is in the same plane as the light sheet by rejecting fibres that are "partly-in" in the light sheet, because the measured lengths of such fibrous particles are false. In the present work, the drag coefficient of a long aspect ratio fibre, whilst settling in air, was derived and investigated as a function of Re_d and orientation. The controlling length scale (or equivalent diameter) of the settling fibre in air is reported. It was also found that the scatter of horizontal velocity increases significantly with the volume fraction. An equation was proposed to describe the relationship between the volume fraction and the settling velocity. Two models by Fan *et al*. [1] and Clift *et al*. [2] were also assessed and were found to be in poor agreement with the current measurements.

Paper II: Aerodynamics of long fibres settling in air at 10 < *Re* < 100

This paper reports the aerodynamic behaviour of long aspect ratio nylon fibrous particles also whilst settling in air under super dilute conditions without any influence of secondary flows and at the fibre Re_L = 10 – 100. Measurements of the orientation and velocities of the fibrous particles were also undertaken by two-dimensional Particle Tracking Velocimetry (PTV), based on the two end-points. In this paper, a statistical evaluation of the fibres' mean vertical and horizontal components of settling velocities, angular velocity, and orientation and number density is presented and used to assess the aerodynamics of the fibrous particles. The influence of the volume fraction on the settling velocity and orientation of the fibrous particles was assessed and compared with the work of Salmela *et al*. [24] and Kuusela [33] which were in the range of $Re_L \sim O(1)$, along with the work of Herzhaft and Guazzelli [22] and Butler and Shaqfeh [39] which were in the range of $Re_L \sim O(0)$. It was found that the fibres' orientation depends on their Reynolds numbers, which is consistent with the findings of Hinds [64]. The mean settling velocities of the fibrous particles increase significantly and the fibres' orientations tend to be more vertical with an increase in the number density of the fibres under the low volume fractions. The present work represents the first detailed assessment of the influence of volume fraction under above conditions. It was also found and first reported that the transverse velocity of the fibres whilst settling in air is preferentially aligned with the major axis of the fibres, because a horizontal fibre moving horizontally in this direction has a minimum drag force.

Paper III: The influence of aspect ratio on distributions of settling velocities and orientations of long fibres

This paper reports the influence of the aspect ratios of the fibrous particles on their

settling velocities and orientations under dilute conditions at the fibre Reynolds numbers of 3 – 70 based on the fibre lengths and for aspect ratios of 35, 48 and 60. This study focuses on the bulk settling motion of the fibrous particles in air, which is different from that of a single fibre. The measurements were performed for three cases: 1) for fibres with a constant diameter but different length it has been found that the mean vertical settling velocity of the bulk settling fibres is not independent of the fibre length, the mean settling velocity of the long fibres is a little higher than that of the short ones, which is different from the findings of McKay *et al*. [15] who reported the terminal settling velocity of a single fibre is nearly independent of the aspect ratio; 2) for fibres with the same length but different diameter it has been found that both the mean settling velocity and the normalized settling velocity (V_{cx} /$V_{eq\text{-}sph}$) decrease with an increase in diameter; 3) for fibres with the same aspect ratio but different length and diameter it has been found that the normalized settling velocity (V_{cx} /$V_{eq\text{-}sph}$) decreases with an increase in particle size. It was also found that the fibres swing significantly whilst settling in air and the fibres' tumbling is inhibited by a decrease in the aspect ratio. The vertical angular velocity and their distributions for four types of the fibres are also reported.

Paper IV: Velocity and orientation distributions of fibrous particles in the near-field of a turbulent jet

This paper reports the measurements of the velocity, angular velocity and orientation of the nylon fibrous particles of the long aspect ratio in the super-dilute regime, in the near-field of a co-flowing jet at a jet Reynolds number of 70,000. Measurements were performed in the near-field, i.e. in the axial range of $0 < x/D < 4$, by employing the

similar Particle Tracking Velocimetry method described above. One of the key findings is that at the centre-line of the jet, the fibres' most probable orientation tends to be approximately 50° to the axial direction and that there are few fibres that are aligned with the direction of the flow, which is consistent with the simulation of inertial fibres in a turbulent channel flow [118]. However it contrasts with the previous work of small fibres in a turbulent pipe flow [95]. This difference is attributed to the fibres' inertia. The fibres' inertia in the present case is much more significant than for that in the pipe flow. It is also found that at the centre of the co-flowing jet, the fibres' axial velocity and orientation change little with an increase in volume fractions in the super-dilute regime, which contrasts with the findings of the free-falling cases. This is attributed to the greater significance of inertia and a reduced significance of the interactions between the wakes of proximate particles, because the "background" flow in the carrier phase is turbulent instead of laminar. The fibres' vertical angular velocity is at its lowest at the centre-line of the jet and increases significantly in the radial direction, which is consistent with the previous simulation [51]. At the centre-line of the jet, the fibres' normalized radial velocity is at an order of magnitude larger than that of the spheres'. This is attributed to the fibres' tumbling motion.

Notation

A_p	Surface area of a non-spherical particle (m^2)
$a_r = L/d$	Aspect ratio of length to diameter of a fibrous particle
A_s	Surface area of a sphere (m^2)
d	Diameter of a fibrous particle (m)
d_{ev}	Equivalent diameter of a fibrous particle, based on volume (m)
d_{eq}	Equivalent diameter of a fibrous particle, based on its projected area and its mean orientation (m)
d_{es}	Equivalent diameter of a fibrous particle, based on its surface area (m)
D	Diameter of a spherical particle (m) (Chapters 1 – 5, 7 – 10); Diameter of the supply pipe (Chapter 6)
F_D	Drag force on a particle (N)
F_g	Gravitational force on a particle (N)
H	Thickness of the laser sheet (m)
L	Length of a fibrous particle (m) (Chapters 1 – 5, 7 – 10); Length of the supply pipe (m) (Chapter 6)
L_p	Length of a fibrous particle (m) (Chapter 6)
L_x	Component of the projected length of a fibre in the direction of the x axis
L_y	Component of the projected length of a fibre in the direction of the y axis

n_p	Number of particles on an image
r	Radial direction of the supply pipe (Chapter 6)
R	Resolution of the images (µm/pixel)
Re_{p}	A spherical particle's Reynolds number: $\mathrm{Re}_p = \frac{\rho_{air} V_{rel} D}{\mu}$, where D is the diameter of a sphere
Re_{L}	A fibre's Reynolds number based on its length, $\mathrm{Re}_L = \frac{\rho_{air} V_{rel} L}{\mu}$
Re_{d}	A fibre's Reynolds number based on its diameter, $\mathrm{Re}_d = \frac{\rho_{air} V_{rel} d}{\mu}$
Re_{deq}	A fibre's Reynolds number based on its equivalent diameter
$Re_{\mathrm{de,v}}$	A fibre's Reynolds number based on its diameter of equivalent volume
$Re_{\mathrm{de,s}}$	A fibre's Reynolds number based on its diameter of equivalent surface area
Δt	Time separation between a pair of images (µs)
V_c	Velocity of the centroid of a fibrous particle (m/s)
V_{cx}	Fibres' settling velocity, that is: the velocity of the centroid of a fibrous particle in the vertical direction (m/s)
$\overline{V_{cx}}$	Mean settling velocity of the fibres, that is: mean vertical velocity of the centroid of the fibrous particles in the x axis (vertical) direction (m/s)
V_{cy}	Velocity of the centroid of a fibrous particle in the y axis (horizontal) direction (m/s)
$\overline{V_{cy}}$	Mean velocity of the centroid of the fibrous particles in the y axis (horizontal) direction (m/s)

V_{cz}	Velocity of the centroid of a fibrous particle in the *z* axis direction (m/s)
V_{e1}	Velocity of endpoint 1 of a fibrous particle (m/s)
V_{e1x}	Velocity of endpoint 1 of a fibrous particle in the *x* axis direction (m/s)
V_{e1y}	Velocity of endpoint 1 of a fibrous particle in the *y* axis direction (m/s)
V_{e1z}	Velocity of endpoint 1 of a fibrous particle in the *z* axis direction (m/s)
V_{e2}	Velocity of endpoint 2 of a fibrous particle (m/s)
V_{e2x}	Velocity of endpoint 2 of a fibrous particle in the *x* axis direction (m/s)
V_{e2y}	Velocity of endpoint 2 of a fibrous particle in the *y* axis direction (m/s)
V_{e2z}	Velocity of endpoint 2 of a fibrous particle in the *z* axis direction (m/s)
V_{e1r}	Velocity of endpoint 1 of a fibrous particle in the radial direction of the jet pipe (m/s)
V_{e2r}	Velocity of endpoint 2 of a fibrous particle in the radial direction of the jet pipe (m/s)
$V_{c,0}$	Central-line exit velocity of a single-phase of the jet (m/s)
V_{ts}	Terminal settling velocity of a particle (m/s)
$\overline{V_{ts}}$	Mean terminal settling velocity of the fibrous particles (m/s)
V_{rel}	Relative velocity between a fluid and a particle (m/s)
GREEK	
α	Azimuth of the major axis of a fibrous particle, relative to the viewing plane (°)
δ	The minor axis of the basic rectangle of a fibrous particle on the images
μ	Air viscosity (Pa s), 1.81×10^{-5} at 293K (Lab temperature)

θ	Orientation of a fibrous particle, the angle between the major axis of a fibrous particle and the direction of gravity (°)
$\bar{\theta}$	Mean orientation of the fibrous particles (°)
$\bar{\theta}_{ts}$	Mean orientation of the fibrous particles in terminal settling velocity (°)
ρ_{air}	Density of air (kg/m^3); 1.20 kg/m^3 at 293K (Lab temperature)
ρ_{f}	Density of the fluid (kg/m^3)
ρ_{p}	Density of a particle (kg/m^3)
ρ_{fp}	Density of fibrous particles (kg/m^3); nylon fibre: 1150 kg/m^3
$\overline{\omega}_{vertical}$	Mean angular velocity of the fibrous particles in a vertical direction (rad/s)
$\overline{\omega}_{x}$	Mean angular velocity of the fibrous particles in the *x* axis direction (rad/s)
Φ	Particles' volume fraction within the fluid
χ	Dynamic shape factor, $\chi = \dfrac{F_D}{3\pi\mu V d_{ev}}$
Ψ	Sphericity of a non-spherical particle, $\psi = \dfrac{A_s}{A_p}$, where A_s is the surface area of a sphere that has the same volume as a non-spherical particle
Ψ_{fp}	Sphericity of a fibrous particle, $\psi_{fp} = \dfrac{d_{ev}^{\ 2}}{dL + d^2/2}$

1 Introduction

1.1 Significance of This Research

In 2014, the Intergovernmental Panel on Climate Change (IPCC) reported: "An urgent UN climate deal is needed to meet CO_2 targets and immediate and full participation in global climate agreement is needed to curb temperature rise". It is widely accepted that climate change is, without question, one of the most serious challenges human beings face [124]. CO_2 reduction has become not only a technical issue, but also very much a political one [68]. The International Energy Outlook [100] pointed out that "atmospheric concentrations of carbon dioxide have been rising at a rate of about 0.6 percent annually in recent years, and that growth rate is likely to increase. As a result, by the middle of the 21st century, carbon dioxide concentrations in the atmosphere could be double their pre-industrialization level". The combustion of fossil fuels is the dominant source of energy for industry, transportation and suburbia, which makes these elements integral to the functioning of society in its current form [113]. Much policy analysis has focused on CO_2 from burning fossil fuels, which comprise about 60% of total global greenhouse gas emissions in 2010. Emissions of all greenhouse gases have increased by about 75% since 1970 [124]. Carbon dioxide does not directly impair human health but is a 'greenhouse gas', trapping the earth's heat and contributing to the potential for global warming, which has the potential to wreck livelihoods, stunt economic growth and change entire ecosystems irreversibly. Fossil fuels also emit nitrogen oxides (NO_x) when they are burned. Nitrogen oxides are precursors to the

formation of ozone and they also contribute to the formation of acid rain. As a direct result of this, there is a need for humans to take various measures to reduce greenhouse gas emissions.

Furthermore, fossil fuels, coal, oil and natural gas are not renewable energy sources. The fossil fuels that are being used today have been forming over millions of years. Fossil fuels currently meet 80% of the global energy demand and the global energy demand in 2035 is projected to rise by 40% [126]. At the present rate of consumption, the known reserves of fossil fuels will be depleted in the foreseeable future. Table 1.1 shows the conventional fossil fuels' reserve-to-production ratio (RPR) of 2013 [125]. It can be seen that at the end of that year, the global total of proven reserves of coal was 891.5 billion tons whilst the world consumption rate throughout that year was 7.89 billion tons. Based upon this, in 113 years the coal reserves will be depleted. Also, in terms of oil, the table shows that the R/P (reserve/production) ratio will last for 53.3 years and natural gas will last for 55.1 years. The International Energy Agency report, Resources to Reserves 2013 [126], also gives a similar range of RPR for conventional fossil fuels. Recently, access to unconventional fossil fuels (tight gas, shale oil, shale gas and coal-bed methane) has seen substantial growth in North America. Although the global resources and reserves bases for unconventional oil are similar to that for conventional oil, these new resources could only extend the global oil supply by decades to a century and that extension only if technologies are developed to harvest them economically [126]. Therefore the resources are still finite in the long-term future. In addition, the IPCC has argued that fossil fuels should be phased out by 2100.

Table 1.1: Conventional fossil fuels reserve-to-production ratio (RPR) [125].

Fuels	**Total proved reserves at end 2013**	**Production rate per year (2013)**	**RPR (years)**
Coal	891.5 Billion tons	7.89 Billion tons	113
Natural gas	185.7 Trillion cubic metres	3.37 Trillion cubic metres	55.1
Oil	1687.9 Billion barrels	31.55 Billion barrels	53.3

One approach to reduce the use of fossil fuels is partial substitution with biomass, or organic matter, which is a renewable and environmentally friendly resource for energy supply, because biomass absorbs carbon dioxide through a process of photosynthesis as it grows [68]. Such fuels can be derived from trees, agricultural residues and other plants and algae. The potential of biomass energy derived from forest and agricultural residues world-wide, is estimated at about 30 EJ/year, compared with an annual world-wide energy demand of over 400 EJ. If biomass is to contribute to a larger extent to the world's energy supply, then energy farming (the cultivation of dedicated crops for energy purposes) will be required, using fallow and marginal lands, the latter being largely unsuited for food crops in any case. When energy crops are considered as a source of biomass, the total energy potential of biomass for energy production may be considerably larger than the energy potential of biomass residues [131]. For example, many countries have tried to alter trends in CO_2 emissions with policies that would make the energy supply system more efficient and shift to low emission fuels, including renewables and nuclear power [124], because nearly all climate-altering gases have atmospheric lifetimes sufficiently long that the location of their emission is immaterial to the damage they cause. CO_2 emissions spread worldwide and affect the climate everywhere.

Although the percentage of biomass being used around the world is increasing [50, 127] and policies encouraging the development of forest biomass energy have generally adopted a view of biomass as a carbon neutral energy source, there is a debate about the life cycle emissions of CO_2 from biomass for near-term reduction of greenhouse gases. Alsamaq *et al*. [137] assessed agricultural residues and point out that the Life Cycle Assessment results reveal that the utilization of agricultural residues for biogas production would lead to high environmental benefits in terms of their Global Warming Potential. When compared with coal-based power generation systems, sugarcane bioenergy systems are able to avoid CO_2 emissions at rates that range between 1.081 and 1.137 $kgCO_2/kWh$, depending on the cane-residue utilisation strategy adopted [138]. The environmental performance of willow biomass crop production systems in New York (NY) is analysed using life cycle assessment (LCA) methodology. The base-case, which represents current practices in NY, produces 55 units of biomass energy per unit of fossil energy consumed over the biomass crop's 23-year lifetime [139]. An exploration of the literature [128] of this more complex picture in the context of biomass energy development in Massachusetts, reveals that forest biomass generally emits more greenhouse gases than fossil fuels per unit of energy produced. Based on the study of life cycle assessments of wood biomass [128], 32 years are required to recover the carbon debt through forest growth and 100 years to reach greenhouse neutral. Therefore it seems that it is not realistic to meet CO_2 reduction targets in the near-term by substituting fossil fuels with forest biomass. However many forest scientists have expressed concern over equating biogenic carbon emission with fossil fuel emissions, such as is contemplated in the EPA Tailoring Rule. They have also noted, correctly, that carbon dioxide released from the combustion of wood biomass is part of the global cycle of biogenic carbon and “does not increase the amount of carbon in circulation”, as

would fossil fuel emissions [127]. Thus, the implication is that the use of wood biomass for energy will imply no net forest emissions to the atmosphere, given adequate regeneration and sufficient time, so biomass energy is expected to play a major role in the substitution of renewable energy sources for fossil fuels. Raymer [129] pointed out that the use of forest products, either instead of more energy-intensive materials, or instead of fossil fuels, can contribute to a long-term solution on avoiding greenhouse gas emissions. In Australia, over half of the production of biomass energy comes from bagasse and other agricultural residues, which is approximately carbon neutral in the short-term.

With increasing importance being attached to the concept of biomass as an energy supply and with the increasing use of biomass in the existing combustion system, there is a growing awareness of the need to improve biomass combustion. Technological advancements in biomass energy conversion come from three sources - enhanced efficiency of biomass energy conversion technologies, improved fuel processing technologies and enhanced efficiency of end-use technologies [132]. A wide range of combustion technologies exist, most of which have been, or could be, adapted to suit the partial or full utilisation of biomass. Examples include fixed-bed and moving-grade combustors, fluidised bed combustors, gasifiers and conventional furnaces, boilers and kilns. These latter conventional systems, in which the fuel is burned in a flame, are by far the most common system within Australia, along with the rest of the world. In such systems the fuel is typically either blown in a gas or as a fine powder (pulverized fuel), or it is sprayed in as fine droplets. The air is typically blown in around the fuel. Since vast capital is tied up in the infrastructure of these existing combustion systems, it is

usually more cost-effective to adapt them to allow the (perhaps partial) use of biomass than it is to install entirely new technologies for the purpose. Likewise it is usually cost-effective to refine existing facilities which already utilise biomass. These technologies include blending biomass with coal on the fuel stockpile, injecting biomass separately into a boiler, and gasifying biomass for subsequent firing in an electricity generating system [133]. Pulverized, fine coal particles are granular and an almost universal assumption is that coal dust particles are spherical and homogeneous [68], that is, particles of pulverized fossil fuels can be approximated as being spheres. The aerodynamics of spherical particles has been extensively studied for more than 50 years [114]. However, biomass, such as wood, bagasse and straw, are fibrous and not spherical. The aerodynamic behaviour of fibrous particles is observably different from spherical particles, because fibrous particles are orientation-dependent. Some aspects of spherical particles, such as the mechanisms controlling the distribution of isolated spherical particles and clustering effects, terminal settling velocities of spheres, trajectories and concentrations in jet flows, are relatively well understood [134], [135], [136]. However, there is a paucity of data describing the aerodynamics of fibrous particles. For this reason, there is a need to perform a fundamental study of the aerodynamics of fibrous particles in conditions of relevance to biomass combustion, coupled with a need to understand the mechanisms of the aerodynamic behaviours of fibrous particles in furnaces and boilers, although the applications of the research may be broader. For example, the dynamic behaviour of fibrous particles is also of great importance to many other fields of industry, such as aerosol physics and atmospheric science, the paper and pulping industry, compound materials and the textile industry [31], [52], [54], [57], [59].

1.2 Biomass in Australia

Biomass energy is widely available all over the world. The Australian Energy Resource Assessment [141] reported that current global bioenergy resources used for generating electricity and heat are dominated by forestry and agriculture residues and organic waste streams. Bioenergy represents around 10% of the world's primary energy consumption.

In Australia, the potential bioenergy resources are large and diverse. Unused biomass residues and waste are a significant under-exploited resource [141]. Bioenergy accounted for only 3% of Australia's primary energy consumption, which is 7% lower than the world average in 2011–12, but it represented 68% of Australia's renewable energy use [141]. Australia's energy policy aims to balance the growing demand for energy with the promotion of a lower carbon economy, incorporating international commitments regarding climate change. Australia is taking a strong, credible and responsible commitment to the Paris climate change conference in December 2015. The Australian Government will reduce greenhouse gas emissions to 26% – 28% below 2005 levels by 2030. This target represents a 50% – 52% reduction in emissions per capita and a 64% – 65% reduction in the emissions intensity of the economy between 2005 and 2030 [144].

The majority of Australia's bioenergy use is sourced from bagasse (sugar cane residues) and wood waste, which represents 86% of bioenergy use for direct heat and electricity generation [141]. Australia's primary energy consumption of biomass is projected to increase by around 195 PJ to 231 PJ by 2049-50, or at an average rate of 0.5% a year [140]. Therefore, it is generally expected that wood and bagasse will play an increasingly important role in the future as a renewable energy supply in Australia.

The percentage of biomass being used around the world is increasing partially to replace fossil fuels. In Australia, bioenergy for electricity and heat generation is produced predominantly from by-products of sugar production and waste streams. Future energy crops may include tree crops, woody weeds and algae as well as expanding into crop and food residues. The main factors are technology costs, reliable supply and the consistent quality of biomass [140]. Biomass co-firing in coal-fired power stations can reduce carbon dioxide emissions in an amount approximately proportional to the proportion of biomass used. Wood waste is generally used because coal fired boilers can usually co-fire a small amount of wood waste without major modification to the existing equipment [141]. Figure 1.1 presents the potential for stationary biomass electricity generation in Australia. It can be seen that electricity generation from bagasse and forest residues will increase 1.8 and 3 fold, respectively, by 2050.

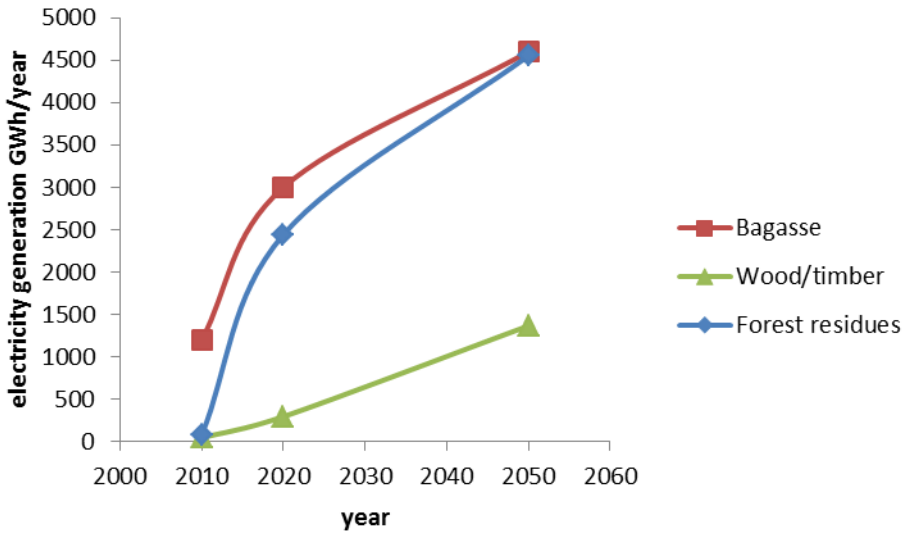

Figure 1.1: Potential for stationary biomass electricity generation in Australia. The data comes from the Australian energy projections to 2049–50 [140].

Figure 1.2 presents the percentage of bagasse and wood, and wood waste used for renewable energy within Australia [145]. Currently most sugar mills burn bagasse, the fibrous residue of sugar cane processing, to generate steam for the mills and generate electricity in Queensland. So maximising the production of steam and electricity is becoming increasingly important for sugar mills to maintain their economic viability in the highly competitive world sugar market. Wood waste and forest residues are only used in a few bioenergy plants in Australia for generating electricity. For the purposes of resource assessment, it is assumed that native forest wood waste will remain constant; the potential from plantations may increase in line with plantation expansion. Wood related waste for energy generation, while having economic benefits, also has to be managed in terms of environmental considerations [140].

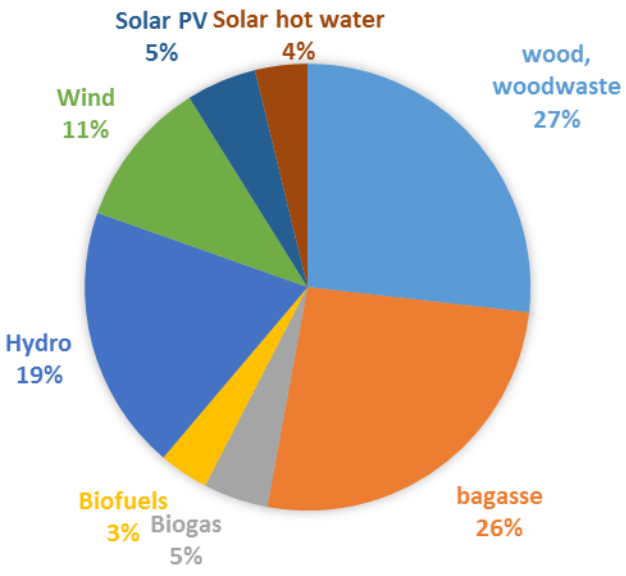

Figure 1.2: Percentage of bagasse and wood, and wood waste used for renewable energy within Australia. The data comes from the Australian Energy Update 2015 [145].

1.3 Pulverized Coal and Spherical Particles

Coal has played a major role in the production of electricity since the first power plants were built. Coal power, an established electricity source that provides vast quantities of inexpensive and reliable power, has become more important as supplies of oil and natural gas diminish, although coal is seen as being an increasingly undesirable fuel due to its high carbon intensity and high ash content. Natural gas is seen as being the transitional fuel toward biomass, since it is cleaner. The last five years have seen an increase in the supply of natural gas due to the increased use of unconventional gas because there are vast reserves of unconventional gas. Nevertheless, coal remains an important fuel source.

Australia is richly endowed with natural energy resources and holds an estimated 9% of the coal resources in the world. Australia is currently the world's largest exporter of coal and coal exports accounted for more than half of all exports on an energy content basis. [141]. In 1999, coal burning produced about 83.9% of the electricity generated in Australia [50]. In 2011–12, total electricity production was around 914 PJ in Australia. Coal accounts for about two-thirds of Australia's electricity generation, followed by gas (19%) [141]. In the 1920s, pulverized coal firing was developed. The concept of burning coal that has been pulverized into a fine powder stems from the belief that if the coal is made fine enough, it will burn almost as easily and efficiently as gas [146]. Figure 1.3 presents a picture of pulverized coal particles.

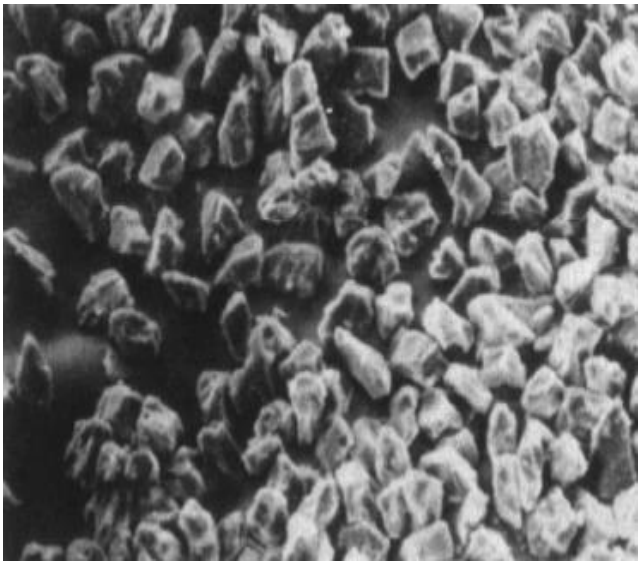

Figure 1.3: Pulverized coal particles (their size is in the range of 75µm) [68].

Prior to combustion in most industrial processes, such as a coal fired power generation plant, the coal is milled into fine particles to be conveyed to the burner [113]. The conveying and combustion of particle-laden flows is the practical realisation of the much broader field of multiphase flow. A multiphase system may be a gas-liquid, gas-solid, liquid-solid, or three phase flow. The conveying and combustion of particles in air is a type of gas-solid flow. All combustion technologies employed to optimize the combustion, performance and to reduce in-flame emissions, rely on optimising and controlling the trajectories and residence times of the fuel through the various stages of its combustion. This, in turn, requires detailed knowledge of fuel properties and furnace aerodynamics.

Currently most existing combustion systems in conventional furnaces, boilers and kilns

are designed for the use of fossil fuels, of which pulverised fuels (PF) are the most common. There have been many advances in combustion technologies for conventional flames. These include a range of technologies to abate oxides of nitrogen, NO_x, such as staged combustion, re-burn and flue gas recirculation [142]. In addition, methods have been devised to minimize problems associated with ash, such as its deposition on boiler tubes. A number of options are also available to achieve modest improvements in efficiency and greenhouse gas reductions at existing coal plants, such as biomass co-firing [141].

1.4 Biomass and Fibrous Particles

The term "fibre" has been applied to a wide variety of particles having an elongated shape. The behaviour of fibrous particles suspended in air is a function of the fibre dimensions. Assuming either a cylindrical or prolate spheroidal shape, these dimensions can be defined by two parameters: length and diameter. A fibrous particle is defined as a particle whose length was at least three times greater than its diameter (i.e., one dimension of the particle is significantly greater than the other two) (Figure 1.4) [47]. Aspect ratio is a third important parameter to describe a fibrous particle. Aspect ratio is defined as the ratio of length to diameter of a fibre. Usually as the aspect ratio of a particle is far greater than one (such as 5, 8, 10, 20, 50), the particle can be regarded as a fibrous particle.

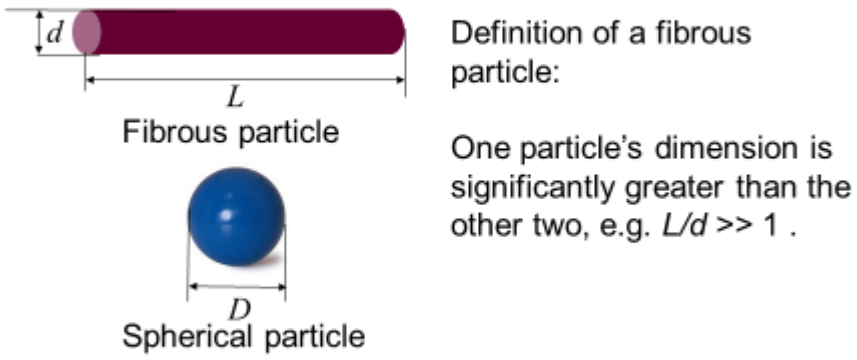

Figure 1.4: The definition of a fibrous particle [47].

Most bio-fuels, such as the saw dust from wood, bagasse and straw, are fibrous. Figures 1.5 and 1.6 present pictures of saw dust particles and bagasse. From these Figures it can be seen that they are fibrous with a tendency towards a cylindrical shape. Also, whilst the real shape of biomass particles is complex, the particles approximate cylinders much better than spheres. Hence it is more reasonable to assume a cylindrical shape when calculating their aerodynamic behaviour. (Please note that the real shapes of particles of pulverized coal are complex too).

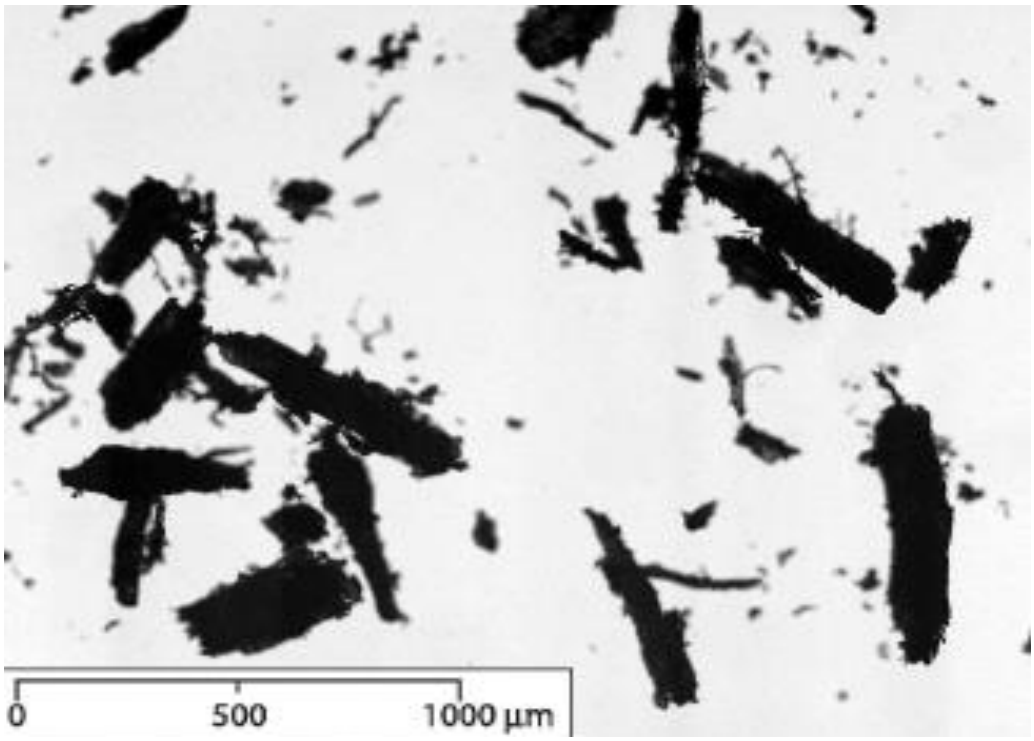

Figure 1.5: Saw dust particles [67].

Figure 1.6: Bagasse [143].

Figure 1.7 presents the settling motions of a fibrous particle and a spherical particle in air. From the Figure it can be seen that different orientations of a fibre will result in different aerodynamic behaviour.

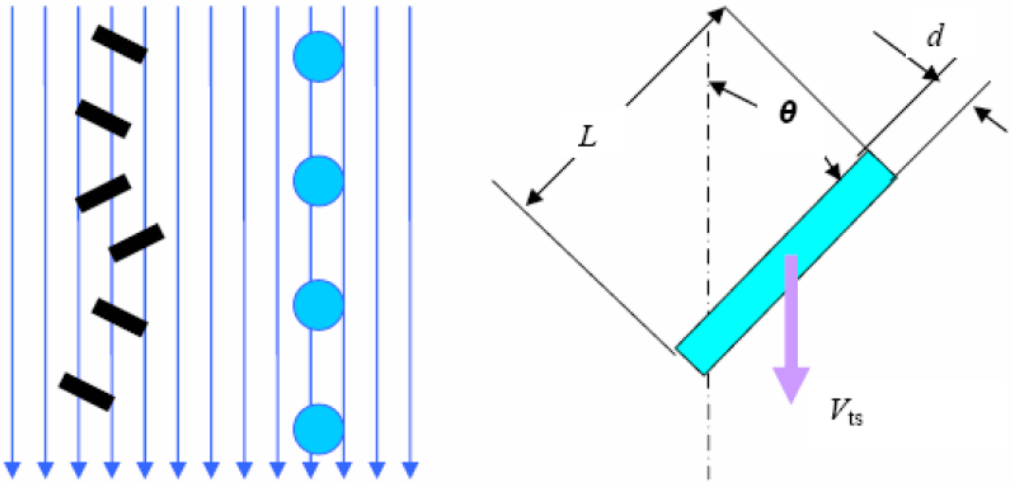

Figure 1.7: The settling motion of a fibrous particle. This Figure derived from references [47] and [68].

1.5 Studies of Fibrous Particles

The diameter, aspect ratio, volume fraction and Reynolds number of a fibrous particle are four important parameters in fibre-air two phase flows. The diameter determines the drag force acting on the fibre [64]. The aspect ratio determines the torque acting on the fibre and fibre-fluid interactions [105]. Furthermore, the aspect ratio influences the spatial orientation of the fibre. The volume fraction determines whether the interactions between fibres are significant. In terms of single fibres, when settling occurs with a fibre Reynolds number, Re_d (defined explicitly in the Notation section), greater than about 10, the fibre is oriented perpendicular to the direction of settling; for $0.1 < Re_d < 10$ there is a partial alignment, and below a Reynolds number of 0.1 there is no alignment [64].

The terminal settling velocity and drag coefficient of a fibrous particle have been used as important design parameters in some industries. Many research studies [3–6], [8], [10], [12], [14], [16–17] have been conducted to develop the equations relating the drag coefficient of a fibre to its Reynolds number. However many of them [3], [5–6], [8], [16–17] introduced the concepts of sphericity, ψ (defined explicitly in the Notation section), or shape factors to simplify the calculation. However these parameters are not applicable to long aspect ratio fibres. For example, Haider and Levenspiel [3] proposed an equation by introduction of sphericity, where the fit is quite good for particles, $\psi > 0.67$. However for the long fibres, such as fibres with $L/d = 40$ and $\psi < 0.67$, the equation is not applicable. Swamee and Ojha [6] also developed a correlation with the Corey shape factor, $\beta = c/(ab)^{1/2}$, where $a > b > c$ are the lengths of the three principal axes of the particle. However, this parameter is only applicable within the range of $0.3 < \beta < 1$.

Therefore the relationship between the drag coefficient of a fibre with a large aspect ratio and its Reynolds number is still largely unknown.

There are not many experimental studies focusing on the aerodynamics of fibrous particles. Herzhaft and Guazzelli [22] investigated the hydrodynamic behaviour of glass-rods in dilute and semi-dilute suspensions for fibre $Re_L \approx 0.0001$ (Re_L is defined explicitly in the Notation section) experimentally. Metzger *et al.* [23] also conducted the experiment under the same Re_L. Salmela *et al*. [24] did some measurements at $Re_L < 9$ in water. However, so far, no measurements are available for fibrous particles at fibre $10 < Re_L < 100$ in dilute conditions with a volume fraction ≈ 0.0005. Because the orientation of fibrous particles depends on their Reynolds number [64], the questions are arising from this: What is the distribution of orientation, settling and horizontal velocities of fibrous particles whist settling in air with $10 < Re_L < 100$ and volume fraction ≈ 0.0005? What is the influence of the number density of fibrous particles on the settling velocities and orientations under this condition?

McKay *et al*. [15] investigated the settling characteristics of cylinders of aspect ratio from 1:1 to 5:1 (with the same diameter) in water with particle Reynolds numbers of 680 – 15,350, based on an equivalent volume diameter. Fan *et al*. [1] investigated the settling motion of slender particles of Reynolds number $Re_d = 0.4 – 100$, based on the fibre's diameter with large aspect ratios from 4 to 40, in stagnant water. Both of them found that the terminal settling velocity is nearly independent of *L/d*. However Hinds [64] pointed out that the bulk mean settling velocity of a "cloud of particles" is

significantly greater than that of individual particles. In terms of a cloud of fibrous particles settling, the influence of the aspect ratio on the aerodynamic behaviour of fibrous particles and a direct assessment of this influence have yet to be investigated and reported.

In practice, combustion occurs in shear flows (typically turbulent jets). Many experiments conducted to measure fibrous particles in turbulent flows are related to the pulp and papermaking industry [26], [27], [63], [78], [90], [93], [106–110], where the density ratio between the fibres and the fluid is unity and most fibres are aligned with the direction of the flows. In fibre-air two phase turbulent jet flows, where the density ratio between two phases is usually very high, the distributions of the orientation and velocities of the fibrous particles in these flows are unknown. An improved understanding of their aerodynamic behaviour is a prerequisite to optimising their performance in applications such as biomass combustion. This, in turn, requires detailed measurements in relevant environments, such as in co-flowing jets, which are not yet available. The objective of the current work is to begin to address this gap.

1.6 Thesis Objectives

The overall objective of the present research is to provide new understandings of the aerodynamic behaviour of long aspect ratio fibrous particles whilst settling in air and whilst being transported in turbulent jet flows under conditions of relevance to biomass combustion.

The primary objective of the first paper is to investigate the drag coefficient for a fibrous particle with a long aspect ratio whilst settling in air. To investigate the drag coefficient of a fibre, it is necessary to measure its orientation and settling velocity simultaneously. The objective of the second paper is to investigate the aerodynamic behaviour of long fibrous particles whilst settling in air. Detailed aims are presented within the paper. The objective of the third paper is to investigate the influence of the aspect ratio on the distributions of orientation and settling velocity of long fibres. To investigate the influence of the aspect ratio, it is necessary to measure orientation and settling velocity by using fibres with the same diameter but different lengths and a second set of fibres with the same length but different diameters. The objective of the fourth paper is to investigate the aerodynamic behaviour of the fibrous particles in the near field of turbulent jet flows for super dilute conditions, including the measurements for the orientation, velocity and angular velocity of the fibrous particles.

2 Literature Review

2.1 Terminal Settling Velocity

When a spherical particle settles in still air, the settling velocity will become steady after a period of time. This occurs when the particle's downward gravitational force is balanced by the air drag force upward (the buoyancy is usually negligible, as the particle's density is much greater than air). This steady velocity is called the terminal settling velocity (V_{ts}).

A key to understanding the aerodynamic properties of an aerosol particle is the Reynolds number, a dimensionless parameter used to characterize fluid flow through a pipe or around an obstacle such as an aerosol particle. Where air is the working fluid, it can be used to characterize the particle's flow regime in air. Hinds [64] pointed out that V_{ts} depends on the particle's Reynolds number (Re_p) as shown in Equation 2.1:

$$\mathrm{Re}_p = \frac{\rho_{air} V_{rel} D}{\mu_{air}}, \quad (2.1)$$

where ρ_{air} is air density, V_{rel} is the relative velocity between air and the spherical particle, D is the diameter of the sphere and μ_{air} is air viscosity, which is 1.81×10^{-5} Pa s at 293K and atmospheric pressure.

Three regimes of the aerodynamic behaviour of a particle have been identified, i.e.

Stokes Law ($Re_p < 1$), transition ($1 < Re_p < 1000$) and Newton's Law ($Re_p > 1000$). In the Stokes regime, Stokes's law can be used to determine the velocity of an aerosol particle undergoing gravitational settling in air. Where a particle is released in air, it quickly reaches its terminal settling velocity. That is

$$F_D = F_g = mg . \quad (2.2)$$

Based on Equation 2.2, Equation 2.3 can be derived to calculate the V_{ts} of a sphere where $Re_p < 1.0$ and air is the working fluid [64]:

$$V_{ts} = \frac{\rho_p D^2 g}{18 \mu_{air}} \quad (D > 1\ \mu m \text{ and } Re_p < 1.0), \quad (2.3)$$

where ρ_p is the particle density, D is the diameter of the spherical particle, and g is the gravitational acceleration.

From Equation 2.3, it can be seen that when the particle's $Re_p < 1$, its terminal settling velocity increases significantly with the particle's size, being proportional to D^2. Also it is inversely proportional to air viscosity and does not depend on air density.

In practice, no particle is a perfect sphere. An aerosol particle adjusts to its terminal settling velocity almost instantly. Furthermore, Equation 2.3 cannot be used for $D < 1\mu m$, and $Re_p > 1$.

2.2 Terminal Settling Velocity Modification

With the recent development of measurement techniques such as laser-based measurements, a particle's displacement can be measured in microns and time separation in microseconds. This allows the fluid regimes where Re_p approaches 1 to be reclassified because it is a sensitive area.

Bonadonna *et al*. [101] modified the equations of a spherical particle's settling velocity based on the particle's Reynolds number. They pointed out that the Stokes regime applies where the particle's Reynolds number is less than 0.4. Equations 2.4, 2.5 and 2.6 can be used to calculate spheres' settling velocities based on the values of Re_p when air is the working fluid.

$$V_{ts} = \sqrt{\frac{3.1 g \rho_p D}{\rho_{air}}} \quad (Re_p > 500), \qquad (2.4)$$

$$V_{ts} = \frac{g \rho_p D^2}{18 \mu} \quad (Re_p < 0.4), \qquad (2.5)$$

$$V_{ts} = D \sqrt[3]{\frac{4 \rho_p{}^2 g^2}{225 \rho_{air} \mu}} \quad (0.4 < Re_p < 500), \qquad (2.6)$$

where ρ_p is the particle's density, D is the diameter of the spherical particle, g is the gravitational acceleration, ρ_{air} is air density and μ is air viscosity.

From these equations it can be seen that, except for the case where Re_p < 0.4, the settling velocities of a spherical particle is dependent on the density of air around it (the working fluid).

2.3 Dynamic Shape Factor

Equations 2.4, 2.5 and 2.6 are based on spherical particles. However in practice most particles are non-spherical. Some have regular geometric shapes, such as cylindrical or ellipsoid, while others are granular or fibrous.

Hinds [64] introduced the dynamic shape factor χ to describe cylindrical particles. Here χ is defined as the ratio of the drag force of a cylindrical particle to the resistance force of a sphere having the same volume and velocity as the cylindrical particle:

$$\chi = \frac{F_D}{3\pi\mu V d_{ev}}, \qquad (2.7)$$

where d_{ev}, is the equivalent volume diameter, which is the diameter of a sphere having the same volume as that of the cylindrical particle. Based on this definition, the terminal settling velocity of a cylindrical particle in Stokes' regime becomes:

$$V_{ts} = \frac{\rho_p d_{ev}^{\ 2} g}{18\mu\chi}. \qquad (2.8)$$

Hinds [64] recommends χ values based on three different aspect ratios of 2, 5 and 10 for a cylindrical particle with $Re_p < 0.1$, as shown in Table 2.1.

Table 2.1: Dynamic shape factors of cylindrical particles with $Re_p < 0.1$ [64].

Aspect ratio of cylindrical particles	2	5	10
Vertical axis	1.01	1.06	1.20
Horizontal axis	1.14	1.34	1.58
Orientation averaged	1.09	1.23	1.43

It is evident that χ depends on orientation, which changes with time, hence the term "dynamic" is used. The dynamic factor, χ, will have a minimum value for a vertical orientation. Thus a fibrous particle's settling velocity when the major axis is vertical will be much faster than that when the major axis is horizontal.

Hinds [64] pointed out that the values in Table 2.1 are the usual situation for aerosol particle motion where $Re_p < 0.1$. This means these values of the shape factor are only suitable for the laminar flow regime. Hinds recommended a minimum value for χ of 1.20 (where the aspect ratio is 10), which implies the terminal settling velocity of the single cylindrical particle is always less than that of a sphere of equivalent volume.

2.4 Sphericity

Sphericity, ψ, is a measurement of how spherical (round) an object is and it can be used for the study of non-spherical particles. Researchers also use it to evaluate fibrous particles. Sphericity was first defined by Wadell [102] to be:

$$\psi = \frac{A_s}{A_p} \quad , \qquad (2.9)$$

where A_s is the surface area of a sphere that has the same volume as a non-spherical particle and A_p is the surface area of the non-spherical particle. Based on this definition, the sphericity of a cylindrical particle becomes:

$$\psi_{fp} = \frac{d_{ev}^{\ 2}}{dL + d^2/2} \quad , \qquad (2.10)$$

where d_{ev} is the diameter of a sphere that has the same volume as a fibrous particle, e.g. a diameter of equivalent volume. d and L are the diameter and the length of the fibrous particle, respectively.

Haider and Levenspiel [3] pointed out that "for close to isometrically shaped particles, those with no one very much longer or very much shorter dimension, the sphericity is a useful measure, most likely the best single parameter for describing the shape for falling particles." Therefore ψ is not appropriate for a fibrous particle with a long aspect ratio. Furthermore particles with entirely different shapes and different aerodynamic

behaviour can have the same sphericity. For example, a disc-shaped particle and a fibrous particle can have the same ψ, but have a totally different aerodynamic behaviour.

2.5 Previous Work on the Drag Coefficient of Fibrous Particle

Studies related to the drag coefficient and terminal settling velocity of a fibrous particle have attracted increasing attention from the engineering process community in recent years [1]. The terminal settling velocity of a fibre is strongly influenced by its orientation [22, 64]. Many equations have been developed and presented in the literature relating the drag coefficient, C_D, to the Reynolds number, Re_p, for non-spherical particles falling at their terminal velocities [1–7], [8–20]. Although research has been conducted on the problem of drag coefficients for cylindrical particles, it seems that no experimental investigations have been undertaken to determine the equivalent diameter of settling fibres in air with large aspect ratios to assess their aerodynamic behaviour.

Figure 2.1 presents the calculated and measured C_D of various regular shapes at right angles of incidence (i.e. the major axis of the cylinders is aligned normally to the flow direction) as a function of each particle's Re_p [68]. However in practice, the orientation of a fibrous particle settling in air varies with time as the density ratio between the fibres and air phase is sufficiently high [68, 64] and does not keep the right angle of incidence all the time.

The drag force consists of two contributions: a viscous drag caused by friction and a form drag caused by pressure. Whilst a particle settles in air, the definition of the drag force acting on the particle is

$$F_D = C_D S \frac{\rho_{air}}{2} \left|\boldsymbol{V}_{air} - \boldsymbol{V}_p\right| (\boldsymbol{V}_{air} - \boldsymbol{V}_p). \quad (2.11)$$

where C_D is the drag coefficient and S is the projected area of the particle normal to the direction of settling. ρ_{air} is the density of air. V_{air} is the velocity of air and V_p is the velocity of the particle.

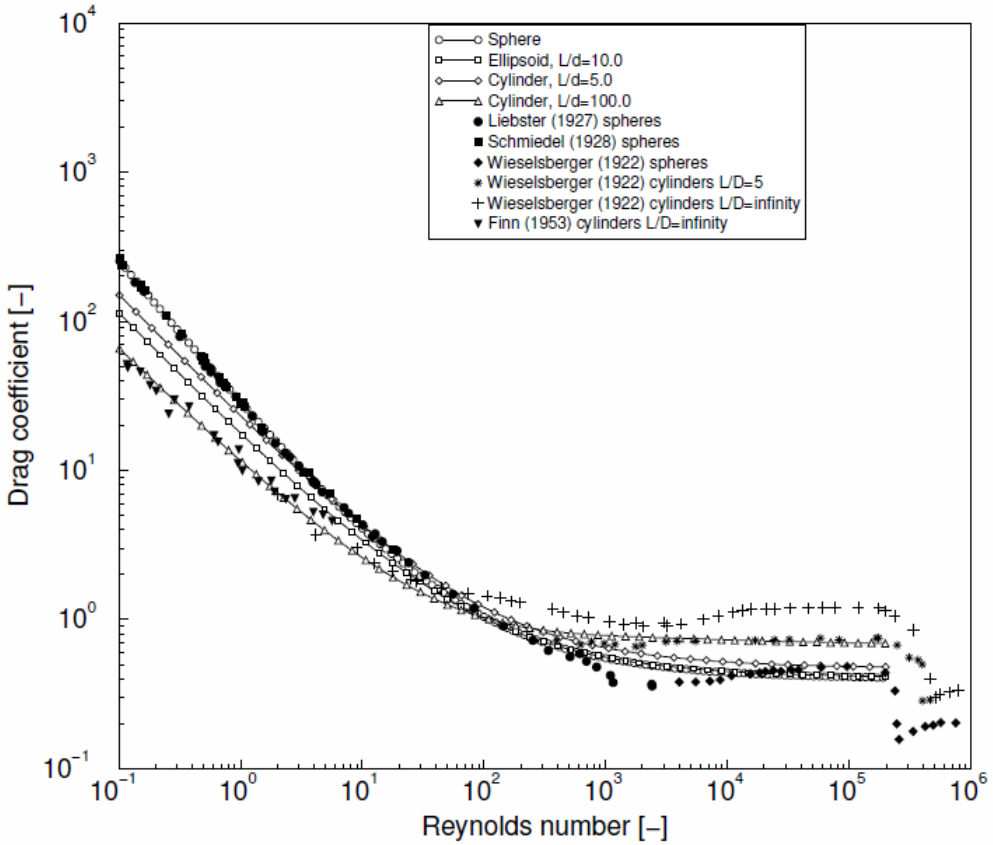

Figure 2.1: The calculated and measured C_D of various regular shapes at right angles of incidence to the flow as a function of a particle Re_p [68].

Fan *et al.* [1] studied the relationship between the drag coefficient (C_D) of slender particles with a large aspect ratio (L/d = 4 – 37) and a Reynolds number (Re_d = 0.4 – 100) experimentally. They proposed the following equation to calculate the drag coefficient, whose validity is yet to be assessed.

$$C_D = \frac{1}{\sin\theta}\left(\frac{\rho_{fp}}{\rho_f}\right)^{-1.537}\left[\frac{d^3(\rho_{fp}-\rho_f)^2 g}{\mu^2}\right]^{0.8524}\frac{24}{\mathrm{Re}_d}(0.006983+0.6224\,\mathrm{Re}_d^{-1.046}) \quad (2.12)$$

Here θ is the orientation of the fibre, which is the angle between the major axis of the fibre and the direction of gravity; ρ_{fp} and ρ_f are the density of the fibre and the fluid, respectively; d is the diameter of the fibre, μ is the viscosity of the fluid and $\mathrm{Re}_d = \rho_{air} V_{fp} d / \mu$.

Clift *et al*. [2] summarized the drag coefficient of non-spherical particles in his book and proposed the following model, which needs to be assessed, to calculate the C_D of a cylindrical particle:

$$C_D = 9.689(Re_d)^{-0.78} + 1.42(Re_d)^{0.04} \quad (0.1 < Re_d < 5). \quad (2.13)$$

After considering the regression analysis for spherical and nonspherical particles and other researchers' results, Haider and Levenspiel [3] proposed the following four-parameter correlation with which to calculate C_D.

$$C_D = \frac{24}{\mathrm{Re}}(1 + A\mathrm{Re}^B) + \frac{C}{1+\frac{D}{\mathrm{Re}}}, \quad (2.14)$$

where the values of *A, B, C* and *D* are functions of sphericity, ψ.

The following four equations were proposed for calculation of *A, B, C* and *D* by Haider and Levenspiel [3].

$$A = \exp(2.3288 - 6.4581\ \psi + 2.4486\ \psi^2), \quad (2.15)$$

$$B = 0.0964 + 0.5565\ \psi, \quad (2.16)$$

$$C = \exp(4.905 - 13.8944\ \psi + 18.4222\ \psi^2 - 10.2599\ \psi^3), \quad (2.17)$$

$$D = \exp(1.4681 + 12.2584\ \psi - 20.7322\ \psi^2 + 15.8855\ \psi^3). \quad (2.18)$$

Equations 2.14 – 2.18 are not only cumbersome to use, but also the number of significant figures is not justifiable in view of the usual 15% – 20% uncertainty inherent in such experimental work. Hence Haider and Levenspiel [3] simplified the equations to read:

$$C_D = \frac{24}{\mathrm{Re}}[1 + \{8.1716\exp(-4.0655\psi)\} \times \mathrm{Re}^{(0.0964+0.5565\psi)}] + \frac{73.69\,\mathrm{Re}\exp(-5.0748\psi)}{\mathrm{Re} + 5.378\exp(6.2122\psi)}. \quad (2.19)$$

The authors pointed out that, while the fit is quite good for isometric particles, $\psi > 0.67$, it is poorer outside this range. That is, Equation 2.19 is not expected to be appropriate for a fibrous particle with a long aspect ratio. Therefore, more work is needed to develop relationships that characterize drag for long aspect ratio fibres.

Swamee and Ojha [6] also developed a correlation with the Corey shape factor, $\beta = c/(ab)^{1/2}$, where $a > b > c$ are the lengths of the three principal axes of the particle. They gave the following expression for drag:

$$C_D = \frac{48.5}{(1 + 4.5\beta^{0.35})^{0.8}\ \mathrm{Re}^{0.64}} + \{(\frac{\mathrm{Re}}{\mathrm{Re} + 100 + 100\beta})^{0.32}\ \frac{1}{\beta^{18} + 1.05\beta^{0.8}}\}. \quad (2.20)$$

However, this parameter, β, is only applicable within the range $0.3 < \beta < 1$, making it unsuitable for long aspect ratio fibres such as those considered here.

Venu Maddhav and Chhabra [4] investigated the cylinder settling in a confined environment. The settling cylinder was observed to retain its initial orientation during settling, which is opposite to the conclusion of Clift *et al.* [2] for a single fibre. Under the conditions where $0.01 < Re < 400$, $0.35 < \psi < 0.7$ and $0.05 < L/d < 50$, Venu Maddhav and Chhabra [4] developed the following expression for C_D:

$$C_D = \frac{24}{\mathrm{Re}}(1 + 0.604\,\mathrm{Re}^{0.529}). \quad (2.21)$$

However, at the terminal settling velocity and in the above range of *Re,* a cylinder falls with its axis oriented horizontally [1, 2]. Therefore it is doubtful that the findings of Venu Maddhav and Chhabra [4] can be extrapolated to an unconfined environment in which the fibrous particles' orientations are not generally horizontal.

As can be seen from the literature, the sphericity and shape factors are not suitable for long aspect ratio fibrous particles. Therefore further investigation is needed to understand the aerodynamics of settling long fibrous particles in the range of $0.5 < Re_d < 2$ and $10 < Re_L < 100$, with a high density ratio of particles to fluids and no boundary limitation. That is why this study aims to investigate the equivalent diameter of a fibre with a large aspect ratio settling in air and the relationship between the drag coefficient and Re_d. A further aim is to assess the two models (Equations 2.12 and 2.13) proposed by previous investigators.

2.6 Previous Work on Aerodynamics (and Hydrodynamics) of Fibres

The settling motion of a particle is a basic class of its motion. The sedimentation of rigid spherical particles has been studied extensively [64]. However the settling motion of a fibrous particle is much more complex and more poorly understood than that of a sphere. The sedimentation behaviour of fibres plays a critical role in many branches of science such as aerosol physics and atmospheric science. A sphere settles in a purely vertical direction. However for a fibrous particle, the instantaneous horizontal drift cannot be neglected. A fibrous particle also exhibits rotation.

A large number of previous investigations have studied the hydrodynamics of fibres. Theoretical treatments include the slender body theory by Batchelor [43] and the concentration instability by Koch and Shaqfeh [44]. Experimental investigations include that of Metzger *et al*. [23], Herzhaft and Guazzelli [22], Salmela, *et al*. [24] and Herzhaft *et al*. [21]. Previous numerical investigations were performed by Shin *et al*. [29], Butler and Shaqfeh [39], Lin and Zhang [45], Lin *et al*. [46], Kuusela *et al*. [33], Kuusela *et al*. [35], Tornberg and Gustavsson [40] and Shin *et al*. [38]. However, none of these investigations provide detailed measurements of bulk settling fibres in the range of $10 < Re_L < 100$.

The Richardson-Zaki's Law presents the relationship between the mean settling velocity of particles and their volume fraction, Φ, under the conditions that apply in a fluidized bed. Based on this law, the mean settling velocity of particles decreases with an increase in solid concentration. The added resistance comes from the hydrodynamic interaction between particles. The level of interaction was first studied systematically by

Richardson and Zaki [103], who proposed a power-law relationship:

$$\frac{V_{ms}(\emptyset)}{V_{ts}} = (1-\emptyset)^n \ , \quad (2.22)$$

where Φ is the volume fraction of particles in the fluidized bed, V_{ms} is the mean settling velocity and V_{ts} is a terminal settling velocity of a single particle in the fluidized bed, n is a parameter dependent upon Re_{p}.

The motion of a fibrous particle in air generally consists of translation and rotation. Based on Newton's Law, the motion is governed by the following set of equations:

$$\frac{d(m_p \vec{v}_p)}{dt} = \sum_i \vec{F}_i = \vec{F}, \quad (2.23)$$

$$\frac{d(I_{x'}\omega_{x'})}{dt} = \sum_i T_{x',i} + \omega_{y'}\omega_{z'}\left(I_{y'} - I_{z'}\right), \quad (2.24a)$$

$$\frac{d(I_{y'}\omega_{y'})}{dt} = \sum_i T_{y',i} + \omega_{z'}\omega_{x'}(I_{z'} - I_{x'}), \quad (2.24b)$$

$$\frac{d(I_{z'}\omega_{z'})}{dt} = \sum_i T_{z',i} + \omega_{x'}\omega_{y'}\left(I_{x'} - I_{y'}\right). \quad (2.24c)$$

where m_p is the mass of the fibrous particle; $\vec{v}_p$ is the centre-of-mass velocity of the fibrous particle; $\sum_i \vec{F}_i$ is the summation of forces acting on the fibrous particle; I is the mass momentum of inertia around the axis; ω is the angular velocity of the fibrous particle and $\sum_i T_i$ is the summation of torques acting on the fibrous particle around the axis.

Figure 2.2 presents the coordinate systems of a settling fibrous particle.

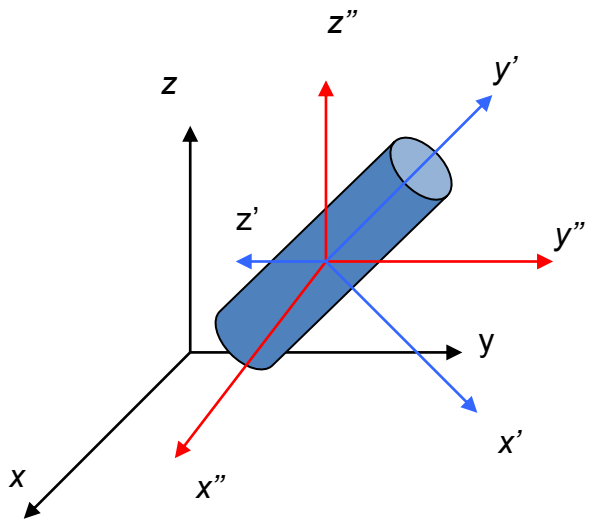

Figure 2.2: The coordinate systems of a settling fibrous particle.

Theoretically, $\vec{F}$ consists of ten kinds of forces acting on a fibrous particle that is moving in air, which are written as:

$$\vec{F} = \vec{F}_g + \vec{F}_B + \vec{F}_D + \vec{F}_p + \vec{F}_m + \vec{F}_{Ba} + \vec{F}_S + \vec{F}_M + \vec{F}_e + \vec{F}_{th}, \qquad (2.25)$$

where $\vec{F}_g$ is the gravitational force acting on the fibrous particle; $\vec{F}_B$ is the buoyant force acting on the fibrous particle; $\vec{F}_D$ is the drag force acting on the fibrous particle; $\vec{F}_p$ is the pressure gradient force acting on the fibrous particle; $\vec{F}_m$ is the virtual mass force acting on the fibrous particle; $\vec{F}_{Ba}$ is the Basset force acting on the fibrous particle; $\vec{F}_S$ is the Saffman lift force acting on the fibrous particle; $\vec{F}_M$ is the Magnus force acting on the fibrous particle; $\vec{F}_e$ is the electrostatic force acting on the fibrous particle and $\vec{F}_{th}$ is the thermophoretic force acting on the fibrous particle.

Zhu and Lin [69] analysed the forces in Equation 2.25 and gave the methods to calculate them, which are discussed below:

(1) Gravitational force:

$$F_g = m_p\, g = \frac{1}{4}\pi d^2 L \rho_{fp} g, \quad (2.26)$$

(2)Buoyancy force:

$$F_B = \frac{1}{4}\pi d^2 L \rho_{air} g. \quad (2.27)$$

The buoyancy, F_B , can be neglected, as the density of the fibrous particle, ρ_{fp}, is far greater than that of air, ρ_{air},

(3)Drag force:

$$F_D = \frac{1}{2}\rho_{air} V_{rel}^2 C_D S, \quad (2.28)$$

where V_{rel} is the relative velocity between the fibrous particle and air; whilst S is the projected area of the fibrous particle.

(4)Pressure gradient force:

Based on the calculation, Zhu and Lin [69] pointed out that the pressure gradient force acting on a fibrous particle moving in air has no relationship to the orientation of the fibre. Assuming the pressure gradient is $\partial p/\partial x$, then the pressure gradient force can be written as:

$$F_p = -\frac{\pi}{4} d^2 L \frac{\partial p}{\partial x} \ . \quad (2.29)$$

The pressure gradient force is not important, as the density of the fibrous particle is far greater than that of air.

(5)Virtual mass force:

Whilst a particle is moving in air, virtual mass or added mass is the inertia added to a system because an accelerating or decelerating body must move (or deflect) some volume of the surrounding air as it moves through it. Added mass is a common issue because the object and surrounding air cannot occupy the same physical space simultaneously. In order to simplify the calculation, it is assumed that the fibrous particle accelerates in air in the direction of the particle's major axis. Then the virtual mass force can be written as follows:

$$F_m = \frac{\pi}{2} d^3 \rho_{air} \times \frac{dV_{cx}(t)}{dt} - \frac{\frac{\pi}{4} d^3 (\frac{d}{2} + L) \rho_{air}}{\sqrt{\left(\frac{d}{2}\right)^2 + L^2}} \times \frac{dV_{cx}(t)}{dt}. \quad (2.30)$$

From the equation it can be seen that virtual mass force is proportional to dV_{cx}/dt, and ρ_{air}. It is also related to the diameter, d, and length, L, of the fibrous particle. The virtual mass force is not important, as the density of the fibrous particle is far greater than that of air.

(6)Basset force:

Whilst a particle is accelerating in air, the unsteady forces acting on the particle due to acceleration can be divided into two parts: the virtual mass force and the Basset force. The Basset term accounts for the viscous effects and addresses the temporal delay in boundary layer development as the relative velocity changes with time. Zhu and Lin

[69] gave the equation to calculate the Basset force for a spherical particle alone.

$$F_{Ba} = \frac{3}{2} D^2 \sqrt{\pi \mu \rho_{air}} \int_{-\infty}^{t} \frac{\frac{dV_{air}}{dt'} - \frac{dV_p}{dt'}}{\sqrt{t - t'}} dt' , \quad (2.31)$$

where D is the diameter of a spherical particle; μ is the viscosity of air and V_{air} and V_{p} are the velocities of air and the particle, respectively.

(7)Saffman force:

Small particles in a shear field are subjected to a lift force perpendicular to the direction of flow. The shear lift originates from the inertia effects in the viscous flow around the particle. This force is called the Saffman force. Assuming the fibrous particle is still in the shear air flow, then the Navier-Stokes equation will read:

$$\mu \nabla^2 \mathbf{v} - \nabla p = \rho \mathbf{v} (\nabla \cdot \mathbf{v}) . \quad (2.32)$$

Under the incompressible assumption, where the density is constant, the continuity equation can be written as:

$$\nabla \cdot \mathbf{v} = 0 . \quad (2.33)$$

Assuming the air flow direction is perpendicular to the major axis of the fibrous particle and using cylindrical coordinates (r, φ, z) for the fibrous particle, the z axis coincides with the major axis of the fibrous particle, with a velocity field $\vec{V} = (v_r, v_\varphi, v_z)$. Then Equations 2.32 and 2.33 become:

r-component:

$$\mu\left(\nabla^2 v_r - \frac{v_r}{r^2} - \frac{2}{r^2}\frac{\partial v_\varphi}{\partial \varphi}\right) - \frac{\partial p}{\partial r} = \rho\left(v_r\frac{\partial v_r}{\partial r} + \frac{v_\varphi}{r}\frac{\partial v_r}{\partial \varphi} + v_z\frac{\partial v_r}{\partial z}\right) - \rho\frac{v_\varphi^2}{r}\,, \quad (2.34a)$$

φ-component:

$$\mu\left(\nabla^2 v_\varphi - \frac{v_\varphi}{r^2} + \frac{2}{r^2}\frac{\partial v_r}{\partial \varphi}\right) - \frac{1}{r}\frac{\partial p}{\partial \varphi} = \rho\left(v_r\frac{\partial v_\varphi}{\partial r} + \frac{v_\varphi}{r}\frac{\partial v_\varphi}{\partial \varphi} + v_z\frac{\partial v_\varphi}{\partial z}\right) + \rho\frac{v_r v_\varphi}{r}\,,$$

$$(2.34b)$$

z-component:

$$\mu\nabla^2 v_z - \frac{\partial p}{\partial r} = v_r\frac{\partial v_z}{\partial r} + \frac{v_\varphi}{r}\frac{\partial v_z}{\partial \varphi} + v_z\frac{\partial v_z}{\partial z}\,, \quad (2.34c)$$

where $\nabla^2 = \frac{1}{r}\frac{\partial}{\partial r} + \frac{\partial^2}{\partial r^2} + \frac{1}{r^2}\frac{\partial^2}{\partial \varphi^2} + \frac{\partial^2}{\partial z^2}$.

continuity equation:

$$\frac{1}{r}\frac{\partial(r v_r)}{\partial r} + \frac{1}{r}\frac{\partial v_\varphi}{\partial \varphi} + \frac{\partial v_z}{\partial z} = 0\,, \quad (2.35)$$

because the flow field is perpendicular to the major axis of the fibre, so $\partial/\partial z = 0$ and also $v_z = 0$. The angle φ is discretized at a step of $\Delta\varphi$. Assuming $\varphi_j = j\,\Delta\varphi$, $j = 0, 1, 2, \ldots, J–1$. $J = 2\pi / \Delta\varphi$. Then the Saffman lift force $F_{S\perp}$ is:

$$F_{S\perp} = \frac{d}{2}L\Delta\varphi\sum_{j=0}^{J-1} p_j \sin\varphi_j\,, \quad (2.36)$$

where p_j is the surface pressure of the fibre on the j grid point.

As the flow direction is parallel to the major axis of the fibrous particle, the Saffman lift force $F_{S\|}$ is:

$$F_{S\|} = dL\Delta\varphi \sum_{j=-J}^{J} p_j \sin\varphi_j \ , \quad (2.37)$$

where $j = -J, -J+1, \ldots 0, 1, 2, \ldots, J$. $J = \pi/2\ \Delta\varphi$. d and L are the diameter and length of the fibrous particle, respectively.

(8)*Magnus force:*

Whilst a fibrous particle is moving and spinning in air, the Magnus force is produced in the direction perpendicular to the relative movement, which causes the particle to change its direction away from its principal flight path. Zhu and Lin [69] pointed out that the Magnus force is proportional to the angular velocity of the fibrous particle, the density of air and the relative velocity of the particle to air. The direction of the angular velocity, ω, of the fibrous particle has little effect on the Magnus force based on this calculation. The force can be written as:

$$F_M = \frac{\pi}{4} d^2 LK\rho_{air}\omega(V_{cx} - V_{air}), \quad (2.38)$$

where K is a constant.

(9)Electrostatic force:

The electrostatic force between two fibrous particles can be obtained by Coulomb's law, which is written below as:

$$F_e = k_e \frac{q_1 q_2}{S_p^2}, \quad (2.39)$$

where k_e is Coulomb's constant, $k_e = 8.99\times10^9$ N·m^2·C^{-2}. q_1 and q_2 are the signed magnitudes of the charges. S_p is the distance between the two charges. The force of interaction between the charges is attractive if the charges are opposite signed and repulsive if like signed.

(10) Thermophoretic force:

Assuming that the temperature gradient is perpendicular to the major axis of the fibrous particle, the thermophoretic force acting on the fibrous particle can be written as:

$$F_{th} = -92\pi \frac{\mu^2}{\rho_{air} T_{air}} \times \frac{1}{13C_m\lambda + 2d} \times \frac{\frac{k_{air}}{k_p} + C_t\lambda}{\frac{k_{air}}{k_p} + C_t\lambda + \frac{d}{2}} \times \frac{d^2}{4} L|\Delta T_\infty|, \quad (2.40)$$

where μ is air viscosity; T_{air} is air temperature; C_m is the velocity slip coefficient and C_t is the temperature jump coefficient; λ is the mean free path of air; k_{air} and k_p are the thermal conductivity of air and the fibrous particle, respectively; ΔT_∞ is the temperature gradient and d and L are the diameter and length of the fibrous particle, respectively.

Not all the forces mentioned above play a role when a fibrous particle is settling in ambient air. For example, if the particle's density is far greater than that of air, the buoyancy force, the virtual mass force and the pressure gradient force can all be neglected. The electrostatic force and thermophoretic force are also negligible. The Basset force can also be neglected as the fibrous particle will have reached its terminal settling velocity. Therefore only the influences of the gravitational force, the drag force, the Magnus force and the Saffman force acting on the fibrous particle need to be considered in this case.

Clift *et al*. [2] reported that, for a single fibrous particle's Reynolds number $Re_d > 0.01$, a cylinder falls with its axis oriented horizontally and exhibits steady motion with this orientation up to Re_d of order 100. However, this is yet to be extended to a cloud of interacting particles in suspensions. Kuusela *et al*. [33] simulated the settling of spheroids under steady state sedimentation at $0.5 < Re_L < 3.5$. They predicted the orientation distribution that arises from a competition between inertial forces acting on individual particles and hydrodynamic interactions between particles. For super dilute systems, inertial effects tend to align fibres to a horizontal position, whereas, in sufficiently concentrated systems, the interactions tend to align the fibres with gravity. Around the transition from a horizontal to a vertical orientation, the mean settling velocity increases with increasing of Φ to a maximum that may even exceed the terminal settling velocity of a single spheroid. These accord with the experimental results of Salmela *et al*. [24]. However like the work of Salmela *et al*. [24], the Re_L of this investigation was limited to less than 3.5. Koch and Shaqfeh [44] studied the instability of a dispersion of sedimenting theoretically. They also argued that the convective motion (cluster formation) may lead to an average sedimentation velocity which is larger than the maximum possible value for a particle in a quiescent fluid. This theory can be verified by accurate measurements of the settling velocity and the orientation of fibres.

Herzhaft and Guazzelli [22] experimentally investigated sedimenting suspensions of fibres with $Re_L \approx 0.0001$, also in a liquid. In this study, the inertia acting on the fibrous particles approaches zero, causing the fibres to tend to align in the direction of gravity for dilute and semi-dilute suspensions. This contrasts with the case of $Re_L \sim O(1)$ where the fibre orientations are horizontal. Butler and Shaqfeh [39] performed a numerical

simulation of inhomogeneous sedimentation of rigid fibres in the limit of zero of Re_L. Their simulation revealed that the steady settling velocity increases with the number density of fibrous particles simulated in the dilute regime. The predictions of orientation distribution agreed with the experimental results of Herzhaft and Guazzelli [22]**.** Furthermore the simulation showed that the orientation of fibrous particles tends to become more vertical with any increase in the number density of the dilute regime. However this assessment is yet to be extended to higher Reynolds numbers. Metzger *et al*. [23] experimentally investigated the instability of a sedimenting suspension of fibres with $Re_L \approx 0.0001$ by using PIV. Like the work of Herzhaft and Guazzelli [22], only the projected angles of fibres were calculated. Furthermore the PIV method only provides the flow field of a group of particles and does not calculate either the settling velocity or the orientation of individual fibrous particles. That is, it cannot provide details of the dynamic behaviour of a settling fibre. In conclusion, there is little literature examining the aerodynamics of fibrous particles under the conditions of relevance to combustion in boilers and furnaces. In the light of the above review, this thesis seeks to further the understanding of the aerodynamics of settling fibrous particles in the range of $Re_L = 10 – 100$. These conditions have yet to be reported.

2.7 Previous Work on the Influence of the Aspect Ratio of Fibrous Particles

McKay *et al*. [15] and Fan *et al*. [1] investigated a single fibrous particle settling in stagnant water and concluded that the terminal settling velocity of the fibrous particle is independent of the *L/d* of the fibre. However there are some situations in which individual particle motion is nearly negligible, compared with motion on a larger scale [64]. Hinds [64] raised the concept of an "aerosol cloud", in which the gas phase containing the particles is regarded as the cloud compared with the surrounding air. He further pointed out that cloud settling occurs as the particle concentration is sufficient to cause the entire cloud to move as an entity at a velocity significantly greater than the individual particle settling velocity. There are three kinds of cases of cloud-like settling. The first one is that whilst the cloud is settling with a low particle concentration, air will pass through the cloud and each particle will experience a relative velocity to air. The second case is that at a sufficiently high particle concentration, the resistance to airflows through the cloud will be so great that the air will flow around the cloud, because this is the path of least resistance. In this case the relative velocity of the particles inside the cloud is zero. The third case lies in between these two extreme conditions and is a common case in practice. In this condition, both mechanisms mentioned above operate simultaneously. Therefore the aerodynamic behaviour of fibrous particles settling as an entire cloud is different from that of the individual fibre. The influence of the aspect ratio of the fibrous particles on the bulk settling motion is the focus of the present research.

Hinds [64] introduced a coefficient, G, to describe the relationship between a settling velocity of individual particles and that of a cloud. G is defined as follows:

$$G = \frac{V_{cloud}}{V_p}, \quad (2.41)$$

where V_{cloud} and V_{p} are settling velocities of the cloud and the individual particle, respectively.

Whilst the cloud is settling in air, the cloud density, ρ_{cloud}, is simply the particle mass concentration. Assuming that the cloud is spherical and the diameter is d_{cloud}, the cloud settling velocity, V_{cloud}, is obtained by equating the force of gravity to Newton's drag:

$$\frac{\rho_{cloud}\pi d_{cloud}^3 g}{6} = C_D \frac{\pi}{8}\rho_{air} d_{cloud}^2 V_{cloud}^2, \quad (2.42)$$

and solving for the cloud settling velocity:

$$V_{cloud} = \sqrt{\frac{4\rho_{cloud} d_{cloud} g}{3C_D \rho_{air}}}. \quad (2.43)$$

At low particle Reynolds numbers, the individual particle settling velocity is given by Equation 2.3, so that Equation 2.41 becomes:

$$G = \frac{V_{cloud}}{V_p} = \frac{12\mu}{\rho_p D^2}\sqrt{\frac{3\rho_{cloud} d_{cloud}}{C_D \rho_{air} g}}. \quad (2.44)$$

When $G >> 1$, cloud settling is the predominant motion; when $G << 1$, only particle settling occurs and when G is in the range of 2 – 5, both mechanisms operate. However in practice, a spherical shaped cloud does not exist because of dilution, breakup and deformation, especially in the case that the particles are fibrous. Therefore in this case a cloud settling motion is very complex.

McKay *et al*. [15] investigated the settling characteristics of discs and cylinders of an aspect ratio from 0.25:1 to 5.0:1 (with the same diameter) in water with the particles' Reynolds numbers being 680 – 15,350 based on their equivalent volume diameter. The particles used in their experiments were large, non-spherical particles with diameters of 16mm and 20mm. The terminal settling velocity of cylinders of $L/d < 1$ was found to increase with increasing L/d. However for cylinders with $L/d > 1$, the terminal settling velocity was found to be nearly independent of L/d. Importantly, it is not yet known whether this finding extends to small fibrous particles with bulk settling and a large L/d. Lin *et al*. [31] studied the sedimentation of a single fibrous particle with aspect ratios of 2, 3, 5, 7.5 and 10 in a Newtonian fluid, employing the Lattice Boltzmann method at terminal Reynolds numbers of 1 – 10. Their simulation showed that the stable orientation of these fibres is horizontal. They also found that the terminal Reynolds number increases with increasing L/d and then remains constant for $L/d > 5$, which supports the conclusion of McKay *et al.* [15]. They further found that the horizontal component of velocity of a fibrous particle increases with increasing L/d. However, these conclusions are yet to be verified with experimental data for fibres with a large L/d.

Herzhaft and Guazzelli [22] studied the steady state settling velocity and orientation

distribution of glass-rods in dilute and semi-dilute suspensions for Reynolds number less than 0.0001. The fibrous particles used in their experiments were of length of 500 – 3,000μm and diameter of 100μm. They used fibres with aspect ratios of 5, 11, 20 and 32 to investigate the influence of aspect ratio. They found that, over this range, the aspect ratio has little influence on the fibre's orientation, but that the dimensionless settling velocity decreases with increasing aspect ratio for particles of constant diameter. Nevertheless, this dependence decreases with L/d so that the absolute velocity of fibres with aspect ratios of 10 and 20 is nearly identical, while the absolute velocity of fibres with an aspect ratio of 5 is much smaller. However, their investigation was undertaken in a configuration that induces a recirculating flow within the working section, so that approximately 40% of their data have negative velocities. In addition, no details of the influence of an aspect ratio at higher Reynolds numbers $Re_L \sim O(10)$ are available. Hence it is necessary to assess whether their findings extend to bulk free-falling particles at higher Reynolds numbers.

In the light of the above review, it is clear that the influence of the aspect ratio of fibrous particles on their bulk settling motion is complex compared with a single fibrous particle's settling motion, because the fibres' interaction and the cloud mechanism operate when the number density of the fibrous particles is sufficient high. Especially in the case of the fibres' Reynolds numbers being of the order of 10, to date, no detailed statistical assessment of the influence of aspect ratio on other parameters, such as the distribution of the settling velocity or on the horizontal velocity, have been reported. Therefore, the aim of the present work is to assess the influences of aspect ratio within the asymptotic regime, i.e. for $L/d > 20$, on the distribution of settling velocity, horizontal velocity and orientation of fibres.

2.8 Motion of Fibrous Particles in a Turbulent Flow

2.8.1 Fokker-Planck Equation

In the papermaking industry, the extent of anisotropy in the orientation of fibres within a suspended turbulent flow has a significant impact on the final product quality. Therefore extensive studies [26, 27, 53, 63, 78, 90, 93, 106–112] have been conducted in turbulent suspensions of fibres using water as the working fluid, which is of relevance to paper making. The fibre orientation distribution at the end of a headbox (the container in a papermaking machine in which cleaned pulp is collected for uniform distribution across the wire) tends to be highly anisotropic where the majority of the fibres are oriented close to the flow direction. The main mechanism for aligning the fibres is the positive streamwise rate-of-strain in the headbox [111].

Olson and Kerekes [53] analysed the motion of a single fibre suspended in a turbulent fluid and obtained equations of mean and fluctuating velocities in rotation and translation. They derived the following rotational and translational dispersion coefficients of a fibre:

$$D_r = 24\overline{u'^2}\frac{\tau}{L^2}\frac{\Lambda}{L}\left(\mathrm{erf}\left(\frac{\pi^{0.5}\mathrm{L}}{2\Lambda}\right)+\frac{16}{\pi^2}\left(\frac{\Lambda}{L}\right)^3\left(1-e^{-\frac{\pi L^2}{4\Lambda^2}}\right)+\frac{2}{\pi}\frac{\Lambda}{L}\left(e^{-\frac{\pi L^2}{4\Lambda^2}}-3\right)\right). \quad (2.45)$$

$$D_t = 2\overline{u'^2}\tau\frac{\Lambda}{L}\left(\mathrm{erf}\left(\frac{\pi^{0.5}\mathrm{L}}{2\Lambda}\right)+\frac{2}{\pi}\frac{\Lambda}{L}\left(e^{-\frac{\pi L^2}{4\Lambda^2}}-1\right)\right). \quad (2.46)$$

This model implies that for long fibres, rotational and translational dispersion coefficients, D_r and D_t are functions of the fluid's Eulerian integral time scale, τ, the

Eulerian integral length scale, Λ, and the streamwise component of the fluctuating velocity, u'. Based on the convection-dispersion function that governs the evolution of the fibres' orientation distribution, $\Gamma(r, p, t)$, in turbulent flows, they further derived a form of the Fokker-Planck equation to describe the orientation distribution of a fibre in turbulent flows, as follows:

$$\frac{\partial \Gamma}{\partial t} = D_r \nabla_r^2 \Gamma - \nabla_r \cdot (\omega \Gamma) + D_t \nabla^2 \Gamma - \nabla \cdot \left(\overline{V} \Gamma\right), \quad (2.47)$$

where $\nabla_r = \boldsymbol{p} \times \partial/\partial \boldsymbol{p}$ is the rotational operator, $\boldsymbol{p}$ is the unit orientation vector. $\overline{V}$ is the fibres' mean velocity and ω is the fibres' angular velocity. Equation 2.47 relies on many assumptions, some of which do not apply in the present experiments. Firstly it assumes that the fibres are neutrally buoyant, which is far from true in the present experiments. It also assumes that the inertial forces on the fibre are negligible, i.e. that the Stokes number is $<<1$ and that the relative velocity between the fibre and the fluid is zero. None of these assumptions are true for the present case, therefore the extent to which they apply is not known in particle-laden flows with air as the working fluid and sufficiently large fibres for $Sk > 1$, as occurs in this instance. Olson [92] pointed out that modelling the suspension using "two-way coupling" is very complex.

2.8.2 Steady Axisymmetric and plane turbulent Jet

Although the governing equations in gas-solid flows are still being debated, the N-S equations are thought to describe the motion of single phase flows completely. When analysing a steady axisymmetric and plane turbulent jet, a number of assumptions can be made to simplify the N-S equations. The first such assumption is of axisymmetry for

the case of a round jet and an infinitely long thin section for the case of a plane jet. Therefore the number of variables in the N-S equation can be reduced. The second simplification is an assumption of steadiness. With these simplifications, the Reynolds averaged N-S equations are as follows:

$$v_x\frac{\partial v_x}{\partial x}+v_y\frac{\partial v_x}{\partial y}=-\frac{1}{\rho}\frac{\partial p}{\partial x}+\nu\left(\frac{\partial^2 v_x}{\partial x^2}+\frac{\partial^2 v_x}{\partial y^2}\right)-\left(\frac{\partial\overline{v_x{}'^2}}{\partial x}+\frac{\partial\overline{v_x{}'v_y{}'}}{\partial y}\right), \quad (2.48)$$

$$v_x\frac{\partial v_y}{\partial x}+v_y\frac{\partial v_y}{\partial y}=-\frac{1}{\rho}\frac{\partial p}{\partial y}+\nu\left(\frac{\partial^2 v_y}{\partial x^2}+\frac{\partial^2 v_y}{\partial y^2}\right)-\left(\frac{\partial\overline{v_x{}'v_y{}'}}{\partial x}+\frac{\partial\overline{v_y{}'^2}}{\partial y}\right). \quad (2.49)$$

Based on Equations 2.48 – 2.49 and some assumptions, the centreline velocity of the jet, u_c and half width, $r_{1/2}$ can be derived [113]:

$$\frac{u_o}{u_c}=K_1\frac{x}{D}, \quad (2.50)$$

$$\frac{r_{1/2}}{D}=K_2\frac{x}{D}, \quad (2.51)$$

where K_1 and K_2 are the centreline decay coefficient and the spreading coefficient, respectively. D is the jet exit nozzle diameter. u_0 is the jet exit velocity of the gas phase. In terms of a particle-laden turbulent axisymmetric jet, Melville and Bray [147] neglect both the Reynolds and Stokes numbers effects and they write the gas-phase centreline velocity and the gas-phase velocity half width as:

$$\frac{u_o}{u_c}=K_1\frac{x}{D}e^{-0.69\emptyset_0}, \quad (2.52)$$

$$\frac{r_{1/2}}{D}=K_2\frac{x}{D}e^{-0.69\emptyset_0}, \quad (2.53)$$

where Φ_0 is the exit mass loading (i.e. the ratio of the solid phase mass flow rate to the gas phase exit mass flow rate). However Equations 2.52 – 2.53 are based on spherical particles for the solid phase. It is not known whether they can apply in fibre-laden turbulent jet flows.

2.8.3 Governing Equations for Fibre Suspensions

Lin *et al*. [104] simulated dilute suspensions of the fibres in a round turbulent jet and they gave the following governing equations.

The incompressible continuity equation:

$$\frac{\partial u_i}{\partial x_i} = 0. \quad (2.54)$$

Navier-Stokes equation supplemented by the fibre stress tensor:

$$\frac{Du_i}{Dt} = -\frac{1}{\rho}\frac{\partial p}{\partial x_i} + \nu\frac{\partial^2 u_i}{\partial^2 x_j} + \frac{\mu_f}{\rho}\frac{\partial}{\partial x_j}\left(a_{ijkl}\varepsilon_{kl} - \frac{1}{3}(I_{ij}a_{kl})\varepsilon_{kl}\right), \quad (2.55)$$

where u_i is the suspension velocity, p is the pressure, ν is the kinematic viscosity of the fluid, ε is the tensor of rate of strain, μ_f is the apparent viscosity of the suspension and a_{ijkl} is the fourth-order orientation tensor of the fibre. ε, μ_f and a_{ijkl} are given by:

$$\varepsilon_{ij} = \frac{1}{2}\left(\frac{\partial u_i}{\partial x_j} + \frac{\partial u_j}{\partial x_i}\right). \quad (2.56)$$

$$\mu_f = \frac{\pi n \mu L^3}{48\ln(2L/d)}, \quad (2.57)$$

where L and d are the fibre's length and diameter, respectively. n is the fibre's number density.

$$a_{ij} = \oint p_i p_j \Gamma(\boldsymbol{p}) d\boldsymbol{p}. \quad (2.58)$$

$$a_{ijkl} = \oint p_i p_j p_k p_l \Gamma(\boldsymbol{p}) d\boldsymbol{p}, \quad (2.59)$$

where $\boldsymbol{p}_i$ is a unit vector parallel to the fibre's major axis. $\Gamma(\boldsymbol{p})d\boldsymbol{p}$ is the probability that the fibre orientations are located between $\boldsymbol{p}$ and ($\boldsymbol{p}$+$d\boldsymbol{p}$).

Being similar to Equation 2.47, Equation 2.55 relies on an assumption that the inertia acting on the fibre is negligible. That is, the fibre dispersion is influenced only by the rms of turbulent fluctuations. However, this assumption may not be true for the present case because the fibre inertia is significant.

2.8.4 The work of Bernstein et al.

The most relevant experiment to the transport of biomass fibres in air is the measurements of Bernstein and Shapiro [95] in water. They measured the orientation distribution of glass fibres with a wide range of Reynolds numbers on the axis of pipe flow using an optical technique. Their measurement of the orientation distribution on the axis is of relevance to the exit plane of a co-flowing jet, although the transport medium is different. Their results will be compared with the present work. Jayageeth *et al*. [51] studied the effect of a bounding wall on the dynamics of suspended fibres in a

boundary layer using a Stokesian dynamics simulation and they found that the fibres' rotation increased significantly as each fibre approaches a region of maximum shear. This prediction needs to be verified with experimental data. Kvasnak and Ahmadi [54] simulated sedimentation of ellipsoidal particles in turbulent duct flows and reported the results for particles with diameters from 1 to 50μm and aspect ratios from 1 to 10. Zhang *et al*. [56] studied transport and deposition of ellipsoidal particles in turbulent channel flows. A fibre's motion in shear flow was investigated by Broday *et al*. [58] and Ku and Lin [59], while a heuristic model of orientation was developed by Klett [62] under conditions of relevance to atmospheric conditions. Importantly, none of these previous studies provide any detailed assessments of the behaviour of particles within a turbulent jet environment, such as the fibres' preferred orientation, or the influence of the number density of fibres on the velocity and angular velocity distribution. Hence, there remains a need for this new information. In the light of the previous investigations described above, this research seeks to provide new understanding of the aerodynamic behaviour of fibrous particles with a large aspect ratio in the near field of co-flowing turbulent jets in the super-dilute regime. It further aims to provide new understanding of the radial distribution of the statistical properties at the exit plane of the jet, to provide new understanding of the flow within a long pipe. In particular, it aims to assess the distributions of the orientation, angular velocity, axial velocity and number density of the fibres, none of which have been reported previously in a co-flowing jet.

3 PTV Measurement of Drag Coefficient of Fibrous Particles with Large Aspect Ratio

Guo Q. Qi, Graham J. Nathan and Richard M. Kelso

School of Mechanical Engineering and Centre for Energy Technology, The University of Adelaide, Adelaide SA 5005 AUSTRALIA

Email: guo.qi@adelaide.edu.au

Powder Technology 229 (2012) 261–269

Statement of Authorship

Title of Paper	PTV measurement of drag coefficient of fibrous particles with large aspect ratio
Publication Status	☑ Published ☐ Accepted for Publication ☐ Submitted for Publication ☐ Unpublished and Unsubmitted work written in manuscript style
Publication Details	Guo Q. Qi, Graham J. Nathan and Richard M. Kelso. PTV measurement of drag coefficient of fibrous particles with large aspect ratio. Powder Technology, 229 (2012), 261–269.

Principal Author

Name of Principal Author (Candidate)	Guo Qiang Qi
Contribution to the Paper	I was responsible for the development of both the measurement technique and analytical model under the principal supervision of Professor Nathan. I performed the measurements and data processing, wrote the first draft of the manuscript and incorporated and addressed all comments and suggestions by other authors and reviewers in subsequent revisions of the manuscript. I acted as corresponding author.
Overall percentage (%)	55%
Certification:	This paper reports on original research I conducted during the period of my Higher Degree by Research candidature and is not subject to any obligations or contractual agreements with a third party that would constrain its inclusion in this thesis. I am the primary author of this paper.
Signature	Date 13/06/2016

Co-Author Contributions

By signing the Statement of Authorship, each author certifies that:

i. the candidate's stated contribution to the publication is accurate (as detailed above);

ii. permission is granted for the candidate in include the publication in the thesis; and

iii. the sum of all co-author contributions is equal to 45% less the candidate's stated contribution.

Name of Co-Author	Graham J. Nathan
Contribution to the Paper	I was principal supervisor for the development of work, contributed to both data interpretation and refining of the manuscript.
Signature	Date 14/6/16

Name of Co-Author	Richard M. Kelso
Contribution to the Paper	I, co-supervisor, jointly supervised the development of work.
Signature	Date 14/6/2016.

Please cut and paste additional co-author panels here as required.

Powder Technology 229 (2012) 261–269

Contents lists available at SciVerse ScienceDirect

Powder Technology

journal homepage: www.elsevier.com/locate/powtec

PTV measurement of drag coefficient of fibrous particles with large aspect ratio

Guo Q. Qi *, Graham J. Nathan, Richard M. Kelso

School of Mechanical Engineering and Centre for Energy Technology, The University of Adelaide, Adelaide, SA 5005, Australia

ARTICLE INFO

Article history:
Received 17 November 2011
Received in revised form 9 May 2012
Accepted 24 June 2012
Available online 1 July 2012

Keywords:
Sedimentation
Aerodynamics
PTV
Fibrous particle
Drag coefficient

ABSTRACT

The aerodynamic behaviour of long aspect ratio nylon fibrous particles has been investigated experimentally while settling in air under super dilute conditions without any influence of secondary flows and at fibre Reynolds numbers of 0.5–2 based on fibre diameter. A method for laser-based measurement of the orientations and velocities of fibrous particles is also presented. The experimental apparatus employs a two-dimensional Particle Tracking Velocimetry (PTV) to calculate orientation and velocity based on the two end-points. The controlling length scale in the relationship between Reynolds number and drag coefficient was investigated and the equivalent diameter of settling fibre in air was reported. Finally the influence of volume fraction and fibre straightness were assessed.

1. Introduction

A fibrous particle settling in air under the influence of gravity will accelerate until the gravitational force is exactly balanced by the drag force, because the buoyancy can be ignored in this case. The constant velocity reached is called terminal settling velocity. The terminal settling velocity of a fibre is strongly influenced by its orientation [16]. Although research has been conducted on the problem of drag for cylindrical particle, it seems that no experimental investigations have been undertaken to determine the equivalent diameter of a settling fibre in air with large aspect ratio to assess its aerodynamic behaviour.

Fan et al. [1] experimentally studied the relationship between drag coefficient (C_D) of slender particles with large aspect ratios ($L/d = 4$–37) and Re_d (0.4–100). They proposed the following equation to calculate drag coefficient, which needs to be assessed.

$$C_D = \frac{1}{\sin\theta}\left(\frac{\rho_{fp}}{\rho_f}\right)^{-1.537}\left[\frac{d^3\left(\rho_{fp}-\rho_f\right)^2 g}{\mu^2}\right]^{0.8524} \times \frac{24}{Re_d}\left(0.006983 + 0.6224 Re_d^{-1.046}\right). \quad (1)$$

Here θ is the orientation of the fibre, which is the angle between the major axis of the fibre and the direction of the gravity; ρ_{fp} and ρ_f are the fibre and fluid density respectively; d is the diameter of the fibre, μ is the viscosity of fluid and $Re_d = \rho_{air} V_{fp} d/\mu$.

Clift et al. [2] reported that for a single fibrous particle with Reynolds number $Re_d > 0.01$, a cylinder falls with its axis oriented horizontally and exhibits steady motion with this orientation up to Re_d of order 100. However, this work is yet to be extended to a cloud of interacting particles in suspension. Also Clift proposed the following model to calculate C_D of a cylindrical particle:

$$C_D = 9.689(Re_d)^{-0.78} + 1.42(Re_d)^{0.04} \quad (0.1 < Re_d < 5). \quad (2)$$

Sphericity, ψ, is a measure of how closely a particle conforms to a spherical shape. It is widely used in the study of non-spherical particles and has also been used to evaluate fibrous particles. Sphericity is defined to be:

$$\psi = \frac{A_s}{A_p} \quad (3)$$

where A_s is the surface area of sphere that has the same volume as the non-spherical particle and A_p is the surface area of the non-spherical particle. Based on this definition, the sphericity of a cylindrical particle becomes:

$$\psi_{fp} = \frac{d_{ev}^2}{dL + d^2/2} \quad (4)$$

where d_{ev} is the diameter of the sphere that has the same volume as the fibrous particle, e.g. equivalent volume diameter, and d and L are the diameter and length of the fibrous particle respectively. For the present fibres, $\psi = 0.38$.

* Corresponding author.
E-mail address: guo.qi@adelaide.edu.au (G.Q. Qi).

0032-5910/$ – see front matter.
doi:10.1016/j.powtec.2012.06.049

Haider and Levenspiel [3] proposed the following four parameter correlation to calculate C_D.

$$C_D = \frac{24}{Re}\left(1 + ARe^B\right) + \frac{C}{1 + \frac{D}{Re}} \quad (5)$$

where the values of A,B,C,D are functions of ψ. The authors pointed out that, while the fit is quite good for isometric particles, $\psi > 0.67$, it is poorer outside this range. They also argued that "for close to isometrically shaped particles, those with no one very much longer or very much shorter dimension, the sphericity is a useful measure, most likely the best single parameter for describing the shape for falling particles." That is, Eq. (5) is not expected to be appropriate for a fibrous particle with a long aspect ratio. Furthermore particles with entirely different shapes and different aerodynamic behaviour can have the same sphericity. For example, a disc particle and a fibrous particle can have the same Ψ, but have a totally different aerodynamic behaviour. Therefore, more work is needed to develop relationships that characterise drag for long aspect ratio fibres.

Venu Maddhav and Chhabra [4] investigated cylinders settling in a confined environment. The settling cylinders were observed to retain their initial orientation during settling, which is opposite to the conclusion of Clift et al. [2] for a single fibre. Under the conditions of $0.01 < Re < 400$, $0.35 < \Psi < 0.7$ and $0.05 < L/d < 50$, Venu Maddhav and Chhabra [4] developed the following expression to calculate C_D:

$$C_D = \frac{24}{Re}\left(1 + 0.604Re^{0.529}\right). \quad (6)$$

However the terminal settling velocity with the above range of Re, the cylinder falls with its axis oriented horizontally [2]. Therefore it doubtful that the findings of Venu Maddhav and Chhabra [4] can be extrapolated to an unconfined environment in which the orientation is not generally horizontal.

In addition to the above investigations on cylindrical particles, numerous studies have been conducted by employing equal volume diameter and sphericity to investigate C_D of non-spherical particles [8–15]. Based on the work of Haider and Levenspiel [3], Ganser [5] introduced two shape factors to a drag correlation. But like Haider's work, for particles where $\psi < 0.5$, Ganser's work is applicable to disc only. Swamee and Ojha [6] also developed a correlation with the Corey shape factor, $\beta = c/(ab)^{1/2}$, where $a > b > c$ are the lengths of the three principal axes of the particle. However this parameter is only applicable in the range of $0.3 < \beta < 1$, making it unsuitable for long aspect ratio fibres such as those considered here. For the present fibre the Corey shape factor is 0.16, so is not applicable.

In the light of the previous investigations described above, we seek to further the understanding of the aerodynamics of settling long fibrous particles in the range of $Re_d = 0.5$–2, with a high density ratio of particle to fluid and no boundary limitation. Furthermore we would investigate the equivalent diameter of a fibre with large aspect ratio settling in air. As can be seen from the literature review this equivalent diameter has yet to be reported previously. Therefore, the first aim of the present work is to develop a novel method to measure the velocity and orientation of a fibrous particle simultaneously. The second aim is to employ this method to obtain the relationship (equations) between a fibre's number density and its settling velocity in the super dilute regime. The third aim is to investigate the equivalent diameter that suits a fibre with large aspect ratio and drag coefficient and assess the two models proposed by previous investigators.

2. Experimental apparatus/facility

2.1. Measurement techniques and set-up of PTV system

Fig. 1 presents a schematic diagram of the experimental apparatus. To avoid any influence of electrostatics, the pipe was earthed. The experimental method employed a typical Particle Tracking Velocimetry (PTV) technique. The laser was operated in a pulsed mode and the camera in a two-frame mode. The laser sheet was formed by telescopic and diverging lenses. The settling fibrous particles were illuminated by the laser sheet at regular intervals of time and the CCD camera used to record two images of the fibres separated by a delay of about 2.5 ms. An oscilloscope and delay generator were also employed in the experiments. The oscilloscope was used to monitor and validate the time separation chosen for the experiments. A DG-535 delay generator was employed to trigger both the laser flash-lamps and the camera. The laser used in the experiments was a Quantel Brilliant Twins double-cavity pulsed Nd:YAG 10 Hz laser, frequency doubled to provide a wavelength of 532 nm. The output energy of the laser head was set to provide either 250 mJ/pulse or 400 mJ/pulse. The camera was a Kodak MegaPlus ES1.0 with a CCD array of 1008 pixels × 1018 pixels. The resolution was around 26 μm/pixel and the viewing area was 26 mm × 26 mm. Xcap software was used as the operating system.

The settling chamber was of nominally square cross section with 650 mm × 620 mm, height of 2000 mm and was made of Perspex. The fibrous particles were introduced into the top of the chamber and settled over a distance of 2.5–3.0 m through a 2000 mm long pipe of 60 mm diameter. Not only did this ensure sufficient length to reach their terminal settling velocities before entering the chamber, it also ensured that any background currents induced by the particles in the chamber were negligible. With a volume fraction in order of 10^{-5}, and the cross sectional area of the "jet" of falling particles to the chamber in the order 10^{-2}, any induced chamber flows will be at most 1% that of the particles, which is within experimental error. This neglect ensured that the dilute phase was not influenced by any chamber currents in contrast to previous investigations [16]. Also fibres settling velocities were measured for settling distances of both 2.5 m and 3.0 m. The mean settling velocities obtained were identical for both cases, confirming that the fibres have reached their terminal settling velocities and steady state conditions.

The particle delivering system is axisymmetric, which greatly facilitates the measurement, because the measurement can be performed at any vertical plane through the centre line of the pipe. The system can also accommodate spherical particles under identical

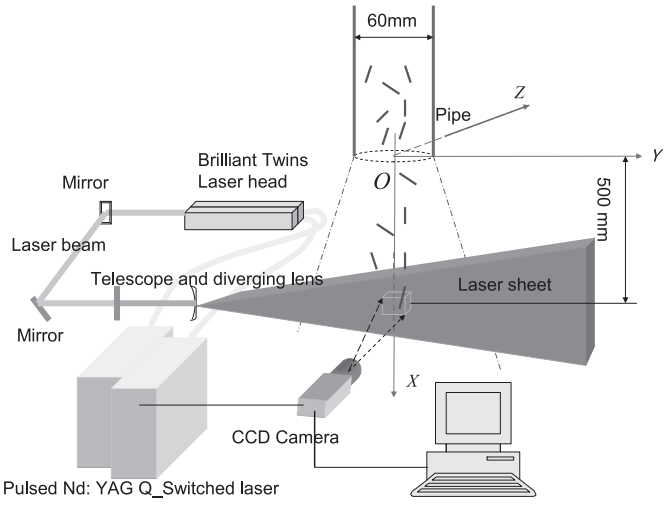

Fig. 1. Experimental arrangement (not to scale). The surrounding settling chamber (650 mm × 620 mm cross section) is not shown for clarity.

Table 1
Nylon fibre used in the experiments.

Length, L, μm	2000
Diameter, d, μm	49.6
Density, ρ_{fp}, kg/m^3	1150
Aspect ratio, L/d	40
Material	Nylon
Denier	20

conditions. This allows direct comparisons to be performed between spherical particles and fibrous particles.

The intensity distribution of the laser sheet is nearly Gaussian, as shown in Fig. 7. This property is exploited to determine whether a fibre is fully or partly within the light sheet, as described below. The thickness of the laser sheet was chosen to be around 5 mm to provide good illumination of entire particles.

2.2. Properties of the fibres

The particles used in the experiments are nylon fibres whose properties are shown in Table 1. A micrograph of a sample of the fibres is shown in Fig. 2, at a resolution of 18 μm/pixel. It can be seen that they are of constant diameter and, while many are straight, a significant number have a slight bend.

The length of each fibrous particle (i.e. the major axis) is defined as the maximum distance between any two pixels in the object. This distance is measured from an optical image converted to binary form (see Fig. 3). The minor axis is defined to be perpendicular to the major axis and the rectangle defined by the two axes can enclose the perimeter of the region. This rectangle we call the "basic rectangle" (Gonzalez et al. [7]). The concept of a basic rectangle can also be used to define the fibrous particle's straightness, as shown in Eq. (7).

$$\varepsilon = 1 - \frac{\delta - d_i}{L_i} \tag{7}$$

where ε is the straightness of a fibrous particle; δ is the minor axis of the basic rectangle on a binary image; d_i and L_i are the diameter and length of the fibre respectively on the binary image and the subscript "i" refers to "image". As a fibre's straightness tends toward unity, the fibre approaches being straight.

Fig. 4 presents the distribution of the straightness of the fibrous particles based on a sample size of 1139. It can be seen that 90.1% of these fibres have straightness $\varepsilon > 0.85$ and some 38% are perfectly straight.

Fig. 5 presents the distribution of the fibres length, L, which were measured directly from the two endpoints. It can be seen that 82% of the fibres have a length between 1900 and 2100 μm and over 95% between 1800 and 2200 μm, with a standard deviation of 196 μm.

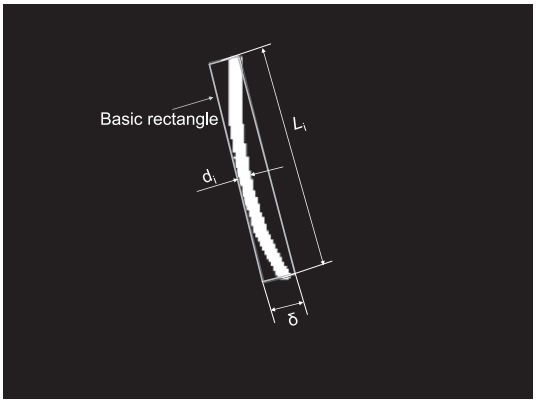

Fig. 3. A binary image of a fibre and its "basic rectangle" used to define its characteristic dimensions.

2.3. Number density, orientation and velocity measurement

Fig. 6 presents the orientation definition of a fibre. The plane of x–y is an image plane. The angle of α is defined to be azimuth of a fibre and θ the orientation of a fibre.

In the present study, we define the volume fraction of fibrous particles as:

$$\phi = \frac{n_p \pi (d/2)^2 L}{1008 \times 1018 R^2 H} \tag{8}$$

where n_p is the number of fibrous particles in the viewing volume, R is the magnification of camera image system, H is the thickness of the laser sheet and $1008 \times 1018 R^2 H$ is the viewing volume.

In the present experiments of measuring settling velocity and Φ, the volume fractions were controlled to be in the range of $\Phi \leq 0.0001$, which is a super dilute condition so that there were few particles which exhibited clumping. Hence the number density of fibrous particle in the viewing area (volume) was calculated by counting the number of particles, and the volume fraction was computed exactly. The volume fractions were also binned by the number of particles to obtain statistically the influence of particle number density on the fibres' aerodynamic behaviour.

The coordinates of the two endpoints of each object (fibrous particle) were obtained. Since the length L of these fibres is constant, the spatial orientation θ (the angle between the X axis and

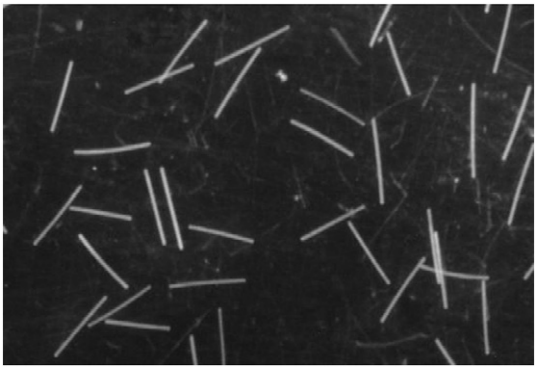

Fig. 2. A micrograph of the sample of nylon fibres.

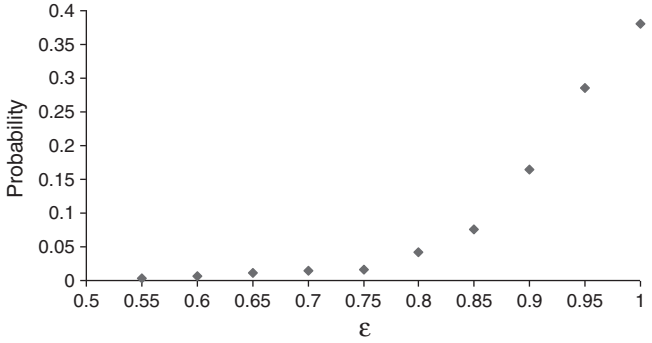

Fig. 4. The distribution of straightness, ε (see Eq. (7)) for the present fibres.

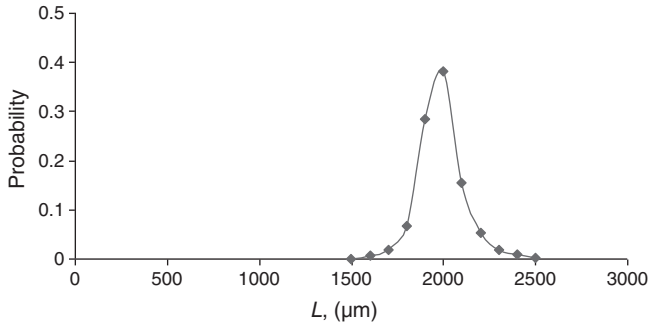

Fig. 5. The distribution of the length, L, of the present fibres.

the major axis of the fibrous particle) of the fibres was calculated by following trigonometric function (Figs. 6 and 7):

$$\theta = \left(\arccos\frac{|x_{e2}-x_{e1}|R}{L}\right)\times\left(\frac{180}{\pi}\right)(^\circ) \tag{9}$$

where x_{e2} and x_{e1} are coordinates of X values of two endpoints.

Any fibres that are only partly in the laser sheet will give a false measurement of the projected length and the coordinates of endpoints, so must be rejected. This can be achieved by comparing the intensities of the signal at the two endpoints of the fibre. Because of the Gaussian light sheet intensity distribution, a partly-in fibrous particle will exhibit a significant difference between the intensity values of the two endpoints (Fig. 7). This is used to reject such particles as described in the Appendix A.

The coordinate system used in the calculation is Cartesian, with the x axis directed downwards in the direction of gravity. We define the two endpoint velocities of the fibrous particle as V_{e1} and V_{e2}. Each endpoint velocity has three components V_{e1x}, V_{e1y}, V_{e1z} and V_{e2x}, V_{e2y}, V_{e2z}, as shown in Fig. 8 and Eq. (10).

$$\vec{V}_{e1} = \vec{V}_{e1x} + \vec{V}_{e1y} + \vec{V}_{e1z} \qquad \vec{V}_{e2} = \vec{V}_{e2x} + \vec{V}_{e2y} + \vec{V}_{e2z} \tag{10}$$

Based on Eq. (10), we define V_{e1x} and V_{e2x} as vertical components of the settling velocity of the endpoints 1 and 2 respectively of the fibrous particle. Similarly V_{e1y} and V_{e2y} are the horizontal components of settling velocity of endpoints 1 and 2 of the fibrous particle respectively.

Image pairs were recorded by the digital camera with a known time separation (Δt). After image processing the displacements of two endpoints of fibrous particles along the x and y axis can be obtained. From this V_{e1x}, V_{e1y} and V_{e2x}, V_{e2y} can be calculated by Eq. (11), as follows:

$$V_{e1x} = \frac{(x_{e12}-x_{e11})R}{\Delta t},\quad V_{e1y} = \frac{(y_{e12}-y_{e11})R}{\Delta t},$$
$$V_{e2x} = \frac{(x_{e22}-x_{e21})R}{\Delta t},\quad V_{e2y} = \frac{(y_{e22}-y_{e21})R}{\Delta t} \tag{11}$$

where V_{e1x} is the velocity of endpoint 1 in the x direction; V_{e1y} is the velocity of endpoint 1 in the y direction; V_{e2x} is the velocity of endpoint 2 in the x direction; V_{e2y} is the velocity of endpoint 2 in the y direction; x_{e12} is the x axis coordinate of endpoint 1 from the second image, x_{e11} is the x axis coordinate of endpoint 1 from the first image; y_{e12} is the y axis coordinate of endpoint 1 from the second image and so on.

Fig. 8 shows the definition of settling velocity of centroid of a fibrous particle. The velocity of the centroid of a fibre V_c is defined by Eq. (12):

$$\begin{aligned}\vec{V}_c &= \vec{V}_{cx} + \vec{V}_{cy} + \vec{V}_{cz}\\ V_{cx} &= \frac{1}{2}(V_{e1x} + V_{e2x})\\ V_{cy} &= \frac{1}{2}\left(V_{e1y} + V_{e2y}\right)\\ V_{cz} &= \frac{1}{2}(V_{e1z} + V_{e2z}).\end{aligned} \tag{12}$$

In present study, V_{cx} and V_{cy} represent the vertical and horizontal components of settling velocities of a fibrous particle respectively. Because the particle delivery system is vertical and axisymmetric, the distributions of V_{cy} and V_{cz} are identical and V_{cy} is representative. So V_{cz} is ignored.

Since data are obtained from an image pair, the orientation of a fibrous particle equals the average orientation of the fibre from the first and second images:

$$\theta = \frac{1}{2}(\theta_1 + \theta_2) \tag{13}$$

$$\theta_1 = \arccos\frac{|x_{e21}-x_{e11}|R}{L}\times\left(\frac{180^\circ}{\pi}\right) \tag{14}$$

$$\theta_2 = \arccos\frac{|x_{e22}-x_{e12}|R}{L}\times\left(\frac{180^\circ}{\pi}\right) \tag{15}$$

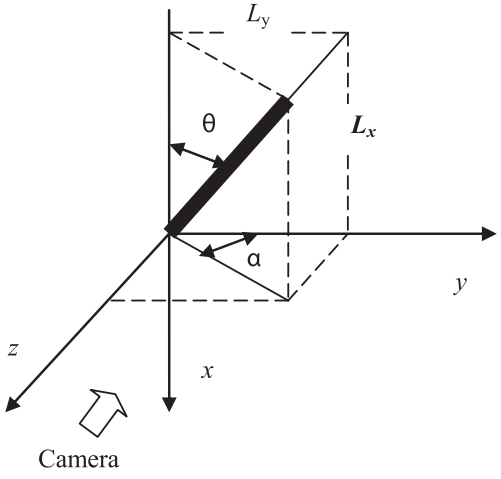

Fig. 6. The definition fibre orientation, where x–y is an image plane.

3. Experimental results and discussions

3.1. Distribution of fibre's settling velocity and orientation

Fig. 9 presents the distribution of the vertical settling velocity obtained from 29,364 samples for a volume fraction less than 5×10^{-4} along with Herzhaft and Guazzelli's data [16]. It can be seen that the distribution is Gaussian. Fig. 9 indicates that the relatively small size of the error bars shows that the variation in straightness of the fibres does not have a large influence on the settling velocity of these fibres. Furthermore, the absence of any bimodality in the curve implies that there is no fundamental difference in the aerodynamics of perfectly straight and slight curved fibres under the conditions assessed here. That is, the presence of a slight curve may increase the scatter in the velocity distribution but does not result in any fundamental change in aerodynamic behaviour, since some fibres are perfectly straight. Finally the significantly lower spread in V_{cx}/V_{ts} compared with the measurements of Herzhaft and Guazzelli [16], who did use perfectly straight fibres, suggests that the influence of volume fraction is more significant than that of straightness.

Fig. 10 shows the orientation distribution of fibrous particles obtained from 29,364 samples over the range of a volume fraction,

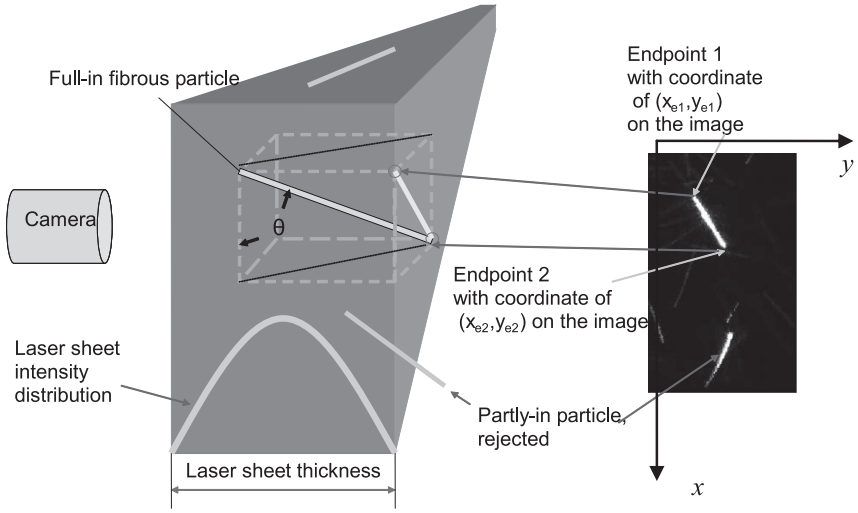

Fig. 7. Schematic diagram of the orientation measurement, the detection of "part-in" fibres and key notation.

$\Phi<5\times10^{-4}$. It can be seen that the majority of fibres are broadly, but not exactly, horizontal. This agrees with Fan et al. [1] and Clift et al. [2].

3.2. Influences of volume fraction on vertical component of settling velocity of fibrous particles

Fig. 11 presents the relationship between volume fraction (Φ) and the mean vertical component of settling velocity ($\overline{V_{cx}}$) under the condition of low number density (0.1×10^{-5}–10×10^{-5}). The measurements conducted in super dilute condition. Thousands of runs were performed and per volume fraction were sorted out by image processing. The data point corresponding to the lowest volume fraction in Fig. 11 represents the case of one isolated particle per image and highest volume fraction is 98 fibres per image. Each data point of $\overline{V_{cx}}$, $\overline{\theta}$ and $\overline{V_{cy}}$ comes from the average of per volume fraction which has hundreds of data in Figs. 11–13. It can be seen that $\overline{V_{cx}}$ increases monotonically with Φ. Furthermore the scatter in the data also increases with Φ, the RMS of the data has a similar trend. Eq. (16) is proposed to describe relationship between the number density and the vertical component of settling velocity for the dilute regime.

$$\frac{\overline{V}_{cx}(\phi)}{\overline{V}_{ts}} = a\phi^{n} \tag{16}$$

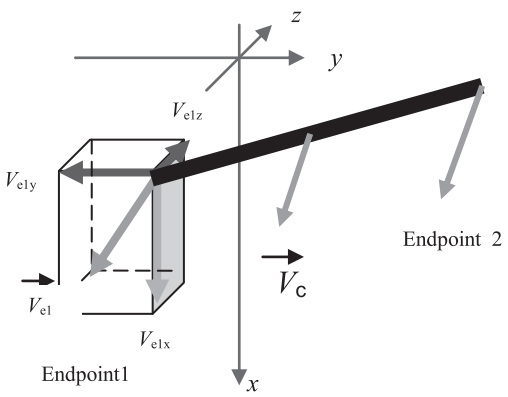

Fig. 8. Two endpoint and centroid velocities of a fibre.

where $\overline{V_{ts}}$ is average terminal settling velocity of a single fibre; a and n are constants that are expected to depend on fibre's aspect ratio and Reynolds number. The constants in Eq. (16) for the present fibres are: $\overline{V_{ts}}=0.375$, $a=7.310$ and $n=0.1519$. That is

$$\overline{V}_{cx}(\phi) = 2.743\phi^{0.1519}. \tag{17}$$

The data point corresponding to the lowest volume fraction in Fig. 11 represents the minimum of $\overline{V_{cx}}$ (terminal settling velocity of an isolated fibre), with all other values of $\overline{V_{cx}}$ exceeding it in $\Phi=0.1\times10^{-5}$–10×10^{-5} regime.

3.3. Influences of volume fraction on orientation of fibrous particles

Fig. 12 presents the relationship between the Φ and mean orientation ($\overline{\theta}$). It can be seen that $\overline{\theta}$ decreases with Φ, i.e. the fibrous particles tend to become more horizontal with decreasing Φ. These data can also be described by a power relationship:

$$\overline{\theta}(\phi) = \frac{b}{\phi^{n}}\overline{\theta}_{ts}(^{\circ}) \tag{18}$$

where b is a constant and $\overline{\theta_{ts}}$ is the average orientation of a single fibre

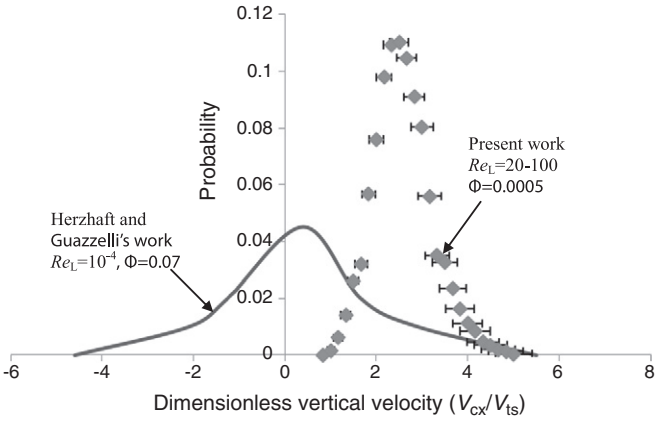

Fig. 9. The measured distribution of settling velocity V_{cx} relative to the terminal velocity of an isolated particle, V_{ts}, at volume fraction $\Phi<5\times10^{-4}$.

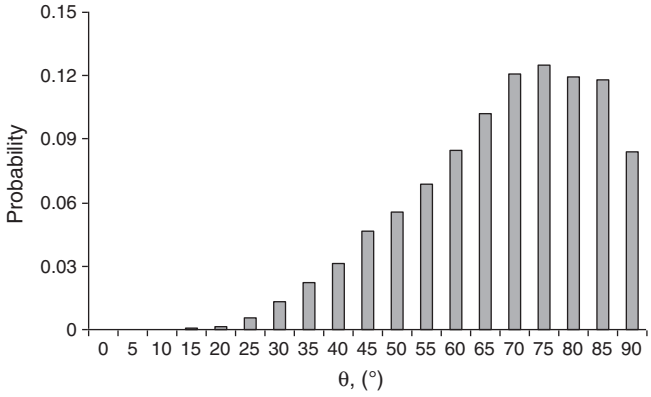

Fig. 10. The measured distribution of the orientation of present fibres from the vertical direction, at volume fraction $\Phi < 5\times10^{-4}$.

when settling in air. In the above case, $\overline{\theta_{ts}} = 81.38°$ and $n = 0.0654$, $b = 0.428$. This result can explain why the value of $\overline{V_{cx}}$ increases with Φ. An increase in Φ causes the fibre's major axis to tend to be more vertical, causing $\overline{V_{cx}}$ to increase, due to increased aerodynamic interaction between particles.

3.4. Influences of volume fraction on horizontal component of settling velocity of fibrous particles

Fig. 13 presents the relationship between mean horizontal component of settling velocity $\overline{V_{cy}}$ and Φ. It can be seen that $\overline{V_{cy}}$ is zero on average and the fluctuation of $\overline{V_{cy}}$increases monotonically with Φ. The RMS is well characterised by a power law as follows:

$$\text{RMS of } \overline{V_{cy}} = 0.0167\Phi^{0.2495}. \tag{19}$$

The fluctuation in $\overline{V_{cy}}$ values indicates that the trajectories of settling fibres are not straight lines. The aerodynamic interaction increases the absolute value of $\overline{V_{cy}}$.

3.5. Assessment of characteristic length of a fibre when settling in air

The definition of the Reynolds number of a settling fibrous particle in air requires a characteristic length scale. The *Re* of a fibre can be calculated using diameter d, length L or equivalent d_{eq} . Assuming that an equivalent "diameter" d_{eq} can be found, it is possible to define a Reynolds number Re_{eq} of a single fibre as follows:

$$Re_{eq} = \frac{\rho_{air} V_{ts} d_{eq}}{\mu}. \tag{20}$$

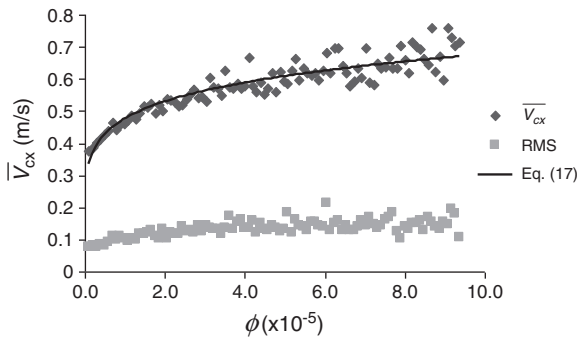

Fig. 11. The relationships between Φ and $\overline{V_{cx}}$ for fibrous particles settling in air.

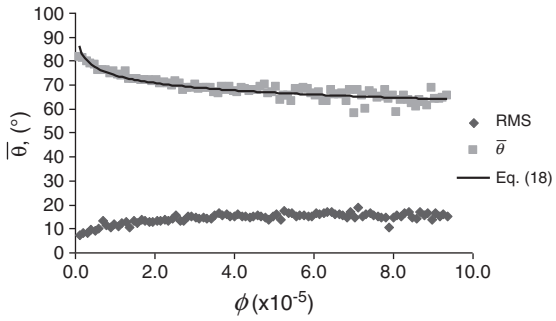

Fig. 12. The relationship between $\overline{\theta}$ and Φ.

When settling in air, the fibre's drag force can then be defined as follows:

$$F_D = \frac{1}{2}\rho_{air} C_D V_{ts}{}^2 A_{eq} = \frac{1}{2}\rho_{air} C_D V_{ts}{}^2 \pi\left(\frac{d_{eq}}{2}\right)^2. \tag{21}$$

The force due to gravity is $F_g = \rho_{fp}\pi\left(\frac{d}{2}\right)^2 Lg$, and when the fibre reaches its terminal settling velocity $F_g = F_D$:

$$\rho_{fp}\pi\left(\frac{d}{2}\right)^2 Lg = \frac{1}{2}\rho_{air} C_D V_{ts}{}^2 \pi\left(\frac{d_{eq}}{2}\right)^2. \tag{22}$$

Combining Eqs. (20) and (22) gives $C_D\,(Re_{eq})^2$:

$$C_D\left(Re_{eq}\right)^2 = \frac{2\rho_{fp}\rho_{air} d^2 Lg}{\mu^2} = K \tag{23}$$

In Eq. (23), K is a constant for a given fibre, so we can obtain the relationship of the present fibre between C_D and $(Re_{eq})^{-2}$ theoretically, as shown in Fig. 14:

$$C_D = K\left(Re_{eq}\right)^{-2} = 412.81\left(Re_{eq}\right)^{-2}. \tag{24}$$

If we define d_{eq} based on the fibre's projected area, in the vertical direction it is:

$$A_{eq} = \pi\left(\frac{d_{eq}}{2}\right)^2 = dL\sin\theta + \pi\left(\frac{d}{2}\right)^2\cos\theta. \tag{25}$$

We can experimentally measured C_D from Eq. (26):

$$C_D = \frac{F_D}{\frac{1}{2}\rho_{air} V_{ts}{}^2 A_{eq}} = \frac{\rho_{fp}\pi\left(\frac{d}{2}\right)^2 Lg}{\frac{1}{2}\rho_{air} V_{ts}{}^2\left(dL\sin\theta + \pi\left(\frac{d}{2}\right)^2\cos\theta\right)}. \tag{26}$$

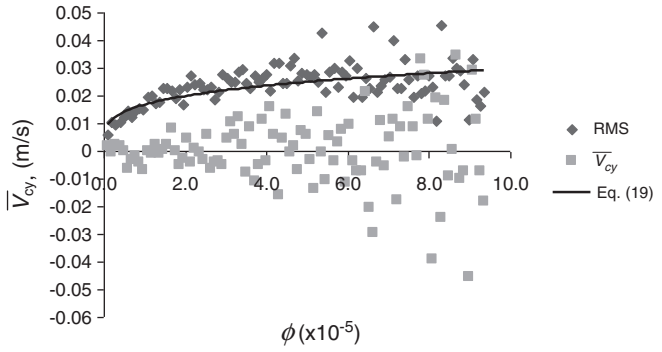

Fig. 13. The relationship between $\overline{V_{cy}}$ and Φ.

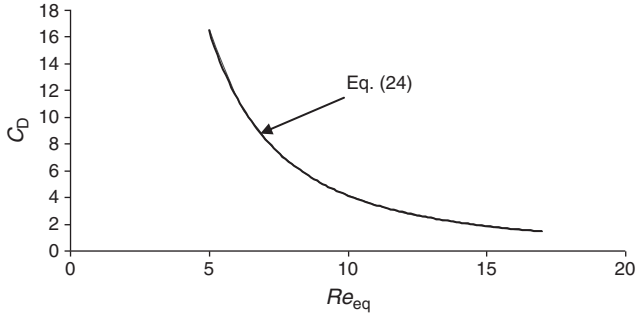

Fig. 14. The theoretical relationship between Re_{eq} and C_D.

Meanwhile $Re_d = \frac{\rho_{air} V_{ts} d}{\mu}$, so that combining this with Eq. (26) and gives:

$$C_D = \frac{\rho_{air}\rho_{fp}\pi d^3 Lg}{2Re_d{}^2\mu^2\left(L\sin\theta + \frac{1}{4}\pi d\cos\theta\right)}. \quad (27)$$

Eq. (27) is the relationship between C_D, Re_d and orientation θ.

Fig. 15 presents the experimental relationship between Re and C_D based on 94 single settling fibres and the Re were calculated using the fibre's diameter d, length L, volume equivalent diameter d_{ev} and surface equivalent diameter d_{es} respectively. We plot C_D–Re (Eqs. (26) and (20)) by changing d_{eq} until the curve of Fig. 15 coincides Fig. 14, then we obtained $d_{eq} = 354$ μm for the present fibre, see Fig. 16. After that Eq. (25) becomes:

$$396800.00\sin\theta + 7728.82\cos\theta = 393691.82. \quad (28)$$

Solving Eq. (28), we can obtain $\theta_{eq} = 81.62°$. Comparing with Eq. (18), $\overline{\theta_{ts}} = 81.38°$ it can be seen that average orientation of a settling single fibre can be used in Eqs. (25), (26) and (27). Therefore from Eq. (25) the equivalent "diameter" d_{eq} of a fibre settling in air is as follows:

$$d_{eq} = \sqrt{\frac{4Ld\sin\overline{\theta}_{ts}}{\pi} + d^2\cos\overline{\theta_{ts}}}. \quad (29)$$

The models proposed by Fan et al. [1] and Clift et al. [2] are based on diameter, d, of the fibre. Hence we use this characteristic length to assess their models in Fig. 17. From the figure we can see that these models do not describe the behaviour of the present particles. For Fan's model, as can be seen from Eq. (1), the term $\left(\frac{\rho_{fp}}{\rho_f}\right)^{-1.537}$ plays an important role when ρ_{fp} is far greater than ρ_f. For the present case $\rho_{fp}/\rho_f = 958$, it predicts C_D far less than the present values. Hence their model is poorly suited to fibre-gas two-phase flow. For Clift's model $C_D = 9.689(Re_d)^{-0.78} + 1.42(Re_d)^{0.04}$ $(0.1 < Re_d < 5)$, the power of -0.78 is far greater than -2, so its slope is much lower than that of the present fibres. As mentioned in Section 3.1, the presence of a slight curve of the fibres increases the scatter in settling velocity distribution, this can cause a bias on C_D. However no comparable data are available against which to provide a quantitative assessment of the effect.

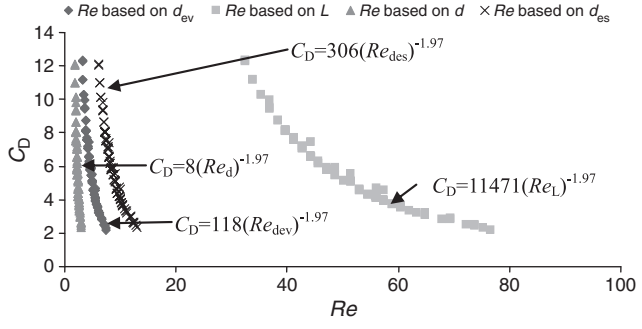

Fig. 15. The experimental dependence of the drag coefficient on Reynolds number based on length Re_L, on diameter Re_d, on equivalent surface area diameter Re_{des} and on equivalent volume diameter Re_{dev}.

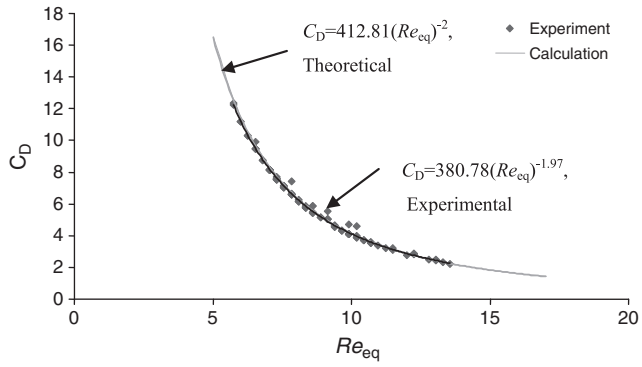

Fig. 16. Theoretical and experimental relationships between C_D and Re_{eq}, where d_{eq} is defined in Eq. (29).

4. Conclusions

In this work, we measured the vertical and horizontal components of settling velocities, orientation and number density for long fibres settling in air with $Re \sim O(1)$ and for volume fractions $\Phi = 10^{-6}$–5×10^{-4}. The mean vertical settling velocities were found to increase monotonically with Φ. The mean orientations decrease with Φ. We show that all the mean steady state settling velocities of multiple fibres exceed the mean terminal settling velocity of a single fibre under $\Phi < 10^{-4}$. This phenomenon is attributed to the fibres' orientation transition from a horizontal state to a vertical state under a super dilute regime that stems from increasing aerodynamic interactions between fibres. The mean horizontal settling velocity was zero on average. However the fluctuations of the horizontal components of settling velocities of settling fibres were found to increase with volume fraction. It is also found that there is no fundamental difference in the aerodynamic behaviour of particles that are fully straight or exhibit a slight bend, although the presence of a bend increases the spread in the probability distribution. Finally the controlling length scale in the relationship between Reynolds number and drag coefficient was assessed. It is found that the diameter based on the projected area with mean orientation describes the relationship well, while all other length scales fail. The models of Fan et al. [1] and Clift et al. [2] were also found to be in poor agreement with the present measurements.

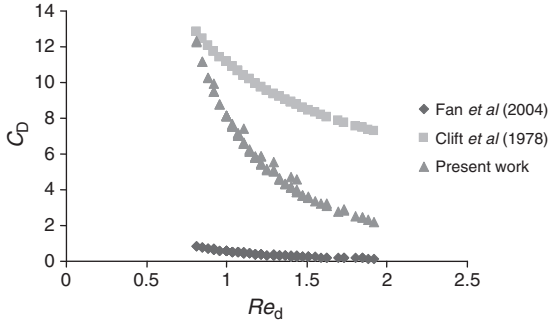

Fig. 17. The relationship of Re_d and C_D between the present, Fan's, and Clift's work.

Acknowledgement

This study has been supported by the Faculty of Engineering, Computer & Mathematical Science of The University of Adelaide and by an ARC Discovery Grant, both of which are gratefully acknowledged.

Appendix A. *A.1. Image processing*

The purpose of the image processing is to extract measurements for each particle using Eqs. (9)–(15) and to thus allow the aerodynamic behaviour of the fibrous particle to be assessed statistically under various conditions. From the coordinates of two endpoints it is possible to calculate the orientation and velocities of a fibre.

Those fibrous particles located at the edges of an image yield a false measurement of its length. Therefore first step of image processing is to remove these fibrous particles from the images. The second step is to convert the image into binary form. The third step is to remove small objects. Binary images typically contain "noise" which comprises spurious signal in one or two isolated pixels. They are not real fibrous particles and so need to be removed. The fourth step is to label the fibres. This is a very important and useful step in images processing. By using this tool the background pixels were labelled 0. The pixels that made up the first object were labelled 1, (see Fig. A1) those labelled 2, the second object, and so on. If there were n particles in the viewing volume the last pixels (object) would be labelled n. Therefore this tool can be used to count the number of fibres in the image exactly.

The fifth step is removing fibrous particles "partly-in" the laser sheet. As previously noted, the measured lengths of such fibrous particles are false. Therefore these part-in fibres must also be removed from the images when processing. Fig. A2 displays the different characteristics of full-in and part-in fibrous particles. For a "full-in" fibrous particle, the intensity along the major axis of the fibre is nearly constant while for a part-in one, the intensity at the two endpoints differs significantly (Fig. A2). Hence it is possible to discriminate by either comparing the intensity of the two endpoints of the fibre, or by comparing the standard deviation of the intensity along the major axis. If the standard deviation is less than the threshold, it is a full-in fibrous particle.

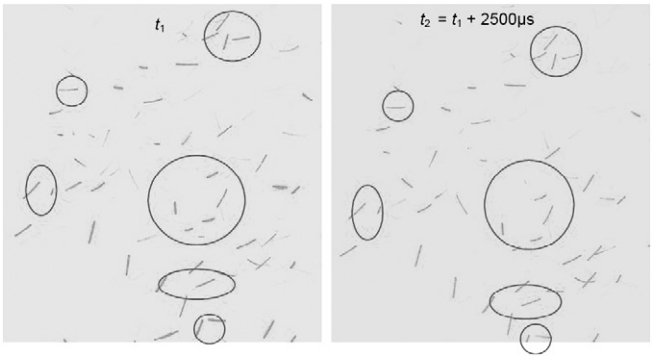

Fig. A3. A pair of images of fibres with a known time separation of 2500 μs, sets of obviously matching pairs are encircled.

The last step is tracking particles and calculating velocities and orientations. Fig. A3 presents a pair of images of fibres with a known time separation of 2500 μs. The circles highlight those fibrous particles that are pairs. It can be seen that if the time separation is short enough, any changes in the fibre's length are small, and orientation and area are small. Based on these characteristics on the images, tracking particles (matching pairs) becomes easier than for spherical particles.

The accurate matching of pairs of fibrous particles within a known time separation is the most important step in image processing. From this, the vertical and horizontal displacements of each particle can be obtained, and hence the vertical and horizontal components of settling velocities can be calculated. After collecting of the two

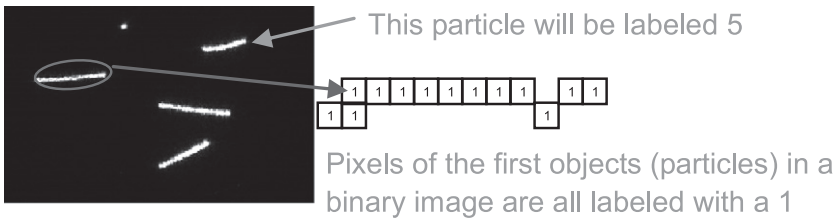

Fig. A1. Step 4 — labelling pixels of fibrous particles in a binary image.

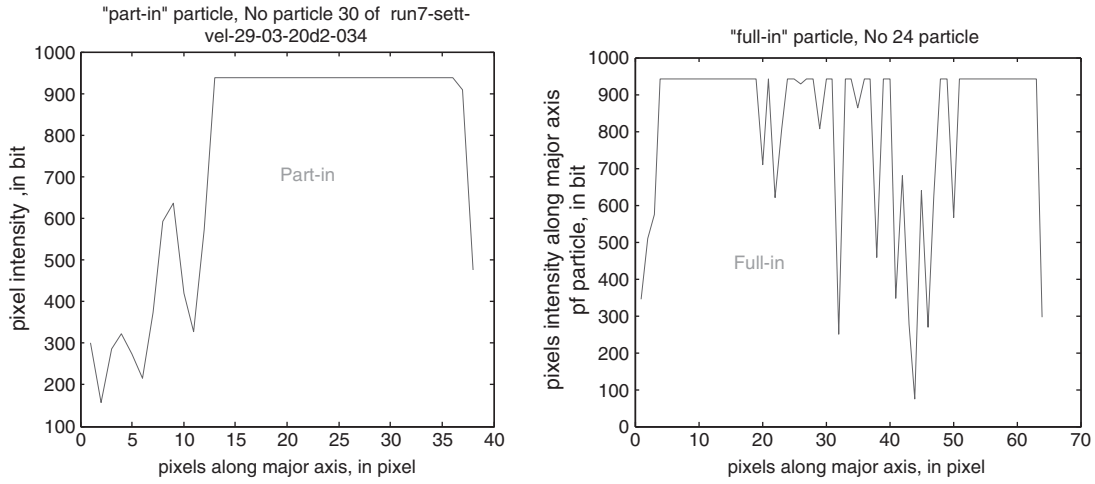

Fig. A2. The distributions of intensity along the major axis for part-in and full-in fibrous particles in the laser sheet.

endpoint's coordinates and matching particle pairs in each pair of images, all components of settling velocities (translational and rotational) of the centroid and orientation of a fibrous particle can be obtained from Eqs. (9)–(15). The end point of a fibre moves by an average of 50 pixels, and the total uncertainty in the position of the end point is 4 pixels, then this corresponds to a relative uncertainty in the spatial position of the end point of 8%.

References

[1] L. Fan, Z. Mao, C. Yang, Experiment on settling of slender particles with large aspect ratio and correlation of the drag coefficient, Industrial and Engineering Chemistry Research 43 (2004) 7664–7670.

[2] R. Clift, J. Grace, M. Weber, Bubbles, Drops, and Particles, Academic Press, New York0-12-176950-X, 1978..

[3] A. Haider, O. Levenspiel, Drag coefficient and terminal velocity of spherical and nonspherical particles, Powder Technology 58 (1989) 63–70.

[4] G. Venu Madhav, R.P. Chhabra, Drag on non-spherical particles in viscous fluids, International Journal of Mineral Processing 43 (1995) 15–29.

[5] G.H. Ganser, A rational approach to drag prediction of spherical and nonspherical particles, Powder Technology 77 (1993) 143–152.

[6] P.K. Swamee, C.P. Ojha, Drag coefficients and fall velocity of non-spherical particles, Journal of Hydraulic Engineering 117 (1991).

[7] R. Gonzalez, R. Woods, S. Eddins, Digital Image Processing using Matlab, Pearson Education0-13-008519-7, 2004..

[8] R.P. Chhabra, L. Agawal, N.K. Sinha, Drag on non-spherical particles: an evaluation of available methods, Powder Technology 101 (1999) 288–295.

[9] Z.L. Arsenijevic, Z.B. Grbavcic, R.V. Grulovic, F.K. Zdanski, Determination of non-spherical particle terminal velocity using particulate expansion data, Powder Technology 103 (1999) 265–273.

[10] H.Y. Xie, D.W. Zhang, Stokes shape factor and its application in the measurement of sphericity of non-spherical particles, Powder Technology 114 (2001) 102–105.

[11] P. Rajitha, R.P. Chhabra, N.E. Sabiri, J. Comiti, Drag on non-spherical particles in power law non-Newtonian media, International Journal of Mineral Processing 78 (2006) 110–121.

[12] S. Tran-Cong, M. Gay, E.E. Michaelides, Drag coefficient of irregularly shaped particles, Powder Technology 139 (2004) 21–32.

[13] A. Unnikrishnan, R.P. Chhabra, An experimental study of motion of cylinders in Newtonian fluids: wall effects and drag coefficient, The Canadian Journal of Chemical Engineering 69 (1991).

[14] J. Gabitto, C. Tsouris, Drag coefficient and settling velocity for particles of cylindrical shape, Powder Technology 183 (2008) 314–322.

[15] G. McKay, W.R. Murphy, M. Hillis, Settling characteristics of discs and cylinders, Chemical Engineering Research and Design 66 (1988).

[16] B. Herzhaft, E. Guazzelli, Experimental study of sedimentation of dilute and semi-dilute suspensions of fibres, Journal of Fluid Mechanics 384 (1999) 133–158.

Powder Technology 289 (2016) 20

Contents lists available at ScienceDirect

Powder Technology

journal homepage: www.elsevier.com/locate/powtec

Corrigendum

Corrigendum to "PTV measurements of drag coefficient of fibrous particles with large aspect ratio" [Powder Technol. 229 (2012) 261–269]

Guo Q. Qi*, Graham J. Nathan, Richard M. Kelso

School of Mechanical Engineering and Centre for Energy Technology, The University of Adelaide, Adelaide, SA 5005, Australia

The authors advise that Figures 4 and 5 of the published version of the document are incorrect, although the errors do not affect the conclusions of the paper. The corrected figures and associated text are provided below.

Fig. 4 presents the distribution of the straightness of the fibrous particles based on a sample size of 1139. It can be seen that 90.1% of these fibres have straightness $\varepsilon > 0.97$ and some 38% are perfectly straight. The original overestimated the departure from the straightness. Hence this change does not influence the conclusions of the paper.Fig. 4The distribution of straightness, ε (see Eq. 7) for the present fibres.

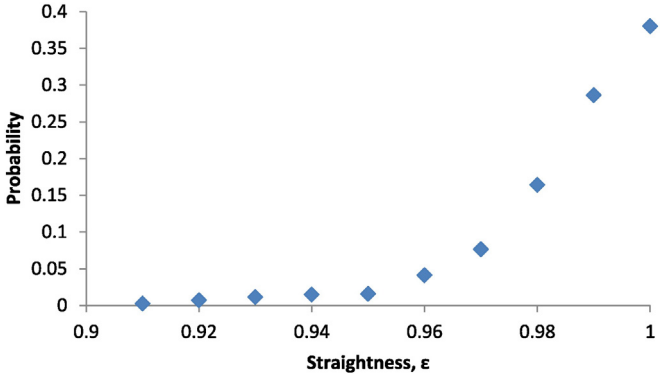

The authors advise that in Table 1 of page 263, the length of the fibre is reported incorrectly as 2000 μm, while it should be 1850 μm. The orientation uncertainty caused by this correction is unchanged because it is within the error bars of 8% as described in the paper. Hence this change does not influence the conclusions of the paper. Fig. 5 of the published document is also incorrect. The correct figure and associated context (lines 43–47, page 263) are given below:

Fig. 5 presents the distribution of the fibres' length, L, which were measured directly from the two endpoints. It can be seen that 82% of fibres have a length between 1750 μm and 1950 μm and over 95% between 1650 μm and 2050 μm, with a standard deviation of 196 μm.Fig. 5The distribution of the length, L, of the present fibres.

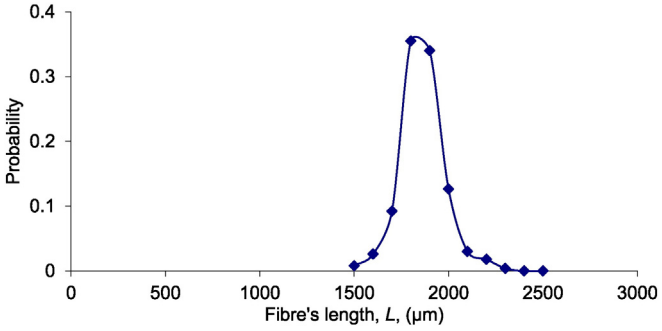

DOI of original article: http://dx.doi.org/10.1016/j.powtec.2012.06.049.
* Corresponding author.
E-mail address: guo.qi@adelaide.edu.au (G.Q. Qi).

http://dx.doi.org/10.1016/j.powtec.2015.11.026

4 Aerodynamics of Long Fibres Settling in Air at $10 < Re < 100$

Guo Q. Qi, Graham J. Nathan and Richard M. Kelso

School of Mechanical Engineering and Centre for Energy Technology, The University of Adelaide, Adelaide SA 5005 AUSTRALIA

Email: guo.qi@adelaide.edu.au

Powder Technology 235 (2013) 550–555

Statement of Authorship

Title of Paper	Aerodynamics of long fibres settling in air at $10 < Re < 100$
Publication Status	☑ Published ☐ Accepted for Publication ☐ Submitted for Publication ☐ Unpublished and Unsubmitted work written in manuscript style
Publication Details	Guo Q. Qi, Graham J. Nathan and Richard M. Kelso. Aerodynamics of long fibres settling in air at $10 < Re < 100$. Powder Technology, 235 (2013), 550–555.

Principal Author

Name of Principal Author (Candidate)	Guo Qiang Qi
Contribution to the Paper	I was responsible for the development of both the measurement technique and analytical model under the principal supervision of Professor Nathan. I performed the measurements and data processing, wrote the first draft of the manuscript and incorporated and addressed all comments and suggestions by other authors and reviewers in subsequent revisions of the manuscript. I acted as corresponding author.
Overall percentage (%)	55%
Certification:	This paper reports on original research I conducted during the period of my Higher Degree by Research candidature and is not subject to any obligations or contractual agreements with a third party that would constrain its inclusion in this thesis. I am the primary author of this paper.
Signature	Date: 13/06/1016

Co-Author Contributions

By signing the Statement of Authorship, each author certifies that:

i. the candidate's stated contribution to the publication is accurate (as detailed above);

ii. permission is granted for the candidate in include the publication in the thesis; and

iii. the sum of all co-author contributions is equal to 45% less the candidate's stated contribution.

Name of Co-Author	Graham J. Nathan
Contribution to the Paper	I was principal supervisor for the development of work, contributed to both data interpretation and refining of the manuscript.
Signature	Date: 14/6/16.

Name of Co-Author	Richard M. Kelso
Contribution to the Paper	I, co-supervisor, jointly supervised the development of work.
Signature	Date: 14/6/2016.

Please cut and paste additional co-author panels here as required.

Powder Technology 235 (2013) 550–555

Contents lists available at SciVerse ScienceDirect

Powder Technology

journal homepage: www.elsevier.com/locate/powtec

Aerodynamics of long fibres settling in air at $10 < Re < 100$

Guo Q. Qi *, Graham J. Nathan, Richard M. Kelso

School of Mechanical Engineering and Centre for Energy Technology, The University of Adelaide, Adelaide, SA 5005, Australia

ARTICLE INFO

Article history:
Received 15 February 2012
Received in revised form 3 September 2012
Accepted 4 November 2012
Available online 19 November 2012

Keywords:
Sedimentation
Aerodynamics
PTV
Fibrous particle

ABSTRACT

The aerodynamics of long aspect ratio nylon fibrous particles has been investigated experimentally whilst settling in air under super dilute conditions without any influence of secondary flows and at fibre Reynolds numbers of 10–100 based on fibre length. Measurement of the orientations and velocities of fibrous particles is undertaken by two-dimensional Particle Tracking Velocimetry (PTV), based on the two end-points. A statistical evaluation of fibres' mean vertical and horizontal components of settling velocities, angular velocity, orientation, number density is presented and used to assess particle aerodynamics.

1. Introduction

One approach to reduce the use of fossil fuels is their partial substitution with biomass, or organic matter, which is a renewable and more environmentally "friendly" resource for energy supply. Such fuels can be derived from trees, agricultural residues and other plants. The percentage of biomass being used is increasing around the world for these reasons. However biomass is fibrous and there is a paucity of data describing the aerodynamics of fibrous particles. In order to increase the efficiency of the combustion of biomass, the aerodynamics of biomass particles needs to be investigated.

The settling motion of a particle is a basic class of its motion. The settling motion of a fibrous particle is much more complex, and more poorly understood than that of a sphere. A sphere settles in a purely vertical direction. However for a fibrous particle, the instantaneous horizontal drift cannot be neglected. A fibrous particle also exhibits rotation. A large number of previous investigations have studied the hydrodynamics of fibres under the conditions of relevance to the paper making industry. But these conditions differ from those in combustion. Theoretical treatments include the slender body theory by Batchelor [1] and the concentration instability by Koch and Shaqfeh [2]. Experimental investigations include that of Metzger et al. [3], Herzhaft and Guazzelli [4], Salmela et al. [5], Herzhaft et al. [6]. Previous numerical investigations were performed by Shin et al. [7], Butler and Shaqfeh [8], Lin and Zhang [9], Lin et al. [10], Kuusela et al. [11], Kuusela et al. [12], Tornberg and Gustavsson [13], Shin et al. [14]. Previous investigations to study the drag coefficient of fibrous particles were performed by Gabitto and Tsouris [15], Fan et al. [16], McKay et al. [17], Unnikrishnan and Chhabra [18], Haider and Levenspiel [19], and so on. The conditions under which these investigations were performed are summarised in Table 1. However none of these investigations provide detailed measurements of a bulk settling fibres in the range of $10 < Re_L < 100$ (fibre's Reynolds number based on its length).

Koch and Shaqfeh [2] studied theoretically the instability of a dispersion of sedimenting spheroids and pointed out that hydrodynamic interactions between sedimenting fibres give rise to an increase in the number of neighbouring particles in the vicinity of any given particle. They suggested that the suspension is unstable to particle number density fluctuations. They also argued that the convective motion (cluster formation) may lead to an average sedimentation velocity which is larger than the maximum possible value for a particle in a quiescent fluid. This theory can be verified by accurate measurements of settling velocity and orientation of fibres.

Clift et al. [20] reported that, for a single fibrous particle Reynolds number $Re_d > 0.01$ (based on its diameter), a cylinder falls with its axis oriented horizontally and exhibits steady motion with this orientation up to Re_d of order 100. However, this is yet to be extended to a cloud of interacting particles in suspension. Salmela et al. [5] experimentally studied the settling of dilute and semi-dilute fibre suspensions for $0.0003 < Re_L < 9$ in a liquid. At $Re_L \sim O(1)$, for small volume fractions $\Phi < 0.0005$ they found that fibres settle with their long-axis preferentially in the horizontal state and the settling velocity and the fluctuation of settling velocity increases with Φ. They also found that the steady-state settling velocity has a maximum that exceeds the velocity of an isolated particle because of a change in average orientation of the fibres from horizontal to vertical. With $\Phi > 0.0005$, fibres settle preferentially with their long-axis aligned with the direction of gravity, i.e. the average orientation gradually changes from horizontal state to vertical. However, from Table 1 it can be seen that, for a bulk settling of fibres of $Re_L \sim O(10)$ and $Re_L \sim O(100)$, no similar investigations seem to be available.

Herzhaft and Guazzelli [4] and Metzger et al. [3] experimentally investigated sedimenting suspensions of fibres with $Re_L \approx 0.0001$,

* Corresponding author.
E-mail address: guo.qi@adelaide.edu.au (G.Q. Qi).

0032-5910/$ – see front matter.
http://dx.doi.org/10.1016/j.powtec.2012.11.005

Table 1
Comparisons between present and previous work.

Authors	L (mm)	L/d	Fluid phase	Re_L	(Φ), $n_p(L/2)^3$	ρ_{fp}/ρ_f	Facility dimensions (mm)				Method
							length	width	height	Width/L	
Present Work	2	40	Air	10-100	(<0.0001), <0.03	958.3	650	620	2000	310	PTV
Salmela et al. [5]	2.3, 5	23, 50	Water, glycerin, oil	0.0004-9	(0.0004-0.5)	2.25, 2.62	100	100	N/A	20	Real time digital image
Herzhaft and Guazzelli [4]	0.5-1.1	5, 11, 20, 32	Water	< 0.0001	0.001-1.0	2.1	65	35	400	32	Real time digital image
Fan et al. [16]	1.5-7	4,6,19, 22,37	Water, glycerin	0.4-100 (Re_d)	Single particle	1.2, 8.0	Diameter 187			27	Real time digital image
Metzger et al. [3]	1.5-2.1	10,13, 16,44	Liquid	0.0004	0.1,0.2, 0.3,0.7,1	1.1, 8.5	200	40	100	19	PIV
Butler and Shaqfeh [8]	N/A	11	N/A	<0.00001	0.154	N/A	Length : width : height 1:1:2 1:1:8				Numerical Simulation
Kuusela et al. [11]	N/A	1,3,5,7	N/A	0.5–3.5	(0.001–0.1)	2.5				32	Numerical Simulation
Tornberg and Gustavsson [13]	N/A		N/A	<0.00001	25, 50, 100 fibres	N/A	Length : width : height 2:2:8 2:2:4				Numerical Simulation
Shin et al. [7]	N/A	2.3–10	N/A	0–10.6	(<0.0057), <0.09	N/A	N/A				Numerical Simulation

also in a liquid. For this case, the inertia acting on the fibrous particles approaches zero, causing the fibres to tend to align with the direction of gravity for dilute and semi-dilute suspensions. This contrasts the case of $Re_L \sim O(1)$ where fibre orientations are horizontal. Herzhaft and Guazzelli [4] pointed out that their experiment demonstrates the existence of an instability but could not confirm whether or not the argument of Koch and Shaqfeh [2] is correct. Herzhaft and Guazzelli also assessed the influence of a fibre's aspect ratio. They found that the aspect ratio has little influence on the fibre's orientation and that the dimensionless settling velocity is much smaller for long fibre than for short one. Although this regime is different from that of Salmela et al. [5], Herzhaft and Guazzelli [4] also found in their experiment that the settling velocity can be larger than the Stokes' velocity of an isolated vertical fibre in dilute suspension. Further, with increasing volume fraction, the fluctuation of settling velocity and fibres' orientation anisotropy was found to increase. The cause of this correlation deserves further investigation.

Kuusela et al. [11] simulated the settling of spheroids under steady state sedimentation at $0.5 < Re_L < 3.5$. The authors assessed the role of aspect ratio of fibres and found the maximum settling velocity to decease with increasing aspect ratio. They also found that the volume fraction of peak velocity increases with increased volume fraction. These results are in good agreement with Herzhaft and Guazzelli's work [4]. They found an orientational transition of the spheroids is characterised by enhanced number density fluctuations. They predicted the orientation distribution that arises from a competition between inertial forces acting on individual particles and hydrodynamic interactions between particles. For super dilute systems, inertial effects tend to align fibres to a horizontal position whereas in sufficiently concentrated systems the interactions tend to align the fibres with gravity. Around the transition from a horizontal to vertical orientation, the mean settling velocity increases with increasing of Φ to a maximum that may even exceed the terminal settling velocity of a single spheroid. These accord with the experimental results of Salmela et al. [5]. However like the work of Salmela et al. [5], see Table 1, the Re_L of this investigation was limited to less than 3.5.

Butler and Shaqfeh [8] performed a numerical simulation of inhomogeneous sedimentation of rigid fibres in the limit of zero of Re_L. Their simulation revealed that the steady settling velocity increases with the number density of fibrous particles simulated in the dilute regime. The predictions of orientation distribution agreed with the experimental result of Herzhaft and Guazzelli [4], i.e. the particles have a most probable orientation that is close to vertical. Furthermore the simulation showed that the orientation of fibrous particles tend to be more vertical with increasing of number density in the dilute regime. However this assessment is yet to be extended to higher Reynolds number.

Table 1 presents a summary of all previous measurements of settling slender particles. It can be seen that there have been 4 experimental and 4 numerical investigations. From the Table we can see there are 3 main features of present work compared with previous work. The first is that for bulk settling fibres, the present Reynolds number in the range of $10 < Re_L < 100$ has not been investigated. The second is that the fluid phase of the present work is air, so the ratio of particle density to fluid is two orders of magnitude higher than that of previous work. The third is that the ratio of facility dimension to particle's length of the present work is 310, so there is no influence of secondary-flow in the settling chamber.

In the light of above review, we seek to further the understanding of the aerodynamics of settling fibrous particles in the range of $Re_L = 10$–100, with for a range of volumetric loading and with no boundary limitation. As can be seen from Table 1 these conditions have yet to be reported previously. Therefore, the aim of the present work is to use the novel method developed in Qi et al. [21] to measure the velocity and orientation of a fibrous particle simultaneously and to investigate the aerodynamics of these fibres, notably their distribution of settling velocity, horizontal velocity and orientation. We also aim to identify the relationship between settling velocity, orientation, angular velocity and volume fraction, and relationship between settling and horizontal velocity and orientation.

2. Experimental apparatus/facility

Only a brief description of the experimental apparatus and approach is provided here, with details presented by Qi et al. [21]. Fig. 1 presents the orientation definition of a fibre. The plane of x-y is the image plane. The angle α (0°–90°) is defined to be the azimuth of a fibre and θ (0°–90°) its orientation.

Fig. 2 presents a schematic diagram of the experimental apparatus. The experimental method employed a typical Particle Tracking Velocimetry (PTV) technique. The laser used in the experiments was a Quantel Brilliant Twins double-cavity pulsed Nd: YAG 10 Hz laser.

The settling chamber was of nominally square cross section with a 650 mm × 620 mm, height of 2000 mm and was made of Perspex.

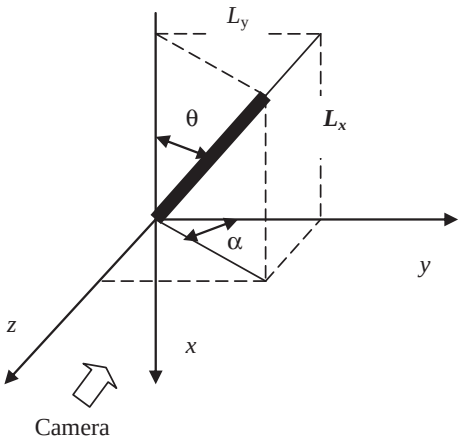

Fig. 1. The orientation definition of a fibre, *x*–*y* plane is the image plane.

The fibrous particles were introduced into the top of the chamber and settled over a distance of 2.5–3.0 m through a 2000 mm long pipe of 60 mm diameter. Fibre's settling velocities were measured for settling distances of both 2.5 m and 3.0 m. The mean settling velocities obtained were identical for both cases, confirming that the fibres have reached their terminal settling velocities and steady state conditions. The intensity distribution of laser sheet is nearly Gaussian. This property is exploited to determine whether a fibre is fully or partly within the light sheet. This can be achieved by comparing the intensities of the signal at two endpoints of the fibre. Because of the Gaussian light sheet intensity distribution, a partly-in fibrous particle will exhibit a significant difference between the intensity values of the two endpoints. For a "full-in" fibrous particle, the intensity along the major axis of the fibre is nearly constant while for a part-in one, the intensity at the two endpoints differs significantly. Hence it is possible to discriminate by either comparing the intensity of two endpoints of the fibre, or by comparing the standard deviation of intensity along the major axis. If the standard deviation is less than the threshold, it is a full-in fibrous particle. Full details of this approach are provided by Qi et al. [21].

To measure the settling velocity and Φ, the volume fraction was controlled here to be in the range of volume fraction $\Phi \leq 0.0001$, which is a super dilute condition so that there were few particles that exhibited clumping. Hence the number density of fibrous particle in the viewing area (volume) was calculated by counting the number of particles, and the volume fraction was computed exactly. The coordinates of the two endpoints of each object (fibrous particle) were obtained. Since the length L of these fibres is constant, the spatial orientation θ of fibres was calculated by following trigonometric function:

$$\theta = \left(\arccos\frac{|x_{e2}-x_{e1}|R}{L}\right)\times\left(\frac{180}{\pi}\right)\quad(^\circ), \tag{1}$$

where R is magnification of camera image system; x_{e2} and x_{e1} are coordinates of x values of two endpoints.

Image pairs were recorded by the digital camera with a known time separation (Δt). After image processing the displacements of two endpoints of fibrous particles along the x and y axis can be obtained. From this $\mathbf{V}_{e1x}$, $\mathbf{V}_{e1y}$ and $\mathbf{V}_{e2x}$, $\mathbf{V}_{e2y}$ can be calculated by Eq. (2), as follows:

$$V_{e1x}=\frac{(x_{e12}-x_{e11})R}{\Delta t}, V_{e1y}=\frac{(y_{e12}-y_{e11})R}{\Delta t}, \tag{2}$$
$$V_{e2x}=\frac{(x_{e22}-x_{e21})R}{\Delta t}, V_{e2y}=\frac{(y_{e22}-y_{e21})R}{\Delta t},$$

where V_{e1x} is the velocity of endpoint 1 in the x direction; V_{e1y} is the velocity of endpoint 1 in the y direction; V_{e2x} is the velocity of endpoint 2 in the x direction; V_{e2y} is the velocity of endpoint 2 in the y direction; x_{e12} is the x axis coordinate of endpoint 1 from the second image, x_{e11} is the x axis coordinate of the endpoint 1 from the first image; y_{e12} is the y axis coordinate of the endpoint 1 from the second image and so on. A fibre's centroid velocity $V_{cx}=1/2\ (V_{e1x}+V_{e2x})$ and $V_{cy}=1/2(V_{c1y}+V_{c2y})$ represents the vertical and horizontal components of settling velocities, respectively. Since data are obtained from an image pair, the orientation of a fibrous particle equals the average orientation from the first and second images:

$$\theta=\frac{1}{2}(\theta_1+\theta_2), \tag{3}$$

$$\theta_1=\arccos\frac{|x_{e21}-x_{e11}|R}{L}\times\left(\frac{180^\circ}{\pi}\right), \tag{4}$$

$$\theta_2=\arccos\frac{|x_{e22}-x_{e12}|R}{L}\times\left(\frac{180^\circ}{\pi}\right), \tag{5}$$

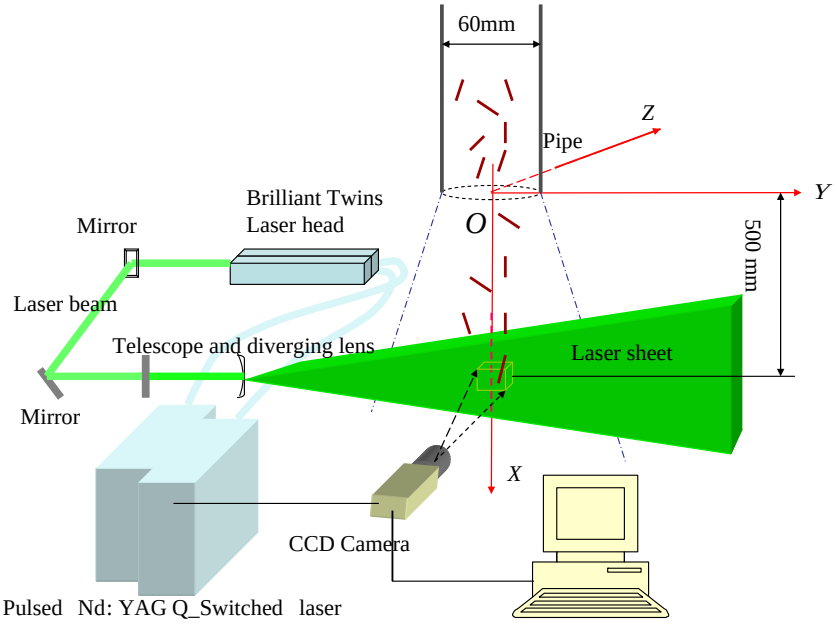

Fig. 2. Experimental arrangement (not to scale). The surrounding settling chamber (650 mm×620 mm cross section) is not shown for clarity.

$$\alpha_1 = \arccos\frac{|y_{e21}-y_{e11}|R}{L\sin\theta_1}\times\left(\frac{180^\circ}{\pi}\right), \quad (6)$$

$$\alpha_2 = \arccos\frac{|y_{e22}-y_{e12}|R}{L\sin\theta_2}\times\left(\frac{180^\circ}{\pi}\right). \quad (7)$$

The angular velocities (rad/s) of a fibre are defined to be:

$$\omega_{vertical} = \frac{(\theta_1-\theta_2)\times\left(\frac{\pi}{180}\right)}{\Delta t}, \quad (8)$$

$$\omega_x = \frac{(\alpha_1-\alpha_2)\times\left(\frac{\pi}{180}\right)}{\Delta t}. \quad (9)$$

3. Experimental results and discussions

3.1. Influences of volume fraction on vertical component of settling velocity of fibrous particles

Fig. 3 presents the dependence of $\overline{V_{cx}}$ on the volume fraction Φ for both the present work and previous work on logarithmic axes. The present measurements were conducted in the super dilute condition (0.1×10^{-5} to 10×10^{-5}). About 6000 runs were performed and the volume fraction for image was calculated by post-processing. The data point corresponding to the lowest volume fraction in Fig. 3 represents the case of one isolated particle per image, while the highest volume fraction is 98 fibres per image. Each data comes from the average of each volume fraction in Figs. 3, 4 and 5. It can be seen that $\overline{V_{cx}}$ increases monotonically with Φ. It is also clear that the present data is consistent with the trends in previous measurements with the differences attributed to the substantial differences in conditions, notably in Reynolds number and density ratio, but also in aspect ratio and confinement for some cases. The present work represents the first detailed assessment of this influence in the dilute regime.

3.2. Influences of volume fraction on orientation of fibrous particles

Fig. 4 compares the present measurements of orientation with previous work. It can be seen that $\overline{\theta}$ decreases with Φ, i.e. the fibrous particles tend to become more horizontal with decreasing Φ. This result can explain why the value of $\overline{V_{cx}}$ increases with Φ. An increase in Φ causes the fibre's major axis to tend to be more vertical, causing $\overline{V_{cx}}$ to increase, due both to a lower projected area and to increased aerodynamic interaction between vertically aligned particles. From the figure we can also see, in all cases, that the orientations of the fibrous particles tend to become more vertical with increasing Φ. The present work is in the range $Re_L\sim O(10)$; while Salmela [5] and Kuusela [11] was in the range $Re_L\sim O(1)$; Herzhaft and Guazzelli [4] and Butler and Shaqfeh [8] belong to $Re_L\sim O(0)$. From the figure it can be seen

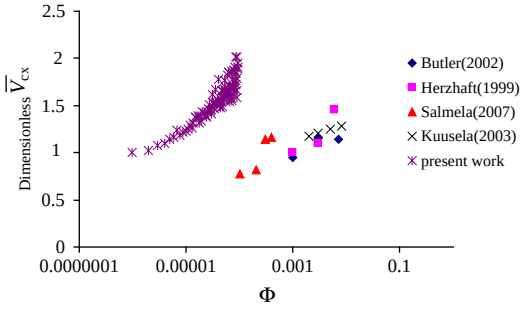

Fig. 3. A comparison between the measured settling velocity of present and previous work. The measured mean settling velocity V_{cx} is normalised relative to the mean terminal settling velocity of an isolated particle, V_{ts}. See Table 1 for full details in experimental conditions.

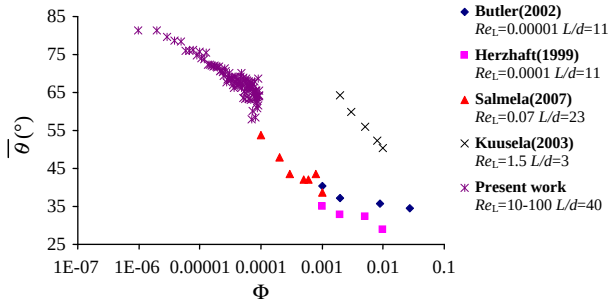

Fig. 4. A comparison of present and previous orientation measurements.

that there are some difference in range of orientation transition across the three orders of magnitude Re_L regimes. For $Re_L\sim O(10)$, an increase in Φ causes settling fibres' orientation transition to vary from about 85° to 55°. That is, the settling fibres' orientations changes from horizontal state to a less horizontal one. For $Re_L\sim O(1)$, the settling fibres' orientations becomes increasingly vertical as Φ is increased (65° to 45°). Also for $Re_L\sim O(0)$, the settling fibres' orientations increases to become nearly vertical (45° to 25°). This agrees with Kuusela [11], who reported that the torque forcing a single fibre to become horizontally aligned is proportional to the Reynolds number of the fibre.

3.3. Influences of volume fraction on angular velocity component of fibrous particles

Because a fibre's change in orientation and azimuth can be measured over a time step Δt, the angular velocity ω can be calculated. In Fig. 5, the data come from the average of per volume fraction. Fig. 5 presents dependence on Φ of the two components of mean angular velocity $\overline{\omega}_{vertical}$ and $\overline{\omega}_x$. It can be seen that $\overline{\omega}_{vertical}$ and $\overline{\omega}_x$ are both close to zero, indicating no preferred angular velocity, as expected. Also the scatter in $\overline{\omega}_{vertical}$ and $\overline{\omega}_x$ increase with Φ. It can also be seen that the RMS of $\overline{\omega}_{\text{vertical}}$, $\overline{\omega}_x$ is much more significant and also increases with Φ. These data show that the interactions between fibres, which increase with Φ, increase the tumbling and rotation of fibres, although with no preferred direction over this measurement range.

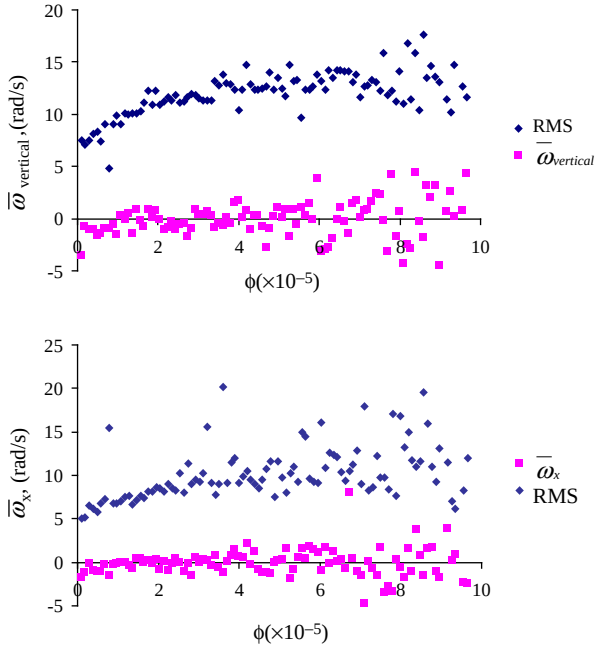

Fig. 5. The measured dependence on volume fraction, Φ, of $\overline{\omega}_{\text{vertical}}$ and $\overline{\omega}_x$.

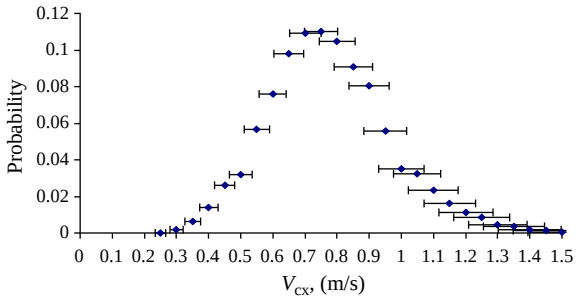

Fig. 6. The measured distribution of settling velocity V_{cx}.

3.4. Velocity and orientation distribution

Fig. 6 presents distribution of V_{cx} obtained from 29,364 samples for $\Phi < 9\times10^{-4}$. It can be seen that the mean settling velocity is about 0.75 m/s with a skewness of 0.76 and kurtosis of −0.97.

Fig. 6 indicates that there is no fundamental difference in the aerodynamic behaviour associated with the variation in straightness (refer to Qi et al. [21] for measurement of straightness). Specifically no bimodality is evident, suggesting that there is no fundamental difference in the aerodynamics of perfectly straight and slightly curved fibres. That is the presence of a slight curve may increase the scatter in the velocity distribution but does not result in any fundamental change in aerodynamic behaviour. However, no comparable data is available against which to provide a quantitative assessment of the effect.

The motions of rotation, tumbling and swaying observed when fibrous particles settle in air induce a horizontal component of motion for fibres that does not occur with spherical particles. Fig. 7 shows the distribution of V_{cy} obtained from a sample size of 29,364. It can be seen that $\overline{V_{cy}}$ is approximately zero, showing that there is no preferred horizontal motion, as expected. The standard deviation of distribution of V_{cy} is 0.07, which is approximately 9% of $\overline{V_{cx}}$, while the maximum value of V_{cy} is 0.2, which is approximately 30% of V_{cx}.

Fig. 8 shows the orientation distribution of fibrous particles over the range of a volume fraction, $\Phi < 9\times10^{-4}$. It can be seen that the majority of fibres are broadly, but not exactly, horizontal. Indeed 88% of the fibres have an orientation of >45°. This agrees with Clift et al. [20] for a cylinder falling with its axis horizontal for $Re_d > 0.01$. Kuusela et al. [11] argued that for $Re_L \sim O(1)$ sufficient torque is generated to change a fibre's orientation to horizontal. Nevertheless, there is significant departure from a truly horizontal orientation, with the most probable angle being 75° and with 0.2% of fibres being oriented at only 20° from the vertical direction.

3.5. Relationship between $\overline{V_{cx}}$, $\overline{V_{cy}}$ and θ

In Figs. 9–10 the different orientations of fibres are presented for the sample size of 29,364 binned by orientation with increments of 5°. Here $\overline{V_{cx}}$ and $|\overline{V_{cy}}|$ are the average velocities for each bin. Fig. 9 shows that $\overline{V_{cx}}$ decreases linearly with θ for θ>30° but exhibits a complex behaviour for θ<30°. This shows that particles with a nearly vertical orientation have a slightly higher settling velocity than those with a more horizontal orientation, as expected, but the maximum difference is only 30%.

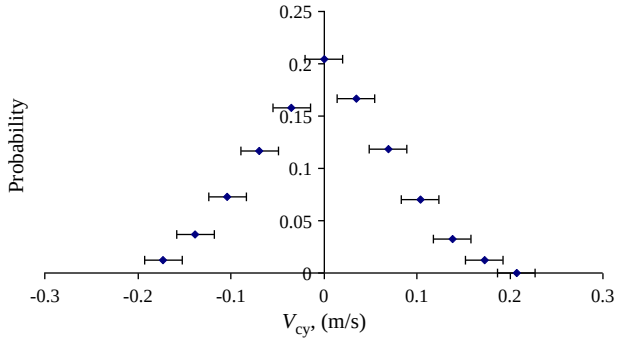

Fig. 7. The measured distribution of horizontal velocity V_{cy}.

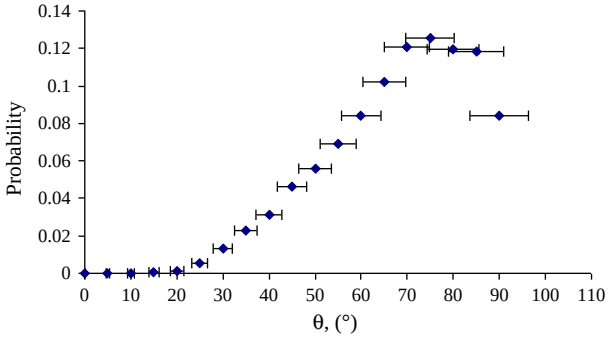

Fig. 8. The measured distribution of the orientation of the present fibrous particles from the vertical direction.

Fig. 10 presents the relationship between $|\overline{V_{cy}}|$ and θ from the sample size of 29,364. It can be seen that this relationship can also be divided into the same two regions: θ<30° and θ>30°. For small angles from the vertical direction, $|\overline{V_{cy}}|$ is highly sensitive to angle. The greatest horizontal velocity occurs for 0° to 10°. For θ>30°, the horizontal component of velocity is non zero and only weakly dependent on θ. Interestingly $|\overline{V_{cy}}|$ is also non zero for θ=90°, showing that these particles are not stable, even for the most extreme cases in the data set. That is, no particles fall with a purely vertical motion and all exhibit some lateral motion, which is only weakly dependent on orientation. A slight maximum in $|\overline{V_{cy}}|$ occurs at 45°.

3.6. Relationship between $|\overline{V_{cy}}|$ and azimuth (α)

In Fig. 11 the different azimuth of fibres are presented for the sample size of 29,364 binned by orientation for increments of 10°. It can be seen that $|\overline{V_{cy}}|$ decreases linearly with α but is non zero at α=90°. This indicates that, while the largest component is within the plane of the fibre,

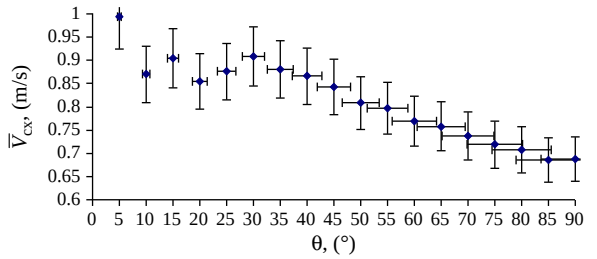

Fig. 9. The measured dependence of settling velocity, $\overline{V_{cx}}$, on orientation from the vertical direction, θ.

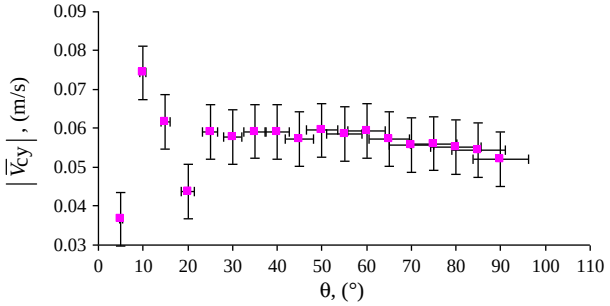

Fig. 10. Relationship between $|\overline{V_{cy}}|$ and θ.

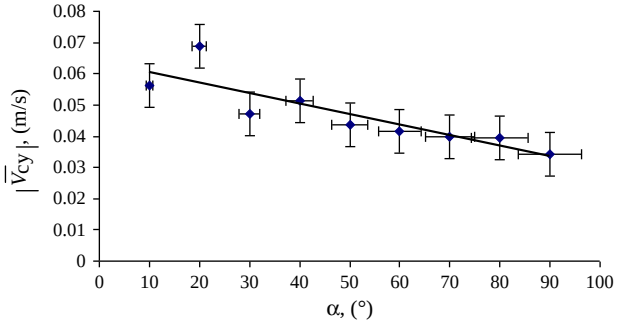

Fig. 11. The relationship between α and $|\overline{V_{cy}}|$.

the component normal to it is 55% as large on average, because a horizontal fibre moving horizontally within its major axis plane has the minimum drag force. This shows that the motion of the fibre is highly three dimensional, and that the fibre does not simply tumble in a two-dimensional plane.

4. Conclusions

The vertical components of settling velocities, angular velocity, orientation and number density of fibres settling in air with $Re_L \sim O(10)$ for volume fractions less than 9×10^{-4} are reported for the first time. It is found that the distribution of settling velocity is nearly Gaussian for these long aspect ratio fibres. Kuusela [11] and Herzhaft [4] argued that the aspect ratio has influences on settling velocity. The magnitude of $\overline{V_{cx}}$ is at maximum for vertical orientation and decreases nearly linearly with θ, the fluctuation of angular velocity increases with Φ, the directions of V_{cy} tend toward within the plane of the major axis of a fibre. The fibre's orientation tends to be more horizontal than that with $Re_L \sim O(1)$. Finally we find that these results qualitatively support the previous work under different regimes in finding that all the mean steady state settling velocities of fibres exceed the mean terminal settling velocity of a single fibre. This phenomenon is attributed to fibres' orientation transition from a horizontal to vertical state under super dilute conditions, which stems from increasing aerodynamic interactions between fibres.

Acknowledgement

This study has been supported by the Faculty of Engineering, Computer & Mathematical Science of The University of Adelaide and by an ARC Discovery Grant, both of which are gratefully acknowledged.

References

[1] G.K. Batchelor, Slender-body theory for particles of arbitrary cross-section in Stokes flow, Journal of Fluid Mechanics 44 (1970) 419–440.
[2] D.L. Koch, E.S.G. Shaqfeh, The instability of a dispersion of sedimenting spheroids, Journal of Fluid Mechanics 209 (1989) 521–542.
[3] B. Metzger, J.E. Butler, E. Guazzelli, Experimental investigation of the instability of a sedimenting suspension of fibre, Journal of Fluid Mechanics 575 (2007) 307–332.
[4] B. Herzhaft, E. Guazzelli, Experimental study of sedimentation of dilute and semi-dilute suspensions of fibres, Journal of Fluid Mechanics 384 (1999) 133–158.
[5] J. Salmela, D.M. Martinez, M. Kataja, Settling of dilute and semidilute fiber suspensions at finite Re, AIChE Journal 53 (2007) (No.8).
[6] B. Herzhaft, E. Guazzelli, M.B. Mackaplow, E.S.G. Shaqfeh, Experimental investigation of the sedimentation of a dilute fiber suspension, Physical Review Letters 77 (1996) (No. 2).
[7] M. Shin, D.L. Koch, G. Subramanian, Structure of dynamics of dilute suspensions of finite-Reynolds number settling fibres, Physics of Fluids 21 (2009) 123304.
[8] J.E. Butler, E.S.G. Shaqfeh, Dynamic simulation of the inhomogeneous sedimentation of rigid fibres, Journal Fluid Mech 468 (2002) 205–237.
[9] J.Z. Lin, L. Zhang, Numerical simulation of orientation distribution function of cylindrical particle suspensions, Applied Mathematics and Mechanics 23 (8) (2002) 906–912.
[10] J.Z. Lin, Y.L. Wang, W.X. Wang, Z.S. Yu, Numerical simulation of the sedimentation of cylindrical pollutant particles in fluid, Journal of Environmental Sciences 14 (4) (2002) 433–438.
[11] E. Kuusela, J.M. Lahtinen, T. Ala-Nissila, Collective effects in settling of spheroids under steady-state sedimentation, Physical review letter 90 (2003) (No 9).
[12] E. Kuusela, K. Hofler, S. Schwarzer, Computation of particle settling speed and orientation distribution in suspensions of prolate spheroids, Journal of Engineering Mathematics 41 (2001) 221–235.
[13] A.K. Tornberg, K. Gustavsson, A numerical method for simulations of rigid fiber suspensions, Journal of Computational Physics 215 (2005) 172–196.
[14] M. Shin, D.L. Koch, G. Subramanian, A pseudospectral method to evaluate the fluid velocity produced by an array of translating slender fibers, Physics of Fluids 18 (2006) 063301.
[15] J. Gabitto, C. Tsouris, Drag coefficient and settling velocity for particles of cylindrical shape, Powder Technology 183 (2008) 314–322.
[16] L. Fan, Z. Mao, C. Yang, Experiment on Settling of Slender Particles with Large Aspect Ratio and Correlation of the Drag Coefficient, Industrial and Engineering Chemistry Research 43 (2004) 7664–7670.
[17] G. McKay, W.R. Murphy, M. Hillis, Settling characteristics of discs and cylinders, Chemical Engineering Research and Design 66 (1988).
[18] A. Unnikrishnan, R.P. Chhabra, An experimental study of motion of cylinders in Newtonian fluids: wall effects and drag coefficient, Canadian Journal of Chemical Engineering 69 (1991).
[19] A. Haider, O. Levenspiel, Drag coefficient and terminal velocity of spherical and nonspherical particles, Powder Technology 58 (1989) 63–70.
[20] R. Clift, J. Grace, M. Weber, Bubbles, drops, and particles, Academic Press, New York0-12-176950-X, 1978.
[21] G.Q. Qi, G.J. Nathan, R.M. Kelso, PTV measurement of drag coefficient of fibrous particles with large aspect ratio, Powder Technology 229 (2012) 261–269.

5 The Influence of Aspect Ratio on Distributions of Settling Velocities and Orientations of Long Fibres

Guoqiang Qi, Graham J. Nathan and Richard M. Kelso

School of Mechanical Engineering and Centre for Energy Technology, The University of Adelaide, Adelaide SA 5005 AUSTRALIA

Email: guo.qi@adelaide.edu.au

Powder Technology 257 (2014) 192–197

Statement of Authorship

Title of Paper	The influence of aspect ratio on distributions of settling velocities and orientations of long fibres
Publication Status	☑ Published ☐ Accepted for Publication ☐ Submitted for Publication ☐ Unpublished and Unsubmitted work written in manuscript style
Publication Details	Guoqiang Qi, Graham J. Nathan and Richard M. Kelso. The influence of aspect ratio on distributions of settling velocities and orientations of long fibres. Powder Technology, 257 (2014), 192–197.

Principal Author

Name of Principal Author (Candidate)	Guo Qiang Qi
Contribution to the Paper	I was responsible for the development of both the measurement technique and analytical model under the principal supervision of Professor Nathan. I performed the measurements and data processing, wrote the first draft of the manuscript and incorporated and addressed all comments and suggestions by other authors and reviewers in subsequent revisions of the manuscript. I acted as corresponding author.
Overall percentage (%)	55%
Certification:	This paper reports on original research I conducted during the period of my Higher Degree by Research candidature and is not subject to any obligations or contractual agreements with a third party that would constrain its inclusion in this thesis. I am the primary author of this paper.
Signature	Date 13/06/2016

Co-Author Contributions

By signing the Statement of Authorship, each author certifies that:

i. the candidate's stated contribution to the publication is accurate (as detailed above);

ii. permission is granted for the candidate in include the publication in the thesis; and

iii. the sum of all co-author contributions is equal to 45% less the candidate's stated contribution.

Name of Co-Author	Graham J. Nathan
Contribution to the Paper	I was principal supervisor for the development of work, contributed to both data interpretation and refining of the manuscript.
Signature	Date 14/6/16

Name of Co-Author	Richard M. Kelso
Contribution to the Paper	I, co-supervisor, jointly supervised the development of work.
Signature	Date 14/6/2016

Please cut and paste additional co-author panels here as required.

Powder Technology 257 (2014) 192–197

Contents lists available at ScienceDirect

Powder Technology

journal homepage: www.elsevier.com/locate/powtec

The influence of aspect ratio on distributions of settling velocities and orientations of long fibres

Guoqiang Qi, Graham J. Nathan, Richard M. Kelso

School of Mechanical Engineering, The University of Adelaide, Adelaide, SA 5005, Australia
Centre for Energy Technology, The University of Adelaide, Adelaide, SA 5005, Australia

ARTICLE INFO

Article history:
Received 9 October 2013
Received in revised form 7 February 2014
Accepted 18 February 2014
Available online 26 February 2014

Keywords:
Fibrous particle
Aspect ratio
Settling velocity
Aerosol

ABSTRACT

The influence of the aspect ratios of fibrous particles on their settling velocities and orientations is reported under super dilute conditions in which fibrous particles settle in air at Reynolds number of 3–70 based on fibre length and at aspect ratios of 35, 48 and 60. Measurements were performed using Particle Tracking Velocimetry (PTV) to calculate orientation and velocity based on the two end-points, following a method reported previously. With the mean volume fraction of 0.0005, the key findings are: 1) for a constant diameter of 20.1 μm, the absolute mean vertical settling velocity, $\overline{V_{cx}}$, is not independent of fibre length, the long fibre $\overline{V_{cx}}$ is a little higher, while the settling velocity normalized by that of an equivalent sphere, $V_{cx}/V_{eq\text{-}sph}$, decreases with an increase in fibre length over the range 700 μm to 1200 μm; 2) for a constant length of 700 μm, both $\overline{V_{cx}}$ and $V_{cx}/V_{eq\text{-}sph}$ decrease with an increase in diameter over the range 14.5 μm to 20.1 μm; 3) for a constant aspect ratio but different length and diameter, $\overline{V_{cx}}$ slightly increases with an increase in particle size, while $V_{cx}/V_{eq\text{-}sph}$ decreases with an increase in particle size; 4) angular velocities and their distributions for four types of fibrous particles were reported.

1. Introduction

The settling of fibrous particles through a fluid toward the ground is a common phenomenon in nature and also occurs in industrial processes such as paper making. The understanding of the motions of fibrous particles in this basic environment is also a prerequisite to that of their motions in more complex conditions, such as in the turbulent flows of relevance to biomass combustion. The percentage of biomass being used is increasing around the world because it is a renewable and more environmentally "friendly" resource for energy supply. However, biomass is fibrous, there is a paucity of data describing the aerodynamics of fibrous particles and gaps remain in the present understanding of the aerodynamic behaviour of settling fibrous particles. The settling motion of a fibrous particle is much more complex than that of a sphere. While a sphere settles in a purely vertical direction, for a fibrous particle, the instantaneous horizontal drift cannot be neglected. A fibrous particle also exhibits rotation. Many previous works such as those of Qi et al. [1,2], Shin et al. [3], Salmela et al. [4], Lin and Zhang [10], Stover et al. [11] and Zhang et al. [12], have investigated the dynamics of fibrous particles. McKay et al. [5] investigated the settling characteristics of discs and cylinders of aspect ratio (cylinder length/diameter, L/d) from 0.25:1 to 5.0:1 (with the same diameter) in water with particle's Reynolds number of 680–15,350 based on equivalent volume diameter. The particles used in their experiments were large non-spherical particles with diameters of 16 mm and 20 mm. The terminal settling velocity of cylinders of $L/d < 1$ was found to increase with increasing L/d. However for cylinders of $L/d > 1$, the terminal settling velocity was found to be nearly independent of L/d. Importantly it is not yet known whether this finding extends to small fibrous particle with a large L/d.

Lin et al. [6] studied the sedimentation of a single fibrous particle with aspect ratios of 2, 3, 5, 7.5 and 10 in a Newtonian fluid employing the Lattice Boltzmann method at terminal Reynolds number of 1–10. Their simulation showed that the stable orientation of these fibres is horizontal. They also found that the terminal Reynolds number increases with increasing L/d and then remains constant for $L/d > 5$, which supports the conclusion of McKay et al. [5]. They further found that the horizontal component of velocity of a fibrous particle increases with increasing L/d. However, these conclusions are yet to be verified with experimental data for fibres with large L/d.

Fan et al. [7] investigated the settling motion of slender particles of Reynolds number $Re_d = 0.4$–100 based on the fibre's diameter with large aspect ratios from 4 to 40 in stagnant water. They found that the orientation of a fibre approaches gradually from any original orientation to a final stable horizontal orientation which agreed with simulation of Lin et al. [6]. However, this contrasts the finding of Qi et al. [1,2], who found that particles of similar aspect ratio and Reynolds number in a dilute suspension do not retain a fixed orientation, but continue to swing. However, no measurement of the distribution of the angular velocity of fibres has been reported previously. Fan et al. [7] also reported that the

E-mail address: guo.qi@adelaide.edu.au (G. Qi).

http://dx.doi.org/10.1016/j.powtec.2014.02.050
0032-5910/

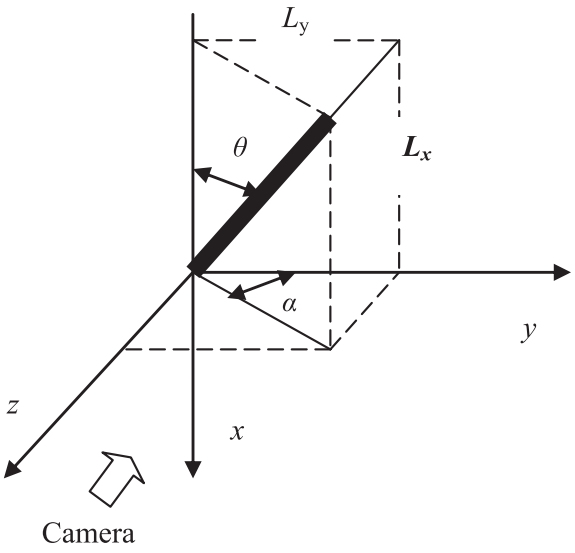

Fig. 1. The notation used to define orientation of a fibre, relative to the *x*–*y* image plane.

behaviour of the drag coefficient for fibres is independent of its aspect ratio. However no direct assessment of the influence of aspect ratio on settling velocities has been reported.

Kuusela et al. [8] simulated the settling of spheroids under steady state sedimentation at $0.5 < Re_L < 3.5$ (Reynolds number based on length) with aspect ratios of 1, 3, 5 and 7 for particles of constant diameter. The authors assessed the role of aspect ratio of fibres and found the maximum dimensionless settling velocity to decease with increasing aspect ratio. They also found that the volume fraction of peak velocity increases with increased volume fraction. These results are in good agreement with Herzhaft and Guazzelli's work [9]. Herzhaft and Guazzelli [9] studied the steady-state settling velocity and orientation distribution of glass-rods in dilute and semi-dilute suspensions for Reynolds number less than 0.0001. The fibrous particles used in their experiments were of length of 500–3000 μm and diameter of 100 μm. They used fibres with aspect ratios of 5, 11, 20 and 32 to investigate the influence of aspect ratio. They found that, over this range, the aspect ratio has little influence on the fibre's orientation, but that the dimensionless settling velocity decreases with increasing aspect ratio for particles of constant diameter. Nevertheless, this dependence decreases with L/d so that the absolute velocity of fibres with aspect ratios of 10 and 20 is nearly identical, while the absolute velocity of fibres with aspect ratio of 5 is much smaller. However, their investigation was undertaken in a configuration that induces a recirculating flow within the working section, so that approximately 40% of their data have negative velocities. In addition, no details of the influence of aspect ratio at higher Reynolds number $Re \sim O(10)$ are available. Hence it is necessary to assess whether their findings extend to free-falling particles at higher Reynolds number.

In the light of the above review, it is clear that previous work suggests that the mean settling velocity depends asymptotically on aspect ratio, to become independent of it at sufficient aspect ratio for particles of the same diameter. However this is yet to be confirmed, particularly for Reynolds numbers of order 10. In addition, to date no detailed statistical assessment of the influence of aspect ratio on other parameters, such as the distribution of the settling velocity or on horizontal velocity, has been reported. Therefore, the aim of the present work is to assess the influences of aspect ratio within the asymptotic regime, i.e. for $L/d > 20$, on the distribution of settling velocity, horizontal velocity and orientation of fibres, using the method developed by Qi et al. [1].

2. Experimental apparatus

Only a brief description of the experimental apparatus and approach is provided here, with details reported by Qi et al. [1]. Fig. 1 presents the notation used to define a fibre's orientation relative to the x–y image plane. The angle α (0°–90°) is defined to be the azimuth of a fibre relative to the viewing plane and θ (0°–90°) its orientation relative to gravity.

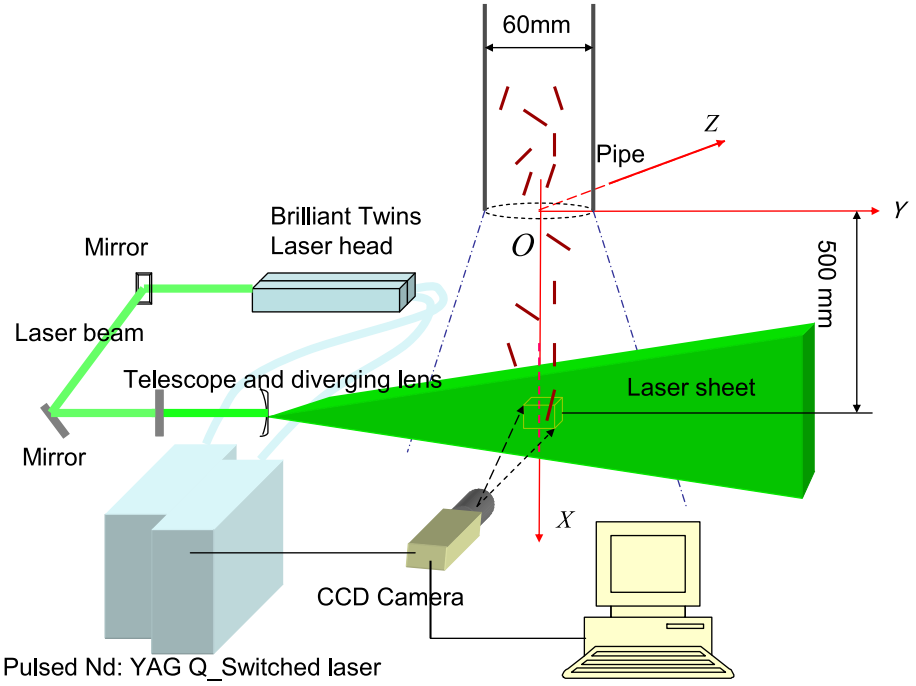

Fig. 2. Experimental arrangement (not to scale). The surrounding settling chamber (650 mm × 620 mm cross section) is not shown for clarity.

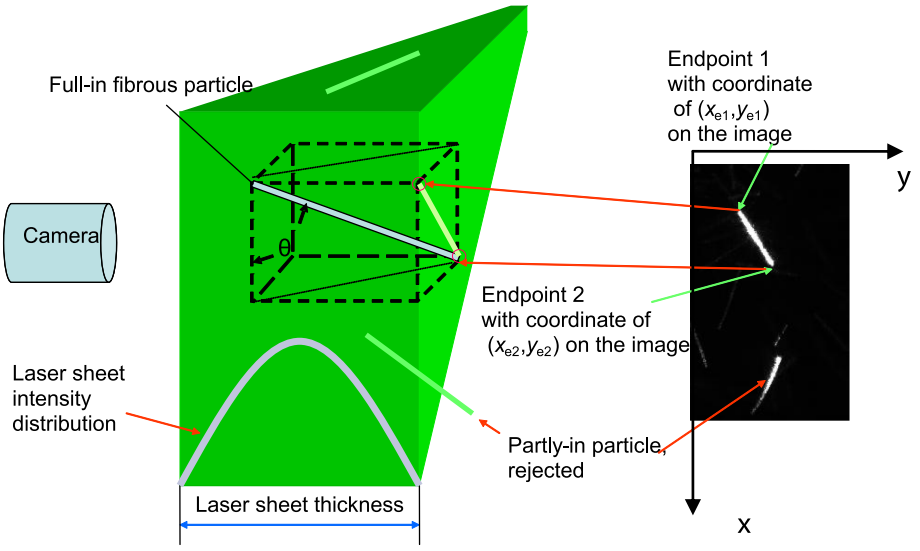

Fig. 3. Schematic diagram of the orientation measurement, the detection of "part-in" fibres and key notation.

Fig. 2 presents a schematic diagram of the experimental apparatus. Particle Tracking Velocimetry (PTV) was employed, using a Quantel Brilliant Twins double-cavity pulsed Nd:YAG 10 Hz laser as the light source.

The settling chamber was of nominally square cross section of dimensions 650 mm × 620 mm, a height of 2000 mm and was made of Perspex. The nylon fibrous particles were introduced into the top of the chamber through a 2000 mm long pipe of 60 mm diameter, to achieve a total settling distance of 2.5–3.0 m. Measurements of settling velocity were performed at settling distances of 2.5 m. The thickness of laser sheet is 5 mm. The coordinates of the two endpoints of each object (fibrous particle) were obtained. Since the length L of these fibres is all nominally identical, the spatial orientation θ of fibres was calculated with the following trigonometric function:

$$\theta = \left(\arccos\frac{|x_{e2}-x_{e1}|R}{L}\right)\times\left(\frac{180}{\pi}\right)(^\circ), \tag{1}$$

where R is magnification of camera image system; x_{e2} and x_{e1} are coordinates of x values of two endpoints. Image pairs were recorded by a digital camera with a known time separation (Δt). After image processing the displacements of two endpoints of fibrous particles along the x and y axes can be obtained. From this V_{e1x}, V_{e1y} and V_{e2x}, V_{e2y} can be calculated by Eq. (2), as follows:

$$V_{e1x}=\frac{(x_{e12}-x_{e11})R}{\Delta t}, V_{e1y}=\frac{(y_{e12}-y_{e11})R}{\Delta t},$$
$$V_{e2x}=\frac{(x_{e22}-x_{e21})R}{\Delta t}, V_{e2y}=\frac{(y_{e22}-y_{e21})R}{\Delta t}, \tag{2}$$

where V_{e1x} is the velocity of endpoint 1 in the x direction; V_{e1y} is the velocity of endpoint 1 in the y direction; V_{e2x} is the velocity of endpoint 2 in the x direction; V_{e2y} is the velocity of endpoint 2 in the y direction; x_{e12} is the x axis coordinate of endpoint 1 from the second image, x_{e11} is the x axis coordinate of the endpoint 1 from the first image; y_{e12} is the y axis coordinate of the endpoint 1 from the second image and so on. Fig. 3 presents a schematic diagram of the orientation measurement, the detection of "part-in" fibres and key notation. Any fibres that are only partly in the laser sheet will give a false calculation of the projected length and the coordinates of endpoints, so must be rejected. This can be achieved by comparing the intensities of the signal at two endpoints of the fibre. Because of the Gaussian light sheet intensity distribution a partly-in fibrous particle will exhibit a significant difference between the intensity values of the two endpoints. This is used to reject such particles. A fibre's centroid velocity $V_{cx} = 1/2\ (V_{e1x} + V_{e2x})$ and $V_{cy} = 1/2\ (V_{c1y} + V_{c2y})$ represents the vertical and horizontal components of settling velocities, respectively. Table 1 presents a summary of fibres used in the experiments and the previous work. In addition, particles with a straightness of less than 0.85, as defined by our earlier work Qi et al. [1], were removed from the analysis by post-processing. In this way, approximately 85% of the particles assessed were perfectly straight and the influence of any small differences in curvature from the different particles sizes is removed as a possible influence on the assessment.

3. Results

3.1. Distribution of settling velocity of fibrous particles with the same diameter but different lengths

Fig. 4 shows the distributions of V_{cx} of fibrous particles with the same diameter of 20.1 μm, but with lengths of 700 μm and 1200 μm respectively. It can be seen that the distributions are well described by a Gaussian curve fit. The values of V_{cx} are normalized by the terminal

Table 1
A summary of fibres used in the experiments and previous work.

Author	Fibres	L (μm)	d (μm)	L/d	Re_L	$\overline{V_{cx}}$ (m/s)	$V_{eq\text{-}sph}$ (m/s)	$\overline{V_{cx}}/V_{eq\text{-}sph}$	Volume fraction	Fluid phase
Present work	Nylon	1200	20.1	60	40 ± 30	0.52	0.300	1.73	0.0005	Air
Present work	Nylon	700	20.1	34.8	20 ± 17	0.42	0.190	2.21	0.0005	Air
Present work	Nylon	700	14.5	48	23 ± 19	0.47	0.118	3.98	0.0005	Air
Present work	Nylon	500	14.5	34.5	13 ± 10	0.39	0.100	3.90	0.0005	Air
McKay et al. [5]	Nylon	80,000	20,000	4	18,000	0.20			Single particle	Water
Qi et al. [2]	Nylon	2000	49.6	40	67 ± 50	0.75	1.30	0.58	0.0005	Air
Herzhaft and Guazzelli [9]	Glass	1900	100	20	<0.0001	0.009			0.006	Liquid

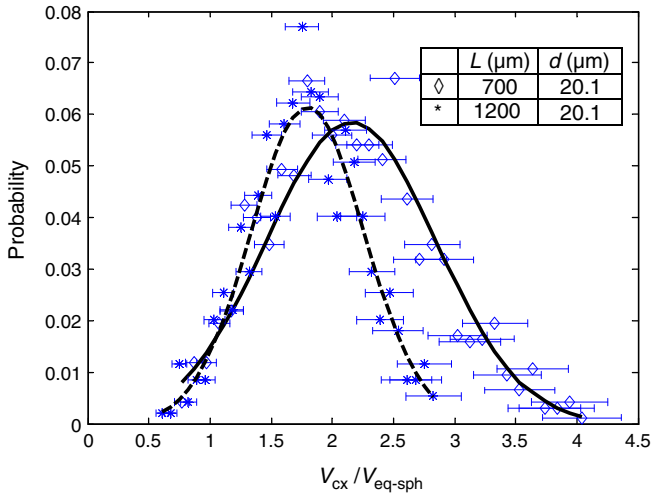

Fig. 4. Probability distribution of the vertical component of settling velocity, normalized by that of an equivalent sphere, for fibrous particles with the same diameter but different lengths, together with the Gaussian curve fit. The error bars correspond to an uncertainty of ±8% and the values of $V_{eq\text{-}sph}$ are shown in Table 1.

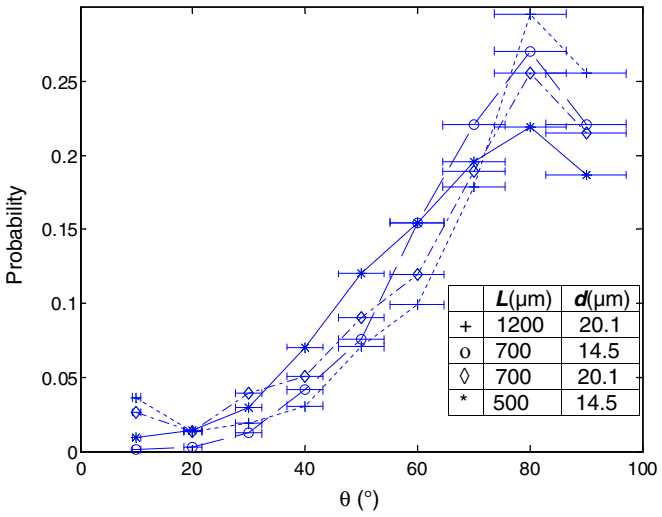

Fig. 6. Probability distribution of the orientation of the fibrous particles. The error bars correspond to an uncertainty of ±8%.

settling velocity of a sphere of equivalent volume, whose values are shown in Table 1. It can be seen that $V_{cx}/V_{eq\text{-}sph}$ decreases by a factor of 0.48 as the particle length is increased. Meanwhile the mean absolute settling velocity, $\overline{V_{cx}}$, increases by a factor of 0.1 with the length, which is slightly inconsistent with the finding of McKay et al. [5].

In contrast to Herzharf's work [9], there are no negative velocities in the present data, while nearly 40% of the range of Herzharf's settling velocities was measured to be negative. Hence the present data are unique in avoiding the influence of secondary cell flow currents.

The motions of rotation, tumbling and swinging observed when fibrous particles settle in air induce a horizontal component of motion for fibres that does not occur with spherical particles. Fig. 5 presents the probability distribution of V_{cy} for fibrous particles with the same diameter but different length. It can be seen that the shorter particles exhibit a higher percentage of zero horizontal velocity. This implies that tumbling is inhibited by a decrease in aspect ratio. It can also be seen that the average V_{cy} is zero, which confirms the absence of any significant bias in the apparatus.

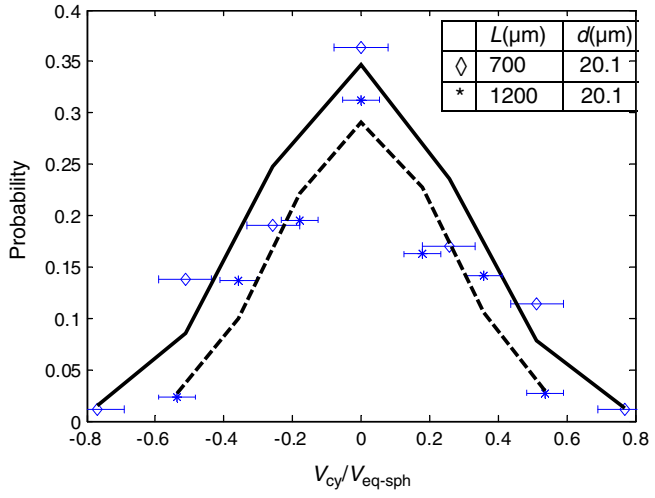

Fig. 5. Distribution of the horizontal component of settling velocity normalized by that of an equivalent sphere for the two types of fibrous particles with the same diameter but different lengths. The error bars correspond to an uncertainty of ±0.077 (◊) and ±0.054 (*), shown with a Gaussian curves fit.

Fig. 6 presents the probability distribution of fibre orientations for the four types of fibrous particles. It can be seen that the most probable orientation of the fibres is almost horizontal. This measurement is in broad agreement with the work of Lin et al. [6] and Fan et al. [7], who reported that the stable orientation is horizontal, in contrast to Herzhaft and Guazzelli's [9] result obtained in a confined chamber in which most of the glass-rods were found to be nearly vertical. This finding is also broadly consistent with the absolute settling velocity not changing significantly with aspect ratio, since the drag for a steady cylinder in cross flow is controlled only by the diameter of the cylinder. However, on closer inspection, it can also be seen that the most probable orientation of these fibres is around 80°, rather than the 90° of a truly horizontal orientation. This implies that the fibres swing significantly because of the large density ratio between solid phase and air phase. It can also be seen that the shorter particles have a tendency to have a more vertical orientation than the longer ones. This also contrasts Herzhaft and Guazzelli's [9] finding that the aspect ratio has little influence on the fibre's orientation.

Some of the long fibres exhibit asymmetrical features at one end, such as a lump, a kink or a wiggle. In addition, some of the fibres are not perfectly straight, as noted in Section 2. The combination of a lack of symmetry, together with the large density ratio between the fibre

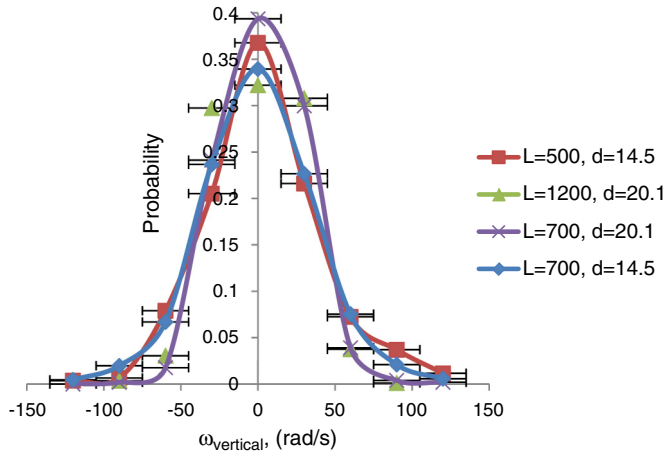

Fig. 7. Probability distribution of the vertical component of angular velocity of the fibrous particles. The error bars correspond to an uncertainty of ±30 rad/s.

and the fluid is deduced to be responsible for the non-zero angular velocities measured in Fig. 7. Fig. 7 presents the probability distribution of angular velocity of the fibrous particles. It can be seen that nearly 40% of the present fibres have a stable orientation (i.e. a rotational velocity of zero). Furthermore longest fibres have more percentage of rotational velocity, suggesting that these are the most unstable because the long fibres can be easier to be unsymmetrical than short ones, for example, the most stable particle is the case with a length of 700 μm and diameter of 20.1 μm, which has the shortest aspect ratio. This suggests that further increases in aspect ratio will make the particle more unstable. However, returning to Fig. 6, it can be seen that the longest aspect ratio particles have the greatest probability of both the most vertical and the most horizontal positions, suggesting more of a bi-stable condition. That is, the longer particles are more likely to be either stable or rotating more quickly.

3.2. Distribution of settling velocity of fibrous particles with the same length but different diameters

Fig. 8 presents the probability distribution of settling velocity of fibrous particle with the same length (700 μm), but different diameters of 14.5 μm and 20.1 μm, respectively. From the figure it can be seen that, for these fibres, the velocity distribution of the thicker fibre is narrower than that of the thinner one. This trend is consistent with Fig. 7, providing further evidence that contradicts the asymptotic argument, which proposes that as $L/d \rightarrow 1$, the distribution will become a delta function with a single value of vertical velocity. This implies that further increases in aspect ratio cause increased instability in the orientation, at least for these Reynolds numbers. It can also be seen that the value of $V_{cx}/V_{eq\text{-}sph}$ increases by a factor of 1.77 as L/d is increased by a factor of 13.2. The absolute values of V_{cx} also increases, but by a smaller factor of 0.05. These trends are also consistent with the particles becoming more unstable as L/d is increased.

Fig. 9 presents the probability distribution of the horizontal component of settling velocity. Consistent with Fig. 7, it can be seen that the thicker particle has a narrow range of horizontal velocity distribution. This provides further evidence that the higher aspect ratio particles are more unstable. Returning to Fig. 6, it can also be seen that, for these particles, the longer aspect ratio have a higher probability both of a nearly horizontal orientation and of a wide range of other orientations. This provides further evidence for a bi-modal behaviour, with the particles being more likely to be either horizontal or tumbling.

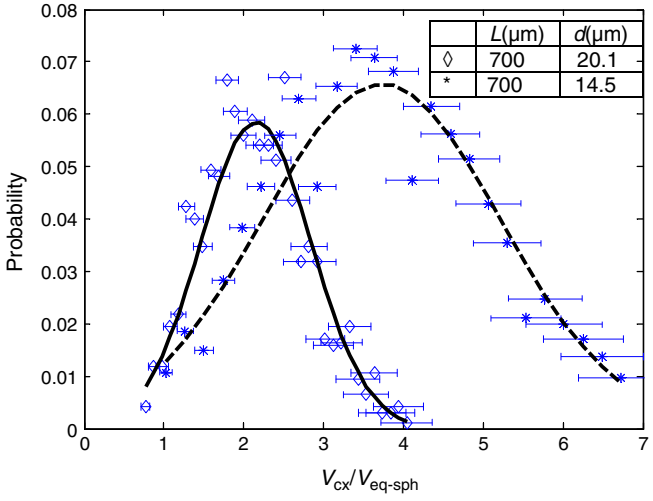

Fig. 8. The probability distribution of the vertical component of settling velocity normalized by that of an equivalent sphere, for fibres of the same length but different diameter, together with their Gaussian curve fit. The error bars correspond to an uncertainty of ±8%.

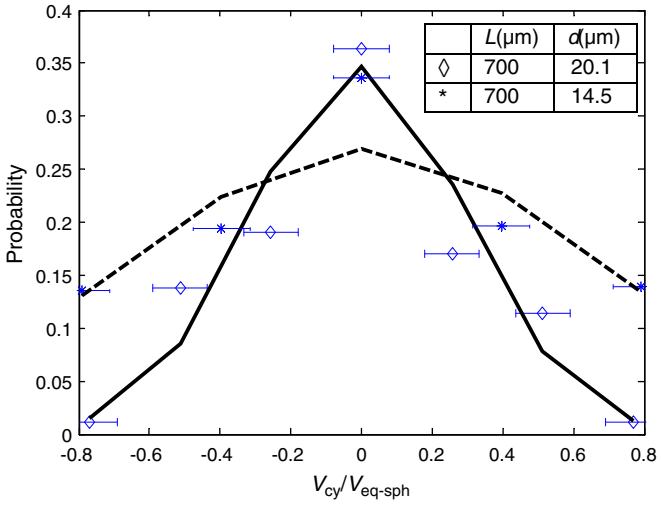

Fig. 9. The probability distribution of the horizontal component of settling velocity normalized by the vertical settling velocity of an equivalent sphere for particles with the same length but different diameter, together with the Gaussian curve fit. The error bars correspond to an uncertainty of ±0.077 (◊) and ±0.079 (*).

3.3. Distribution of settling velocity of fibrous particles with the same aspect ratio but different lengths and diameters

Fig. 10 presents the probability distribution of the relative settling velocity of fibres with constant L/d but different size. It can be seen that $V_{cx}/V_{eq\text{-}sph}$ decreases with an increase in size. At the same time, the absolute velocity is about the same for both sizes of particle.

Fig. 11 presents the probability distribution of $V_{cy}/V_{eq\text{-}sph}$ for fibres with constant L/d but different size. It can be seen that the smaller particles exhibit a greater range of V_{cy}, consistent with the results in Fig. 10. This can be explained by returning to Fig. 6, which presents the orientation distribution for fibres with same aspect ratio. It can be seen that the larger particles have a tendency to be horizontal.

4. Conclusions

The influences of aspect ratio of long, nylon fibrous particles with a small range of different degrees of straightness settling in air under

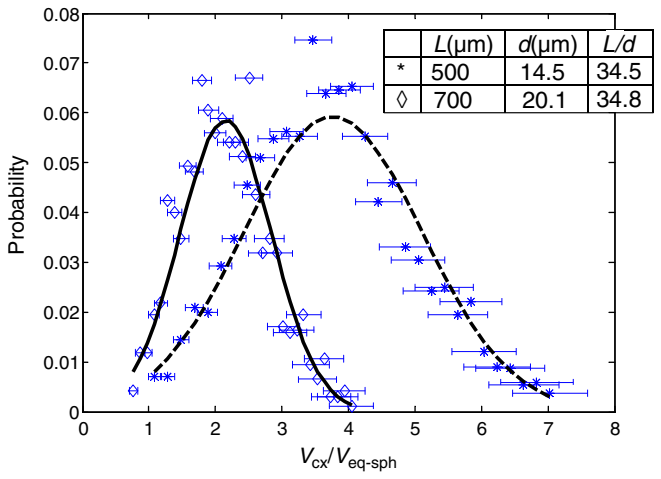

Fig. 10. The probability distribution of the vertical component of settling velocity normalized by that of an equivalent sphere, for fibrous particles with the same aspect ratio but different length and diameter, together with their Gaussian curves fit. The error bars correspond to an uncertainty of ±8%.

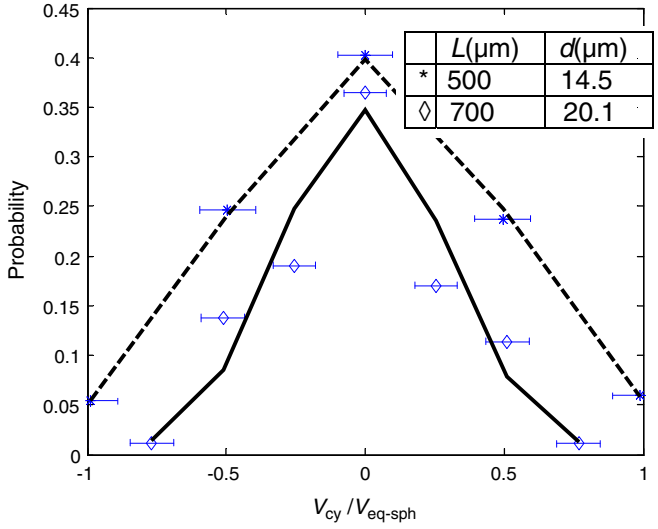

Fig. 11. The probability distributions of the horizontal component of settling velocity, normalized by the settling velocity of an equivalent sphere, for fibres with the same aspect ratio but different size, together with their Gaussian curves fit. The error bars correspond to an uncertainty of ±0.099 (*) and ±0.077 (◊).

super dilute conditions at $3 < Re_L < 70$ and without any influence of secondary flows have been investigated by employing PTV. It is found that the aspect ratio has influence both on vertical settling velocity and orientation and that 60% of these long aspect ratio particles settling in air exhibit a high probability of unstable orientation, causing them to rotate and exhibit a wide range of horizontal velocities. This contrasts the stable orientations that were reported previously by Lin et al. [6] and Fan et al. [7] in water. This difference is attributed primarily to the much higher density ratio between air phase and solid phase than for the previous experiments, although it is possible that the small fraction of curved particles included in the analysis may also play a minor role. The greater instability of the higher aspect ratio figures also explains why the absolute mean vertical settling velocity of longer particles is a little faster than the shorter ones (with the same diameter).

- For those fibres with the same diameter, the dimensionless vertical settling velocity of the longer particle, normalized by the settling velocity of a sphere of equivalent volume, is lower than the shorter one and the fibres with large aspect ratio exhibit a little more horizontal motion;
- For those fibres with the same length, the distribution of dimensionless settling velocity of thicker fibres is narrower than the thinner ones. The thinner particles have a tendency to be a little more horizontal;
- For fibres with the same aspect ratio but different length and diameter, the dimensionless vertical settling velocity of the smaller particles is greater than that of the larger particles.

Acknowledgement

This study has been supported by the Faculty of Engineering, Computer & Mathematical Science of The University of Adelaide and by an ARC Discovery Grant, both of which are gratefully acknowledged.

Appendix A. A.1. Straightness distribution of the fibres

Supplementary data to this article can be found online at http://dx.doi.org/10.1016/j.powtec.2014.02.050.

References

[1] G.Q. Qi, G.J. Nathan, R.M. Kelso, PTV measurement of drag coefficient of fibrous particles with large aspect ratio, Powder Technol. 229 (2012) 261–269.
[2] G.Q. Qi, G.J. Nathan, R.M. Kelso, Aerodynamics of long fibres settling in air at $10 < Re < 100$, Powder Technol. 235 (2013) 550–555.
[3] M. Shin, D.L. Koch, G. Subramanian, Structure of dynamics of dilute suspensions of finite-Reynolds number settling fibres, Phys. Fluids 21 (2009) 123304.
[4] J. Salmela, D.M. Martinez, M. Kataja, Settling of dilute and semidilute fiber suspensions at finite Re, AIChE J 53 (2007) (No.8).
[5] G. McKay, W.R. Murphy, M. Hillis, Settling characteristics of discs and cylinders, Chem. Eng. Res. Des. 66 (1988).
[6] J.Z. Lin, X. Shi, Z. You, Effects of the aspect ratio on the sedimentation of a fiber in Newtonian fluids, Aerosol Sci. 34 (2003) 909–921.
[7] L. Fan, Z. Mao, C. Yang, Experiment on settling of slender particles with large aspect ratio and correlation of the drag coefficient, Ind. Eng. Chem. Res. 43 (2004) 7664–7670.
[8] E. Kuusela, J.M. Lahtinen, T. Ala-Nissila, Collective effects in settling of spheroids under steady-state sedimentation, Phys. Rev. Lett. 90 (9) (2003).
[9] B. Herzhaft, E. Guazzelli, Experimental study of sedimentation of dilute and semi-dilute suspensions of fibres, J. Fluid Mech. 384 (1999) 133–158.
[10] J.Z. Lin, L. Zhang, Numerical simulation of orientation distribution function of cylindrical particle suspensions, Appl. Math. Mech. 23 (2002) 906–912.
[11] C.A. Stover, D.L. Koch, C. Cohen, Observation of fibre orientation in simple shear flow of semi-dilute suspensions, J. Fluid Mech. 238 (1992) 277–296.
[12] L. Zhang, J.Z. Lin, T.L. Chan, Orientation distribution of cylindrical particles suspended in turbulent pipe flow, Phys. Fluids 17 (2005) 093105.

Powder Technology 289 (2016) 18–19

Contents lists available at ScienceDirect

Powder Technology

journal homepage: www.elsevier.com/locate/powtec

Corrigendum

Corrigendum to "The influence of aspect ratio on distribution of settling velocities and orientations of long fibres" [Powder Technol. 257 (2014) 192–197]

Guoqiang QI *, Graham J. Nathan, Richard M. Kelso

School of Mechanical Engineering and Centre for Energy Technology, The University of Adelaide, Adelaide, SA 5005, Australia

In Table 1 of this paper, the settling velocities of the equivalent sphere were calculated by using the equation for Stokes flow, which applies for $Re < 1$. This method results in errors of 10%–27% since the Reynolds number is above the Stokes number regime. It is more accurate to calculate $C_D(Re)^2$ first, then obtain the Reynolds number of the equivalent sphere by interpolating from Table 3.4 in Aerosol Technology by Hinds. From this the settling velocity can be obtained based on its Reynolds number. The correct values of settling velocities and their Reynolds numbers are shown in the table below. Note that these changes to settling velocity do not alter the conclusions of the paper.

Fibre's length, L	Fibre's diameter, d	$V_{eq\text{-}sph}$	$Re_{eq\text{-}sph}$
1200 μm	20.1 μm	0.236 m/s	1.40
700 μm	20.1 μm	0.173 m/s	0.86
700 μm	14.5 μm	0.118 m/s	0.47
500 μm	14.5 μm	0.112 m/s	0.40
2000 μm	49.6 μm	0.763 m/s	9.80

The authors also advise that Figs 6, 7, 11 and A1 that appeared in the published version are incorrect. The corrected figures are given below. These changes do not influence any conclusions of the paper.

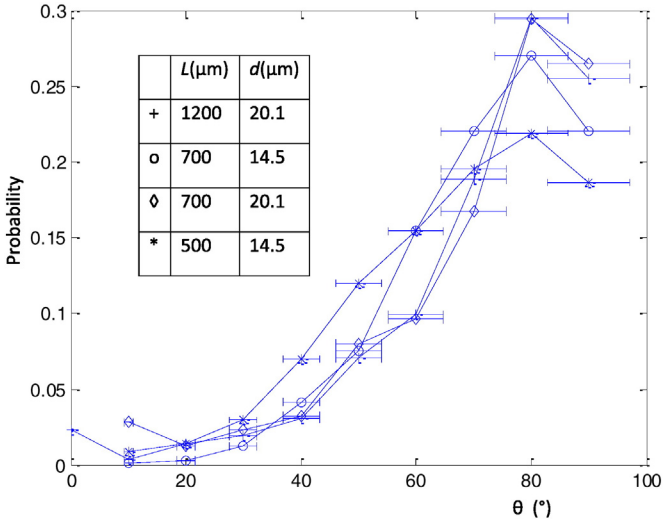

Fig. 6. Probability distribution of the orientation of the fibrous particles. The error bars correspond to an uncertainty of ±8%.

DOI of original article: http://dx.doi.org/10.1016/j.powtec.2014.02.050.
* Corresponding author.
E-mail address: guo.qi@adelaide.edu.au (Q.I. Guoqiang).

http://dx.doi.org/10.1016/j.powtec.2015.11.027
0032-5910/

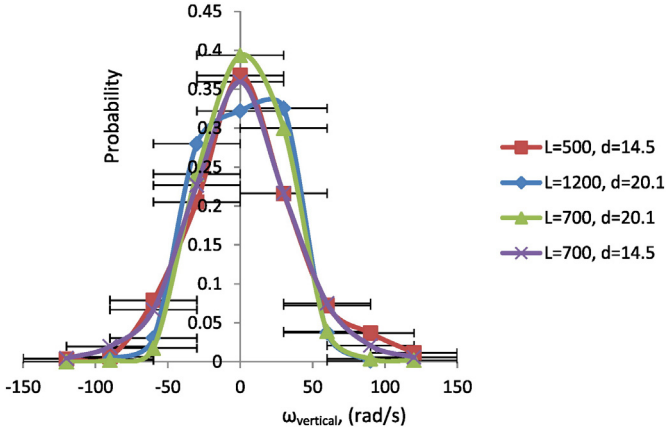

Fig. 7. Probability distribution of the vertical component of angular velocity of the fibrous particles. The error bars correspond to an uncertainty of ±30 rad/s.

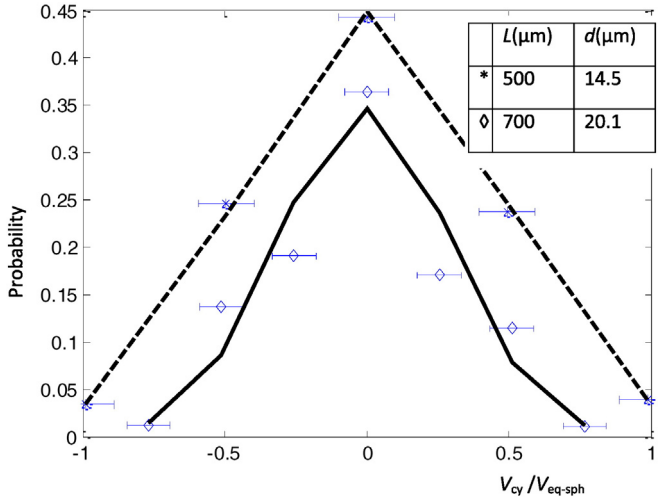

Fig. 11. The probability distributions of the horizontal component of settling velocity, normalized by the settling velocity of an equivalent sphere, for fibres with the same aspect ratio but different size, together with their Gaussian curves fit. The error bars correspond to an uncertainty of ±0.099 (*) and ±0.077 (◊).

On page 197, line 12, delete the sentence "The greater instability of the higher aspect ratio figures also explains why the absolute mean vertical settling velocity of long particles is a little faster than short ones (with the same diameter)." This change is not associated with the error corrected.

Fig. A1 presents the distribution of straightness of the fibre with lengths of 500 μm and 1850 μm and diameters of 14.5 μm and 50 μm used in the experiments. From the figure it can be seen that, while the fibres are not perfectly straight, the distribution of straightness is very similar for the two sizes of fibre, although there are few fibres for $L = 500$ μm with straightness less than 0.90. However these fibres were removed by image processing. Furthermore, the fraction of fibres that are perfectly straight is identical at 40%. Hence it can be seen that differences in fibre straightness are not responsible for the difference in aerodynamic behaviour identified in the paper. The changes do not influence the conclusions of the paper.

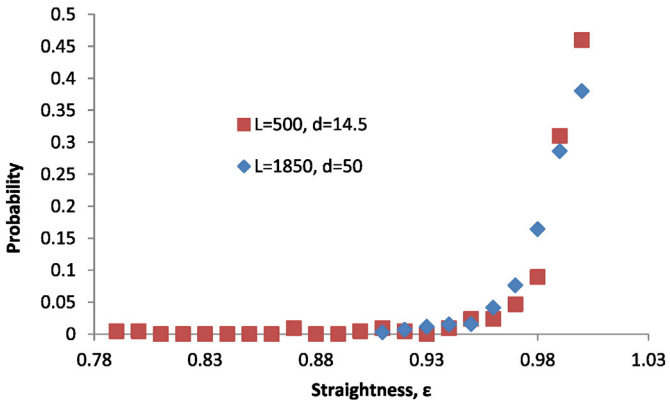

Fig. A1. Straightness distribution of the fibres.

6 Velocity and Orientation Distribution of Fibrous Particles in the Near-field of a Turbulent Jet

Guoqiang Qi, Graham J. Nathan and Timothy C.W. Lau

School of Mechanical Engineering and Centre for Energy Technology, The University of Adelaide, Adelaide SA 5005 AUSTRALIA

Email: guo.qi@adelaide.edu.au

Powder Technology 276 (2015) 10–17

Statement of Authorship

Title of Paper	Velocity and orientation distributions of fibrous particles in the near-field of a turbulent jet
Publication Status	☑ Published ☐ Accepted for Publication ☐ Submitted for Publication ☐ Unpublished and Unsubmitted work written in manuscript style
Publication Details	Guoqiang Qi, Graham J. Nathan and Timothy C.W. Lau. Velocity and orientation distributions of fibrous particles in the near-field of a turbulent jet. Powder Technology, 276 (2015), 10–17.

Principal Author

Name of Principal Author (Candidate)	Guo Qiang Qi		
Contribution to the Paper	I was responsible for the development of both the measurement technique and analytical model under the principal supervision of Professor Nathan. I performed the measurements and data processing, wrote the first draft of the manuscript and incorporated and addressed all comments and suggestions by other authors and reviewers in subsequent revisions of the manuscript. I acted as corresponding author.		
Overall percentage (%)	55%		
Certification:	This paper reports on original research I conducted during the period of my Higher Degree by Research candidature and is not subject to any obligations or contractual agreements with a third party that would constrain its inclusion in this thesis. I am the primary author of this paper.		
Signature		Date	13/06/2016

Co-Author Contributions

By signing the Statement of Authorship, each author certifies that:

i. the candidate's stated contribution to the publication is accurate (as detailed above);

ii. permission is granted for the candidate in include the publication in the thesis; and

iii. the sum of all co-author contributions is equal to 45% less the candidate's stated contribution.

Name of Co-Author	Graham J. Nathan		
Contribution to the Paper	I was principal supervisor for the development of work, contributed to both data interpretation and refining of the manuscript.		
Signature		Date	14/6/16

Name of Co-Author	Timothy C.W. Lau		
Contribution to the Paper	I jointly contributed to both data interpretation and refining of the manuscript.		
Signature		Date	16/6/16

Please cut and paste additional co-author panels here as required.

Powder Technology 276 (2015) 10–17

Contents lists available at ScienceDirect

Powder Technology

journal homepage: www.elsevier.com/locate/powtec

Velocity and orientation distributions of fibrous particles in the near-field of a turbulent jet

Guoqiang Qi, Graham J. Nathan, Timothy C.W. Lau

School of Mechanical Engineering, The University of Adelaide, Adelaide, SA 5005, Australia
Centre for Energy Technology, The University of Adelaide, Adelaide, SA 5005, Australia

ARTICLE INFO

Article history:
Received 2 July 2014
Received in revised form 4 February 2015
Accepted 8 February 2015
Available online 15 February 2015

Keywords:
Fibrous particle
Turbulent jet
Orientation

ABSTRACT

Measurements of velocity, angular velocity and orientation of nylon fibrous particles of long aspect ratio in the super-dilute regime in the near field of a turbulent air jet with a Reynolds numbers of 70,000 are reported. These measurements were performed using Particle Tracking Velocimetry (PTV) based on the two end-points of each fibre, following a method reported previously. The particles were fed via a hopper into a pipe of 34 diameters in length. The fibres' vertical and horizontal velocity and orientation were calculated to analyse the aerodynamic behaviour of these fibrous particles. The key findings are as follows: 1) fibre orientations at the centre of the jet are distributed over a wide range spanning 30° to 90° and the most probable orientation of the fibres is at 54° to the axial, while few fibres are aligned with the direction of the flow, which contrasts with previous findings in a turbulent pipe flow using water as the working fluid; 2) the axial velocity of the fibres on the jet axis is found to change little with an increase in number density, which contrasts with previous findings in free-falling cases where the fibres' settling velocity increases significantly with the volume fraction; 3) the influence of number density on orientation of the fibres in this turbulent jet within the super dilute regime is much weaker than that for the free-falling case, where the orientations decrease with the volume fraction; 4) the absolute mean angular velocity of the fibres increases significantly with the radial distance from the axis to the location of the greatest mean shear; and 5) at the centre-line of the jet, the fibres' normalised radial velocity is an order of magnitude larger than that of spheres with a similar Stokes number.

1. Introduction

The transport of fibrous particles in suspension within a turbulent flow occurs in numerous industries, including pulp and paper making, the combustion of biomass in boiler and polymer suspensions. However, the motion of these particles is much less well understood than that of their spherical counterparts due to the added complexity caused by their more complex shape. In addition to translation, fibrous particles exhibit rotation and their drag coefficient also depends on their orientation. An improved understanding of their aerodynamic behaviour is a prerequisite to optimising their performance in applications such as biomass combustion. This, in turn, requires detailed measurements in relevant environments, such as in co-flowing jets, which are not yet available. The objective of the current work is to begin to address this gap.

The most relevant experiment to the transportation of biomass fibres in air is the measurements of Bernstein and Shapiro [1] in water. They measured the orientation distribution of glass fibres with a wide range of Reynolds numbers on the axis of a pipe flow using an optical technique. These measurements are directly comparable with the exit plane of a jet issuing from a long pipe because the conditions at the exit plane of a pipe are nominally identical to those within it. A comparison of their data with new measurements performed in a jet using air as the working fluid will provide insight into the effect of density ratio, which is three orders of magnitude different. Zhang et al. [2] simulated the suspension of fibres in a turbulent pipe flow at *Re* of 11,000 and proposed a model to predict the orientation distribution of the fibres. They validated their model against the data of Bernstein and Shapiro's [1] work and found quite good agreement. Marchioli et al. [3] simulated inertial fibres in turbulent channel flow and found the fibres' orientation at the centre of the channel (i.e., far from the wall) to be approximately 60° to the flow direction. The results of their simulation will also be compared with those of the present experimental data.

E-mail address: guo.qi@adelaide.edu.au (G. Qi).

http://dx.doi.org/10.1016/j.powtec.2015.02.003
0032-5910/

Mandϕ and Rosendahl [4] studied orientation-dependent models of non-spherical particles at high Reynolds numbers and pointed out that the inertial effect is sufficient to force non-spherical particles to change their motion state. They gave the following equation to calculate the torque due to resistance acting on fibrous particles:

$$T = \rho d\left(\omega_f - \omega_p\right)^2 L_p^4 \left(\frac{1}{64} + \frac{1}{3.36\left(\frac{\rho d\left(\omega_f-\omega_p\right)L_p}{\mu}\right)^{\frac{2}{3}}}\right), \quad (1)$$

where L_p and d are the length and diameter of the fibrous particles, respectively, while ω_f and ω_p are the angular velocities of the fluid and particles. This equation can be used to estimate the torque acting on the fibre in the present study. Rosendahl [5] also proposed that the location of the centre of pressure is a function of the orientation and aspect ratio of the fibres according to the following relationship:

$$x_{cp} = \frac{L_p}{4}\left(1 - e^{1-\frac{L_p}{d}}\right)\left(1 - \sin^3\theta\right), \quad (2)$$

where θ is the incidence angle.

Stover et al. [6] investigated experimentally the fibres' orientation in simple shear flow by employing a cylindrical Couette device. They found that the fibres are approximately aligned with the flow direction under these conditions. Carlsson [7] measured the distributions of fibre orientations at different wall normal positions in a turbulent headbox. He found that the fibres were more aligned with the flow direction at the position nearest to the wall, where the shear rate is the highest. Lin et al. [8] simulated the fibres' orientation distribution in a round turbulent jet of fibre suspensions. They found that the fibres' orientation increases with radial distance. However, this simulation needs to be verified with experimental data.

Lin et al. [9] simulated suspensions of fibres in a round jet flow. They assessed the influence of the volume fractions of the fibres on the mean axial velocity profile and concluded that the volume fraction does not significantly influence the shape of the mean axial velocity profile of the gas phase. However, the authors did not report on the effect of volume fraction on the fibrous particle phase. Hence, a particular aim of the present work is to explore this effect using experimental data. Jayageeth et al. [10] studied the effect of a bounding wall on the dynamics of suspended fibres in a boundary layer using a Stokesian dynamics simulation and they found that the fibres' rotation increases significantly as a fibre approaches a region of maximum shear.

Olson and Kerekes [11] analysed the motion of a single fibre suspended in turbulent fluid and obtained equations of mean and fluctuating velocities in rotation and translation. They derived the following rotational and translational dispersion coefficients of a fibre:

$$D_r = 24\overline{u'^2}\frac{\tau}{L^2}\frac{\Lambda}{L}\left(\mathrm{erf}\left(\frac{\pi^{0.5}\mathrm{L}}{2\Lambda}\right) + \frac{16}{\pi^2}\left(\frac{\Lambda}{L}\right)^3\left(1 - e^{-\frac{\pi L^2}{4\Lambda^2}}\right) + \frac{2}{\pi}\frac{\Lambda}{L}\left(e^{-\frac{\pi L^2}{4\Lambda^2}} - 3\right)\right). \quad (3)$$

$$D_t = 2\overline{u'^2}\tau\frac{\Lambda}{L}\left(\mathrm{erf}\left(\frac{\pi^{0.5}\mathrm{L}}{2\Lambda}\right) + \frac{2}{\pi}\frac{\Lambda}{L}\left(e^{-\frac{\pi L^2}{4\Lambda^2}} - 1\right)\right). \quad (4)$$

This model implies that for long fibres, rotational and translational dispersion coefficients, D_r and D_t are functions of the fluid Eulerian integral time scale, τ, the Eulerian integral length scale, Λ, and the streamwise component of the fluctuating velocity, u'. Based on convection–dispersion function that governs the evolution of the fibre orientation distribution, $\Gamma(r, p, t)$, in turbulent flows, they further derived a form of the Fokker–Planck equation to describe the orientation distribution of the fibre in turbulent flows, as follows:

$$\frac{\partial\Gamma}{\partial t} = D_r\nabla_r^2\Gamma - \nabla_r\cdot(\omega\Gamma) + D_t\nabla^2\Gamma - \nabla\cdot(\overline{V}\Gamma), \quad (5)$$

where $\nabla_r = \boldsymbol{p}\times\partial/\partial\boldsymbol{p}$ is the rotational operator, $\boldsymbol{p}$ is the unit orientation vector, $\overline{V}$ is the fibres' mean velocity and ω is the fibres' angular velocity. Eq. (5) relies on many assumptions, some of which do not apply in the present experiments. Firstly it assumes that the fibres are neutrally buoyant, which is far from true in the present experiments. It also assumes that the inertial forces on the fibre are negligible, i.e., that the Stokes number is $\ll 1$ and that the relative velocity between the fibre and the fluid is zero. None of these assumptions are true for the present case, therefore this equation does not apply in particle-laden flows with

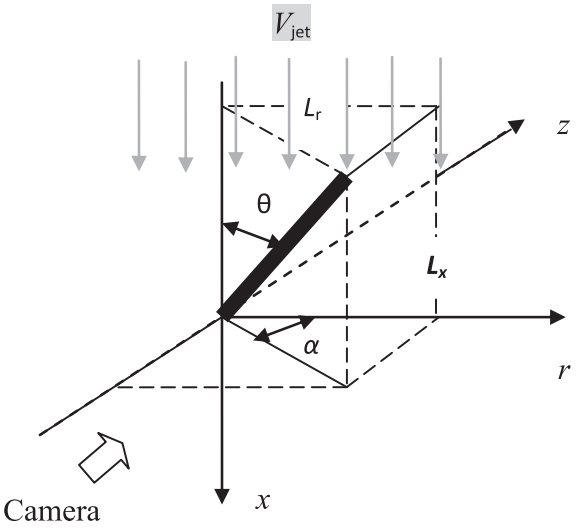

Fig. 1. The notation used to define orientation of a fibre in jet flows, relative to the axis of the jet and to the camera image plane.

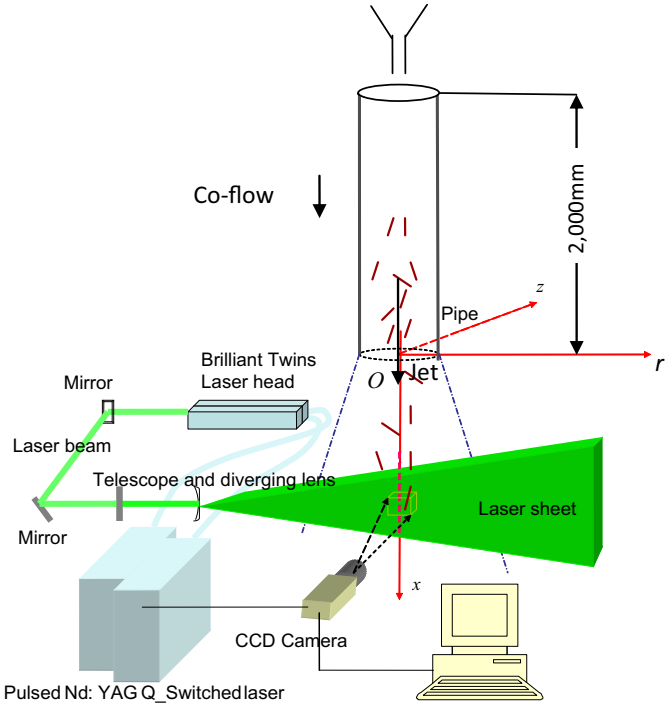

Fig. 2. Experimental arrangement (not to scale). The walls of the surrounding wind tunnel (650 mm × 620 mm cross section) and the cyclone are not shown for clarity. The bulk-mean velocity of the jet was 18 m/s, while the co-flow velocity was 8 m/s.

Table 1
The experimental conditions compared with previous work.

Authors	Configuration	Length of supply pipe L	Diameter of supply pipe D	Fibre length L_p	Fibre and sphere diameter d	L_p/d	L_p/D	d/D	Stokes number of fibre and sphere	Flow velocity	Density ratio ρ_p/ρ_f	Re of flow
Present work	Pipe-jet	2000 mm	60 mm	2000 μm	50 μm	40	0.03	0.0008	$Sk_d = 2.6$ $Sk_{l_p} = 4200$	18 m/s	958	70,000
Bernstein and Shapiro [1]	Pipe	4500 mm	38 mm	20 μm	2 μm	10	0.0005	0.00005	$Sk_d = 2 \times 10^{-6}$ $Sk_{l_p} = 2 \times 10^{-4}$	0.235 m/s	1.5	11,000
Zhang et al. [2]	Pipe simulation	N/A	38	N/A	N/A	10, 30, 100	N/A	N/A	N/A	N/A	1	11,000
Lin et al. [8]	Jet simulation	N/A	N/A	180 μm 600 μm	N/A	3, 5, 10	N/A	N/A	≪1	N/A	1, 1.1, 2	10,000
Lau and Nathan [19]	Pipe-jet	2080 mm	12.7 mm	Sphere	$d = 20$ μm	N/A	N/A	0.002	$Sk_d = 1.4$	12 m/s	1000	10,000

air as the working fluid and sufficiently large fibres for $Sk > 1$, as occurs in this instance. Olson [12] pointed out that modelling the suspension using "two-way coupling" is very complex.

Kvasnak and Ahmadi [13] simulated the sedimentation of ellipsoidal particles in turbulent duct flows and reported the results for particles with diameters from 1 to 50 μm and aspect ratios from 1 to 10. Zhang et al. [14] studied the transport and deposition of ellipsoidal particles in turbulent channel flows. A fibre's motion in shear flow was investigated by Broday et al. [15] and Ku and Lin [16], while a heuristic model of orientation was developed by Klett [17] under conditions of relevance to atmospheric conditions. Importantly, none of these previous studies provide any detailed measurements of the behaviour of particles within a turbulent jet environment, such as the fibres' most probable orientation, the influence of the number density of fibres on the velocity or the angular velocity distribution. Hence, there remains a need for this new information.

In the light of the previous investigations described above, this study seeks to provide new understanding of the aerodynamic behaviour of fibrous particles with a large aspect ratio in the near field of co-flowing turbulent jet in the super-dilute regime. It is further aimed to provide new understanding of the radial distribution of the statistical properties at the exit plane of the jet and so to provide new understanding of the flow within a long pipe. In particular, the study aims to assess the distributions of orientation, angular velocity, axial velocity and number density, none of which have been reported previously in a co-flowing jet.

2. Experimental apparatus

Only a brief description of the experimental apparatus and approach is provided here, with details reported previously by Qi et al. [18]. Fig. 1 presents the notation used to define a fibre's orientation relative to the axial and radial direction of the jet, x and r, respectively, noting that the axis of the jet is aligned with gravity. The angle θ (0°–90°) is defined to be the orientation relative to gravity and α (0°–90°) is the azimuth of a fibre, relative to the viewing plane.

Fig. 2 presents a schematic diagram of the experimental apparatus. Particle Tracking Velocimetry (PTV) was employed. A Quantel Brilliant Twins double-cavity pulsed Nd:YAG 10 Hz laser was used as the light source. The camera was a Kodak MegaPlus ES1.0 with a CCD array of 1008 pixels × 1018 pixels and 10 bit resolution. The fibrous particles were introduced into the top of the pipe via a hopper.

The working section of the wind tunnel was made of Perspex with a nominally square cross section of 650 mm × 620 mm. The facility was operated with a bulk-mean velocity of the jet at 18 m/s and the co-flow with a uniform velocity of 8 m/s. The length, L, and diameter, D, of the supply pipe were 2000 mm and 60 mm, respectively. These dimensions were chosen within the constraints of the laboratory to achieve a trade-off between a sufficiently large development length to approach a fully-developed flow, while also providing a sufficiently large ratio of pipe diameter to the length of the fibres, $D/L_p = 30$, for the velocity gradients in the shear flows to influence rotation.

Measurements of the velocity and orientation of the fibres were performed in the near field of the jet flow along the axis of the pipe. The coordinates of the two endpoints of each object (fibrous particle) were obtained. Since the length L_p of these fibres is all nominally identical at 2 mm (Table 1), the spatial orientation θ of fibres was calculated with the following trigonometric function:

$$\theta = \left(\arccos\ \frac{|x_{e2} - x_{e1}|R}{L_p}\right) \times \left(\frac{180}{\pi}\right) \quad (^\circ), \tag{6}$$

where R is the magnification of the camera image system and the coordinates of the two endpoints are x_{e2} and x_{e1}, respectively. Image pairs were recorded by the digital camera with a known time separation (Δt). After image processing, the displacements of the two endpoints of

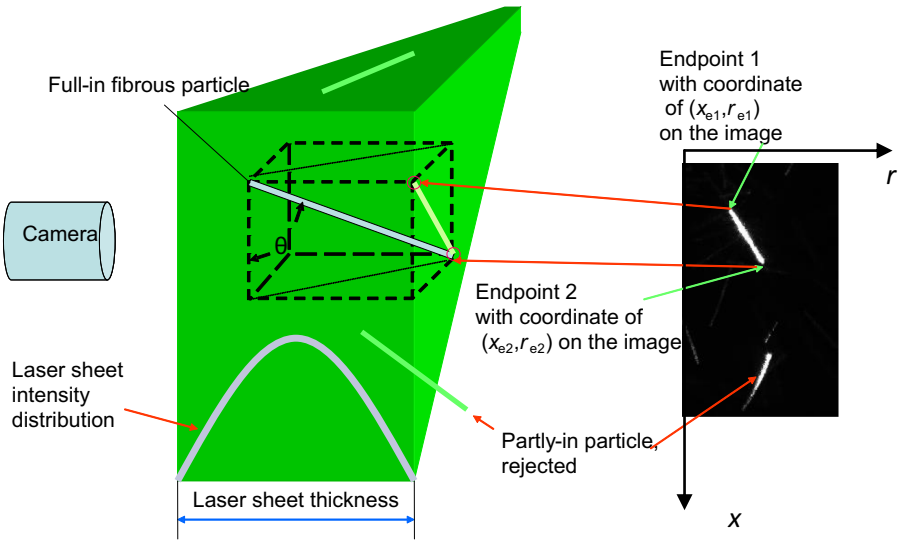

Fig. 3. A schematic diagram of the orientation measurement, the detection of "part-in" fibres and key notation.

fibrous particles along the x and r axis can be obtained. From this $\boldsymbol{V}_{e1x}$, $\boldsymbol{V}_{e1r}$ and $\boldsymbol{V}_{e2x}$, $\boldsymbol{V}_{e2r}$ can be calculated using Eq. (7), as follows:

$$V_{e1x}=\frac{(x_{e12}-x_{e11})R}{\Delta t},\quad V_{e1r}=\frac{(r_{e12}-r_{e11})R}{\Delta t},$$
$$V_{e2x}=\frac{(x_{e22}-x_{e21})R}{\Delta t},\quad V_{e2r}=\frac{(r_{e22}-r_{e21})R}{\Delta t}, \tag{7}$$

where V_{e1x} is the velocity of endpoint 1 in the x direction; V_{e1r} is the velocity of endpoint 1 in the r direction; V_{e2x} is the velocity of endpoint 2 in the x direction; V_{e2r} is the velocity of endpoint 2 in the r direction; x_{e12} is the x axial coordinate of endpoint 1 from the second image, x_{e11} is the x axial coordinate of endpoint 1 from the first image; r_{e12} is the radial coordinate of endpoint 1 from the second image; and r_{e11} is the radial coordinate of endpoint 1 from the first image and so on.

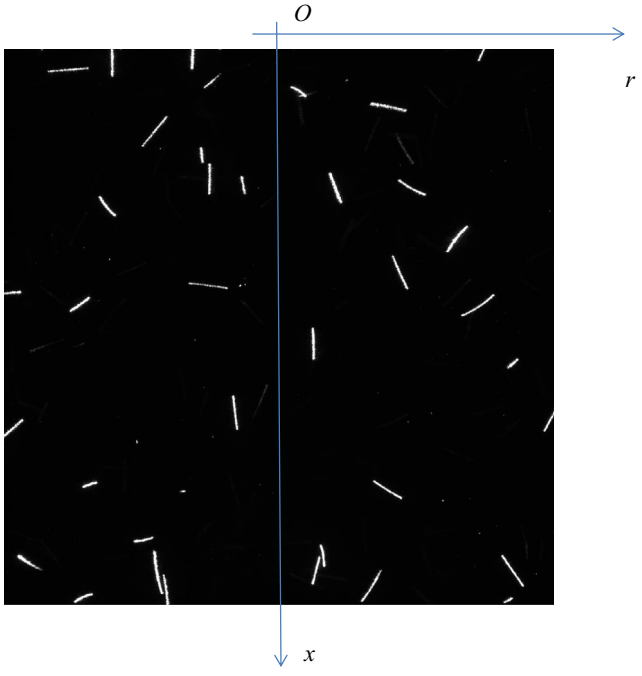

Fig. 4. A typical raw image obtained at the exit plane of the jet together with the coordinate system for the fibrous particles.

In the present two phases turbulent jet flow, the fibre's Stokes numbers, based on their diameter, Sk_d, and length, Sk_{Lp}, respectively, are defined as follows:

$$Sk_d=\frac{\rho_p d V_{c,0}}{18\mu D}\qquad Sk_{Lp}=\frac{\rho_p L_p V_{c,0}}{18\mu D}, \tag{8}$$

where ρ_p is the fibre's density; d and L_p are the fibre's diameter and length, respectively; $V_{c,0}$ is the centre-line velocity for a single-phase jet of the same bulk-mean velocity; μ is the viscosity of the fluid phase and D is the diameter of the supply pipe.

Fig. 3 presents a schematic diagram of the orientation measurement, the detection of "part-in" fibres and the key notation. Any fibres that are only partly in the laser sheet will give a false calculation of the projected length and the coordinates of endpoints, so must be rejected. This was achieved by comparing the intensities of the signal at two endpoints of the fibre. Because of the Gaussian light sheet intensity distribution, a partly-in fibrous particle will exhibit a significant difference between the intensity values of the two endpoints. This is used to reject such particles. A fibre's centroid velocity $V_{c,x}=1/2(V_{e1x}+V_{e2x})$ and $V_{c,r}=1/2(V_{e1r}+V_{e2r})$ represents the axial velocity and radial velocity, respectively, and a fibre's vertical angular velocity is $\omega_{vertical}=d\theta/\Delta t$. Table 1 shows the experimental conditions compared with previous work. It can be seen that the main differences are that the work of

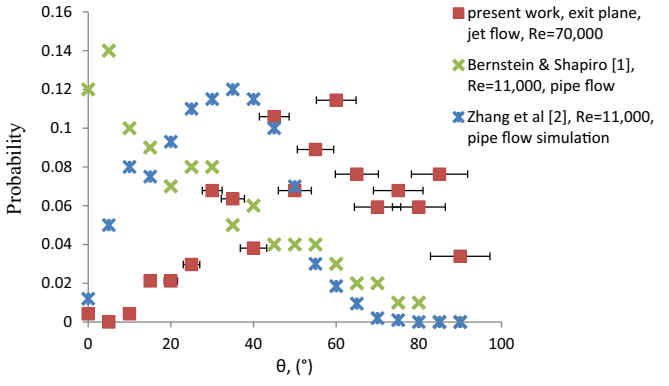

Fig. 5. The distribution of fibre orientations for the present measurements and previous work, both obtained on the axis of a pipe flow. For the present case, these data were measured in the exit plane of a jet emerging from a pipe flow. The error bars correspond to an uncertainty of ±8%.

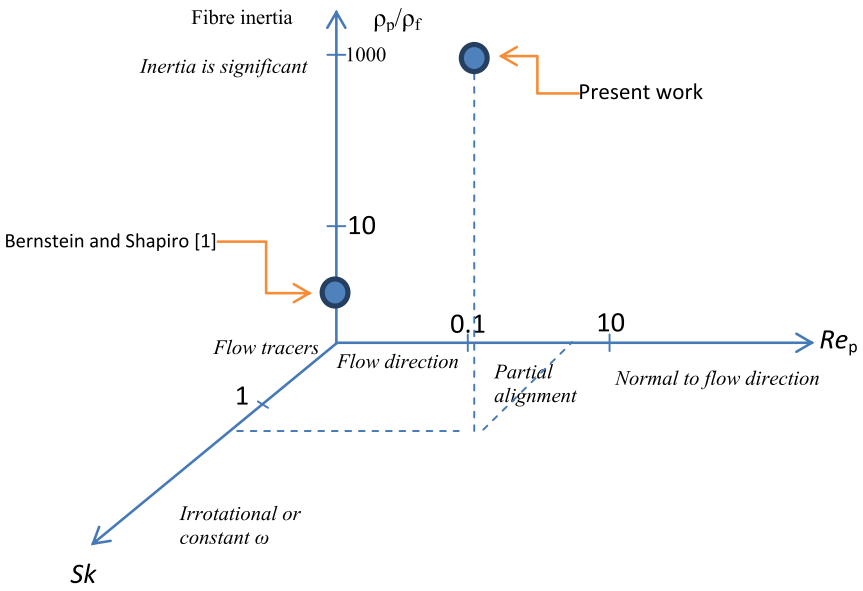

Fig. 6. The influence of a fibre's Stokes number, Reynolds number and density ratio between two phases on the fibre's behaviour in two-phase flow.

Bernstein and Shapiro [1] was performed in water, instead of air, and that their fibres were physically much shorter, resulting in both a different range of Stokes number, $Sk \ll 1$ in contrast with the present data where $Sk \sim 1$ and $L_p/D \lll 1$ in contrast with the present case where $L_p/D \ll 1$. The data of Lau and Nathan [19] was performed for spherical particles instead of fibres and with a higher volumetric loading of particles, but are otherwise under similar conditions.

Fig. 4 presents a sample of the raw image obtained at the exit plane of the jet flow, together with the coordinate system for the fibrous particles. The viewing area of the measurements was 26 mm × 26 mm, while the thickness of the light sheet was 5 mm, which is 2.5 times the length of the fibres (Table 1). This value was found experimentally to provide a good compromise between a sufficiently high fraction of fibres fully within the light sheet and a reasonable spatial resolution.

3. Results

Fig. 5 presents the probability distribution of the fibres' orientations, θ, for both the present measurements at the initial plane of the turbulent jet flow and the previous measurements in a turbulent pipe flow. At the centre of the exit plane of the present turbulent jet flow, the fibres are found over a wide range of orientation between 30° and 90° and the most probable orientation is at an angle of approximately 54° to the flow direction, while there are few fibres that align with the direction of flow. This is consistent with the simulation by Marchioli et al. [3], who reported that the inertial fibre mean orientation is approximately 60° to the flow direction at the centre of the turbulent channel. However, from the figure it can be seen that there is a big difference between the present measurements and those from previous work by Bernstein and Shapiro [1] and Zhang et al. [2], who reported that the fibrous particles tend to align with the flow direction in the centre of pipe turbulent flows. This difference can be attributed to the combination of different conditions in the two investigations, as shown in Table 1 and Fig. 6. Based on Elghobashi's definition [20], the present regime of interaction between particles and turbulence is in the two-way coupling regime. The present conditions comprise much larger values of L_p/D, higher values of the fibre's Stokes number (Sk), higher values of the density ratio between the particle phase and the fluid phase (ρ_p/ρ_f) and a shorter development length, L/D. Of these parameters, the differences in $Sk_d = 2.6$ (present) compared with $Sk_d = 2 \times 10^{-6}$ (previous, [1]) and the difference in ρ_p/ρ_f are expected to be the most significant. Bernstein and Shapiro [1] employed ρ_p/ρ_f of order unity, while in the present case the density ratio is in the order of 1000. These differences imply that the inertia of the fibre is significant for the present case. Parsheh et al. [21] pointed out that the fibres' velocity induced by the drag force in two-phase flow is dependent on the fibres' diameter and the density ratio of the particle to the carrier phase. However it is obvious that the slip between the two phases is also associated

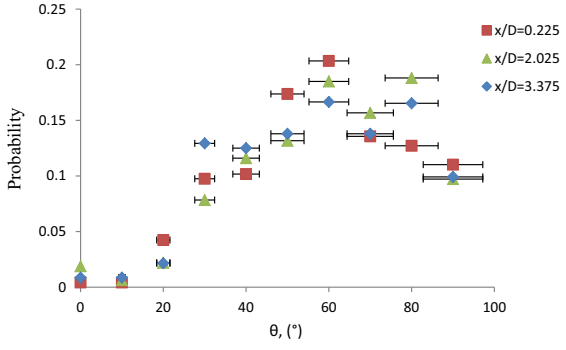

Fig. 7. The distribution of fibre orientations at three axial positions on the axis in the near field of the present jet. The error bars correspond to an uncertainty of ±8%.

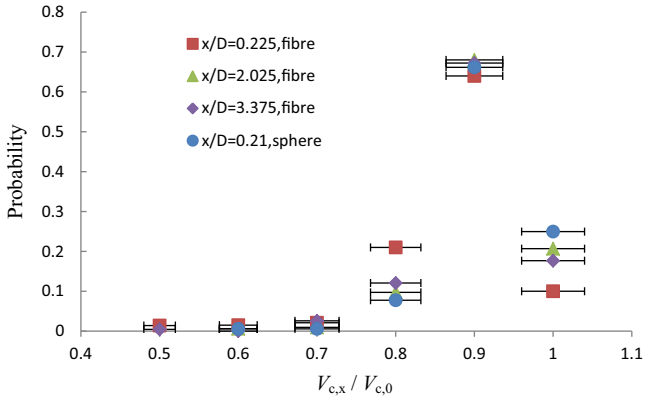

Fig. 8. The distributions of fibres' normalised mean axial velocity at three near-field axial positions on the centre-line compared with spherical particles. Here $V_{c,0}$ is the centre-line velocity for a single-phase jet of the same bulk-mean velocity. The error bars correspond to an uncertainty of ±4%.

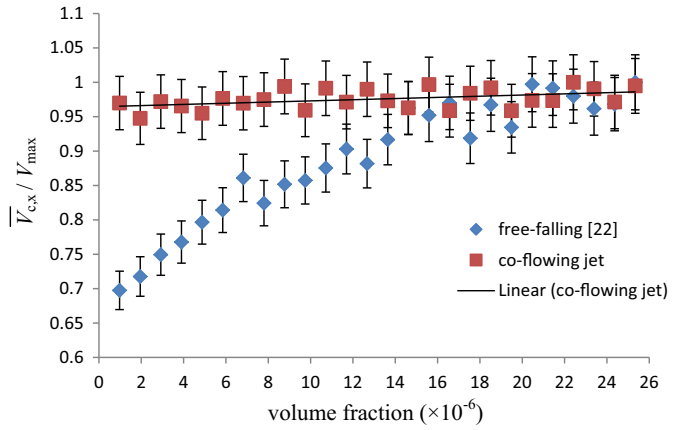

Fig. 9. The dependence on volume fraction of the fibres' axial velocities relative to the maximum velocity in each data set. Data of the co-flowing jet were obtained at $x/D = 1.575$. The error bars correspond to an uncertainty of ±4%.

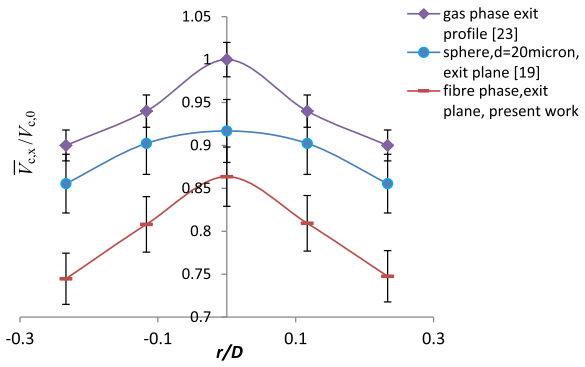

Fig. 11. The radial distributions of fibres' mean axial velocity in the exit plane of the present jet compared with spherical particles and a gas single-phase, normalised by the value, $V_{c,0}$, the centre-line velocity for a single-phase jet of the same bulk-mean velocity. The error bars correspond to an uncertainty of ±4% and ±2% (gas single-phase [23]).

with the initial orientation of the fibres and the fibres' Reynolds number depends on the slip velocity between the two phases. In addition, each individual fibre's orientation depends on its Reynolds number (Fig. 6). For the present case, each fibre's Reynolds number, based on its diameter and slip velocity, is between 2 and 10. At these Reynolds numbers, the fibres' pressure centre being behind the mass centre tends to align the particle as normal to the flow [4]. The wide range of Re_p makes the fibres exhibit a wide range of orientation between 30° and 90°, but the most probable orientation is approximately 54°. In contrast, the fibres' inertia in Bernstein and Shapiro's [1] work is negligible so that the particles approach being flow tracers. Under these conditions the fibres can be expected to follow the flow and align with the local flow direction which, on average, is axial on the centre-line of the pipe.

Based on Eq. (1), given by Mandϕ and Rosendahl [4], the torque acting on the fibre in the present study is of the order of 10^{-12} Nm. The distance between the pressure centre and the mass centre at the mean orientation is estimated to be 235 μm, based on Eq. (2) from Rosendahl [5]. This is some five diameters of the fibre, which is sufficiently great to result in significant variations in torque and significant variations in particle orientations despite retaining a preferred orientation.

Fig. 7 presents the distribution of fibre orientations at three near-field axial locations on the axis of the jet. Data from Figs. 5, 7 and 8 were averaged over a measurement volume of $\Delta x = 26$ mm and $\Delta r = 5.2$ mm. It can be seen in Fig. 7 that the distributions on the axis do not change significantly over the first four diameters from the exit plane, which is consistent with these data being on the centre-line of the potential core region of the jet.

Fig. 8 presents the distribution of the normalised axial velocity of the fibres, $V_{c,x}/V_{c,0}$, at the three axial positions on the centre-line compared with those for spherical particles [19]. Here $V_{c,0}$ is the centre-line velocity for a single-phase jet of the same bulk-mean velocity. In the figure, it can be seen that the velocity distribution of the fibres closely approximates that of the spheres, although that of the spheres is skewed slightly to higher velocities than that of the fibres. The fibres also exhibit a broader range of velocities. This is consistent with the fibres being relatively long compared with their diameter and being larger in terms of mass and inertia, so that they are subjected to a wider range of flow velocities for the same mean position, together with their exhibiting a more complex aerodynamic behaviour.

Fig. 9 presents the dependence on volume fraction of the fibres' axial velocity for cases of free-falling streams of particles and a co-flowing jet. The velocities are normalised by the maximum velocity in each data set. In the figure, it can be seen that the dependence on volume fraction of the axial velocity of the fibres in the co-flowing jet is much weaker than that for the free-falling fibrous particles, and that the axial velocity changes little with an increase in volume fraction. The increase in settling velocity with volume fraction under the free-falling conditions measured previously was attributed to the transition in the orientation away from the horizontal (Fig. 10) because of increased interactions between the wakes of proximate particles [22]. However, in contrast, this transition does not occur in a turbulent jet, with the orientation being nearly independent of volume fraction (Fig. 10). This is attributed

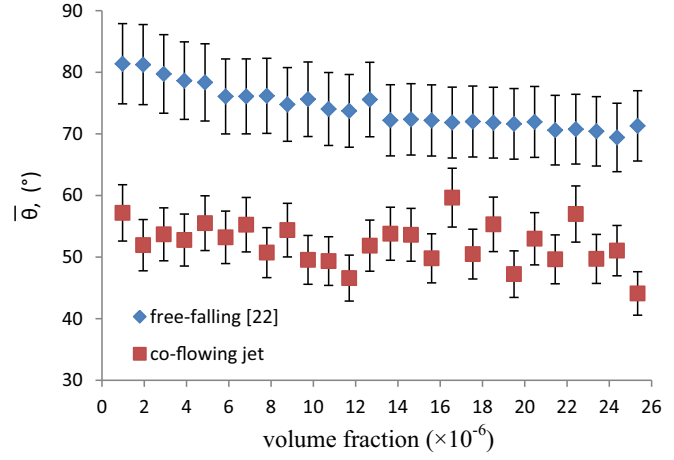

Fig. 10. The dependence on volume fraction of the fibres' mean orientations for cases of co-flowing jet and free-falling. Data of the jet were obtained at $x/D = 1.575$. The error bars correspond to an uncertainty of ±8%.

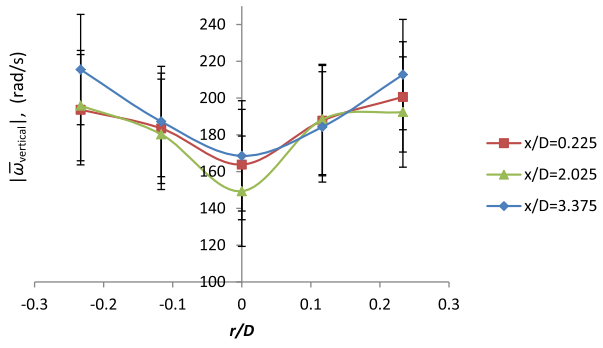

Fig. 12. The radial distributions of mean absolute vertical angular velocity of the fibrous particles at three axial positions in the near field of the present jet flows. The error bars correspond to an uncertainty of ±30 rad/s.

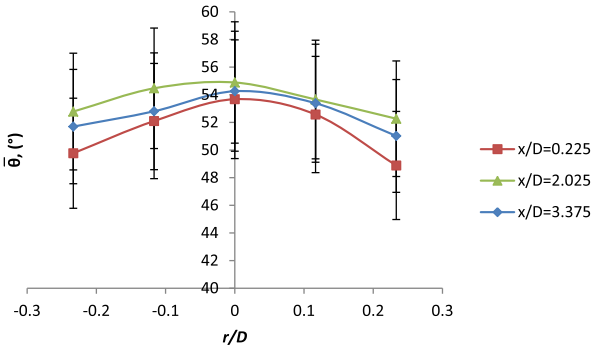

Fig. 13. The radial distributions of fibre mean orientations at three axial positions in the near field of the co-flowing jet flow. The error bars correspond to an uncertainty of ±8%.

to the greater significance of inertia, owing to the higher speed of the particles (together with the carrier phase being air, although this is true in both cases), and to a reduced significance of the interactions between the wakes of proximate particles because the "background" flow in the carrier phase is turbulent instead of laminar.

Fig. 10 presents the dependence on volume fraction of the fibres' mean orientations within the super dilute regime. In the figure, it can be seen that the influence of volume fraction on the distribution of these fibre orientations in the co-flowing jet is much weaker than that for the free-falling case [22], where the orientations decrease with the volume fraction. This is attributed to a reduction in the relative significance of the interactions between the wakes of proximate particles, as described above.

Fig. 11 presents radial distributions of $\overline{V_{c,x}}/V_{c,0}$ at the exit plane of the present jet compared with the comparable cases of suspended spherical particles [19] and a single-phase gas jet [23]. Here $V_{c,0}$ is the centre-line velocity for a single-phase jet of the same bulk-mean velocity. The data were averaged over a measurement volume of $\Delta x = 26$ mm and $\Delta r = 5.2$ mm. It can be seen that the fibres' $V_{c,x}$ is the highest at the centre-line of the pipe, as expected. The radial profile for the spheres is flatter than those of the fibres. Part of the explanation for this is the higher mass loading ($>10^{-3}$) of the spheres, which takes them into the four-way coupling regime based on Elghobashi's definition [20]. That is, the volume loading of the spheres is sufficiently high for them to influence the velocity of the gas phase, while the loading of the fibres is too low to have such influence.

Fig. 12 presents distributions of the fibres' mean absolute angular velocity $|\overline{\omega}_{vertical}|$ in the radial direction at three axial positions in the near field of the present jet flows. The data were averaged over a measurement volume of $\Delta x = 26$ mm and $\Delta r = 5.2$ mm. It can be seen that

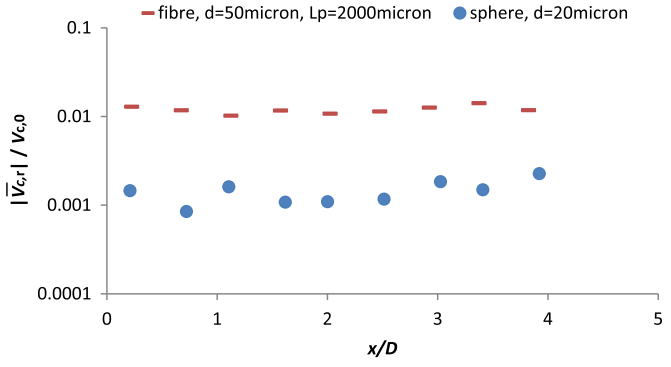

Fig. 14. The axial evolution of distributions of fibrous particles' radial velocity in the near field of the co-flowing jets compared with the spherical particles. Here $V_{c,0}$ is the centre-line velocity for a single-phase jet of the same bulk-mean velocity. The uncertainty in the data is approximately ±8%, which is approximately the same size as the symbols.

$|\overline{\omega}_{vertical}|$ is the lowest at the centre-line of the jet, where the mean shear is the lowest. The angular velocity, $|\overline{\omega}_{vertical}|$, increases with the radial distance toward the location of maximum mean shear, which is consistent with the simulations by Jayageeth et al. [10].

Fig. 13 presents distributions of mean orientation, $\overline{\theta}$, of the fibres at the three axial positions in the near field of the turbulent co-flowing jet flow. In the figure, it can be seen that the most probable mean angle of the fibres to the flow is 54° at the centre-line of the jet. The fibres' orientation tends to be slightly more axial as the radial distance increases. This is attributed to the slight increase in shear with radial distance, which is relatively weak here because the radial distance only spans the range to 0 to 0.23D on the centre-line of the jet, so the decrease in orientation is not significant. This observation is consistent with the simulations by Zhang et al. [2] and Marchioli et al. [3], who reported that the fibres are more aligned with the flow direction at positions far from the centre-line and near the wall. It is also consistent with the previous measurements of Stover et al. [6] and Carlsson [7], who reported that fibres' orientations tend to align with the flow direction at the point where the shear rate is high. However it contrasts with the simulation by Lin et al. [8], who reported that fibres' orientations increase with radial distance. This may be attributed to the different orders of magnitude in Sk. The fibres followed the eddy because of $Sk \ll 1$ in Lin et al.'s [8] simulation.

Fig. 14 presents the axial evolution of the distributions of fibrous particles' relative radial velocity, $\overline{V_{c,r}}/V_{c,0}$, for both the fibrous and the spherical particles in co-flowing jets. It can be seen that the values of $\overline{V_{c,r}}/V_{c,0}$ for the fibrous particles are an order of magnitude larger than that of the spheres. This can be attributed both to the influence of the fibres' tumbling and to their significant orientation to the flow, both of which will cause some the axial velocity to be converted to a radial component, which does not occur for spherical particles. This observation is consistent with the previous measurements of Qi et al. [22], who reported that the value of the horizontal velocity component of the free-falling fibres is approximately 10% of that of the vertical velocity component.

4. Conclusions

In this work, the distributions of velocity and orientation of long aspect ratio fibrous particles in the near-field of turbulent jet flows at an air jet Reynolds number of 70,000 are reported for the first time. It is found that in the exit plane of the turbulent jet flow, the fibres most probable orientation tends to be approximately 54° and there are few fibres that are aligned with the direction of the flow. This is consistent with the simulation by Marchioli et al. [3]. However the results contrast with the work of Bernstein and Shapiro [1] and Zhang et al. [2] undertaken with water as the transporting fluid, who reported that the fibres are aligned with the direction of the flow at the centre-line of a pipe. This difference is attributed to the fibres' inertia. The fibres' inertia is significant for the present jet flow because the density ratio between the particle and fluid phase for the present case is three orders of magnitude larger than that of Bernstein and Shapiro [1]. At the centre of the co-flowing jet, the fibres' $\overline{V_{c,x}}$ and $\overline{\theta}$ is found to change little with an increase in volume fractions in the super dilute regime, which contrasts with the findings of Qi et al. [22] under free-falling conditions. These differences are attributable to a reduction in the relative significance of the interactions between the wakes of the proximate particles. The fibres' $|\overline{\omega}_{vertical}|$ is the lowest at the centre-line of the jet and increases significantly in the radial direction, which is consistent with the simulation by Jayageeth et al. [10]. At the centre-line of the jet the fibres' normalised radial velocity is much higher than that of the spheres with a similar Stokes number, based on diameter. This is attributed to the dual effects of the significant orientation of the fibres to the flow and to their tumbling, both of which induce radial velocity, which does not occur with spheres.

Acknowledgement

This study has been supported by the Faculty of Engineering, Computer & Mathematical Science of The University of Adelaide for the scholarship of the first author and by an ARC Discovery Grant (Grant No. DP120102961), both of which are gratefully acknowledged. The helpful comments of the anonymous reviewers are also gratefully acknowledged.

References

[1] O. Bernstein, M. Shapiro, Direct determination of the orientation distribution function of cylindrical particles immersed in laminar and turbulent shear flows, J. Aerosol Sci. 25 (1) (1994) 113–136.
[2] L. Zhang, J. Lin, T.L. Chan, Orientation distribution of cylindrical particles suspended in turbulent pipe flow, Phys. Fluids 17 (2005) 093105.
[3] C. Marchioli, M. Fantoni, A. Soldati, Orientation, distribution, and deposition of elongated, inertial fibers in turbulent channel flow, Phys. Fluids 22 (2010) 033301.
[4] M. Mandϕ, L. Rosendahl, On the motion of non-spherical particles at high Reynolds number, Powder Technol. 202 (2010) 1–13.
[5] L. Rosendahl, Using a multi-parameter particle shape description to predict the motion of non-spherical particle shapes in swirling flow, Appl. Math. Model. 24 (2000) 11–25.
[6] C.A. Stover, D.L. Koch, C. Cohen, Observation of fibre orientation in simple shear flow of semi-dilute suspensions, J. Fluid Mech. 238 (1992) 277–296.
[7] A. Carlsson, Near wall fibre orientation in flowing suspensions(PhD Thesis) KTH Mechanics, Royal Institute of Technology, Stockholm, Sweden, 2009.
[8] J.Z. Lin, X.Y. Liang, S.L. Zhang, Numerical simulation of fiber orientation distribution in round turbulent jet of fiber suspension, Chem. Eng. Res. Des. 90 (2012) 766–775.
[9] J.Z. Lin, X.Y. Liang, S.H. Shen, Numerical prediction of the flow property in round turbulent jet of fiber suspension, Sci. China Phys. Mech. Astron. 56 (2013) 298–305.
[10] C. Jayageeth, V.I. Sharma, A. Singh, Dynamics of short fibers suspensions in bounded shear flow, Int. J. Multiphase Flow 35 (2009) 261–269.
[11] J.A. Olson, R.J. Kerekes, The motion of fibres in turbulent flow, J. Fluid Mech. 377 (1998) 47–64.
[12] J.A. Olson, The motion of fibres in turbulent flow, stochastic simulation of isotropic homogeneous turbulence, Int. J. Multiphase Flow 27 (2001) 2083–2103.
[13] W. Kvasnak, G. Ahmadi, Deposition of ellipsoidal particles in turbulent duct flow, Chem. Eng. Sci. 51 (1996) 5137–5148.
[14] H. Zhang, G. Ahmadi, F. Fan, J.B. McLaughlin, Ellipsoidal particles transport and deposition in turbulent channel flow, Int. J. Multiphase Flow 27 (2001) 971–1009.
[15] D. Broday, M. Fichman, M. Shapiro, C. Gutfinger, Motion of spheroidal particles in vertical shear flows, Phys. Fluids 10 (1998) 86–100.
[16] X.K. Ku, J.Z. Lin, Inertial effects on the rotational of a fibre in simple shear flow between two bounding wall, Phys. Scr. 80 (2009) 1–10.
[17] J.D. Klett, Orientation model for particles in turbulence, J. Atmos. Sci. 52 (1995) 2276–2285.
[18] G.Q. Qi, G.J. Nathan, R.M. Kelso, PTV measurement of drag coefficient of fibrous particles with large aspect ratio, Powder Technol. 229 (2012) 261–269.
[19] T.C.W. Lau, G.J. Nathan, New understanding of the influence of Stokes number on particle-laden jets from simultaneous planar measurements of number density and velocity, 4th International conference on jets, wakes and separated flows, ICJWSF2013, Nagoya, Japan, 2013.
[20] S. Elghobashi, On predicting particle-laden turbulent flows, Appl. Sci. Res. 52 (1994) 309–329.
[21] M. Parsheh, M.L. Brown, C.K. Aidun, On the orientation of stiff fibers suspended in turbulent flow in a planar contraction, J. Fluid Mech. 545 (2005) 245–269.
[22] G.Q. Qi, G.J. Nathan, R.M. Kelso, Aerodynamics of long fibres settling in air at $10 < Re < 100$, Powder Technol. 235 (2013) 550–555.
[23] J.C. Mi, D.S. Nobes, G.J. Nathan, Influence of jet exit conditions on the passive scalar field of an axisymmetric free jet, J. Fluid Mech. 432 (2001) 91–125.

Powder Technology 288 (2016) 407–408

Contents lists available at ScienceDirect

Powder Technology

journal homepage: www.elsevier.com/locate/powtec

Corrigendum to "Velocity and orientation distributions of fibrous particles in the near-field of a turbulent jet" [Powder Technol. 276(2015) 10–17]

Guoqiang QI *, Graham J. NATHAN, Timothy C.W. Lau

School of Mechanical Engineering and Centre for Energy Technology, The University of Adelaide, Adelaide, SA 5005, AUSTRALIA

The authors provide corrections to seven figures, which constitute changes to the values of some data, but do not alter the key findings of the paper. Changes to Figs. 5, 7, 10, 12 and 13 result from an error in the measured length of the fibres, from $L = 2000$ μm to $L = 1850$ μm which changes the derived angle and angular velocity slightly. Small errors have also been corrected in Figs 8 and 14. The authors apologize for these errors and the corrected figures are given below:

Supplementary data to this article can be found online at http://dx.doi.org/10.1016/j.powtec.2015.11.008.

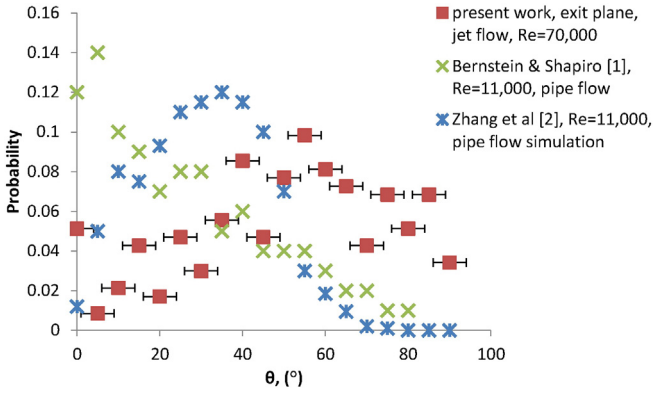

Fig. 5. The distribution of fibre orientations for the present measurements and previous work, both obtained on the axis of the pipe flow. For the present case, these data were measured in the exit plane of a jet emerging from a pipe flow. The error bars correspond to an uncertainty of ±4°.

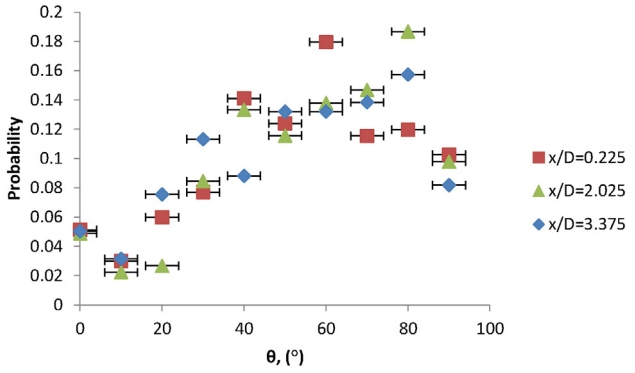

Fig. 7. The distribution of fibre orientations at three axial positions on the axis in the near field of the present jet. The error bars correspond to an uncertainty of ±4°.

DOI of original article: http://dx.doi.org/10.1016/j.powtec.2015.02.003.

* Corresponding author.
E-mail address: guo.qi@adelaide.edu.au (G. QI).

http://dx.doi.org/10.1016/j.powtec.2015.11.008

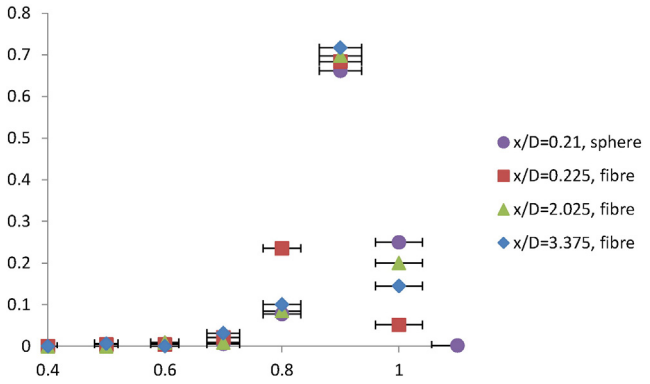

Fig. 8. The distributions of fibres'normalized mean axial velocity at three near-field axial positions on the centre-line compared with spherical particles. Here $V_{c,0}$ is the centre-line velocity for a single-phase jet of the same bulk-mean velocity. The error bars correspond to an uncertainty of ±4%.

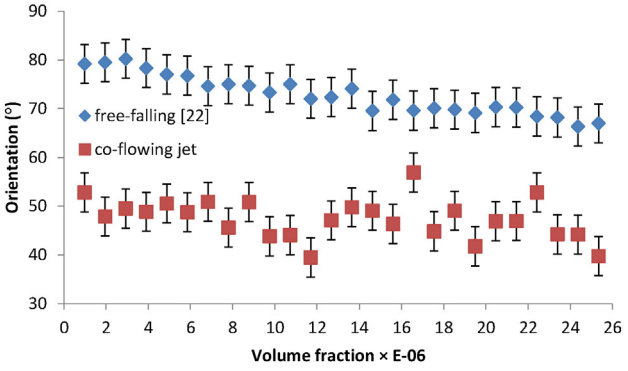

Fig. 10. The dependence on volume fraction of the fibres' mean orientations for cases of co-flowing jet and free-falling. Data of the jet were obtained at $x/D = 1.575$. The error bars correspond to an uncertainty of ±4°.

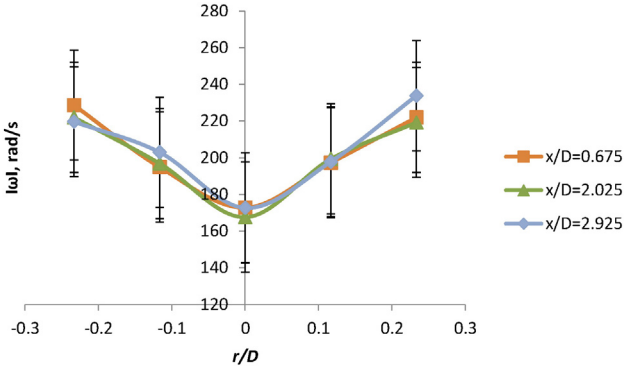

Fig. 12. The radial distributions of mean absolute vertical angular velocity of the fibrous particles at three axial positions in the near field of the present jet flows. The error bars correspond to an uncertainty of ±30rad/s.

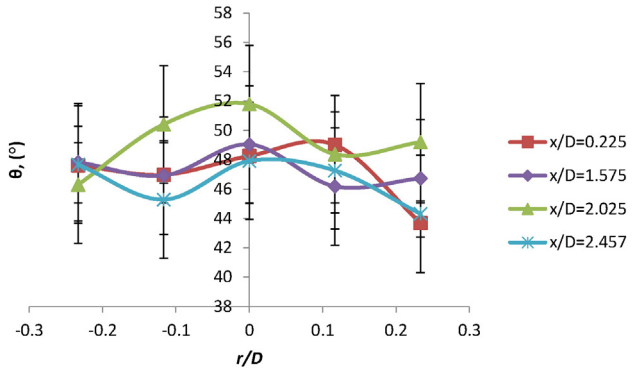

Fig. 13. The radial distributions of fibre mean orientations at four axial positions in the near field of the co-flowing jet flow. The error bars correspond to an uncertainty of ±4°.

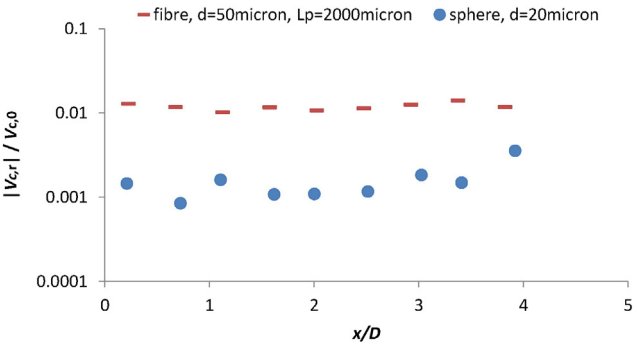

Fig. 14. The axial evolution of distributions of fibrous particles' radial velocity in the near field of the co-flowing jets compared with the spherical particles. Here $V_{c,0}$ is the centre-line velocity for a single-phase jet of the same bulk-mean velocity. The uncertainty in the data is approximately ± 8%, which is approximately the same size as the symbols.

7 The Influence of Number Density of Fibrous Particles on the Distribution of Settling Velocities and Fibre Orientations

G. Q. Qi, G. J. Nathan and R. M. Kelso

Fluid-TEC (Turbulence, Energy and Combustion) Group, School of Mechanical Engineering,

Faculty of Engineering, Computer and Mathematical Sciences

The University of Adelaide, Adelaide SA 5005 AUSTRALIA

Email: guo.qi@mecheng.adelaide.edu.au

3rd International Solar Cities Conference, 17–21 February, 2008, Adelaide, South Australia, Australia. ISBN 978-0-9803168-7-2.

Statement of Authorship

Title of Paper	The influence of number density of fibrous particles on the distributions of settling velocities and fibre orientations
Publication Status	☑ Published ☐ Accepted for Publication ☐ Submitted for Publication ☐ Unpublished and Unsubmitted work written in manuscript style
Publication Details	G.Q. Qi, G.J. Nathan and R.M. Kelso. The influence of number density of fibrous particles on the distributions of settling velocities and fibre orientations. 3th International Solar Cities Congress 2008, ISBN978-0-9803168-7-2, pp201-210. Adelaide, Australia, 2008.

Principal Author

Name of Principal Author (Candidate)	Guo Qiang Qi		
Contribution to the Paper	I was responsible for the development of both the measurement technique and analytical model under the principal supervision of Professor Nathan. I performed the measurements and data processing, wrote the first draft of the manuscript and incorporated and addressed all comments and suggestions by other authors in subsequent revisions of the manuscript. I acted as corresponding author.		
Overall percentage (%)	55%		
Certification:	This paper reports on original research I conducted during the period of my Higher Degree by Research candidature and is not subject to any obligations or contractual agreements with a third party that would constrain its inclusion in this thesis. I am the primary author of this paper.		
Signature		Date	13/06/2016

Co-Author Contributions

By signing the Statement of Authorship, each author certifies that:

i. the candidate's stated contribution to the publication is accurate (as detailed above);

ii. permission is granted for the candidate in include the publication in the thesis; and

iii. the sum of all co-author contributions is equal to 45% less the candidate's stated contribution.

Name of Co-Author	Graham J. Nathan		
Contribution to the Paper	I was principal supervisor for the development of work, contributed to both data interpretation and refining of the manuscript.		
Signature		Date	14/6/16.

Name of Co-Author	Richard M. Kelso		
Contribution to the Paper	I, co-supervisor, jointly supervised the development of work.		
Signature		Date	14/6/2016.

Please cut and paste additional co-author panels here as required.

The influence of Number Density of Fibrous Particles on the Distribution of Settling Velocities and Fibre Orientations

G. Q. Qi, G. J. Nathan and R. M. Kelso
Fluid-TEC (Turbulence, Energy and Combustion) Group, School of Mechanical Engineering,
Faculty of Engineering, Computer and Mathematical Science
The University of Adelaide
Adelaide SA 5005
AUSTRALIA
E-mail: guo.qi@mecheng.adelaide.edu.au

Abstract

The paper presents new measurements of the settling velocity of fibrous particles. This is of relevance to the aerodynamics of biomass particles in furnace and boiler. As such it will contribute to the replacement of fossil fuels with biomass, which is renewable and nearly greenhouse neutral. The influence of the volume fraction of fibrous particles on their settling velocities and orientations is reported for conditions in which fibrous particles settle in air at low number density. A method for laser-based measurement of the orientations and velocities of fibrous particles is presented. The experimental apparatus employs PTV (Particle Tracking Velocimetry. A Matlab code was written to track fibrous particles and calculate orientation and velocity of their two end-points simultaneously. The key findings are as follows: the mean fibrous particles settling velocities increase significantly with increasing number density of fibres under the low volume fractions (super dilute) and the mean orientations of fibrous particles are also deeply influenced by the volume fraction of the particles; the fibres' orientations tend to be vertical when number density increases; Settling and horizontal velocity distributions of fibrous particles are nearly Gaussian.

1. BACKGROUND OF THE PROJECT

Combustion, currently derived predominantly from fossil fuels, provides most of the energy supplied for the industrialized economies. However fossil fuels, such as oil, coal and natural gas, are not sustainable and non-renewable. The fossil fuels used today were formed over millions of years ago. With the present consumption rates and the known reserves, fossil fuels will be depleted in the foreseeable future. IEP (2004) predicted "Proven coal reserves worldwide total 907 billion tones or almost 200 years of production at current rate" and for oil it reported "the R/P (reserve/production) ratio is 41 years according to BP and 36 years according to *World Oil*". Furthermore in combustion fossil fuels emit a significant quantity of NO_x and CO_2. Nitrogen oxides are precursors to the formation of ozone and they also contribute to the formation of acid rain. Carbon dioxide does not directly impair human health, but it is widely believed to be a major contributor to global warming which pose serious environmental threats to our eco-systems and society. The higher global temperature rises may result in disastrous consequences.

One approach to reduce the use of fossil fuels is the partial substitution with biomass, or organic matter, which is a renewable and more benign resource for energy supply. Such fuels can be derived from trees, agricultural residues and other plants. Also, biomass is nearly greenhouse neutral since it absorbs carbon dioxide through photosynthesis as it grows. The percentage of biomass being used around the world is increasing.

In Australia, wood and bagasse, a by-product of sugar-making industry (sugar-cane waste), are major sources of bio-fuels. The percentage of biomass in renewable energy supply in Australia is 72%, and this number is expected to increase by 3.3% annually by the year of 2011, 2.5% by 2030 (ABARE, 2006). Therefore, it is generally expected that wood and bagasse will play an increasingly important role in the future as a renewable energy supply in Australia.

Importantly, all combustion technology employed to optimize the combustion and performance, and reduce in-flame emissions rely on optimising and controlling the trajectories and residence times of the fuel through the various stages of its combustion. This, in turn, requires detailed knowledge of fuel properties and furnace

aerodynamics. Currently most existing combustion systems in conventional furnaces, boilers and kilns are designed for the use of fossil fuels, of which pulverised fuels (PF) are most common. Hence considerable research has been conducted over the past years to enhance the utilization of pulverized coal, which consists of nearly spherical particles. This research includes the fundamental study of the aerodynamic behaviour of spherical particles. Therefore the aerodynamics of spherical particles under conditions relevant to most combustion environments is relatively well understood. However biomass is fibrous and pulverized biomass particles are not spherical particles that is, one dimension of the fibrous particle is far greater than the other two.

There is a paucity of data describing the aerodynamic behaviour of fibrous particles. The aerodynamic behaviour of fibrous particles is completely different from spherical particles. The drag force of a fibrous particle aligned parallel to the direction of gravitational force is obviously much less than that of perpendicular to the direction. Figure 1 shows the settling of a fibrous particle and a spherical particle as they are falling in still air and the definition of fibrous particle length L, diameter d, orientation γ and terminal settling velocity V_{ts} .

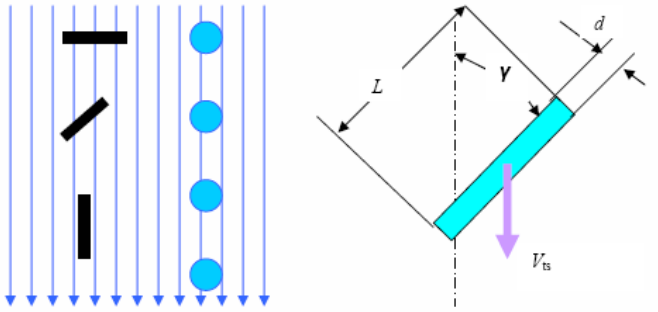

(a) **(b)**

Figure 1: (a) Different orientation of fibrous particles obviously result in different aerodynamic behaviour (b) Definition of a fibrous particle's length, diameter and orientation in present study

Herzhaft and Guazzelli (1999) experimentally investigated hydrodynamic behaviour of glass-rods with length of 0.5 – 3mm in dilute and semi-dilute suspensions. They found a fibre's settling velocity strongly depends on its orientation and also "there is a substantial alignment of the fibres along directions close to the vertical direction". Compared to the work of Herzhaft and Guazzelli on measurements of fibrous particles there are some distinct features in the current experimental setup and they are listed in table 1.

Table 1. Comparisons between present and Herzhaft and Guazzelli 's work

Present work	Work of Herzhaft and Guazzelli
Fibrous particle-gas phase	Fibrous particle-liquid (buoyancy can not be neglected)
Boundary influence can be neglected (cross section of settling chamber: 650mm×620mm)	Boundary limitation (65mm×35mm)
Data of volume fraction nearly continuous	Limited data points
Volume fraction < 0.00035	Volume fraction > 0.00052
Density ratio of two phase = 958.33	Density ratio of two phase = 2.056
Laser-based measurement of PIV apparatus	Real time digital image system
Viewing area: 27mm × 27mm	Viewing area: 10mm × 10mm

From the table 1 and based on literatures review it can be seen that the measurements under the range of this volume fraction, density ratio and experimental method have not been done before. The orientation and velocity distributions and the influence of number density of fibrous particles on the settling velocities have not been investigated. This is the aims of present project. This paper includes literature review, experimental setup, key findings and discussions.

2. PREVIOUS WORK

2.1. Terminal settling velocity of particles

When a particle settles in air, the settling velocity will become steady after a period of time, e.g. the particle's

gravitational force downward is balanced by air drag force upward (when particle's density is much greater than air, the buoyancy can usually be neglected). This steady velocity is called terminal settling velocity (V_{ts}). Hinds (1998) pointed out that V_{ts} depends on particle Reynolds number (Re_p). Equations (1) and (2) are definition of Re_p and V_{ts} of a sphere derived by Hinds respectively:

$$\mathrm{Re}_p = \frac{\rho_p V d}{\eta} \tag{1}$$

$$V_{ts} = \frac{\rho_p d^2 g}{18\eta} \quad (d > 1\ \mu\mathrm{m} \text{ and } Re < 1.0) \tag{2}$$

where ρ_p is the particle density, d is the particle diameter, g is gravitational acceleration and η is the fluid viscosity. When the Reynolds number of the particle is approach 1, V_{ts} needs to be modified to account for transition for the Stoke regime. Equation (3) is a version modified by Bonadonna et al (1998).

$$V_{ts} = d \sqrt[3]{\frac{4\rho_p{}^2 g^2}{225\,\rho_{air}\eta}} \quad (0.4 < Re < 500) \tag{3}$$

Hinds also presented an equation to describe the settling velocity of a cylindrical particle by introduction of the dynamic shape factor χ, shown equation (4), which is defined as the ratio of the drag force of a cylindrical particle to that a sphere having the same volume and velocity as the cylindrical particle:

$$\chi = \frac{F_D}{3\pi\eta V d_e} \qquad V_{ts} = \frac{\rho_p d_e{}^2 g}{18\eta\chi} \tag{4}$$

where d_e, is the equivalent volume diameter, which is the diameter of a sphere having the same volume as that of the cylindrical particle. However these two equations are only valid at $\mathrm{Re}_p \le 0.1$. It is apparent that χ depends on orientation, hence the term "dynamic", and will have a minimum value for a vertical orientation. Hinds recommended a minimum value for χ of 1.20 (where the aspect ratio is 10), which implies the terminal settling velocity of the cylindrical particle is always less than that of an equivalent volume sphere. This is yet to be verified and appears to be highly questionable.

2.2. Sphericity (ψ) of fibrous particle

Sphericity, ψ, is widely used for the study of non-spherical particle and researchers also use it to evaluate fibrous particles. Sphericity was first defined by Wadell (1933) to be: $\Psi = A_s/A_p$,where A_s is the surface area of sphere that has the same volume as the non-spherical particle and A_p is the surface area of the non-spherical particle. Based on this definition the sphericity of a cylindrical particle becomes:

$$\psi_{fp} = \frac{d_{evs}{}^2}{dL + d^2/2} \tag{5}$$

where d_{evs} is the diameter of the sphere that has the same volume as the fibrous particle, e.g. equivalent volume diameter, and d and L are diameter and length of the fibrous particle respectively. Pettyjohn and Unnikrishnan et al (1990) further developed this to be:

$$\frac{V_{fp}}{V_{evs}} = 0.459 + 0.468\left(\frac{d_{evs}}{d}\right)\psi_{fp}{}^{1/2} + 0.0084\left(\frac{d_{evs}}{d}\right)^2\psi_{fp} \tag{6}$$
$$(0.068 \le d_{evs}/d \le 1.44)$$

where V_{fp} is the fibre's settling velocity and V_{evs} is settling velocity of an equivalent volume sphere. Obviously

the limitation of d_{evs}/d renders this equation unsuitable for the fibrous particle with a relatively large aspect ratio. For example, in the present study, d_{evs}/d = 3.93 and equation (6) can not be used. Furthermore particles with entirely different shapes and different aerodynamic behaviour can have the same sphericity. For example, a disc particle and a fibrous particle can have the same χ, but have a totally different aerodynamic behaviour.

2.3. Richardson-Zaki's Law

The Richardson-Zaki's Law presents the relationship between a particle's mean V_s and its volume fraction Φ under the conditions that apply in a fluidized bed. A particle's mean settling velocity decreases with increasing of solid concentration. The added resistance comes from the hydrodynamic interaction between particles. The level of interaction was firstly systematically studied by Richardson and Zaki (1954), who proposed a power-law relation:

$$\frac{V(\phi)}{V_{ts}} = (1-\phi)^n \tag{7}$$

where Φ is a particle's volume fraction in the fluidized bed, V is the mean settling velocity and V_{ts} is a terminal settling velocity of a single particle in the fluidized bed, n is a parameter dependent upon Re_p. Herzhaft (1999), have pointed out this formula is likely to under-predict velocity as the loading approach the dilute limit. However to date there has been no experimental data available to evaluate this conclusion, even for spherical particles.

2.4. Analytical results of fibrous particle under low Reynolds number

Kim et al (1991) studied spheroid hydrodynamic behaviour under the condition of $Re_p \rightarrow 0$ in an infinite system and they derived equation (8) to describe the terminal settling velocity:

$$V_{ts}(\gamma) = \frac{3V_0}{16e^3}[\cos^2\gamma(-4e + (2+2e^2)\ln\frac{1+e}{1-e})^{-1} + \sin^2\gamma(2e + (3e^2-1)\ln\frac{1+e}{1-e})^{-1}]^{-1} \tag{8}$$

where γ is the angle between gravity and fibre's major axis, V_0 denotes the terminal settling velocity of a sphere with unit radius; and e denotes the eccentricity of the fibrous particle (for cylinder $e = L/d$). The orientation $\gamma = 0$ and $\pi/2$, correspond to the maximum and minimum settling velocities respectively. This equation assumes that there is no torque on the spheroid and the orientation is stable.

2.5. Previous researchers

The settling motion of fibrous particles is much more complex than that of spheres. A sphere settles in a purely vertical direction. However for a fibrous particle, the horizontal drift cannot be neglected. Fibrous particles also exhibit rotation. Importantly there has been no previous report of the simultaneous (e.g. laser-based) measurement of a fibrous particle's settling velocity and orientation. Fan et al (2004) investigated a single particle settling in water using both brass wire and synthetic fibres. They found that the preferred orientation of a fibrous particle is approximated horizontal, when it becomes stable.

Herzhaft and Guazzelli (1999) studied the settling velocity of fibres in dilute and semi-dilute suspensions. The fibrous particles used in his experiments were glass-rods with the lengths of 500-3000μm and diameters of 90-100μm. Their conclusion about orientation distribution is in contrast to the work by Fan et al, i.e. that the probable orientation is nearly vertical. They also found the settling and horizontal velocity distributions to be nearly Gaussian. However because the size of cross-section of their water cell was only 65mm by 35mm, a back-flow occurred in the cell and some particle's settling velocities were negative. They also found that settling velocity decreased with the increase of volume fraction, which agrees with Richardson-Zaki's Law, but did not provide experimental data at low concentrations, although they noted that the mean settling velocity increases with increasing of volume fractions. Furthermore they used projected angles to measure the particles' orientation, which will result in some error because sometimes fibrous particles may be nearly horizontal even though the projected angles are vertical.

3. EXPERIMENTAL APPRATUAS

3.1. Nylon fibrous particles and experimental apparatus

The fibrous particles used in the present study are nylon with a nominal length of 2000μm and diameter of 49.6μm (aspect ratio = 40) and the experimental apparatus which employs a typical PIV setup is shown in Figure 2.

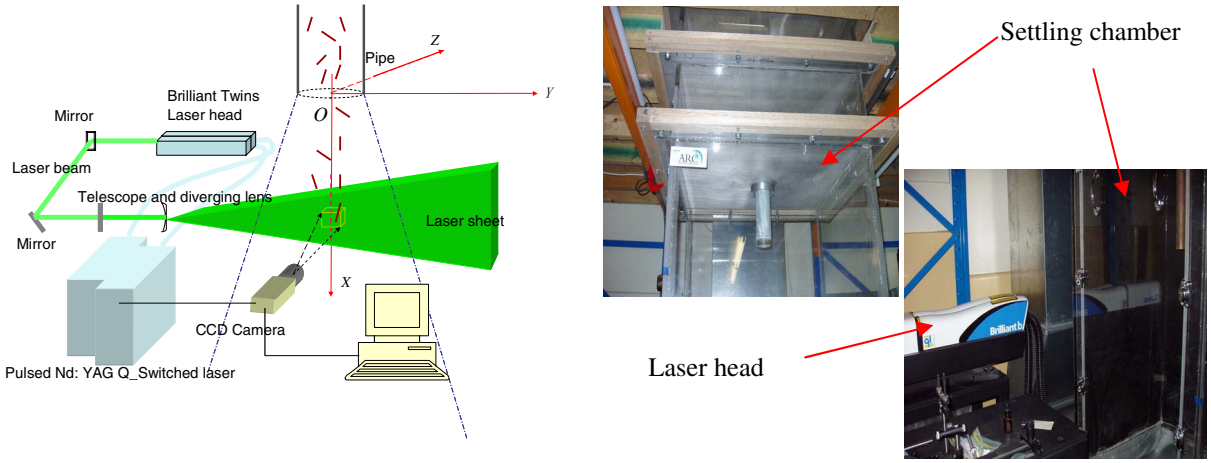

Figure 2: Nylon fibrous particles settle with the height of 2.5 - 3m to camera in the wind tunnel which was made of Perspex and the fibres are illuminated by a pulse laser sheet and fibrous particle positions and orientations are captured by CCD camera within known time separation

The settling chamber had square cross section of 650mm by 620mm and height of 2000mm and was made of Perspex. The particles were introduced into the top of the chamber through through a 2m long pipe of 60mm diameter. Not only did this ensure sufficient settling length to reach their settling velocity, it also ensure that any background eddy current induced by the particles in the chamber were negligible. With a volume fraction of order of 10^{-4}, and cross sectional area of the "jet" of falling particles to the chamber of the order 10^{-2}, any induced chamber flows will be at most 1% of the particles, which is within experimental error. This neglect ensures the dilute phase is not influenced by the chamber current in contrast to previous investigations.

The laser was a 400 mJ per pulse dual cavity Nd:YGA laser at 532nm (green) and the laser sheet was formed by telescopic and diverging lens. The thickness of the sheet is chosen to be around 5mm to provide good illumination of entire particles. The camera was a Kodak MegaPlus ES1.0 with a CCD array of 1008pixels × 1018pixels. the minimum resolution eas therefore 26 μm/pixel. Xcap software was used as the operating system and a DG-535 delay generator was employed to trigger both the laser flash-lamps and the camera.

3.2. Number density measurement

The volume fraction of fibrous particles is defined to be:

$$\phi = \frac{m\pi(d/2)^2 L}{1008 \times 1018 R^2 H \zeta} \tag{9}$$

where m is the number of fibrous particle, R is the resolution of camera setup, H is the thickness of laser sheet and ζ is factor of modification which depends on feeding rate and clumping of particles.

Because $\Phi \leq 0.00025$ in the present experiments, which is a super dilute condition, there were few particles that exhibit clumping. In this case the number density of fibrous particle in the viewing area (volume) was calculated by counting the number of particles, providing an accurate measure of Φ on shot by shot basis, influence of particle number density on the fibres' aerodynamic behaviour can be measured statistically.

Image processing involved converting the image into binary form, then labeling connected particles, and then removing the noise. The background pixels were labeled 0. The pixels that made up the first object were labeled 1, (see Figure 3) those labeled 2, the second object, and so on. If there were *m* particles in the viewing volume the last pixels (object) would be labeled *m*.

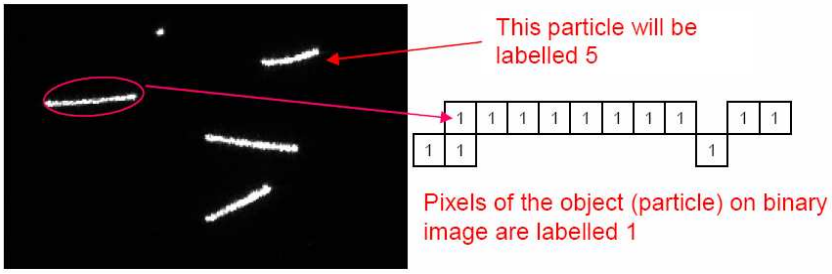

Figure 3: The method used to measure number density of nylon fibres can within the viewing volume by counting the number of objects in a binary image

3.3. Orientation measurement

The projected length and angle of fibrous particles on the digital image was computed by collecting the coordinates of two endpoints of the object (fibrous particle). Since the length *L* of the fibre was known, the spatial orientation γ of fibres can be calculated by trigonometric function (refer to figure 4). Specifically:

$$\gamma = (\frac{\pi}{2} - \sin^{-1}\frac{|y_2 - y_1|R}{L}) \times (\frac{180}{\pi}) \quad (^\circ) \tag{10}$$

where y_2 and y_1 are coordinates of *Y* values of endpoints. Before calculation of a fibrous particle's orientation, the fibres which are partly-in the laser sheet must be removed since they would provide false information on the projected lengths and endpoints. This was achieved by comparing the intensities of two endpoints of the fibre. A fibrous particle that only partly in the light sheet will exhibit a significant difference between the intensity values of the two endpoints due to the non-uniform intensity profile of the laser sheet.

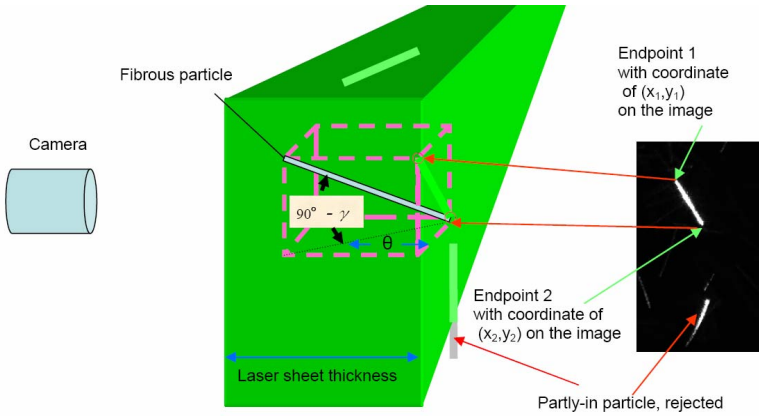

Figure 4: The method used to calculate the orientation of nylon fibres based on known length and coordinates of two endpoints of each object

3.4. Velocity measurement

The vertical (settling) and horizontal velocities of the fibrous particle were measured using Particle Tracking Velocimetry (PTV). The experimental method was validated by using hollow glass beads with a diameter of 45 micron and a density of 700kg/m^3. The glass beads settling velocity can be calculated theoretically by using equation (2) and also their settling velocity can be measured by a PTV setup in the settling chamber. There was a

very good agreement (within 1%) between experimental data and theoretical computation.

The average of the velocities of two endpoints of the fibre along *X* axis (refer to Figure 2), and horizontal velocity was the velocity along *Y* direction because of the use of only one camera. Figure 5 shows a pair of raw images of fibrous particles with length of 2000μm and diameter of 49.6μm; the time separation between them is 2500μs.

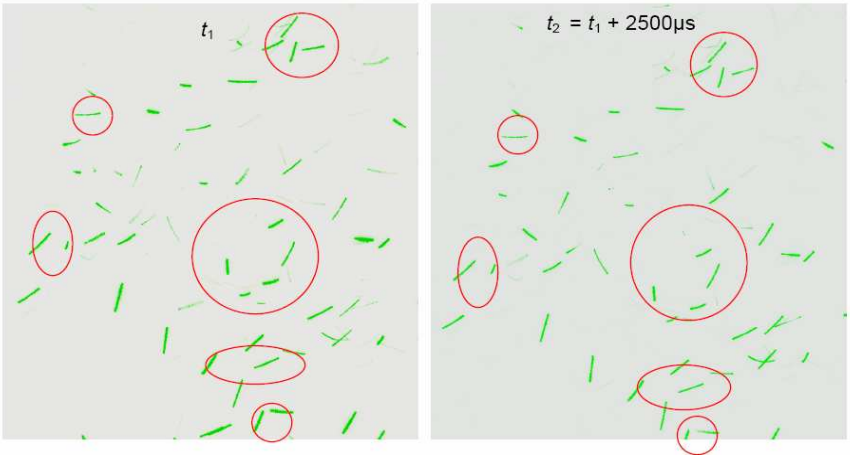

Figure 5: A pair of raw images of fibrous particles settling in still air with a time separation of 2500 μs (the circles highlight matching particles)

From Figure 5 it can be seen that if the time separation is short enough there are few changes in projected lengths and orientation of a fibrous particle. This allows particle tracking to be used reliably, since it is clear the particle has not undergone more than one rotation. After matching pairs of particles between a pair of images, the vertical and horizontal displacements of two endpoints of a fibrous particle can be obtained. Therefore the velocities of two endpoints of fibrous particles can be calculated by the simple formula: velocity = displacement / time separation.

4. EXPERIMENTAL RESULTS

4.1. Settling and horizontal velocities distributions

Figure 6 (a) and (b) shows the settling velocity distribution within the ranges of volume fractions of $1.5\times10^{-5} < \Phi < 3.5\times10^{-4}$ and $4.5\times10^{-5} < \Phi < 5.5\times10^{-5}$ respectively. It can be seen that the distributions of settling velocities are Gaussian under conditions spanning both a wide and a narrow range of volume fractions and that consist with Herzharf's work. However in contrast to Herzharf's work in which some 40% of the range of settling velocities were negative, no negative velocities are found in present data.

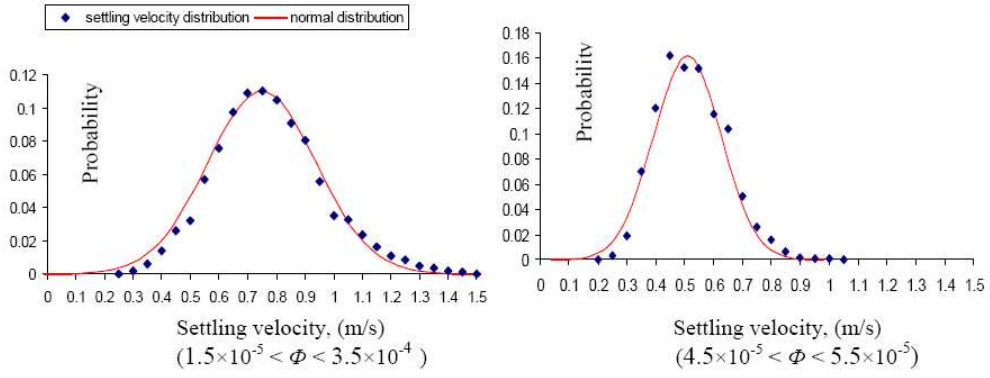

Figure 6: Distribution of settling velocities of fibrous particles

Figure 7 shows the horizontal velocity distribution within the range of volume fractions of $1.5\times10^{-5} < \Phi < 3.5\times10^{-4}$. It can be seen that the average horizontal velocity is nearly zero. There is nearly the same result for a narrow range of number density of fibrous particles.

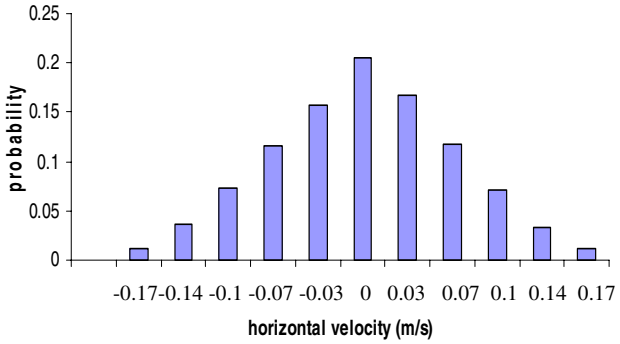

Figure 7: Horizontal velocities distribution of fibrous particles

4.2. Orientation distribution

Figure 8 shows spatial orientation (angle of γ) distribution of fibrous particles under the range of a volume fractions of $1.5\times10^{-5} < \Phi < 3.5\times10^{-4}$. It can be seen that the majority of fibres are nearly horizontal. This finding is in contrast to the Herzhaft and Guazzelli's result in which most of the glass-rods were nearly vertical.

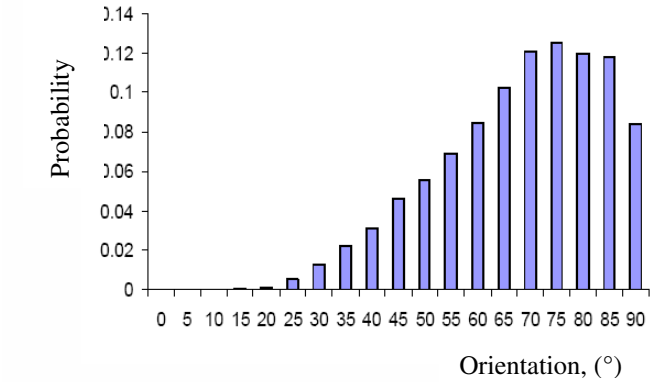

Figure 8: Orientation distribution of fibrous particles with length of 2000μm and diameter of 49.6μm

4.3. Influence of volume fractions on the mean settling velocity of fibrous particle

Figure 9 shows the relationship between volume fraction and mean settling velocity under the condition of low number density, and with negligible influence of external boundaries. The mean settling velocities are found to increase significantly with volume fraction. Furthermore it can be seen that the scatter in the data also increases with an increase in volume fraction. Clearly this result does not obey Richardson-Zaki's Law, since under this range of volume fractions the data calculated by using the Richardson-Zaki's Law are nearly constant. Based on the present study, equation (11) can be used to describe the relationship between the mean settling velocity of fibrous particles in air and the number density:

$$\frac{\overline{V}_{ts}(\phi)}{\overline{V}_0} = a\phi^n \qquad (a = 10.18936) \quad \text{and} \quad (n = 0.2017) \qquad (11)$$

$$(1.4\times10^{-5} < \Phi < 2.5\times10^{-4})$$

where $\overline{V_{ts}}$ is the mean settling velocity of fibrous particles in air and $\overline{V_0}$ is mean settling velocity of a single fibrous particle in air under the condition of no boundary influence; a is the parameter which depends on aspect ratio of fibrous particles (L/d) and n is the parameter which depends on fibres' settling velocity (Reynolds

number of the fibrous particle); Φ is the volume fraction of fibres. It should be note that the generality of this equation is yet to be assessed, however it may be an important supplement to Richardson Zaki's law.

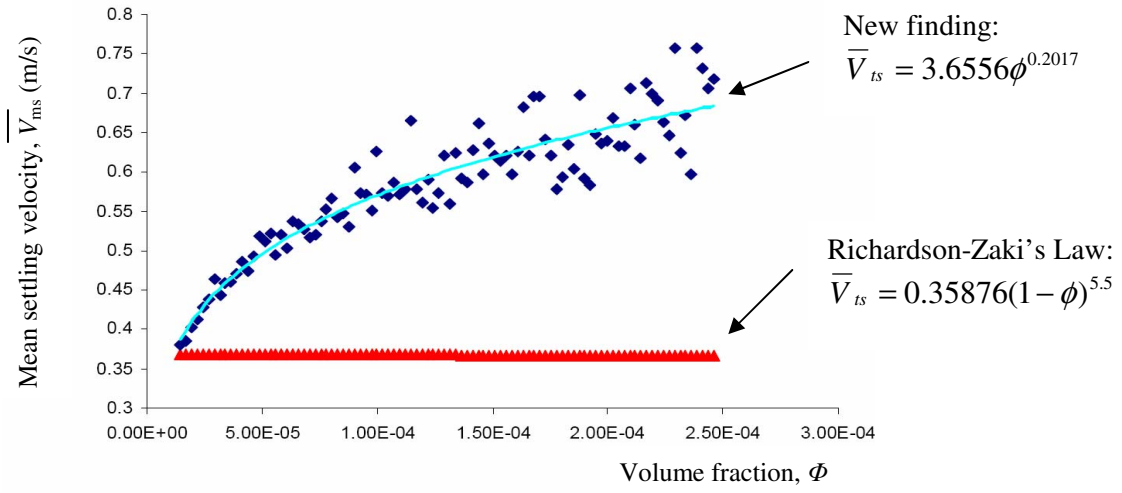

Figure 9: Influence of volume fractions (number density) of fibrous particles on their settling velocity

4.4. Influence of volume fractions on the mean orientation and fluctuation of horizontal velocity

Figure 10 (a) displays the relationship between volume fractions and mean orientations of fibrous particles when settling in air under the condition of low number density. It indicates that interactions between fibrous particles caused by an increase of volume fraction results in a tendency toward a more vertical orientations of the fibres. This also explains why the settling velocity increases significantly with the increase in number of fibrous particles.

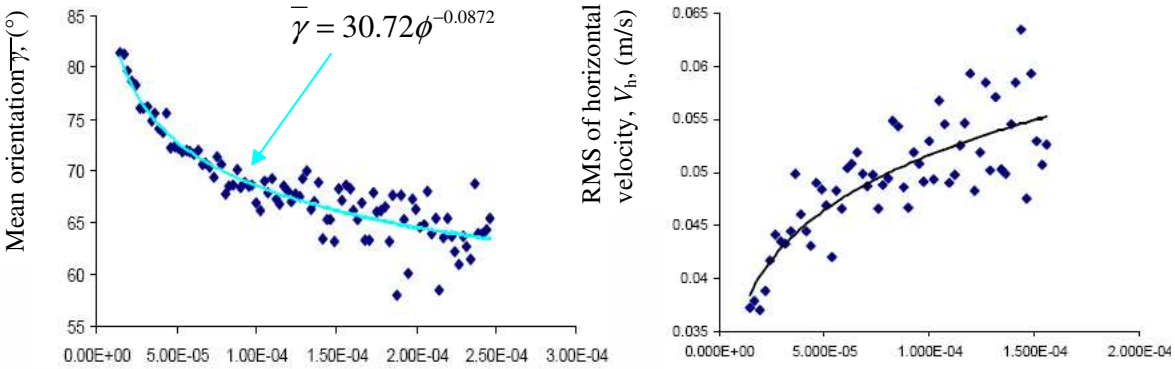

Figure 10: The influence of volume fractions of fibrous particle (a) on their mean orientation; (b) on the fluctuation of mean horizontal velocity

Figure 10 (b) represents the effect of number density of fibrous particles on deviations of horizontal velocities. It shows that the fluctuation of horizontal velocity increases dramatically with the increase of the volume fraction.

5. CONCLUSIONS

The aerodynamic behaviour of nylon fibrous particles has been investigated experimentally whilst settling in air under the super dilute suspension without the limitation of boundary by using PIV. It has been found that the mean settling velocities increase and the orientation tend to be more vertical with increasing of volume fractions.

Fibrous particles terminal settling velocities distribution is Gaussian and majority of particles' orientation distribution is nearly horizontal. Also the Richardson-Zaki Law does not describe the influence of volume fraction under this regime. Instead a power law function provide a much better describtion.

6. ACKNOWLEDGEMNETS

This study has been supported by the Faculty of Engineering, Computer & Mathematical Science of The University of Adelaide and by an ARC Discovery Grand, which are gratefully acknowledged.

7. REFERENCES

ABARE, (2006), *Australian energy national and states projections to 2029-30,* abare research report 06.26, 26.

Bonadonna, C., Ernst G. G. J., and Sparks, R. S. J. (1998). Thickness variations and volume estimates of tephra fall deposits: the importance of particle Reynolds number: Jour Volc Geoth Res 81: 173-184.

Fan, L., Mao, Z., Yang, C.,(2004), *Experiment on Settling of Slender Particles with Large Aspect Ratio and Correlation of the Drag Coefficient*, Ind. Eng. Chem. Res. 43, 7664 - 7670.

Haider A., Levenspiel O., *Drag coefficient and terminal velocity of spherical and non-spherical particle*, Power Technology, 58, 1989,63-70.

Herzhaft, B. and Guazzelli E. (1999). *Experimental study of sedimentation of dilute and semi-dilute suspensions of fibres*, J. Fluid Mech, Vol 384, pp133-158.

Hinds, W. C. (1998), *Aerosol Technology properties, behaviour, and measurement of airborne particles*, second Edition, A Wiley-Interscience Publication John Wiley & Sons, INC, New York.

IEA, (2004), *World energy outlook 2004,* International Energy Agency, 2004.

IPCC Working Group I, (2007), *Climate change 2007: the physical science basis,* Chapter 10, Global Climate Projection, IPCC.

Kim, S. and Karrila, S. J., (1991) *Microhydrodynamics: Principle and selected applications*, Butterworth-Heinemann, Boston.

Mayer, (2006), *Investigating the aerodynamics of fibrous particles for application to the combustion of pulverized wood*, Institute of Energy Process Engineering and Fuel Technology, Clausthal University, Germany and School of mechanical Engineering, The University of Adelaide, Australia.

Rosendahl, (1998), *Extending the modelling framework for gas-particle systems, Application of multiparameter shape descriptions to non-conventional solid fuels in reacting and non-reacting environments*, Institute of Energy Technology, Aalborg University, Denmark.

Unnikrishnan, (1990), *Slow paralell motion of cylinder in non-Newtonian media: wall effects and drag coefficient*, Chemical Engineering Process, 28, 121-125.

Wadell, Hakon (1935), *Volume, Shape and Roundness of Quartz Particles*. Journal of Geology **43**: 250–280.

Zhu, F. and Lin, J. Z., (1999), *dynamics of fibrous particles in suspension*, (Chinese version), China Textile Press, Shanghai, China.

8 Aerodynamics of Long Aspect Ratio Fibrous Particles under Settling

Guo Q. Qi, Graham J. Nathan and Richard M. Kelso

School of Mechanical Engineering and Centre for Energy Technology, The University of Adelaide, Adelaide SA 5005 AUSTRALIA

Email: guo.qi@adelaide.edu.au

Proceedings of the ASME/JSME 2011 8th Thermal Engineering Joint Conference, AJTEC2011, March 13–17, 2011, Honolulu, Hawaii, USA

Statement of Authorship

Title of Paper	Aerodynamics of long aspect ratio fibrous particles under settling
Publication Status	☑ Published ☐ Accepted for Publication ☐ Submitted for Publication ☐ Unpublished and Unsubmitted work written in manuscript style
Publication Details	Guo Q. Qi, Graham J. Nathan and Richard M. Kelso. Aerodynamics of long aspect ratio fibrous particles under settling. Proceedings of the ASME/JSME 2011 8th Thermal Engineering Joint Congress AJTEC 2011, Honolulu, Hawaii, USA.

Principal Author

Name of Principal Author (Candidate)	Guo Qiang Qi
Contribution to the Paper	I was responsible for the development of both the measurement technique and analytical model under the principal supervision of Professor Nathan. I performed the measurements and data processing, wrote the first draft of the manuscript and incorporated and addressed all comments and suggestions by other authors and reviewers in subsequent revisions of the manuscript. I acted as corresponding author.
Overall percentage (%)	55%
Certification:	This paper reports on original research I conducted during the period of my Higher Degree by Research candidature and is not subject to any obligations or contractual agreements with a third party that would constrain its inclusion in this thesis. I am the primary author of this paper.
Signature	Date 13/06/2016

Co-Author Contributions

By signing the Statement of Authorship, each author certifies that:

i. the candidate's stated contribution to the publication is accurate (as detailed above);

ii. permission is granted for the candidate in include the publication in the thesis; and

iii. the sum of all co-author contributions is equal to 45% less the candidate's stated contribution.

Name of Co-Author	Graham J. Nathan
Contribution to the Paper	I was principal supervisor for the development of work, contributed to both data interpretation and refining of the manuscript.
Signature	Date 14/6/16

Name of Co-Author	Richard M. Kelso
Contribution to the Paper	I, co-supervisor, jointly supervised the development of work.
Signature	Date 14/6/2016

Please cut and paste additional co-author panels here as required.

Proceedings of the ASME/JSME 2011 8th Thermal Engineering Joint Conference
AJTEC2011
March 13-17, 2011, Honolulu, Hawaii, USA

AJTEC2011-44061

AERODYNAMICS OF LONG ASPECT RATIO FIBROUS PARTICLES UNDER SETTLING

Guo Q. Qi
School of Mechanical Engineering and Centre for Energy Technology, The University of Adelaide
Adelaide, SA 5005, Australia

Graham J. Nathan
School of Mechanical Engineering and Centre for Energy Technology, The University of Adelaide
Adelaide, SA 5005, Australia

Richard M. Kelso
School of Mechanical Engineering and Centre for Energy Technology, The University of Adelaide
Adelaide, SA 5005, Australia

ABSTRACT

In present study, the aerodynamic behaviour of long aspect ratio fibrous particles has been investigated experimentally whilst settling in air under super dilute conditions without any influence of secondary flows and at particle Reynolds numbers of 30-80 based on fibre length. A method for laser-based measurement of the orientations and velocities of fibrous particles is presented. The experimental apparatus employs Particle Tracking Velocimetry (PTV) to calculate orientation and velocity based on the two end-points. Fibres' mean vertical and horizontal components of settling velocities, angular velocity, orientation, number density and drag coefficient were calculated to analyze their aerodynamics.

INTRODUCTION

Fossil fuels, coal, oil and natural gas are not renewable energy sources. At the present rate of consumption, the known reserves of fossil fuels will be depleted in the foreseeable future [1]. Furthermore, fossil fuels emit significant quantities of stored carbon dioxide (CO_2) and also nitrogen oxides (NO_x) when they are burned. Carbon dioxide does not directly impair human health but is a 'greenhouse gas' and does trap the earth's heat and contribute to the potential for global warming. One approach to reduce the use of fossil fuels is partial substitution with biomass, or organic matter, which is a renewable and more environmentally "friendly" resource for energy supply. Such fuels can be derived from trees, agricultural residues and other plants. The percentage of biomass being used is increasing around the world to partially replace fossil fuels [1]. However biomass is fibrous and there is a paucity of data describing the aerodynamics of fibrous particles. In order to increase the efficiency of the combustion of biomass, the aerodynamics of biomass particles needs to be investigated.

The settling motion of a particle is a basic class of its motion. The settling motion of a fibrous particle is much more complex, and more poorly understood, than that of a sphere. A sphere settles in a purely vertical direction. However for a fibrous particle, the instantaneous horizontal drift cannot be neglected. A fibrous particle also exhibits rotation. A large number of previous investigations have studied the hydrodynamics of fibres under the conditions of relevance to the paper making industry. Theoretical treatments include the slender body theory [2] and the concentration instability [3]. Experimental investigations include that of Metzger et al (2006) [4], Herzhaft and Guazzelli (1999) [5], Salmela, et al (2007) [6], Herzhaft and Guazzelli (1996) [7]. Previous numerical investigations were performed by Butler and Shaqfeh (2002) [8], Kuusela et al (2003) [9], Kuusela, et al (2001) [10], Saintillan et al (2004) [11], Tornberg and Gustavsson (2005) [12], Shin et al (2006) [13]. Previous investigations to study the drag coefficient of fibrous particles were performed by Gabitto and Tsouris (2007) [14], Fan et al (2004) [15], McKay et al (1988) [16], Unnikrishnan and Chhabra (1991) [17], Haider and Levenspiel (1988) [18], and so on. However, none of these investigations provides detailed measurements of bulk settling fibrous particles in the range of $10 < Re_L < 100$.

Koch and Shaqfeh (1989) [3] theoretically studied the instability of a dispersion of sedimenting spheroids and pointed out that hydrodynamic interactions between sedimenting fibres give rise to an increase in the number of neighboring particles in the vicinity of any given particle. They suggested that the suspension is unstable to particle number density fluctuations. They also argued that the convective motion (cluster formation) may lead to an average sedimentation velocity which is larger than the maximum possible value for a particle in a quiescent

fluid. This theory can be verified by accurate measurements of settling velocity and orientation of fibres.

Clift et al (1978) [19] reported that for a single fibrous particle Reynolds number $Re_d > 0.01$, a cylinder falls with its axis oriented horizontally and exhibits steady motion with this orientation up to Re_d of order 100. However this is yet to be extended to a cloud of interacting particles in a suspension. Salmela et al (2007) [6] experimentally studied settling of dilute and semi-dilute fibres suspensions for $0.0003 < Re_L < 9$. At $Re_L \sim O(1)$, for small volume fractions $\Phi < 0.0005$ they found that fibres settle with their long-axis preferentially in the horizontal state and the settling velocity and the fluctuation of settling velocity increases with Φ. They also found that the steady-state settling velocity has a maximum that exceeds the velocity of an isolated particle because of a change in average orientation of the fibres from horizontal to vertical. With $\Phi > 0.0005$, fibres settle preferentially with their long-axis aligned in the direction of gravity, i.e. the average orientation gradually changes from horizontal state to vertical. However for a bulk settling of fibres of $Re_L \sim O(10)$ and $Re_L \sim O(100)$, no similar investigations seem to be available.

Kuusela et al (2003) [9] simulated the settling of spheroids under steady state sedimentation at $0.5 < Re_L < 3.5$. They found an orientational transition of the spheroids characterized by enhanced density fluctuations. They predicted the orientation distribution that arises from a competition between inertial forces acting on individual particles and hydrodynamic interactions between particles. For super dilute systems, inertia rotates the fibres to horizontal position whereas in sufficiently concentrated systems the interactions tend to align the fibres with gravity. Around the transition from a horizontal to vertical orientation, the mean settling velocity increases with increasing of Φ to a maximum that may even exceed the terminal settling velocity of a single spheroid. This accords with the experimental results of Salmela et al (2007) [6]. However like the work of Salmela et al (2007) [6], the Re_L of this investigation was limited to less than 3.5.

Herzhaft and Guazzelli (1999) [5] and Metzger et al (2006) [4] experimentally investigated sedimenting suspensions of fibres with $Re_L \approx 0.0001$. For this case, the inertia acting on the fibrous particles approaches zero, causing the fibres to tend to align in the direction of gravity for dilute and semi-dilute suspensions. This contrasts the case of $Re_L \sim O(1)$ where fibre orientations are horizontal. Herzhaft and Guazzelli (1999) [5] pointed out their experiment demonstrates the existence of an instability but could not confirm whether the argument of Koch and Shaqfeh (1989) [3] is correct. Although this is different regime compared with Salmela et al (2007) [6], Herzhaft and Guazzelli (1999) [5] also found in their experiment that the settling velocity can be larger than the Stokes' velocity of an isolated vertical fibre in dilute suspension. Further with increasing volume fraction, the fluctuation of settling velocity and fibres' orientation anisotropy were found to increase. The cause of this similarity deserves further investigation.

Butler and Shaqfeh (2002) [8] performed a numerical simulation of inhomogeneous sedimentation of rigid fibres in the limit of zero of Re_L. The simulation revealed that the steady settling velocity increases with increasing of number density of fibrous particles simulated in the dilute regime. The prediction of orientation distribution agreed with the experimental result of Herzhaft and Guazzelli (1999) [5], i.e. the particles have a most probable orientation that is close to vertical. Furthermore the simulation showed that the orientation of fibrous particles tend to be more vertical with increasing of number density in the dilute regime. However this assessment is yet to be extended to high Reynolds number.

Fan et al (2004) [15] experimentally studied the relationship between drag coefficient (C_D) of slender particles with large aspect ratio and Re_d. They proposed following equation to calculate drag coefficient, which needs to be assessed.

$$C_D = \frac{1}{\sin\theta}\left(\frac{\rho_{fp}}{\rho_f}\right)^{-1.537}\left[\frac{d^3(\rho_{fp}-\rho_f)^2 g}{\mu^2}\right]^{0.8524}\frac{24}{\mathrm{Re}_d}\left(0.006983+0.6224\mathrm{Re}_d^{-1.046}\right) \quad (1)$$

Here θ is orientation of the fibre which is the angle between major axis of the fibre and direction of the gravity; ρ_{fp} and ρ_f are fibre and fluid density respectively; d is diameter of the fibre and μ is viscosity of fluid; Re_d is fibre's Reynolds number based on d.

In the light of the previous investigations described above, we seek to further the understanding of the aerodynamics of settling fibrous particles in the range of $Re_L = 30 - 80$, with a high density ratio of particle to fluid and no boundary limitation. Therefore, the first aim of present work is to develop a novel method to measure the velocity and orientation of a fibrous particle simultaneously. The second aim is to employ this method to obtain the relationship (equations) between a fibre's number density and its settling velocity in super dilute regime. The third aim is to investigate the aerodynamics of these fibres, such as its angular velocity, the relationship between settling velocity and orientation and drag coefficient.

NOMENCLATURE

L	length of a fibrous particle
d	diameter of a fibrous particle
$\mathrm{Re_L}$	Reynolds number of a fibre based on L
$\mathrm{Re_d}$	Reynolds number of a fibre based on d
ω	angular velocity of a fibre
ε	straightness of a fibrous particle
θ	orientation of a fibrous particle
V_{cx}	centroid vertical velocity of a fibrous particle
V_{cy}	centroid horizontal velocity of a fibre
Φ	volume fraction of fibrous particles
V_{e1x}	endpoint 1 velocity along x axis of a fibre
μ	viscosity of fluid
V_{e1y}	velocity of endpoint 1 of a fibre along y axis

EXPERIMENTAL APPARATUS

Property of the fibres

The particles used in the experiments are nylon fibres whose properties are shown in Table 1. A micrograph of a sample of the fibres is shown in Fig.1, at a resolution of 18 μm/pixel. It can be seen that they are of constant diameter and, while many are straight, a significant number have a slight bend.

Table 1 nylon fibres used in the experiments

Length, L, μm	2,000
Diameter, d, μm	49.6
Density, ρ_{fp}, kg/m^3	1,150
Aspect ratio, L/d	40
Material	Nylon
Denier	20

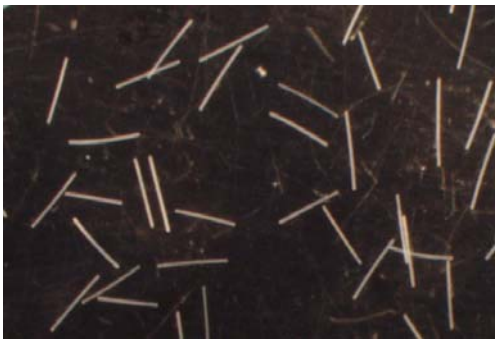

Fig. 1 A micrograph of the sample of nylon fibres.

The length of each fibrous particle (i.e. the major axis) is defined as the maximum distance between any two pixels in the object. This distance is measured from an optical image converted to binary form (see Fig. 2). The minor axis is defined to be perpendicular to the major axis and the rectangle defined by the two axes can enclose the perimeter of the region. This rectangle we call the "basic rectangle" [20]. The concept of a basic rectangle can also be used to define fibrous particle's straightness, as shown in Eq. (2).

$$\varepsilon = 1 - \frac{\delta - d_i}{L_i} \qquad (2)$$

where ε is straightness of a fibrous particle; δ is minor axis of the basic rectangle on a binary image; d_i and L_i is the diameter and length of the fibre respectively on the binary image and the subscript " i " refers to "image". If a fibre's straightness tends toward unity, the fibre approaches being straight.

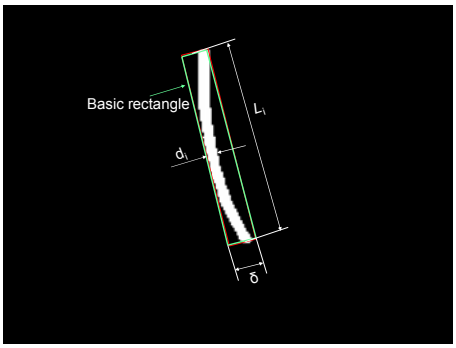

Fig. 2 A binary image of a fibre and its "basic rectangle" used to define its characteristic dimensions.

Fig. 3 presents the distribution of the straightness of the fibrous particles based on a sample size of 1,139. It can be seen that 90.1% of these fibres have straightness ε > 0.85 and some 38% are perfectly straight.

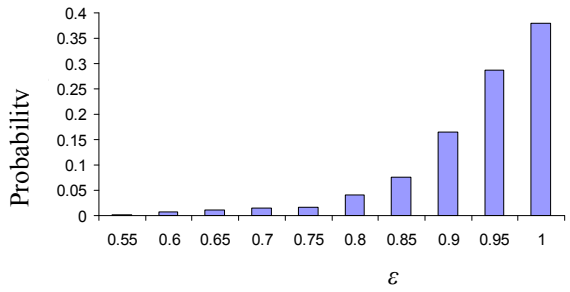

Fig. 3 The distribution of fibre's straightness, ε (see Eq. 2)

Fig. 4 presents the distribution of the fibres length, L, which were measured directly from the two endpoints. It can be seen that 82% of fibres have a length between 1,900 and 2,100 μm and over 95% between 1,800 and 2,200 μm, with a standard deviation of 196μm.

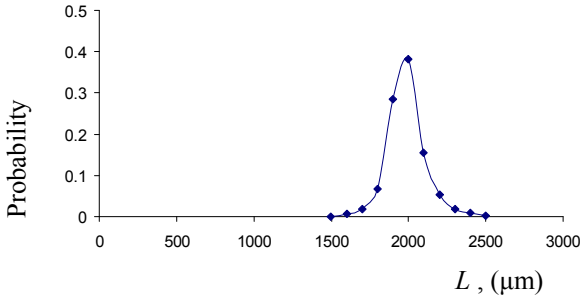

Fig. 4 The distribution of the length, L, of fibres

Measurement techniques

Fig. 5 presents a schematic diagram of experimental apparatus. To avoid any influence of electrostatics, the pipe was earthed. The experimental method employed a typical Particle Tracking Velocimetry (PTV) technique. The laser was operated

in a pulsed mode and the camera in a two-frame mode. The laser sheet was formed by telescopic and diverging lenses. The settling fibrous particles were illuminated by the laser sheet at regular intervals of time and the CCD camera used to record two images of the fibres separated by a delay of about 2.5 ms. The oscilloscope and delay generator were employed in the experiments. The oscilloscope was used to monitor and validate the time separation chosen for the experiments. A DG-535 delay generator was employed to trigger both the laser flash-lamps and the camera. The laser used in the experiments was a Quantel Brilliant Twins double-cavity pulsed Nd: YAG 10 Hz laser, frequency doubled to provide a wavelength of 532nm. The output energy of laser head was set to provide either 250 mJ/pulse or 400 mJ/pulse. The camera was a Kodak MegaPlus ES1.0 with a CCD array of 1008pixels × 1018pixels. The resolution was around 26 μm/pixel and the viewing area was 26mm× 26 mm. Xcap software was used as the operating system.

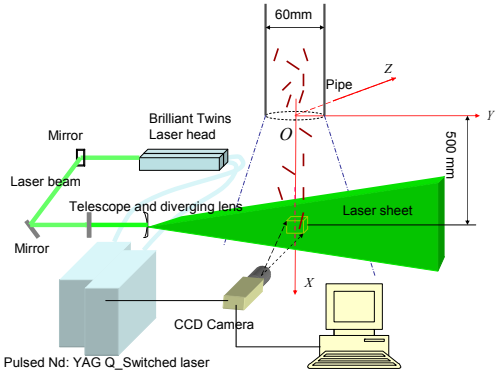

Fig. 5 Experimental arrangement (not to scale). The surrounding settling chamber is not shown for clarity

The settling chamber was of nominally square cross section with a 650mm × 620mm, height of 2,000mm and was made of Perspex. The fibrous particles were introduced into the top of the chamber and settled over a distance of 2.5-3.0m through a 2,000 mm long pipe of 60mm diameter. Not only did this ensure sufficient length to reach their terminal settling velocities before entering the chamber, it also ensured that any background currents induced by the particles in the chamber were negligible. With a volume fraction of order of 10^{-5}, and cross sectional area of the "jet" of falling particles to the chamber of the order 10^{-2}, any induced chamber flows will be at most 1% that of the particles, which is within experimental error. This neglect ensured the dilute phase was not influenced by any chamber currents in contrast to previous investigations. Also fibres settling velocities were measured by changing settling distances of 2.5m and 3.0m. The mean settling velocities obtained were same, so it showed that the fibres have reached their terminal settling velocities and steady state conditions. The system can also accommodate spherical particles under identical conditions. This allows direct comparisons to be performed between spherical particles and fibrous particles.

The intensity distribution of laser sheet is nearly Gaussian, as shown in Fig. 6. This property is exploited to determine whether a fibre is fully or partly within the light sheet, as described below. The thickness of the laser sheet was chosen to be around 5mm to provide good illumination of entire particles.

Number density, orientation and velocity measurement

In the present study, we define the volume fraction of fibrous particles as:

$$\phi = \frac{n_p \pi (d/2)^2 L}{1008 \times 1018 R^2 H} \qquad (3)$$

where n_p is the number of fibrous particles in viewing volume, R is the magnification of camera image system, H is the thickness of laser sheet and $1008 \times 1018 R^2 H$ is the viewing volume.

The present experiments were controlled to be in the range of $\Phi \leq 0.0001$, which is a super dilute condition, so that there were few particles which exhibited clumping. Hence the number density of fibrous particle in the viewing area (volume) was calculated by counting the number of particles, and the volume fraction was computed exactly. The volume fractions were also binned by the number of particles to obtain the influence of particle number density on the fibres' aerodynamic behaviour statistically.

The coordinates of two endpoints of each object (fibrous particle) were obtained. Since the lengths L of these fibres are constant, the spatial orientation θ (the angle between the X axis and the major axis of the fibrous particle) of fibres was calculated by following trigonometric function (Fig. 6):

$$\theta = (\arccos \frac{|x_{e2} - x_{e1}|R}{L}) \times (\frac{180}{\pi}) \quad (°), \qquad (4)$$

where x_{e2} and x_{e1} are coordinates of X values of two endpoints.

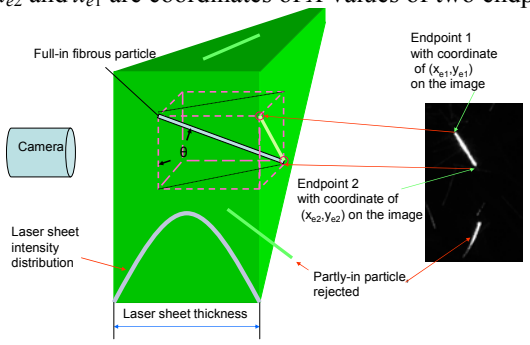

Fig. 6 Schematic diagram of the orientation measurement, the detection of "part-in" fibres and key notation

Any fibres that are only partly in the laser sheet will give a false calculation of the projected length and the coordinates of endpoints, so must be rejected. This can be achieved by

comparing the intensities of the signal at two endpoints of the fibre. Because of the Gaussian light sheet intensity distribution a partly-in fibrous particle will exhibit a significant difference between the intensity values of the two endpoints (Fig. 6). This is used to reject such particles as described in section of image processing.

The coordinate system used in the calculation is Cartesian, with the x axis directed downwards in the direction of gravity. We define the two endpoint velocities of the fibrous particle as $\boldsymbol{V}_{e1}$ and $\boldsymbol{V}_{e2}$. Each endpoint velocity has three components $\boldsymbol{V}_{e1x}$, $\boldsymbol{V}_{e1y}$, $\boldsymbol{V}_{e1z}$ and $\boldsymbol{V}_{e2x}$,$\boldsymbol{V}_{e2y}$,$\boldsymbol{V}_{e2z}$, as shown in Fig. 7 and Eq. (5).

$$\vec{V}_{e1}=\vec{V}_{e1x}+\vec{V}_{e1y}+\vec{V}_{e1z}$$
$$\vec{V}_{e2}=\vec{V}_{e2x}+\vec{V}_{e2y}+\vec{V}_{e2z} \qquad (5)$$

Based on Eq. (5), we define V_{e1x} and V_{e2x} as vertical components of the settling velocity of the endpoints 1 and 2 respectively of the fibrous particle. Similarly V_{e1y} and V_{e2y} are the horizontal components of settling velocity of endpoints 1 and 2 of the fibrous particle respectively.

Image pairs were recoded by the digital camera with a known time separation (Δt). After image processing the displacements of two endpoints of fibrous particles along the x and y axis can be obtained. From this $\boldsymbol{V}_{e1x}$, $\boldsymbol{V}_{e1y}$ and $\boldsymbol{V}_{e2x}$, $\boldsymbol{V}_{e2y}$ can be calculated by Eq. (6), as follows:

$$V_{e1x}=\frac{(x_{e12}-x_{e11})R}{\Delta t} \qquad V_{e1y}=\frac{(y_{e12}-y_{e11})R}{\Delta t}$$
$$V_{e2x}=\frac{(x_{e22}-x_{e21})R}{\Delta t} \quad V_{e2y}=\frac{(y_{e22}-y_{e21})R}{\Delta t} \qquad (6)$$

where V_{e1x} is the velocity of endpoint 1 in the X direction; V_{e1y} is the velocity of endpoint 1 in the Y direction; V_{e2x} is the velocity of endpoint 2 in the X direction; V_{e2y} is the velocity of endpoint 2 in the Y direction; x_{e12} is X axis coordinate of endpoint 1 from the second image, x_{e11} is X axis coordinate of the endpoint 1from the first image; y_{e12} is Y axis coordinate of the endpoint 1 from the second image and so on.

Fig. 7 shows the definition of settling velocity of centroid of a fibrous particle. The velocity of the centroid of a fibre V_c is defined by Eq. (7):

$$\vec{V}_{c}=\vec{V}_{cx}+\vec{V}_{cy}+\vec{V}_{cz}$$
$$V_{cx}=\frac{1}{2}(V_{e1x}+V_{e2x}) \qquad (7)$$
$$V_{cy}=\frac{1}{2}(V_{e1y}+V_{e2y})$$
$$V_{cz}=\frac{1}{2}(V_{e1z}+V_{e2z})$$

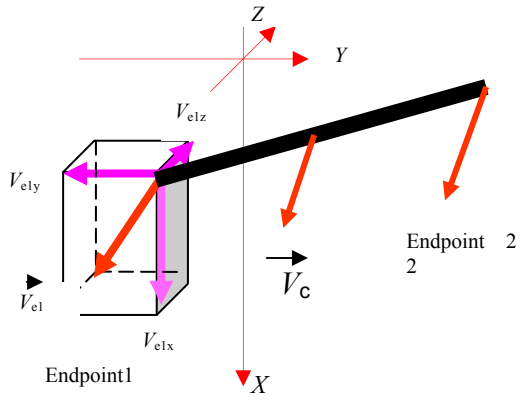

Fig. 7 Two endpoint and centroid velocities of a fibre.

In present study, V_{cx} and V_{cy} represent vertical and horizontal components of settling velocities of a fibrous particle respectively. Since data are obtained from an image pair, the orientation of a fibrous particle equals the average orientation of the fibre from the first and second images:

$$\theta=\frac{1}{2}(\theta_1+\theta_2)$$

So $$\theta=(\arccos\frac{(x_{e21}-x_{e11})R}{L}+\arccos\frac{(x_{e22}-x_{e12})R}{L})\times(\frac{90^{\circ}}{\pi}) \qquad (8)$$

IMAGE PROCESSING

The purpose of the image processing is to extract measurements for each particle using Eqs. (7) and (8) and to thus allow the aerodynamic behaviour of the fibrous particle to be assessed statistically under various conditions. From the coordinates of two endpoints it is possible to calculate the orientation and velocities of a fibre.

Those fibrous particles located at the edges of an image yield a false measurement of its length. Therefore first step of image processing is to remove these fibrous particles from the images. The second step is to convert the image into binary form. The third step is to remove small objects. Binary images typically contain “noise” which comprises spurious signal in one or two isolated pixels. They are not real fibrous particles and so need to be removed. The fourth step is to label the fibres. This is a very important and useful step in images processing. By using this tool the background pixels were labeled 0. The pixels that made up the first object were labeled 1, (see Fig. 8) those labeled 2, the second object, and so on. If there were n particles in the viewing volume the last pixels (object) would be labeled n. Therefore this tool can be used to count the number of fibres in the image exactly.

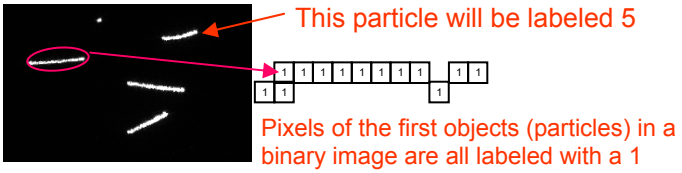

Fig. 8 Step 4--labeling pixels of fibrous particles in a binary image.

The fifth step is removing fibrous particles "partly-in" the laser sheet. As previously noted, the measured lengths of such fibrous particles are false. Therefore these part-in fibres must also be removed from the images when processing. Fig. 6 displays the different characteristics of full-in and part-in fibrous particles. For a "full-in" fibrous particle, the intensity along the major axis of the fibre is nearly constant while for a part-in one, the intensity at the two endpoints differs significantly (Fig. 9). Hence it is possible to discriminate by either comparing the intensity of two endpoints of the fibre, or by comparing the standard deviation of intensity along the major axis. If the standard deviation is less than the threshold, it is a full-in fibrous particle.

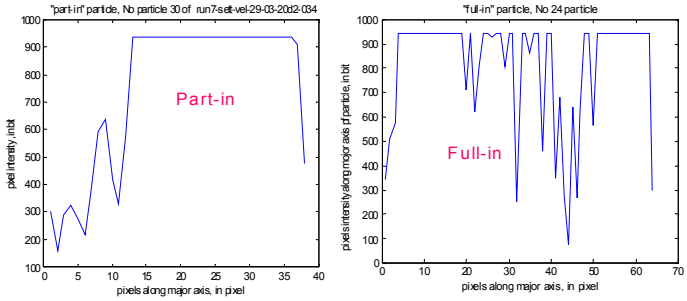

Fig. 9 The distributions of intensity along major axis for part-in and full-in fibrous particles in the laser sheet.

The last step is tracking particles and calculating velocities and orientations. Fig. 10 presents a pair of images of fibres with a known time separation of 2,500 μs. The red circles highlight those fibrous particles that are pairs. It can be seen that if the time separation is short enough, any changes in fibre's length is small, orientation and area are small. Based on these characteristics on the images, tracking particles (matching pairs) becomes easier than for spherical particles.

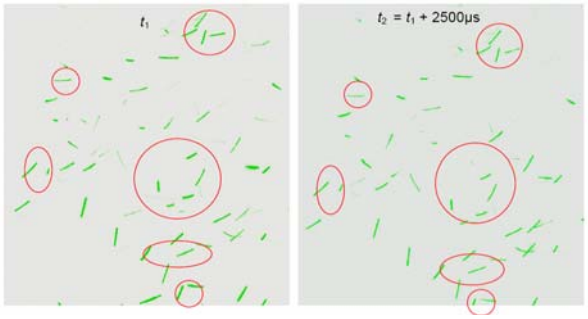

Fig. 10 A pair of images of fibres with a known time separation of 2,500 μs. Sets of obviously matching pairs are encircled.

The accurate matching of pairs of fibrous particles within a known time separation is a most important step in image processing. From this, the vertical and horizontal displacements of each particle can be obtained, and hence the vertical and horizontal components of settling velocities can be calculated. After collecting of the two endpoint's coordinates and matching particle pairs in each pair of images, all components of settling velocities (translational and rotational) of the centroid and orientation of a fibrous particle can be obtained from Eqs. (6), (7) and (8).

EXPERIMENTAL RESULTS AND DISCUSSIONS

Influences of volume fraction on vertical component of settling velocity of fibrous particles

Fig. 11 presents the relationship between volume fraction (Φ) and the mean vertical component of settling velocity ($\overline{V_{cx}}$) under the condition of low number density ($0.1\times 10^{-5} - 10 \times 10^{-5}$). It can be seen that $\overline{V_{cx}}$ increases monotonically with Φ. Furthermore the scatter in the data also increases with Φ. Eq. (9) is proposed to describe relationship between the number density and the vertical component of settling velocity for the dilute regime.

$$\frac{\overline{V}_{cx}(\phi)}{\overline{V}_{ts}} = a\phi^n \qquad (9)$$

where $\overline{V}_{ts}$ is average terminal settling velocity of a isolated single fibre; a and n are "constants" that are expected to depend on the fibre's aspect ratio and Reynolds number; The constants in Eq. (9) for the present fibres are: $\overline{V_{ts}}$=0.375, a=7.310 and n=0.1519. That is

$$\overline{V}_{cx}(\phi) = 2.743\phi^{0.1519} \qquad (10)$$

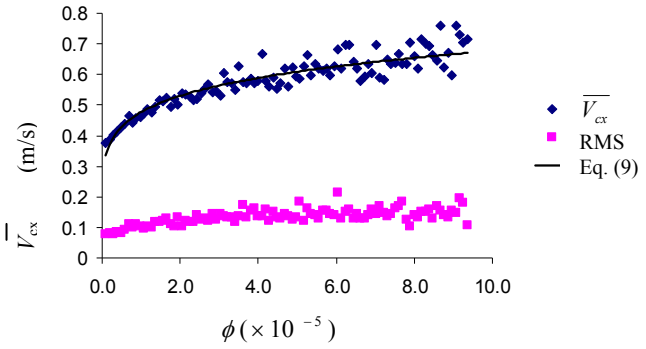

Fig.11 The relationships between Φ and $\overline{V_{cx}}$ of fibrous particles when settling in air.

The data point corresponding to the lowest volume fraction in Fig. 11 represents the case of one isolated particle per image. This case represents the minimum of $\overline{V_{cx}}$ (terminal settling velocity of an isolated fibre), with all other values of $\overline{V_{cx}}$ exceeding it in Φ=0.1× 10^{-5} – 10 × 10^{-5} regime.

Fig. 12 and Table 2 present the dimensionless comparisons between present work (Fig.11) and previous work on logarithmic axes. It is clear that the present data is consistent with the trends in previous measurements, although previous work provides insufficient detail to estimate the constants in Eqs (9) and (10). Table 2 compares present experimental conditions with those assessed previously. It is clear that there are substantial differences especially in Reynolds number and density ratio, but also in aspect ratio and confinement for some cases. The present work represents the first detailed assessment of this influence in the dilute regime.

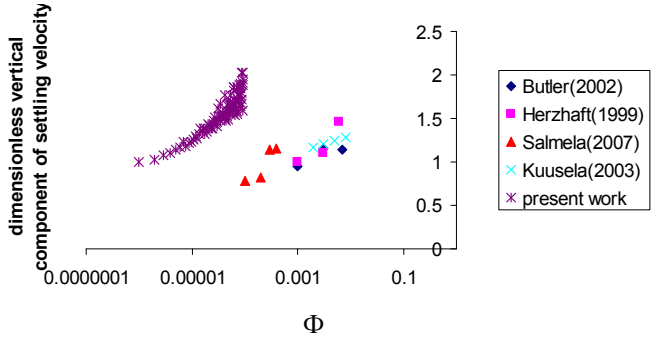

Fig.12 A comparison between present work and previous work.

Table 2 dimensionless comparisons between present and previous work

Authors	Re_L	L/d	ρ_{fp} /ρ_f	Chamber width/L
Butler and Shaqfeh (2002)	0.00001	11		
Herzhaft and Guazzelli (1999)	0.0001	11	2.1	11.7
Salmela et al (2007)	0.07	23	2.62	20
Kuusela et al (2003)	1.5	3	2.5	32
Present work	30 - 80	40	958	310

Eqs. (9), (10) provides a good description of the relationship between Φ and $\overline{V_{cx}}$ for the present case based on 98 data points in super dilute regime. However more data is required under other conditions to assess its generality.

Influences of volume fraction on orientation of fibrous particles

Fig. 13 presents the relationship between the Φ and mean orientation ($\overline{\theta}$). It can be seen $\overline{\theta}$ decreases with Φ, i.e. the fibrous particles tend to become more horizontal with decreasing Φ. These data can also be described by a power relationship, Eq. (11):

$$\overline{\theta}(\phi) = \frac{b}{\phi^n}\overline{\theta}_{ts} \quad (^\circ), \tag{11}$$

where b is a constant and $\overline{\theta_{ts}}$ is average orientation of a single fibre when settling in air. In the above case, $\overline{\theta_{ts}}$ =81.383° and n=0.0654, b=0.428. This result can explain why the value of $\overline{V_{cx}}$ increases with the increasing of Φ. An increase in Φ causes the fibre's major axis to tend to be more vertical, causing $\overline{V_{cx}}$ to increase, due to increased aerodynamic interaction between particles.

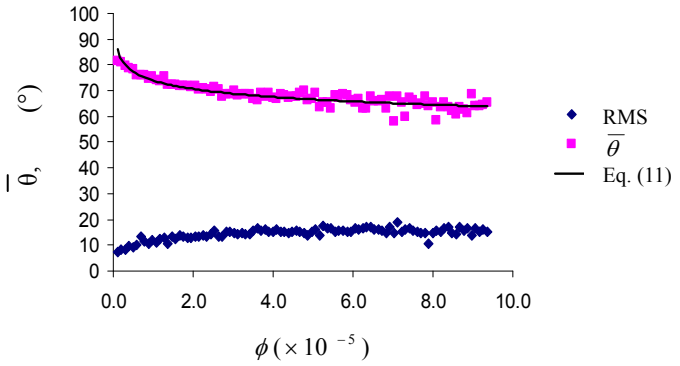

Fig. 13 The relationship between $\overline{\theta}$ and Φ.

Fig. 14 compares the present measurements of orientation with previous work. From the Figure we can see, in all cases,

orientation of the fibrous particle tend to become more vertical with increasing Φ.

Based on magnitude of Re_L (see Fig. 14), present work belong to $Re_L \sim O(10)$; and Salmela (2007) [6] and Kuusela (2003) [9] belong to $Re_L \sim O(1)$; Herzhaft (1999) [5] and Butler(2002) [8] belong to $Re_L \sim O(0)$. From the Figure it can be seen that there are some difference in range of orientation transition under the three orders of Re_L regimes. When $Re_L \sim O(10)$, with increase of Φ, settling fibres' orientation transition become from about 85° to 55°. That is, the settling fibres orientation become from horizontal state to less horizontal. When $Re_L \sim O(1)$, the settling fibres orientation become from less horizontal state to nearly vertical (65° - 45°). And when $Re_L \sim O(0)$, the settling fibres orientation become from nearly vertical state to more vertical (45° - 25°). This agreed with Kuusela (2003) [9] which horizontal alignment is proportional to Reynolds number.

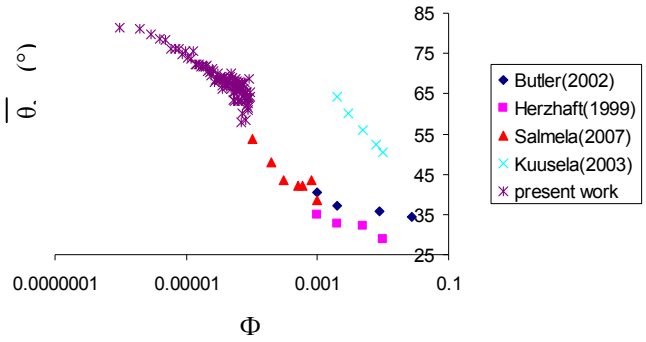

Fig. 14 A comparison of present and previous orientation measurements.

Influences of volume fraction on horizontal component of settling velocity of fibrous particles

Fig. 15 presents the relationship between mean horizontal component of settling velocity $\overline{V_{cy}}$ and Φ. It can be seen that $\overline{V_{cy}}$ is zero on average and the fluctuation of $\overline{V_{cy}}$ increases monotonically with Φ. The RMS is well characterized by a power law as follows:

$$\text{RMS of } \overline{V_{cy}} = 0.0167\, \Phi^{0.2495} \qquad (12)$$

The fluctuation of $\overline{V_{cy}}$ in directions indicates the trajectories of settling fibres are "S" form, which agreed with Brauer (1971). The aerodynamic interaction increases the value of $\overline{V_{cy}}$. This also agreed with Salmela (2007) who found the variance to linearly increase with Φ.

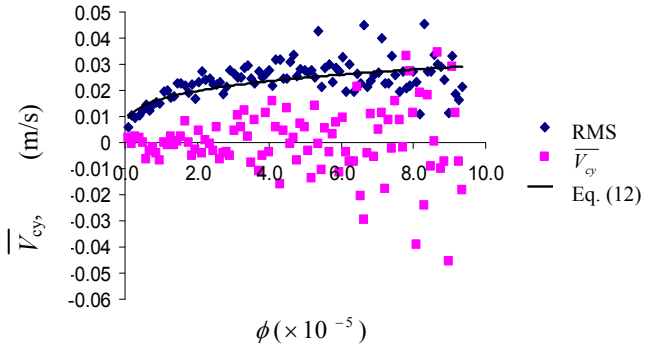

Fig. 15 The relationship between $\overline{V_{cy}}$ and Φ.

Influences of volume fraction on angular velocity component of fibrous particles

Because a fibre's elevation and azimuth can be measured between Δt, the ω of elevation and azimuth can be calculated. Fig. 16a and 16b presents the relationship between mean angular velocities $\overline{\omega_{ele}}, \overline{\omega_{azi}}$ and Φ. It can be seen that $\overline{\omega_{ele}}, \overline{\omega_{azi}}$ are near zero and fluctuation of $\overline{\omega_{ele}}, \overline{\omega_{azi}}$ increases with Φ. It can also be seen that the RMS of $\overline{\omega_{ele}}, \overline{\omega_{azi}}$ have the tendency to increase with Φ. However a small percentage of fibres have a rotational speed of zero and the range of speeds also increases with Φ. It indicates fibres' aerodynamic interactions influence rotations magnitude and "S" trajectories influence rotation's directions.

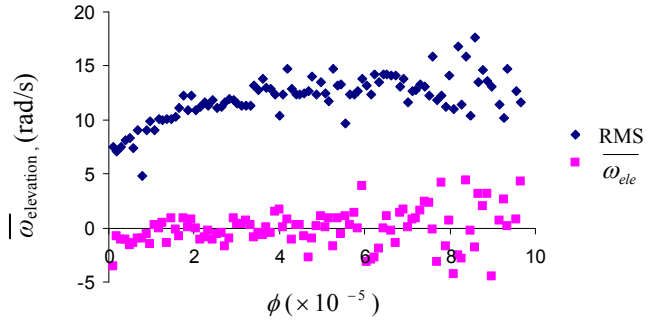

Fig. 16a The relationship between $\overline{\omega_{ele}}$ and Φ.

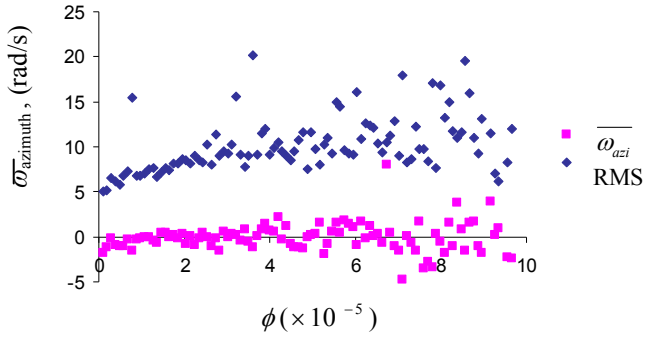

Fig. 16b The relationship between $\overline{\omega_{azi}}$ and Φ.

Velocity and orientation distribution

Fig. 17 presents distribution of V_{cx} obtained from 29,364 samples. It can be seen the mean velocity is about 0.75m/s with a skewness of 0.76 and kurtosis of -0.97.

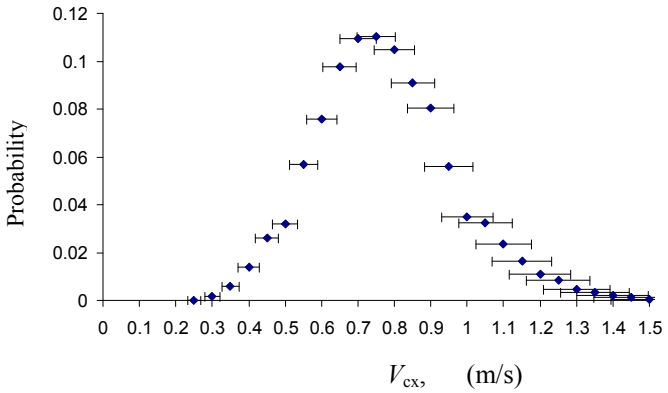

Fig.17 The distribution of V_{cx}

Fig. 17 indicates that there is no fundamental difference in the aerodynamic behaviour associated with the variation in straightness (Fig. 3). Specifically no bimodality is evident, suggesting that no bi-modal distribution. The presence of a slight curve may increase the scatter in the velocity distribution but does not result in any fundamental change in aerodynamic behaviour. However no comparable data is available against which to provide a quantitative assessment of the effect.

The motions of rotation, tumbling and swaying observed when fibrous particles settle in air induce a horizontal component of motion for fibres that does not occur with spherical particles. Fig. 19 shows the distribution of V_{cy} obtained from a sample size of 29,364. It can be seen that $\overline{V_{cy}}$ is nearly zero. The standard deviation of distribution of V_{cy} is 0.07 which is approximately 9% of $\overline{V_{cx}}$.

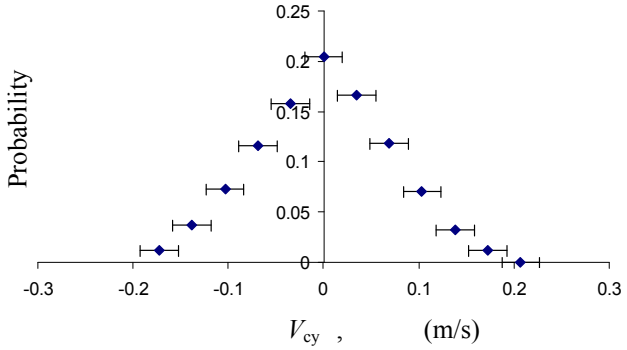

Fig. 18 The distribution of V_{cy}

Fig. 19 shows orientation distribution of fibrous particles over the range of a volume fraction, $1.5\times10^{-5} < \Phi < 8.5\times10^{-4}$. It can be seen the majority of fibres are nearly horizontal. This agrees with Clift et al (1978) [19] for a cylinder falling with its axis horizontal for $Re_d > 0.01$. Kuusela et al (2003) [9] argued for $Re_L \sim O(1)$ sufficient torque is generated to change a fibre's orientation to horizontal.

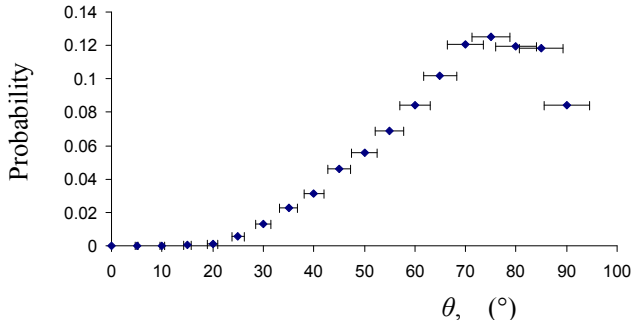

Fig. 19 Orientation distribution of the present fibrous particles.

Drag coefficient C_D of a fibre

When settling in steady motion, the fibre's projected area in vertical direction $A = dL\sin\theta + \pi(d/2)^2\cos\theta$, so we can experimentally measure C_D by Eq. (13):

$$C_D = \frac{F_D}{\frac{1}{2}\rho_{air}V_{ts}^{\ 2}A} = \frac{\rho_{fp}\pi(\frac{d}{2})^2 Lg}{\frac{1}{2}\rho_{air}V_{ts}^{\ 2}(dL\ \sin\ \theta + \pi(\frac{d}{2})^2\ \cos\ \theta)} \qquad (13)$$

In order to assess the models proposed by Fan et al (2004) [15] and Clift et al (1978) [19], diameter, d, of the fibre was introduced as a characteristic length in Fig. 20. And the present work of curve fitting is $C_D = 8.1(\mathrm{Re}_d)^{-1.97}$. From the Figure we can see the two models do not describe the behaviour of present particles. For Fan's model, refer to Eq. (1), the term of $(\rho_{fp}/\rho_f)^{-1.537}$ plays an important role when ρ_{fp} is far greater than ρ_f. For present case $\rho_{fp}/\rho_f = 958$, it predicts C_D far less than the present values. So it seems this model does not suit fibre-gas two-phase flow. For Clift's model $C_D = 9.689(\mathrm{Re}_d)^{-0.78} + 1.42(\mathrm{Re}_d)^{0.04}$ $(0.1 < Re_d < 5)$, the power

of -0.78 is far greater than -2, so its slope is much lower than that of the present fibres.

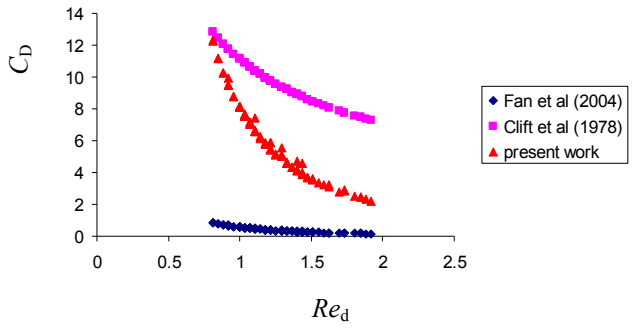

Fig. 20 The relationship of Re_d and C_D between present and Fan's and Clift's work

CONCLUSIONS

In this work, we measured settling fibres' vertical and horizontal components of settling velocities, angular velocity, orientation and drag coefficient in air with $Re_L \sim O$ (10) for volume fractions less than 8.5×10^{-4}. We show that all the mean steady state settling velocities of fibres exceeded the mean terminal settling velocity of a single fibre under $\Phi \leq 10^{-4}$. This phenomenon is attributed to fibres' orientation transition from horizontal state to vertical under super dilute regime that stems from increasing aerodynamic interactions between fibres. Also the fluctuations of the horizontal components of settling velocities and angular velocities of settling fibres were found to increase with Φ. The fibres orientation exhibits more horizontal than that with $Re_L \sim O$ (1). Finally we find that these results qualitatively support the work of Kuusela et al (2003)[9].

ACKNOWLEDGMENTS

This study has been supported by the Faculty of Engineering, Computer & Mathematical Science of The University of Adelaide and by an ARC Discovery Grant, both of which are gratefully acknowledged.

REFERENCES

[1] AEBRE, (2006), Australian energy national and states projections to 2029-30, abare research report 06.26, 26.

[2] G. Batchelor (1970), Slender-body theory for particles of arbitrary cross-section in Stokes flow, Journal of Fluid Mechanics, Vol 44, part 3, 419-440.

[3] D. Koch and E. Shaqfeh (1989), The instability of a dispersion of sedimenting spheroids, Journal of Fluid Mechanics, Vol 209, 521-542.

[4] Metzger, Butler and Guazzelli, (2006), Experimental investigation of the instability of a sedimenting suspension of fibre, Journal of Fluid Mechanics Vol 575, 307-332.

[5] Herzhaft, B. and Guazzelli E. (1999). Experimental study of sedimentation of dilute and semi-dilute suspensions of fibres, J. Fluid Mech, Vol 384, pp133-158.

[6] J. Salmela, D. Martinez and M. Kataja (2007), Settling of dilute and semidilute fiber suspensions at finite Re, AIChE Journal, Vol.53, No.8

[7] B. Herzhaft and E. Guazzelli (1996) , M. Mackaplow and E. Shaqfeh (1996), Experimental investigation of sedimentation of a dilute fiber suspension, Physical Review Letters, Vol. 77 No. 2

[8] J. Butler and E. Shaqfeh (2002), Dynamic simulation of the inhomogeneous sedimentation of rigid fibres, J. Fluid Mech, Vol.468, pp205-237

[9] Kuusela, E. and Lahtinen, J. (2003) Collective effects in settling of spheroids under steady-state sedimentation, Physical review letter, vol 90 No 9.

[10] E. Kuusela, K. Hofler and S. Schwarzer (2001), Computation of particle settling speed and orientation distribution in suspensions of prolate spheroids, J. Engineering Mathematics, 41: 221-235.

[11] D. Saintillan, E. Darve and E. Shaqfeh (2004), dynamic simulation of the instability of sedimenting fibers, XXIICTAM, Warsaw, Poland.

[12] A. Tornberg and K. Gustavsson (2005), A numerical method for simulations of rigid fiber suspensions, J. Computational Physics, 215, 172-196.

[13] M. Shin, D. Koch and G. Subramanian (2006), A pseudospectral method to evaluate the fluid velocity produced by an array of translating slender fibers, Physics of Fluids 18, 063301.

[14] J. Gabitto and C. Tsouris (2008), Drag coefficient and settling velocity for particles of cylindrical shape, Powder Technology 183, 314-322

[15] Fan, L., Mao, Z., Yang, C.,(2004), Experiment on Settling of Slender Particles with Large Aspect Ratio and Correlation of the Drag Coefficient, Ind. Eng. Chem. Res. 43, 7664 - 7670.

[16] G. McKay, W. Murphy and M. Hillis (1988), Settling characteristics of discs and cylinders, Chem Eng Res Des, Vol. 66

[17] A. Unnikrishnan and R. Chhabra (1991), An experimental study of motion of cylinders in Newtonian fluids: wall effects and drag coefficient, the Canadian Journal of Chemical Engineering, Vol. 69

[18] A. Haider and O.Levenspiel (1989), Drag coefficient and terminal velocity of spherical and nonspherical particles, Powder Technology, 58, 63-70.

[19] Clift, J. Grace and M. Weber (1978), Bubbles, drops, and particles, ISBN 0-12-176950-X, Academic Press, New York

[20] Gonzalez, Woods and Eddins, (2004), Digital image processing using Matlab, ISBN 0-13-008519-7, Pearson Education.

9 Conclusions and Future Work

9.1 Conclusions

The use of the PTV technique, along with the employment of a pulse laser sheet to measure orientations and velocities simultaneously of nylon fibrous particles with a long aspect ratio using air as a working fluid, has been successfully demonstrated for the first time and the most important findings of this thesis are as follows:

- The relationship between C_D and Re_d, and the orientation θ of a long fibrous particle whilst settling in air;
- The mean vertical settling velocities of fibrous particles increase monotonically with Φ under super dilute conditions;
- The mean orientations of settling fibrous particles decrease with Φ under super dilute conditions;
- The horizontal component of settling velocity of fibrous particles is preferentially aligned with the major axis of the fibrous particles;
- The settling fibres swing significantly and the tumbling is inhibited by a decrease in the aspect ratio;
- The fibres' vertical angular velocity is lowest at the centre-line of the turbulent jet and increases significantly in the radial direction.
- At the centre-line of the jet, the fibres' most probable orientation tends to be approximately 50° to the axial direction.

Based on the literature review, most of previous work which investigated fibrous particles used water as a working fluid, where the density ratio between two phases is of the order of unity. In the present work, this density ratio is of the order of 1,000 due to the suspensions being in air, which means that the particles' inertia is significant and the buoyancy acting on the particle can be neglected. This difference is the highlight of this thesis.

In the present work, based on the data of a single fibre settling, a simple relationship between C_D and Re_d was found whilst the fibre reached its terminal settling velocity in air:

$$C_D = \frac{\rho_{air}\rho_{fp}\pi d^3 Lg}{2\,\mathrm{Re}_d^{\,2}\,\mu^2(L\sin\theta + \frac{1}{4}\pi d\cos\theta)}. \quad (9.1)$$

For fibres with a long aspect ratio, the fibre length, L, is far greater than its diameter, d. The term of ¼ $\pi d\cos\theta$ can be neglected, thus Equation 9.1 becomes:

$$C_D = \frac{\rho_{air}\rho_{fp}\pi d^3 g}{2\,\mathrm{Re}_d^{\,2}\,\mu^2\sin\theta}. \quad (9.2)$$

It can be seen that C_D is independent of fibre length, L, which is consistent with the findings of McKay *et al*. [15]. Compared with the previous work, Equation 9.2 is simple and accurate.

The influence of the number density of the fibrous particles on their settling velocities and orientations were assessed, whilst the number of the fibrous particles located in the viewing volume varied from one to one hundred. The mean vertical settling velocities were found to increase monotonically with Φ and the mean orientations decreased with Φ. The new power law functions for these interesting findings have been proposed to provide a better description:

$$\frac{\overline{V}_{cx}(\phi)}{\overline{V}_{ts}} = a\phi^{n} \ , \quad \overline{\theta}(\phi) = \frac{b}{\phi^{n}}\overline{\theta}_{ts} \ , \quad (9.3)$$

where $\overline{V_{cx}}$ is the mean settling velocity (the function of Φ) and $\overline{V_{ts}}$ is the mean settling velocity of a single fibre, a is a constant that related to the fibre's aspect ratio, n is the parameter which depends on the fibres' settling velocity (the Reynolds number of the fibrous particle); Φ is the volume fraction of the fibres. $\overline{\theta}$ is the mean orientation of the fibres, $\overline{\theta}_{ts}$ is the average orientation of a single fibre whilst settling and b is a constant. For the fibres with a length of 1,850 μm, the mean settling velocity of the fibres increased from 0.36m/s to 0.72m/s and the mean orientations decreased from 82º to 62º, whilst the number of the fibres varied from one to one hundred in viewing volume. That is, all of the mean steady state settling velocities of multiple fibres were found to exceed the mean terminal settling velocity of a single fibre. This phenomenon is attributed to the bulk settling motion effect and the fibres' orientation transition from a horizontal state to a vertical state under a super dilute regime that stems from the increasing aerodynamic interactions between fibres. This finding is consistent with the simulations of the previous work [33, 39, 40] and with the experiments of the previous work [22, 24] at low Reynolds numbers of the fibres. The mean horizontal settling velocity was found

to be zero on average, as expected. However the fluctuations of the horizontal components of the settling velocity and angular velocities of settling fibres were found to increase with Φ.

The orientations of the bulk settling fibrous particles were found to be around 80º, relative to the gravity at particle Reynolds numbers of $Re_d \sim O(1)$ and $Re_L \sim O(10)$. However the fibres' orientation was found to be more horizontal than that for $Re_L \sim O(1)$ [33]. This is because for fibres with Reynolds numbers of $Re_L \sim O(10)$, the inertia of the settling fibrous particles plays a more important role than that for $Re_L \sim O(1)$. Furthermore, based on computation of the vertical angular velocity, the majority of the fibrous particles were found to exhibit oscillatory and tumbling motions, which contrasts with the fibres settling in water. This is attributed to the fibres' pressure centre being behind the mass centre, whilst settling in air. This information provides new insight into the aerodynamic behavior of fibrous particles at a condition of high density ratio between two phases. Based on the relationship between the absolute horizontal velocities and the angle of azimuths, it is found that the transverse velocity of the fibres is preferentially aligned with their major axis.

Finally, at the centre-line of the jet, the preferred mean orientation of the fibrous particles in the near field of turbulent jet flows was found to be approximately 50º relative to the axial direction. This contrasts with the findings in a headbox [111] where the majority of the fibres are oriented close to the turbulent flow direction. This difference is attributed primarily to the different forces acting on the fibrous particles. In the present study, the density ratio of the solid phase to air phase is in the order of 1,000 and the inertia acting on the fibres plays an important role. However, in the headbox the

density ratio tends to be unity and the positive streamwise rate-of-strain plays an important role. The values of the vertical angular velocities of the fibrous particles in the turbulent jet were found to be much higher than those in the free falling case because of the shear effect. The fibres' vertical angular velocity was found to be the lowest at the centre-line of the jet and to increase significantly in the radial direction, which is consistent with the previous simulations [51]. The influence of number density on the orientations and velocities of the fibres in the turbulent jet flows was found much weaker than that in free falling case. This is attributed to the greater significance of inertia, owing to the higher speed of the particles, and to a reduced significance of the interactions between the wakes of proximate particles, because the "background" flow in the carrier phase is turbulent instead of laminar (as in the free-falling case). At the centre-line of the turbulent jet, the fibres' normalized radial velocities were found to be of an order of magnitude larger than that of the spheres'. This can be attributed to the influence of the fibres' tumbling motion.

The experimental method developed in this thesis, combined with the image processing technique, can measure the number density of the fibrous particles. However this method is only suitable for super dilute conditions. This is the limitation of the present work.

9.2 Future work

The current work about long fibres settling in air has provided support for the existing knowledge, but further investigation is still needed in some aspects. For example, in the third paper of this thesis, it is found that for those fibres with the same diameter but different length, the mean settling velocity of long fibres is about 10% higher than that of short fibres at the same volume fraction. The mechanism for this phenomenon is still unknown. Based on current knowledge, their settling velocities should be identical at the same volume fraction. For Equation 9.3, further investigation could be useful to determine the parameters of *a*, *b* and *n* in the equations by using more general fibres, such as *L/d* = 1, 2, 3, 5, 10, 15, 20…. This equation could be a supplement to Richardson-Zaki's Law in super dilute conditions. Furthermore, work to investigate settling fibre clouds has yet to be undertaken.

The aerodynamics of fibrous particles in a turbulent jet flow is a new research topic based on the literature review. The present work about fibres in a turbulent jet flow only measured the orientation of the fibrous particles in the potential core area. The mechanism controlling the distribution of orientations of fibrous particles in the far field of a turbulent jet flow needs further investigation. Furthermore, in practice, the particles' loading for biomass combustion is not in super dilute conditions, so the regime with higher particle loading needs to be considered in the future. There is also a need to assess the efficacy of various enhanced mixing devices for modifying distributions of the orientation and velocity of fibrous particles, including processing jet (PJ) and oscillating jet nozzles.

10 Bibliographies

1. L. Fan, Z. Mao, and C. Yang, “Experiment on settling of slender particles with large aspect ratio and correlation of the drag coefficient”, *Ind. Eng. Chem. Res*. 43, pp7664–7670, 2004.
2. R. Clift, J. Grace and M. Weber, “Bubbles, drops, and particles”, ISBN 0-12-176950-X, Academic Press, New York, 1978.
3. A. Haider and O. Levenspiel, “Drag coefficient and terminal velocity of spherical and nonspherical particles”, *Powder Technology*, 58, pp63–70, 1989.
4. G. Venu Madhav and R. P. Chhabra, “Drag on non-spherical particles in viscous fluids”, *International Journal of Mineral Processing*, 43, pp15–29, 1995.
5. G. H. Ganser, “A rational approach to drag prediction of spherical and nonspherical particles”, *Powder Technology*, 77, pp143–152, 1993.
6. P. K. Swamee and C. P. Ojha, “Drag coefficients and fall velocity of non-spherical particles” *J. Hydraul. Eng*. 117, 1991.
7. R. Gonzalez, R. Woods and S. Eddins, “Digital image processing using Matlab”, ISBN 0-13-008519-7, Pearson Education, 2004.
8. R. P. Chhabra, L. Agawal and N. K. Sinha, “Drag on non-spherical particles: an evaluation of available methods”, *Powder Technology*, 101, pp288–295, 1999.
9. Z. L. Arsenijevic, Z. B. Grbavcic, R. V. Grulovic and F. K. Zdanski, “Determination of non-spherical particle terminal velocity using particulate expansion data”, *Powder Technology*, 103, pp265–273, 1999.
10. H. Y. Xie and D. W. Zhang, “Stokes shape factor and its application in the

measurement of sphericity of non-spherical particles", *Powder Technology*, 114. pp102–105, 2001.

11. P. Rajitha, R. P. Chhabra, N. E. Sabiri and J. Comiti, "Drag on non-spherical particles in power law non-Newtonian media", *International Journal of Mineral Processing*, 78, pp110–121, 2006.
12. S. Tran-Cong, M. Gay and E. E. Michaelides, "Drag coefficient of irregularly shaped particles", *Powder Technology*, 139, pp21–32, 2004.
13. A. Unnikrishnan and R. P. Chhabra, "An experimental study of motion of cylinders in Newtonian fluids: wall effects and drag coefficient", *the Canadian Journal of Chemical Engineering*, Vol. 69, June 1991.
14. J. Gabitto and C. Tsouris, "Drag coefficient and settling velocity for particles of cylindrical shape", *Powder Technology* 183, pp314–322, 2008.
15. G. McKay, W. R. Murphy and M. Hillis, "Settling characteristics of discs and cylinders", *Chem Eng Res Des*, Vol. 66, Jan. 1988.
16. R. P. Chhabra, K. Rami and P. H. T. Uhlherr, "Drag on cylinders in shear thinning viscoelastic liquids", *Chemical Engineering Science* 56, pp2221–2227, 2001.
17. D. Leith, "Drag on non-spherical objects", *Aerosol Science and technology* 6, pp153–161, 1987.
18. S. C. Lee, "Scattering phase function for fibrous media", *J. Heat Mass Transfer*, 33, pp2183–2190, 1990.
19. D. L. Black and M. Q. McQuay, "Laser-based particle measurements of spherical and non-spherical particles", *International Journal of Multiphase Flow*, 27, pp1333–1362, 2001.
20. H. Barthel, B. Sachweh and F. Ebert, "Measurement of airborne mineral fibres using a new differential light scattering device", *Measurement Science*

Technology, 9, pp210–220, 1998.

21. B. Herzhaft, E. Guazzelli, M. B. Mackaplow and E. S. G. Shaqfeh, "Experimental investigation of the sedimentation of a dilute fibre suspension", *Physical Review Letter*, vol 77 No 2, 1996.
22. B. Herzhaft and E. Guazzelli, "Experimental study of sedimentation of dilute and semi-dilute suspensions of fibres", *J. Fluid Mech*, Vol 384, pp133–158, 1999.
23. B. Metzger, J. Butler and E. Guazzelli, "Experimental investigation of the instability of a sedimenting suspension of fibre", *J. Fluid Mech* Vol 575, pp307–332, 2007.
24. J. Salmela, D. M. Martinez and M. Kataja, "Settling of dilute and semidilute fiber suspensions at finite *Re*", *AIChE Journal*, Vol.53, No.8, 2007.
25. O. Melander and A. Rasmuson, "PIV measurements of velocities and concentration of wood fibres in pneumatic transport", *Experiments in Fluids* 37, pp293–300, 2004
26. B. T. B. Wong and S. I. Green, "A novel device to measure pulp fibre hydrodynamics", *TAPPI Engineering Conference*, Vol 2, No. 3, 2001.
27. K. Yasuda, T. Kyuto and N. Mori, "An experimental study of flow-induced fiber orientation and concentration distributions in a concentrated suspension flow through a slit channel containing a cylinder", *Rheol Acta* 43, pp137–145, 2004.
28. M. B. Mackaplow and E. S. G. Shaqfeh, "A numerical study of the sedimentation of fibre suspension", *Journal of Fluid Mechanics*, 376, pp149–182, 1998.
29. M. Shin, D. L. Koch and G. Subramanian, "Structure of dynamics of dilute suspensions of finite-Reynolds number settling fibres", *Physics of Fluids* 21, 123304, 2009.
30. J. Lin, W. Zhang and Z. Yu, "Numerical research on the orientation distribution

of fibres immersed in laminar and turbulent pipe flow", *Journal of Aerosol Science*, 35, pp63–82, 2004.

31. J. Lin, X. Shi and Z. You, "Effects of the aspect ratio on the sedimentation of a fiber in Newtonian fluids", *Journal of Aerosol Science*, 34, pp909–921, 2003.
32. C. Yin, L. Rosendahl, S. K. Kær and T. J. Condra, "Use of numerical modeling in design for co-firing biomass in wall-fired burners", *Chemical Engineering Science*, 59, pp3281–3292, 2004.
33. E. Kuusela, J. M. Lahtinen and T. Ala-Nissila, "Collective effects in settling of spheroids under steady-state sedimentation", *Physical review letter*, vol 90 No 9, Mar. 2003.
34. A. S. Lubansky, D. V. Boger and J. J. Cooper-White, "Batchelor's theory extended to elongated cylindrical or ellipsoidal particles", *Journal of Non-Newtonian Fluid Mechanics*, 130, pp57–61, 2005.
35. E. Kuusela, K. Hofler and S. Schwarzer, "Computation of particle settling speed and orientation distribution in suspensions of prolate spheroids", *J. Engineering Mathematics*, 41: pp221–235, 2001.
36. P. Y. Huang, H. H. Hu and D. D. Joseph, "Direct simulation of the sedimentation of elliptic particles in Oldroyd-B fluids", *Journal of Fluid Mechanics*, Vol 362, pp297–325, 1998.
37. D. Saintillan, E. S. G. Shaqfeh and E. Darve, "The growth of concentration fluctuation in dilute dispersions of orientable and deformable particles under sedimentation", *Journal of Fluid Mechanics*, Vol. 553, pp347–388, 2006.
38. M. Shin, D. L. Koch and G. Subramanian, "A pseudospectral method to evaluate the fluid velocity produced by an array of translating slender fibers", *Physics of Fluids*, 18, 063301, 2006.

39. J. E. Butler and E. S. G. Shaqfeh, "Dynamic simulation of the inhomogeneous sedimentation of rigid fibres", *Journal Fluid Mech*, Vol.468, pp205–237, 2002.

40. A. K. Tornberg and K. Gustavsson, "A numerical method for simulations of rigid fiber suspensions", *J. Computational Physics*, 215, pp172–196, 2005.

41. H. T. Chung, S. H. Kang and W. R. Hwang, "Numerical simulations of elliptic particle suspensions in sliding bi-periodic frames", *Korea-Australia Rheology Journal*, 17, pp171–180, 2005.

42. D. Saintillan, E. Darve and E. S. G. Shaqfeh, "Dynamic simulation of the instability of sedimenting fibers", *XXIICTAM*, Warsaw, Poland, 2004.

43. G. K. Batchelor, "Slender-body theory for particles of arbitrary cross-section in Stokes flow", *Journal of Fluid Mechanics*, Vol 44, pp419–440, 1970.

44. D. L. Koch and E. S. G. Shaqfeh, "The instability of a dispersion of sedimenting spheroids", *Journal of Fluid Mechanics*, Vol 209, pp521–542, 1989.

45. J. Lin and L. Zhang, "Numerical simulation of orientation distribution function of cylindrical particle suspensions". *Applied mathematics and mechanics*, 23, pp906–912, 2002.

46. J. Lin, Y. L. Wang, W. X. Wang and Z. S. Yu, "Numerical simulation of the sedimentation of cylindrical pollutant particles in fluid". *Journal Environ Sci*. 14, pp433–438, 2002.

47. P. A. Baron and K. Willeke, "Aerosol measurement, Principles, techniques and applications", A John Wiley & sons, INC, Publication, ISBN 0-471-35636-0, 2001.

48. R. G. Cox, "The motion of long slender bodies in a viscous fluid, Part 1, General theory", *Journal Fluid Mechanics*, 44, pp791–810, 1970.

49. R. G. Cox, "The motion of long slender bodies in a viscous fluid, Part 2, Shear

flow", *Journal Fluid Mechanics*, 45, pp625–657, 1970.

50. AEBRE, "Australian energy national and states projections to 2029–30", *abare research report* 06.26, 26, 2006.
51. C. Jayageeth, V. I. Sharma and A. Singh, "Dynamics of short fibers suspensions in bounded shear flow", *International Journal of Multiphase Flow*, 35, pp261–269, 2009.
52. W. Zhang and J. Lin, "Research on the motion of particles in the turbulent pipe flow of fiber suspensions", *Applied Mathematics and Mechanics*, 25, pp741–749. 2004.
53. J. A. Olson and R. J. Kerekes, "The motion of fibres in turbulent flow", *Journal Fluid Mechanics*, 377, pp47–64, 1998.
54. W. Kvasnak and G. Ahmadi, "Deposition of ellipsoidal particles in turbulent duct flow", *Chemical Engineering Science*, 51, pp5137–5148, 1996.
55. C. A. Stover, D. L. Koch and C. Cohen, "Observation of fibre orientation in simple shear flow of semi-dilute suspensions", *Journal Fluid Mechanics*, 238, pp277–296, 1992.
56. H. Zhang, G. Ahmadi, F. Fan, J. B. McLaughlin, "Ellipsoidal particles transport and deposition in turbulent channel flow", *International Journal of Multiphase Flow*, 27, pp971–1009, 2001.
57. J. Lin, J. Li, L. Zhu and J. A. Olson, "New equation of turbulent fibre suspensions and its solution and application to the pipe flow", *Chinese Physics*, 14, pp1185–1192, 2005.
58. D. Broday, M. Fichman, M. Shapiro and C. Gutfinger, "Motion of spheroidal particles in vertical shear flows", *Physics of Fluids*, pp1086–100, 1998.
59. X. K. Ku and J. Z. Lin, "Inertial effects on the rotational of a fibre in simple shear

flow between two bounding wall", *Phys. Scr*. 80, pp1–10, 2009.

60. J. Lin, Y. Wang and C. Wang, "Research on the motion of suspended cylindrical particles in round jets", *Journal of Zhejiang University (Engineering Science)*, 37, pp81–86, 2003.
61. L. Zhang, J. Lin and T. L. Chan, "Orientation distribution of cylindrical particles suspended in turbulent pipe flow", *Physics of Fluids*, 17, 093105, 2005.
62. J. D. Klett, "Orientation model for particles in turbulence", *Journal of the Atmospheric Science*, 52, pp2276–2285, 1995.
63. P. L. Frattini, E. S. G. Shaqfeh, J. L. Levy and D. L. Koch, "Observations of axisymmetric tracer particle orientation during flow through a dilute fixed bed of fibres", *Physics of fluids*, 11, pp2516 – 2528, 1991
64. W. C. Hinds, "Aerosol Technology, properties, behaviour, and measurement of airborne particles", second Edition, ISBN0-417-19410-7, A Wiley-Interscience Publication John Wiley & Sons, INC, New York, 1998.
65. J. Z. Lin, X. Shi and Z. J. You, "Effects of the aspect ratio on the sedimentation of a fibre in Newtonian fluids", *Journal of Aerosol science* 34, 2003.
66. J. Z. Lin, X. Shao, X. Shi and Z. Yu, "Study on the interaction of sedimenting cylindrical particles in still fluid", *Acta Mechanica Sinica*, vol 20, 2004.
67. C. Mayer, "Investigating the aerodynamics of fibrous particles for application to the combustion of pulverized wood", Institute of Energy Process Engineering and Fuel Technology, Clausthal University, Germany and School of mechanical Engineering, The University of Adelaide, Australia, 2006.
68. L. Rosendahl, "Extending the modelling framework for gas-particle systems, Application of multiparameter shape descriptions to non-conventional solid fuels in reacting and non-reacting environments", Institute of Energy Technology,

Aalborg University, Aalborg University, Denmark, 1998.

69. Z. F. Zhu and J. Z. Lin, “dynamics of fibrous particles in suspension”, China Textile Press, Shanghai, ISBN 7-81038-276-4/N05, China, 1999.
70. A. Unnikrishnan, “Slow paralell motion of cylinder in non-Newtonian media: wall effects and drag coefficient”, *Chemical Engineering Process*, 28, pp121–125, 1990.
71. R. Holm and D. SÖderberg, “Shear influence on fibre orientation” *Rheoi Acta*, 46, pp721–729, 2007.
72. P. Laure, A. Megally and T. Coupez, “Collision strategy for the direct simulation of moving fibers in viscous fluid”, Coupled Problems, 2005.
73. H. Shin and M. R. Maxey, “Chaotic motion of non-spherical particles settling in a cellular flow field”, *Physics Review E*, 56, pp5431–54444, Nov. 1997.
74. O. G. Harlen and D. L. Koch, “Simple shear flow of a suspension of fibres in a dilute polymer solution at high Deborah number”, *Journal of Fluids Mechanics*, 252, pp187–207, 1993.
75. J. Lin, Z. Zhang and Z. Yu, “Investigation of the interactions between two contact fibers in the fiber suspensions”, *Journal of Material Science*, 38, pp1499–1505, 2003.
76. E. S. G. Shaqfeh and D. L. Koch, “The effect of hydrodynamic interactions on the orientation of axisymmetric particles flowing through a fixed bed of spheres or fibers”, *Physics of Fluids*, 31, pp728–743, 1988
77. D. L. Koch and E. S. G. Shaqfeh, “The average rotation rate of a fiber in the linear flow of a semidilute suspension”, *Physics of Fluids*, A2, pp2093–2102, 1990.
78. J. Lin, S. Zhang and J. A. Olson, “Computing orientation distribution and

rheology of turbulent fiber suspensions flowing through a contraction", *International Journal for Computer-aided Engineering and Software*, 24, pp52–76, 2007.

79. J. Lin, X. Shi and Z. Yu, "The motion of fibers in an evolving mixing layer", *International Journal of Multiphase Flow*, 29, pp1355–1372, 2003.
80. J. Cai, X. Wu and Z. Yuan, "Number concentration of slender particles in gas-solids circulating fluidized bed", *Chinese Journal of Chemical Industry and Engineering*, 59, pp2490–2497, Oct. 2008.
81. K. Zhou and J. Lin, "Research on the behaviour of fiber orientation probability distribution function in the planar flows", *Journal of Zhejiang University Science, 6A*, pp257–264, 2005.
82. W. D. McComb and K. T. J. Chan, "Laser-Doppler anemometer measurements of turbulent structure in drag-reducing fibre suspensions", *Journal of Fluid Mechanics*, 152, pp455–478, 1985.
83. P. A. Taub, "The interaction of a fibre tangle with an airflow", *Journal of Fluid Mechanics*, 27, pp561–580, 1967.
84. X. Rong, D. Qi, G. He, J. Zhu and T. Scott, "Single curved fiber sedimentation under gravity", *An International Journal Computers & Mathematics with Application*, 55, pp1560–1567, 2008.
85. W. Chen, "Determination of drag coefficient in measuring particle diameters", *Journal of Sedimentary Research*, 73, pp741–719, 2003.
86. L. Baxter, P. Leong, H. Lu and D. Tree, "Distinguishing biomass combustion characteristic and their implications for sustainable energy", 5th Asia-Pacific Conference on Combustion, pp469–472, 2005.
87. H. Collazo, W. A. Crow, L. Gardner, B. L. Phillips, V. A. Marple and B. Olson,

"Inertial impactor to measure aerodynamic diameter of man-made organic fibers", *Aerosol Science and Technology*, 36, pp166–177, 2002.

88. R. Holm, "Fluid mechanics of fibre suspensions related to papermaking", PhD thesis, Royal Institute of Technology, Sweden, 2005.
89. K. Zhou and J. Lin, "Three dimensional fiber orientation distribution in two dimensional flows", *Fibers and Polymers*, 19, pp39–47, 2008.
90. M. Parsheh, M. L. Brown and C. K. Aidun, "Variation of fiber orientation in turbulent flow inside a planar contraction with different shapes", *International Journal of Multiphase Flow*, 32, pp1354–1369, 2006.
91. X. Fan, N. Phan-Thien and R. Zheng, "A direct simulation of fibre suspension", *Journal of Non-Newtonian Fluid Mechanics*, 74, pp113–135, 1998.
92. J. A. Olson, "The motion of fibres in turbulent flow, stochastic simulation of isotropic homogeneous turbulence", *International Journal of Multiphase Flow*, 27, pp2083–2103, 2001.
93. M. Parsheh, M. L. Brown and C. K. Aidun, "On orientation of stiff fibres suspended in turbulent flow in a planar contraction", *Journal of Fluid Mechanics*, 545, pp245–269, 2005.
94. H. Zhang, G. Ahmadi and B. Asgharian, "Transport and deposition of angular fibers in turbulent channel flows", *Aerosol Science and Technology*, 41, pp529–548, 2007.
95. O. Bernstein and M. Shapiro, "Direct determination of the orientation distribution function of cylindrical particles immersed in laminar and turbulent shear flows", *Journal of Aerosol Science*, 25, pp113–136, 1993.
96. X. Ku, J. Lin, "Effects of two bounding walls on the rotational motion of a fiber in the simple shear flow", *Fibers and Polymers*, 10, pp302–309, 2009.

97. Z. Gao, J. Lin and J. Li, “Theoretical research on rotational dispersion coefficient of fiber in turbulent shear flow of fiber suspension”, *Applied Mathematics and mechanics*, 28, pp289–296, 2007.

98. K. F. Larsen, “Investigation of particle velocity and drag with spherical and non-spherical particles through a backward facing step”, PhD thesis, Department of Mechanical Engineering, Brigham Young University, 2007.

99. G. B. Jeffery, “The motion of ellipsoidal particles immersed in a viscous fluid”, Proceedings of the Royal Society of London. Series A. Containing papers of a Mathematical and Physical Character, 102, pp161–179, Nov. 1922

100. Energy Information Administration, U. S. Department of Energy, “International energy outlook 2008”, Forrestal Building, Washington DC

101. C. Bonadonna, G. G. J. Ernst and R. S. J. Sparks, “Thickness variations and volume estimates of tephra fall deposits: the importance of particle Reynolds number”, *Journal of Volcanology and Geothermal Research*, 81, pp173–187, 1998.

102. H. Wadell, “Sphericity and Roundness of rock particles”. *Journal of Geology*, 40, pp 443–451, 1933.

103. J. F. Richardson and W. N. Zaki, “Sedimentation and fluidization Part 1.” *Trans. Inst. Chem.Eng.* 32, pp35–53, 1954.

104. J. Lin, X. Liang and S. Shen, “Numerical prediction of the flow property in round turbulent jet of fiber suspension”. *Sci China-Phys Mech Astron*, 56, pp298–305, 2013.

105. L. Huang, X. Gao and J. Lin, “Cylindrical particulate internal flows: a review”. *Front. Mech. Eng.* 7(4), pp385–393, 2012.

106. M. Parsheh, M.L. Brown and C.K. Aidun, “Investigation of closure

approximations for fiber orientation distribution in contracting turbulent flow". *Journal of Non-Newtonian Fluid Mech*. 136, 38–49, 2006.

107. J.A. Olson, "Analytic estimate of fibre orientation distribution in a headbox flow". *Nordic Pulp and Paper Research journal.* 17, pp302–306, 2002.

108. J. Olson, I. Frigaard, C. Chan and J. Hamalainen, "Modeling turbulent fibre suspension flowing in a planar contraction: the one-dimensional headbox". *International Journal of Multiphase Flow.* 30, pp51–66, 2004.

109. M. Hyensjo, A. Dahlkild, P. Krochak, J. Olson and J. Hamalainen, "Modeling the effect of shear flow on fibre orientation anisotropy in a planar contraction". *Nordic Pulp and Paper Research journal.* 22, pp376–382, 2007.

110. K. Chiba, K. Nakamura and D. Boger, "A numerical solution for the flow of dilute fibre suspensions through an axisymmetric contraction". *Journal of Non-Newtonian Fluid mechanics.*35 (1), 1990.

111. A. Carlsson, "Near wall fibre orientation in flowing suspensions". PhD thesis, Royal Institute of Technology, Stockholm, Sweden, 2009.

112. A. Carlsson, F. Lundell and L.D. Soderberg, "Fibre orientation control related to papermaking". *Journal of Fluids Eng.* 129(4), pp457–465, 2007.

113. R.J. Foreman, "Mass loading and Stokes number effects in steady and unsteady particle-laden jets". Master thesis, The school of Mechanical Engineering, The University of Adelaide, 2008.

114. R.J. Foreman and G.J. Nathan, "Scaling of the gas phase in particle-laden turbulent axisymmetric jets". *International Journal of Multiphase Flow.* 35, pp96–100, 2009.

115. J.C. Mi, D.S. Nobes and G.J. Nathan, "Influence of jet exit conditions on the passive scaler field of an axisymmetric free jet". *Journal of Fluid Mechanics*. 432,

pp91–125, 2001.

116. T.C.W. Lau and G.J. Nathan, "New understanding of the influence of Stokes number on particle-laden jets from simultaneous planar measurements of number density and velocity". 4th International conference on jets, wakes and separated flows, ICJWSF2013, Nagoya, Japan, 2013.
117. W.D. Griffiths and N.P. Vaughan, "The aerodynamic behavior of cylindrical and spheroidal particles when settling under gravity". *Journal of Aerosol Science*. 17(1), pp53–65, 1986.
118. C. Marchioli, M. Fantoni and A. Soldati, "Orientation, distribution, and deposition of elongated, inertial fibers in turbulent channel flow", *Physics of Fluids*, 22, 033301, 2010.
119. M. Parsheh, M.L. Brown and C.K. Aidun, On the orientation of stiff fibers suspended in turbulent flow in a planar contraction, *Journal of Fluid Mechanics*, 545, pp245–269, 2005.
120. J.Z. Lin, X.Y. Liang and S.L. Zhang, Numerical simulation of fiber orientation distribution in round turbulent jet of fiber suspension, Chemical Engineering Research and Design, 90, pp766–775, 2012.
121. S. Elghobashi, On predicting particle-laden turbulent flows, *Applied Scientific Research*, 52, pp309–329, 1994.
122. M. Mandϕ and L. Rosendahl, On the motion of non-spherical particles at high Reynolds number, *Powder Technology*, 202, pp1–13, 2010.
123. L. Rosendahl, Using a multi-parameter particle shape description to predict the motion of non-spherical particle shapes in swirling flow, *Applied Mathematical Modelling*, 24, pp11–25, 2000.
124. Victor D.G., D. Zhou, E.H.M. Ahmed, P.K. Dadhich, J.G.J. Olivier, H-H.

Rogner, K. Sheikho, and M. Yamaguchi, 2014: Introductory Chapter. In: Climate Change 2014: Mitigation of Climate Change. Contribution of Working Group III to the Fifth Assessment Report of the Intergovernmental Panel on Climate Change [Edenhofer, O., R. Pichs-Madruga, Y. Sokona, E. Farahani, S. Kadner, K. Seyboth, A. Adler, I. Baum, S. Brunner, P. Eickemeier, B. Kriemann, J. Savolainen, S. Schlömer, C. von Stechow, T. Zwickel and J.C. Minx (eds.)]. Cambridge University Press, Cambridge, United Kingdom and New York, NY, USA.

125. BPstats, 1 St James's Square London SW1Y 4PD UK, BP Statistical Review of World Energy, June 2014.

126. International Energy Agency, IEA, Resources to Reserves 2013, 2013.

127. Roger A. Sedjo, Comparative Life Cycle Assessments: Carbon Neutrality and Wood Biomass Energy, 1616 P St. NW Washington, DC 20036 202-328-5000 www.rff.org, April 2013.

128. Massachusetts Biomass Sustainability and Carbon Policy Study: Report to the Commonwealth of Massachusetts Department of Energy Resources. Walker, T. (Ed.). Natural Capital Initiative Report NCI-2010-03. Brunswick, Maine. Manomet Center for Conservation Sciences, 2010.

129. A.K.P. Raymer, A comparison of avoided greenhouse gas emissions when using different kinds of wood energy, *Biomass and Bioenergy*, 30, pp605–617, 2006.

130. S. Van Loo and J. Koppejan, The Handbook of Biomass Combustion and Co-firing, Published by Earthscan, UK, 2008, ISBN: 978-1-84407-249-1.

131. P. McKendry, Energy production from biomass (part 1): overview of biomass, *Bioresource Technology* 83, pp37–46, 2002.

132. P.R. Shukla, Biomass energy in India: transition from traditional to modern, *The*

Social Engineer, Vol. 6, No. 2

133. D.A. Tillman, Biomass cofiring: the technology, the experience, the combustion consequences, *Biomass and Bioenergy*, 19, Issue 6, pp365– 384, 2000.

134. J.K. Eaton and J.R. Fessler, Preferential concentration of particles by turbulence, *International Journal of Multiphase Flow*, 20, pp169– 209, 1994.

135. E.K. Longmire and J.K. Eaton, Structure of a particle-laden round jet, *Journal of Fluid mechanics*, 236, pp217–257, 1992.

136. N.L. Smith, N.P. Megalos, G.J. Nathan and D.K. Zhang, Processing jet burners for stable and low NOx pulverized fuel flames— Preliminary results from small scale trials, *Fuel*, 77, pp1013–1016, 1998.

137. S. Alsamaq, C. Kingdom and N.A. Garba, Life cycle assessment (LCA) of agricultural residues utilization for biogas development, Proceedings of the Global Conference on Energy and Sustainable Development, GCESD,2015, February 24-26, 2015, Technology Park, Coventry University, Coventry, UK.

138. R.P. Beeharry, Carbon balance of sugarcane bioenergy systems**,** *Biomass and Bioenergy***,** 20 (5), pp361–370, 2001.

139. M.C. Hellera, G.A. Keoleiana, T.A. Volkb, Life cycle assessment of a willow bioenergy cropping system, *Biomass and Bioenergy* 25, pp147 – 165, 2003.

140. A. Syed and K. Pen, Australian energy projections to 2049–50, BREE report prepared for the Department of Resources, Energy and Tourism, Canberra, December, 2014.

141. Geoscience Australia and ABARE, 2014, Australian Energy Resource Assessment, Canberra, ISBN 978-1-921672-58-3, 2014.

142. C.T. Bowman, Proceedings of the combustion Institute, 28, pp859 – 878, 1992.

143. http://thienkhanhcorp.itrademarket.com/group+110661/bagasse.htm

144. Australia Government, 2015. Australia's 2030 Climate Change Target, 2015.

145. Australian Government, Department of Industry and Science, Office of the Chief Economist, Australian Energy Update 2015.

146. J.G. Speight, The Chemistry and Technology of Coal, Third Edition, CRC Press, Tylor and Francis Group, ISBN 978-1-4398-3646-0, 2012.

147. W.K. Melville and K.N.C. Bray, Two-phase turbulent jet, *Int. Journal of Heat Mass Transfer* 22, pp279 – 287, 1979.

Appendix

Appendix A: PTV Codes

```
%************************************************************************
 % approach to fibrous particle tracking by using low density PIV-images
 % calculation of velocities of two endpoints of fibrous particles
 % calculation of angles of elevation and azimuth of fibrous particles
%************************************************************************

clear all

%------------------------------------------------------------------------
                % experimental settings
%------------------------------------------------------------------------

resolution=27.8;
% resolution of the fibrous particles on the images, in microns/pixel
particle_length=1850;
% fibrous particle length, in microns
% max_image_length=particle_length/resolution;
% maximum length of the fibrous particle on images, in pixels
max_image_width=10;
% set maximum width of the fibrous particle on images, in pixels
% curved and clumping fibres can be removed by this limitation
max_particle_area=800;
% set maximum area of the fibrous particle on images, if larger than this value
% there must be a clump of particles that needs to be removed, in pixels
```

```
min_image_length=5;
% set minimum length of the fibrous particle on images, in pixels
max_image_length=90;
% set maximum length of the fibrous particle on images, in pixels
min_image_length1=5;
max_image_length1=77;
min_image_length2=5;
max_image_length2=77;
% set minimum and maximum lengths of fibrous particles on image, in pixels
% be careful in the case of unbalanced laser power between pulses
max_difference_imagelength = 2.5;
% set maximum difference of fibre image length between a particle pair, in pixels
max_difference_orientation = 9;
% set maximum difference of fibre projected orientation
% between a particle pair, in degrees
max_difference_area = 60;
% set maximum difference of fibre area between a particle pair, in pixels
% if the time separation is short enough, any changes in the fibre's length are small, and
% orientation and area are small. Based on these characteristics on the images, tracking
% fibres (matching pairs) becomes easier than tracking spherical particles

 min_pixel_smallobject=3;
% define small objects (noises) in area which need to be removed, in pixels
threshold_deviation=250;
% threshold of intensity deviation along the major axis of fibrous particle, in bits
% this value was obtained via the pilot run
max_number_particles=960;
% specify the maximum number of particles on a single image
delta_t=2500;
% time delay between a pair of images (laser pulses), in microseconds
delta_y_max=110;
% set maximum displacement in the direction of the y axis to limit
% the search area, the value was estimated based on the pilot run, in pixels
delta_y_min=15;
```

```
% set minimum displacement in the direction of the y axis to limit
% the search area, the value was estimated based on the pilot run, in pixels
delta_x_max=15;
% set maximum displacement in the direction of the x axis to limit
% the search area, the value was estimated based on the pilot run, in pixels
delta_x_min=2;
% set minimum displacement in the direction of the x axis to limit
% the search area, the value was estimated based on the pilot run, in pixels
npairs=358;
% number of pairs of images to be processed
result='U:\260307resultslowend\260307min_pixel_smallobject5_22_25.txt';
fid=fopen(result,'a');
% define the name and path of the output file for the results calculated

graphicaloutput=0;
% specify if the graphical output is given for each processed image pair
% 1 represents the output and 0 = no output

for k=1:npairs

    clear s* area* width* length* points* pixellist* e11x* e11y* e12x*
    clear e12y* majoraxis_intensity* e21x* e21y* e22x* e22y* which* x1 y1
    clear disp_* e1yvelocity* e1xvelocity* e2yvelocity* e2xvelocity*
    clear num_whichone artifi* original* phi* theta* validpairs
    clear standard_deviation* num* da1* da2* diame1* diame2*
    clear delta_e1y* delta_e2y* delta_e1x* delta_e2x* n_pixel number_pairs
    clear todelete

 im1=['F:\260307T2500p20d20open\260307T2500open20d20-3\20d20T2500_', ...
   num2str(2*k-1,'%03d'),'.tif'];
% specify the name and path of the image files
% the No 1 image of the pair, num2str can read a string of images, 2*k-1, 2*k
% for the first image with an odd number in the file, 2*k-2, 2k-1 for an even number
```

```
im2=['F:\260307T2500p20d20open\260307T2500open20d20-3\20d20T2500_', ...
    num2str(2*k-0,'%03d'),'.tif'];
% the No 2 image of the pair

%im1=['F:\29-03\29-03\run7_sett_vel_29-03_20d2\run7_sett_vel_29-03_20d2_506.tif'];
%im2=['F:\29-03\29-03\run7_sett_vel_29-03_20d2\run7_sett_vel_29-03_20d2_507.tif'];
% one pair of images for the purpose of a pilot run

%------------------------------------------------------------------------
          % read first image and label particles
%------------------------------------------------------------------------

I1_1=imread(im1);
% read No 1 image
I1=imclearborder(I1_1,8);
% clear the fibrous particles located on the edges of the image
level1=graythresh(I1);
% specify the gray threshold level for converting binary image
BW1_1_1_1_1=im2bw(I1,level1);
% convert I1 to a binary image
BW1_1_1_1 = bwmorph(BW1_1_1_1_1,'bridge',Inf);
% when there is a separation of one pixel gap within one particle,
% connect the two parts together
BW1_1_1=bwareaopen(BW1_1_1_1,min_pixel_smallobject);
% remove the small objects (noises) (fewer than min_pixel_smallobject)

[L1_1_1,num1_1_1]= bwlabel(BW1_1_1,8);
 num1_1_1
% label the connected objects with an edge or corner connection of 8
% and count the number of objects (particles)
if (num1_1_1 < 22) | (num1_1_1 > 25) ;
   continue
end
% set limitation of number of particles for calculation of density
```

```
s1_1_1=regionprops(L1_1_1,'MinorAxisLength','MajorAxisLength');
width1_1_1=[s1_1_1.MinorAxisLength];
length1_1_1=[s1_1_1.MajorAxisLength];
% calculate a fibrous particle's length and width by using
% region property function

BW1_1=ismember(L1_1_1,...
   find(width1_1_1 <= max_image_width & length1_1_1 >= min_image_length));
% set criteria to select particles
%imshow(BW1_1)
% show binary image
[L1_1,num1_1]= bwlabel(BW1_1,8);
num1_1
% label the connected objects with an edge or corner connection of 8
% and count the number of objects (particles)

%if (num1_1 > max_number_particles)| (num1_1==0) ;
%   continue
%end
% do not process data if there are too many particles

s1_1=diameter(L1_1);
d1=[s1_1.Diameter];
BW1=ismember(L1_1,...
   find(d1 <= max_image_length1 & d1 >= min_image_length1));
% set criteria to select particles again
%imshow(BW1)
%hold on
[L1,num1]= bwlabel(BW1,8);
num1
if (num1 > max_number_particles)| (num1==0) ;
   continue
end
% do not process data if there are too many particles
```

```
 s1=diameter(L1);
% diameter function

% Diameter function measures diameter and related properties of image regions. It
% can compute the diameter, the major axis endpoints, the minor axis endpoints,
% and the basic rectangle of each labelled region in the labelled matrix L.
% Positive integer elements of L corresponding to different regions. For
% example, the set of elements of L equal to 1 corresponding to region 1;
% the set of elements of L equal to 2 corresponding to region 2; and so on.
% s is a structure array including:
%
%       Diameter
%       MajorAxis
%       MinorAxis
%       BasicRectangle
%
% The diameter field, a scalar, is the maximum distance between any two
% pixels in the corresponding region.
%
% The MajorAxis field is a 2 by 2 matrix. The rows contain the row and column
% coordinates for the endpoints of the major axis of the corresponding
% region.
%
% The MinorAxis field is a 2 by 2 matrix. The rows contain the row and column
% coordinates for the endpoints of the minor axis of the corresponding
% region.
%
% The BasicRectangle field is a 4 by 2 matrix. Each row contains the row
% and column coordinates of a corner of the region-enclosing rectangle,
% as defined by the major and minor axis.

s11=regionprops(L1,'All');
% all region information on L1
area11=[s11.Area];
```

```
% fibre area on image
orientation1=[s11.Orientation];
% fibre projected angle on image
da1=[s1.Diameter];
% fibre projected length
majoraxis1=[s1.MajorAxis];
% 2 by 2*num1 array for two endpoints coordinates of fibrous particles

for i=1:num1

   e11x(i)=majoraxis1(1,2*i);
   e11y(i)=majoraxis1(1,2*i-1);
   % x and y coordinates of endpoint 1 of fibrous particles

   e12x(i)=majoraxis1(2,2*i);
   e12y(i)=majoraxis1(2,2*i-1);
   % x and y coordinates of endpoint 2 of fibrous particles

    x1=[e11x(i) e12x(i)];
    % x coordinates of two endpoints of fibrous particles
    y1=[e11y(i) e12y(i)];
    % y coordinates of two endpoints of fibrous particles

    majoraxis_intensity1{i}=improfile(I1,x1,y1);
    % each fibre's intensities along the line segment between two endpoints

   standard_deviation1(i)=std(majoraxis_intensity1{i});
   % standard deviation of intensity along the fibre major axis,
   % the threshold for "part-in" and "full-in" fibrous particles

end
```

```
%-------------------------------------------------------------------------
        % read second image and label particles
%-------------------------------------------------------------------------

I2_1=imread(im2);
% read No 2 image
 I2=imclearborder(I2_1,8);
% clear the fibrous particles located on the edges of the image
level2=graythresh(I2);
% specify the gray threshold level for converting the binary image
BW2_1_1_1_1=im2bw(I2,level2);
% convert I2 to a binary image
BW2_1_1_1 = bwmorph(BW2_1_1_1_1,'bridge',Inf);
% when there is a separation of one pixel gap within one particle,
% connect the two parts together
BW2_1_1=bwareaopen(BW2_1_1_1,min_pixel_smallobject);
% remove the small objects (noises) (fewer than min_pixel_smallobject)
[L2_1_1,num2_1_1]= bwlabel(BW2_1_1,8);
 num2_1_1
% label the connected objects with an edge or corner connection of 8
% and count the number of objects (particles)
s2_1_1=regionprops(L2_1_1,'MinorAxisLength','MajorAxisLength');
% calculate the fibre's length and width by using
% the region property function on image 2

width2_1_1=[s2_1_1.MinorAxisLength];
length2_1_1=[s2_1_1.MajorAxisLength];
BW2_1=ismember(L2_1_1,...
   find(width2_1_1 <= max_image_width & length2_1_1 >= min_image_length));
% set criteria to select particles
%imshow(BW2_1)
% show binary image
[L2_1,num2_1]= bwlabel(BW2_1,8);
num2_1
```

```
% label the connected objects with an edge or corner connection of 8
% and count the number of objects (particles)
if (num2_1 > max_number_particles)| (num2_1==0)
   continue
end

s2_1=diameter(L2_1);
% diameter function
d2=[s2_1.Diameter];
% fibre's projected length
BW2=ismember(L2_1,...
   find(d2 <= max_image_length2 & d2 >= min_image_length2));
% set criteria to select particles again
[L2,num2]= bwlabel(BW2,8);
num2
%imshow(BW2)
if (num2 > max_number_particles)| (num2==0)
   continue
end
% do not process data if there are too many particles

s2=diameter(L2);
s22=regionprops(L2,'All');
area22=[s22.Area];
orientation2=[s22.Orientation];
% fibre's projected angle on image 2
da2=[s2.Diameter];
majoraxis2=[s2.MajorAxis];
% 2 by 2*num2 array for two endpoints coordinates of fibrous particles

for i=1:num2

   e21x(i)=majoraxis2(1,2*i);
   e21y(i)=majoraxis2(1,2*i-1);
```

```
    % x and y coordinates of endpoint 1 of fibrous particle on image 2
    e22x(i)=majoraxis2(2,2*i);
    e22y(i)=majoraxis2(2,2*i-1);
    % x and y coordinates of endpoint 2 of fibrous particle on image 2
    x2=[e21x(i) e22x(i)];
     % x coordinates of two endpoints of fibrous particle on image 2
    y2=[e21y(i) e22y(i)];
     % y coordinates of two endpoints of fibrous particle on image 2
     majoraxis_intensity2{i}=improfile(I2,x2,y2);
     % fibre's intensities along a line segment between two endpoints
    standard_deviation2(i)=std(majoraxis_intensity2{i});
    % standard deviation of intensity along the fibre's major axis
    % the threshold for "part-in" and "full-in" fibrous particles
end


%-------------------------------------------------------------------------------
          % find matching pairs of fibres between images No 1 and No 2
%-------------------------------------------------------------------------------

n=0;
% n is the number of pairs of particles matched between image 1 and 2

for i=1:num1

  if (standard_deviation1(i) <= threshold_deviation)
           %&(length1_1(i) <= max_image_length)
  % these thresholds vary with the different sets of images, and
  % are determined by a pilot run of the codes because of
  % different laser power setups and particle sizes, etc.

       for j=1:num2

          if  (e21x(j) <= e11x(i)+ delta_x_max)...
```

```
            & (e21x(j) >= e11x(i)- delta_x_max)...
            & (e21y(j) <= e11y(i)+ delta_y_max)...
            & (e21y(j) >= e11y(i)+ delta_y_min)...
            & (e22y(j) <= e12y(i)+ delta_y_max)...
            & (e22y(j) >= e12y(i)+ delta_y_min)...
            & (e21x(j) <= e11x(i)+ delta_x_max)...
            & (e21x(j) >= e11x(i)- delta_x_max)...
            & (abs(da2(j)- da1(i))<= max_difference_imagelength)...
& (abs(orientation2(j) - orientation1(i))<= max_difference_orientation)...
            & (abs(area22(j) - area11(i))<=max_difference_area);
        % matching pairs by the displacements of two endpoints of the fibres
        % matching pairs by the area, projected length and orientation of the fibres

          n=n+1;
          whichone(n)=i;
          whichpartner(n)=j;
        % particle i on image 1 (whichone) and particle j on image 2
        % (whichpartner) are a pair for calculation purpose

          disp_e1y(n)=e21y(j)- e11y(i);
          disp_e1x(n)=e21x(j)- e11x(i);
          disp_e2y(n)=e22y(j)- e12y(i);
          disp_e2x(n)=e22x(j)- e12x(i);
       % displacements of two endpoints of fibrous particles
       % in the y and x directions

      if n>1
      % checking for particles on image 1 with multiple
      % partners on image 2

       if whichone(n)==whichone(n-1)
        if abs(area22(j)-area11(i))>...
              abs(area22(whichpartner(n-1))-area11(i));
          % i.e. first partner found was better
```

```
            n=n-1;
        % i.e. that the values found will be overwritten in the next go

            else
         % i.e. second partner found is better
            n=n-1;
            whichone(n)=i;
            whichpartner(n)=j;
         % overwrite first partner values now

        disp_e1y(n)=e21y(j)-e11y(i);
        disp_e1x(n)=e21x(j)-e11x(i);

        disp_e2y(n)=e22y(j)-e12y(i);
        disp_e2x(n)=e22x(j)-e12x(i);
                end
             end
          end
        end
      end
   end
end


if n>0
  % check if last pair found needs to be deleted
   num_whichone=size(whichone);
  % array of 1 by 2, column 2 is the size of whichone

  if n < num_whichone(2)
    whichone(n+1)=[];
    whichpartner(n+1)=[];

    disp_e1y(n+1)=[];
```

```
  disp_e1x(n+1)=[];
  disp_e2y(n+1)=[];
  disp_e2x(n+1)=[];
end


% checking for particle on image 2 with multiple partners
i=0;
j=0;
while i<n
    i=i+1;
    while j<n
        j=j+1;

        if whichpartner(i)==whichpartner(j)& (i<j)
            % e.g. multiple partners found
            % select better partner
            if abs(area22(whichpartner(i))-area11(whichone(i)))-...
                abs(area22(whichpartner(j))-area11(whichone(j))) < 0
                % e.g. pair i is better than pair j


                n=n-1;
                % decrease pair counter
                whichone(j)=[];
                whichpartner(j)=[];

  disp_e1y(j)=[];
  disp_e1x(j)=[];
  disp_e2y(j)=[];
  disp_e2x(j)=[];

            else
                n=n-1;
                whichone(i)=[];
```

```
                whichpartner(i)=[];

    disp_e1y(i)=[];
    disp_e1x(i)=[];
    disp_e2y(i)=[];
    disp_e2x(i)=[];
          end
       end
     end
  end


%-------------------------------------------------------------------------
                % show particle pairs on graphics
%-------------------------------------------------------------------------

  for i=1:n
     artifix(i)=e11x(whichone(i))+disp_e1x(i);
     artifiy(i)=e11y(whichone(i))+disp_e1y(i);
     % calculate positions of endpoint 1 on image 2
     originalx(i)=e11x(whichone(i));
     originaly(i)=e11y(whichone(i));
     % original positions of endpoint 1 on image 1
  end
 % calculate the positions on image 2 according to the
 % displacements of two endpoints of fibrous particles found
     if graphicaloutput==1

     figure
     plot(e21x,(e21y*(-1)),'b+',...
        e11x,(e11y*(-1)),'r+',...
        artifix,(artifiy*(-1)),'bo',...
        originalx,(originaly*(-1)),'ro')
     % mark the positions of particles in time t and t+ delta_t
```

```
      legend('position 2','position 1',...
         'calculated on image 2',...
         'particle with id partner')
   end
  % optional plotting for pairs found


%-------------------------------------------------------------------------
   % calculate the velocity and orientation for fibre pairs identified
%------------------------------------------------------------------------ ------

   e1yvelocity=resolution*[disp_e1y]/(delta_t);
  % vertical velocity of endpoint 1 of the fibre, in m/s
   e1xvelocity=resolution*[disp_e1x]/(delta_t);
   % horizontal velocity of endpoint 1 of the fibre, in m/s
   e2yvelocity=resolution*[disp_e2y]/(delta_t);
   % vertical velocity of endpoint 2 of the fibre, in m/s
   e2xvelocity=resolution*[disp_e2x]/(delta_t);
   % horizontal velocity of endpoint 2 of the fibre, in m/s

for i=1:n
 diame1(i)=da1(whichone(i));
 diame2(i)=da2(whichpartner(i));
    % a pair of fibres' diameters (projected lengths)

 delta_e1y(i)=resolution*abs((e12y(whichone(i))-e11y(whichone(i))));
    % the difference between two endpoints of the fibre in the y direction
    % on the No 1 image, in microns
 delta_e2y(i)=resolution*abs((e22y(whichpartner(i))-e21y(whichpartner(i))));
    % the difference between two endpoints of the fibre in the y direction
    % on the No 2 image, in microns

   phi1_1(i)=asin(delta_e1y(i)/particle_length);
```

```
    % elevation angle of the fibre on the No 1 image, in rad
 phi1(i)= phi1_1(i)*180/pi;
    % elevation angle of the fibre on the No 1 image, in degrees

    phi2_1(i)=asin(delta_e2y(i)/particle_length);
    % elevation angle of the fibre on the No 2 image, in rad
 phi2(i)= phi2_1(i)*180/pi;
    % elevation angle of the fibre on the No 2 image, in degrees

 delta_e1x(i)=resolution*(e12x(whichone(i))-e11x(whichone(i)));
     % the difference between two endpoints of the fibre in the x direction
     % on the No 1 image, in microns
 delta_e2x(i)=resolution*(e22x(whichpartner(i))-e21x(whichpartner(i)));
     % the difference between two endpoints of the fibre in the x direction
     % on the No 2 image, in microns

    theta1_1(i)=acos(delta_e1x(i)/(particle_length*cos(phi1_1(i))));
    % azimuth angle of the fibre on the No 1 image, in rad
 theta1(i)=theta1_1(i)*180/pi;
     % azimuth angle of the fibre on the No 1 image, in degrees

    theta2_1(i)=acos(delta_e2x(i)/(particle_length*cos(phi2_1(i))));
    % azimuth angle of the fibre on the No 2 image, in rad
  theta2(i)=theta2_1(i)*180/pi;
     % azimuth angle of the fibre on the No 2 image, in degrees

  %beta1(i)=orientation1(whichone(i));
  %beta2(i)=orientation2(whichpartner(i));
  % projected angles of the fibre on the images 1 and 2

      end
end
```

```
%------------------------------------------------------------------------
                % output calculated results
%------------------------------------------------------------------------

if k==1
   fprintf(fid,'Y80y30x6width12_20d20T2000\n');
   fprintf(fid,'Vex1 \t Elavation1 \t Elevation2 \t Vex2 \t');
   fprintf(fid,'Vyx1 \t Vyx2 \t');
   fprintf(fid,'azimuth1 \t azimuth2 \t diameter1 \t diameter2 \n');
end
% the titles of the data and columns

for i=1:n
   fprintf(fid,...
      '%g \t %g \t %g \t %g \t %-g \t %g \t %g \t %g \t %g \t %g \n',...
   e1yvelocity(i),phi1(i),phi2(i),e2yvelocity(i),e1xvelocity(i),...
   e2xvelocity(i),theta1(i),theta2(i),diame1(i),diame2(i));
end
% write output data, velocity, orientation and diameter, to the file

validpairs=n
% calculate total number of valid pairs in the present run
if validpairs==0
   continue
end
end
fclose(fid);
```

Appendix B: Uncertainty Analysis of Effect of Fibre Length

For the case of free settling fibres, the typical orientation is 75º, while for the case of a turbulent jet flow, it is 50º. That is, the elevation angle of the fibres for these two cases is 15 º (90º- 75º) and 40º (90º - 50º), respectively. These two typical angles represent the majority of fibres and can be used to estimate the uncertainty associated with the fibre's length. The following Table 1 and Figure 1 show the nominal length of fibre AB, its elevation and actual length for fibre AC. Assuming the real length of fibre AB is 2000 µm, for the free settling case, the calculated elevation angle = arcsin (CD/AB) = 16º, while for the turbulent case, the calculated elevation angle = 44º. So the errors are 1º (16º- 15º) and 4º (44º- 40º), respectively, which are within the existing error bars of figures of the papers. Importantly, the paper figures report the average of the data, so that the orientation errors caused by longer and shorter fibres than nominal length are nearly balanced each other. That is, the real errors are far less than 1º and 4º.

Table 1: The fibre's length and their orientations

	Elevation angle=15º	Elevation angle=40º
AB=1850µm	BE=479µm	BE=1189µm
AC=2000µm	CD=518µm	CD=1286µm

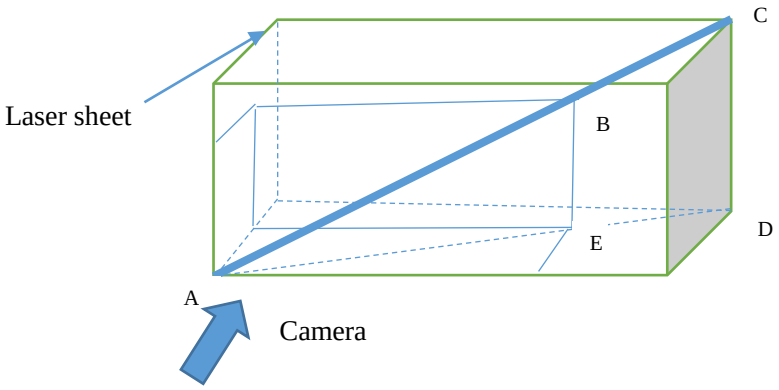

Figure 1: Fibre's length and orientation in the laser sheet

PTV tracks the displacement of fibres, so that it does not depend on the fibre length or orientation. Therefore a fibre's length and orientation have no influence on the velocities of the fibres in image processing. However a difference in intensity between successive laser pulses can influence the velocities where the imbalance between master and slave is sufficient to generate false displacements.